Università degli Studi di Pisa

Facoltà di Ingegneria
Corso di Dottorato in Ingegneria Aerospaziale
XXI Ciclo

Tesi di Dottorato

Design Methodologies of Aeronautical Structures with Acoustic Constraints

1343

Relatore
Prof. Aldo Frediani
Co–relatore
Prof. Luigi Morino

Candidato
Fabio Cetta

Direttore del Corso di Dottorato
Prof. Maria Vittoria Salvetti

Novembre 2009

Alla mia famiglia

Hypotheses non fingo.

Isaac Newton

Considerate la vostra semenza: fatti non foste a viver come bruti, ma per seguir virtute e canoscenza.

Dante Alighieri

Abstract

The aim of this thesis is to present a finite element methodology, based upon a three-dimensional extensions of the *classical Hermite interpolation* and of the *Coons Patch*, for the evaluation of the natural modes of vibration of the air inside cavities (interior acoustics) and of elastic structures (structural dynamics). This methodology is thought for acoustic applications within Multidisciplinary Desing and Optimization, where computational effectiveness is a key attribute, especially during iterative optimization.

The distinguishing feature of the proposed technique is its high efficiency, with the possibility to capture relatively high spatial frequency modes (essential in acoustics) even using a limited number of degrees of freedom. Also, the element is quite flexible and may be used for modeling any three–dimensional geometry. For instance, thin–wall structures like shells and plates are treated with three–dimensional brick elements with a single element along the thickness. An additional advantage is related to the possibility of applying a quasi-static reduction, which allows one to eliminate those degrees of freedom associated with the derivatives while maintaining a high level of accuracy, so that to further improve the effectiveness of the element.

The classical one–dimensional Hermite interpolation is an interpolating technique of order three that uses the function and its derivative at the end points of the element (class $\mathcal{C}^1$). The classical Hermite technique for one–dimensional domains can be extended to higher orders, by including higher derivatives as nodal unknowns, thereby increasing the class of the element (for instance, a Hermite element of order five is of class $\mathcal{C}^2$). Then, the three-dimensional extension is obtained combining the Hermite polynomials in each direction. For example, in the three–dimensional third–order interpolation, the unknowns are the nodal values of the function, of its three partial derivatives, of its three mixed second derivatives, and of its third mixed derivative. Similarly to the one–dimensional approach, higher orders are then obtained by including higher derivatives at nodes.

The Hermite element, even that of order three, is rarely used because of problems that arise whenever the domain is not topologically hexahedral, that is when the coordinate lines (and so the base vectors) of two adjacent blocks present a discontinuity. Specifically, as far as the first-order derivatives are concerned, the problem has been removed by assuming as unknowns the Cartesian coordinates of the gradient, since they are continuous across block boundaries. The problem remains for the higher-order derivatives: in order to express them in terms of Cartesian components, their set should be complete (in particular, we have only the mixed second derivatives and, hence, incomplete information on the Hessian matrix). The remedies to this issue are key features of the present thesis. In particular, two solutions have been proposed in this thesis: (1) the high–order derivatives relative to different blocks are treated as independent unknowns at the block boundaries; (2) a new 3–D high–order internal–nodes family of elements based upon the *Coons Patch* is used: these elements are defined so as to have only the function and the three derivatives as nodal unknowns (thereby, the higher the order of the element the higher the quantity of internal nodes needed for the interpolation).

To be specific, the *Coons Patch* pertain the interpolation over a quadrilateral surface. Given the four edge lines, the Coons Patch is obtained as the sum of the two linear interpolations between opposite boundary lines, minus a bilinear interpolation through the four corner points. From this technique stems the idea of a new family of elements, which edges are generated using the Hermite interpolation. The objective is to extend the use of high–order elements based on a Hermite approach also to generically complicated geometries, so as to take advantage of their effectiveness. These elements will be referred to as *Hybrid* elements.

The validation is based upon the evaluation of the natural eigenvalues (or natural frequencies) and modes of the air vibrating inside hexahedral cavities as well as of those of elastic–thin–plates (in fact, for each of this case exact or accurate solutions are available).

Applications to quite complicated structures, such as curved domains (cylindrical cavities) or very simplified wing–boxes are presented. The results are compared with those obtained using commercial softwares (such as Ansys).

Finally, comparisons with the literature are also included.

Sommario

Lo scopo di questa tesi è presentare una metodologia agli elementi finiti di ordine superiore basata su un'estensione 3–D dell'*interpolazione alla Hermite* e del *Coons Patch*, per valutare i modi naturali di vibrazione sia di strutture elastiche che dell'aria all'interno di cavità (acustica interna). La metodologia è pensata per applicazioni di acustica in un contesto di Ottimizzazione e Progettazione Multidisciplinare (MDO), in cui l'efficienza di calcolo è uno dei requisiti chiave, specie per il fatto di avere frequenti iterazioni numeriche.

Il vantaggio più importante che caratterizza la metodologia proposta è un'elevata efficienza, che consente di catturare modi relativi a frequenze relativamente alte (requisito fondamentale in acustica) anche utilizzando pochi gradi di libertà. Inoltre, lo stesso elemento può essere utilizzato per modellare qualsiasi geometria. Le strutture sottili come piastre e gusci, ad esempio, vengono trattate come domini tridimensionali aventi un solo elemento lungo lo spessore. Un ulteriore vantaggio consiste nel poter applicare in modo efficiente le tecniche di riduzione quasi–statica, che permettono di eliminare i gradi di libertà associati alle derivate, pur mantenendo un alto livello di accuratezza.

La classica interpolazione alla Hermite è una tecnica di interpolazione di ordine tre che utilizza i valori nodali della funzione e della derivata ai due estremi dell'intervallo (classe $\mathcal{C}^1$). Questa tecnica può essere generalizzata ad ordini più elevati, aggiungendo derivate di ordine superiore ai due nodi e, di conseguenza, aumentando la classe dell'elemento (ad esempio, un elemento alla Hermite del quinto ordine risulta di classe $\mathcal{C}^2$). L'estensione a domini tridimensionali del metodo si ottiene combinando i polinomi di Hermite nelle tre direzioni. Ciò comporta, ad esempio, che l'interpolazione alla Hermite del terzo ordine, nello spazio tridimensionale, abbia come incognite nodali: la funzione, le tre derivate prime, le tre derivate seconde miste e la derivata terza mista. L'estensione agli ordini superiori è immediata, una volta considerate tutte le possibili combinazioni degli opportuni polinomi interpolatori.

L'elemento alla Hermite, compreso quello del terzo ordine, è oggi poco utilizzato a causa delle difficoltà che insorgono qualora il dominio non sia topologicamente esaedrico, e cioè quando le linee coordinate (e di conseguenza i vettori di base) di due elementi adiacenti presentano una discontinuità. Per le derivate prime, il problema può essere risolto utilizzando le componenti cartesiane del gradiente delle incognite, dato che queste sono necessariamente continue tra elemento ed elemento. Il problema persiste invece per le derivate di ordine superiore. Infatti, per poterne utilizzare le componenti cartesiane, esse devono costituire un set completo. Già per le derivate seconde, ad esempio, si dispone solo di quelle miste e quindi di una definizione solo parziale della matrice Hessiana. La soluzione a tale problema è un aspetto chiave di questa tesi. In particolare vengono proposti due rimedi distinti: (1) all'interfaccia, le derivate di ordine superiore vengono trattate come variabili indipendenti per ciascun elemento; (2) si utilizza una nuova famiglia di elementi a nodi interni che nasce dalla tecnica di interpolazione alla Coons (il cosiddetto *Coons Patch*), in modo tale da avere solo la funzione e le sue tre derivate prime come incognite nodali (l'ordine dell'elemento è perciò univocamente determinato dal numero dei nodi interni).

Il *Coons Patch* consiste in una tecnica di interpolazione per ricostruire una superficie quadrilatera a partire dai suoi lati. Data l'espressione analitica dei quattro lati, il Coons Patch si ottiene come somma di due interpolazioni lineari tra lati opposti meno un'interpolazione bilineare tra i quattro vertici. Da questa tecnica nasce l'idea di una nuova famiglia di elementi per i quali è stato deciso di generare gli spigoli con una interpolazione alla Hermite. Lo scopo di questa formulazione è di estendere le possibilità di utilizzo degli elementi di ordine superiore basati su tecniche alla Hermite anche a geometrie comunque complicate, in modo tale da sfruttarne le caratteristiche di efficienza ed accuratezza evidenziate in casi semplici. Questi elementi sono stati chiamati *Hybrid elements*.

La validazione del metodo si basa sull'analisi degli autovalori (o delle frequenze naturali) e dei modi dell'aria all'interno di cavità esaedriche e di piastre sottili elastiche (per entrambi i casi, infatti, sono disponibili soluzioni esatte o approssimate).

La metodologia è stata anche applicata a strutture più complesse, come domini a curvatura (ad esempio cavità cilindriche) o cassoni alari estremamente semplificati. I risultati sono stati messi a confronto con quelli ottenuti attraverso i più noti softwares agli elementi finiti (come Ansys).

Infine sono state effettuate analisi di confronto con significativi risultati presenti in letteratura.

Acknowledgements

A first thought goes to Professor Aldo Frediani, that always gave me the support I needed. I wish to express my sincere appreciation for his availability at every hour and in every moment.

A special acknowledgement is dedicated to Professor Luigi Morino: with his intuitions and ideas, in many occasions he brought me closer to the mathematical and physical reality I had initially perceived, enabling me to grasp its complexity. His contribution in this scientific path is on the same plane of his friendship (my piano is still waiting for a piano–clarinet duo!).

Then, I thank Giovanni Bernardini, for his precious help in computing resources and for having shared numerical tricks and suggestions, especially about modeling.

Finally, I wish to thank my parents for the support that I have received throughout this period and – why not – for the strenght they gave me to reach this goal.

Contents

I Part one **1**

1 Introduction **3**
- 1.1 Context 3
- 1.2 Objective and goals 3
- 1.3 Structure of the thesis 7

2 Hermite brick elements **11**
- 2.1 Classical Hermite interpolation 11
- 2.2 The Hermite 3rd order 8−node element 13
- 2.3 The block–boundary problem 14
- 2.4 Remedy: Schemes B and C 15

3 Higher–order Hermite elements **19**
- 3.1 General 1−D Hermite interpolation 19
  - 3.1.1 5th order 2−node interpolation 23
  - 3.1.2 7th order 2−node interpolation 26
- 3.2 Higher–order Hermite bricks 30
  - 3.2.1 The Hermite 5th order 8–node element 30
  - 3.2.2 The Hermite 7th order 8–node element 32
- 3.3 Block–boundary problem 35

4 Hybrid brick elements **37**
- 4.1 State of the art 37
- 4.2 The Coons Patch 38
- 4.3 The three–dimensional extension 39
- 4.4 The Hybrid 3rd order 8−node element 40
- 4.5 Comments 43

5 Higher–order Hybrid element 45
5.1 Higher–order WEP Hybrid elements 45
5.1.1 The Hybrid 7th order $8-$node element 46
5.2 Block–boundary problem 49
5.3 One–dimensional WIP interpolation 49
5.3.1 5th order $3-$node interpolation 51
5.4 Higher–order WIP Hybrid elements 51
5.4.1 The Hybrid 5th order 27–node element 53
5.5 Comments 54

II Part two 55

6 Mass and Stiffness matrices 57
6.1 Mass and stiffness matrices in acoustics 57
6.1.1 One–dimensional eigenvalue problem 58
6.2 Mass and stiffness matrices in structural dynamics 59

7 Validation and assessment 61
7.1 Preliminary definitions 62
7.2 One–dimensional case 63
7.2.1 h–convergence 64
7.2.2 Preliminary WIP p–convergences 77
7.2.3 WEP schemes vs WIP schemes 78
7.3 Three–dimensional interior acoustics 93
7.3.1 $h-$convergences 93
7.3.2 High–frequencies analysis 99
7.3.3 Hermite 3rd order $8-$node element 101
7.3.4 Hermite 5th order $8-$node element 105
7.3.5 Hermite 7th order $8-$node element 111
7.3.6 Hybrid 3rd order $8-$node element 115
7.3.7 Hybrid 7th order $8-$node element 119
7.3.8 Hybrid 5th order $27-$node element 123
7.3.9 IRS for interior acoustics 127
7.4 Structures 132
7.4.1 Guyan for (thin) structures 132
7.4.2 Free and clamped plates 139
7.4.3 Hinged plates 145
7.4.4 From $2-$D plate theory to a $3-$D continuum 156
7.5 Block–boundary problem: Scheme C 158

8 Test cases 165
8.1 Comparisons with the literature 165
8.2 Acoustics 169
8.2.1 Cylindrical cavity 169
8.3 Structures 173
8.3.1 Simplified wing–box 173

9 Concluding remarks 177

III Appendix 179

A Interior acoustics – structural dynamics coupling 181
A.1 Pressure–displacement formulation 181
A.2 Potential velocity–displacement formulation 183

B An algorithm for geometry generation 185
B.1 The basic surface: a Coons patch 185
B.2 The continuous–normal surface 186
B.3 From surfaces to blocks 190

C Differential Geometry 191
C.1 Differential geometry of a surface 191
C.2 Differential geometry for a layer 193

D Moving the hinge of a hinged plate 197

E Reduced Order Model 201
E.1 Guyan's quasi–static reduction 201
E.2 O'Callaghan's IRS technique 204

List of Figures 211

List of Tables 218

List of Acronyms 221

Part I

Part one

Chapter 1

Introduction

1.1 Context

In most of the engineering fields (for example, Aerospace, Automotive, Oil & Gas) the typical design process of a quite complex product consists essentially of three steps: (1) *Conceptual Design*, which is related to the selection of the solution that best fits the requirements; (2) the *Preliminary Design*, which consists in the definition and in a deep analysis of the solution and (3) the *Detailed Engineering*, that is the final phase of the design process in which the whole scope of work is defined at the required level of details (this is also referred to as *Front–End Engineering Design*).

The multidisciplinary nature of the first two phases (at least of the Conceptual Design) requires the integration of the variouos disciplines involved and the introduction of frequent changes in terms of geometrical and physical properties of the solution, in order to satisfy all the requirements simultaneously. This means iterative calculations which, because of the time constraints, often leads to the use of low fidelity and sometimes over–simplified models, despite the need of high–fidelity tools to balance the lack of experimental data.

In addition, all the different models used for the various disciplines are usually derived from a unique CAD model from which customized models are built and adapted for the single discipline.

1.2 Objective and goals

The research activity presented in this thesis pertain the development of a new three–dimensional high–order finite element methodology, for the evaluation of the natural modes of vibration of the air inside a cavity (interior acoustics) and/or of an elastic structure (structural dynamics), for relatively high frequencies, so as to make the technique useful for acoustic applications, in particular for the fluid/structure acoustic coupling. The work is to be considered as a first step towards the development of a tool to be used in Multidisciplinary Optimization and Design (MDO). Therefore, the uman intervention is to be minimized.

Specifically, to analyze the fluid/structure coupling within an MDO context, it is useful to have an element with four major features: (i) the element should be efficient in capturing high spatial frequency modes (as essential in interior acoustics); (ii) the element should be sufficiently general, so as to model efficiently all types of geometries, thereby facilitating the connection of various components (as essential in MDO); (iii) the element should be simple; specifically, it should not require complicated topologies (requiring human intervention), thereby rendering feasible automated-resizing programming for optimal design applications; (iv) the element should be quite accurate, so as to give good results with few elements, an important feature when repeated calculations occur (as in MDO).

High-order finite elements are commonly employed in most of the engineering fields. For example, among the finite elements in the commercial softwares most commonly used (Ansys, Nastran) , one has the 20–nodes brick element, which has quadratic shape-functions or the 32–nodes brick element, which uses cubic shape functions.

This statement needs to be qualified for applications to structure/fluid interaction, which is the main objective of this work. Here, such an interaction is conceived as the coupling of the dynamic of the air inside a cavity and that of the structure that surrounds the cavity. This coupling is best formulated in terms of the natural modes of vibration of both the air and the structure.

The basic idea for the proposed methodology stems from the classical *Hermite interpolation*, which is of order three and uses the nodal values of the interpolating function and of its derivative at the two end–nodes (class $\mathcal{C}^1$). In the field of structural dynamics, the unknown function is the displacement vector $\mathbf{u}$ whereas in interior acoustic problems (without considering the interaction with the external structure) the unknown function is the pressure p (or the velocity potential φ).

In the three–dimensional extension of the third-order Hermite element and for structural dynamics, the unknowns are the nodal values of the three-dimensional displacement vectors, the three partial derivatives, the three second mixed derivatives, and the third mixed derivative. Similarly, in acoustics, the unknowns are the nodal values of the three-dimensional scalar function of the pressure, its three partial derivatives, its three mixed second derivatives, and its third mixed derivative.

Note that, in the Hermite interpolation the derivatives of order higher than first are not all simultaneously present. For example, we have only the three second mixed derivatives and the only third mixed derivative. Hence, we have incomplete information on the Hessian matrix. This causes problems at the block boundaries if the coordinate lines are discontinuous. This last consideration is the source of an important drowback which affects the efficacy of the Hermite element. It will be referred to as the *block–boundary problem* throughout the thesis and will be briefly outlined in the following.

Accordingly, despite their high–accuracy for the study of relatively simple domains, elements based on the Hermite interpolation are rarely used in practice because of problems that arise whenever the domain is not topologically hexahedral. In particular, the problems occur whenever the coordinate lines (and therefore the base vectors) of two adjacent blocks present a discontinuity. This implies that the gradient as well as the second– and higher–order derivatives are discontinuous.

In order to remedy this issue, a first approach has just been developed and preliminarily studied in the past; it is related to the definition of the topology within the domain. As far as the first–order derivatives are concerned, the problem is easily removed by assuming as unknowns the values of the Cartesian coordinates of the gradient of the unknown, since these quantities are continuous across block boundaries.[1] The problem, however, remains for the mixed second–order derivatives, because, in order to express them in terms of Cartesian derivatives, one needs all the second–order derivatives, not just the mixed ones, which are the only ones utilized in the three–dimensional Hermite interpolation. Similar considerations hold for the third-order derivatives.

In order to avoid the situation caused by the block–boundary problem, the technique suggested consists of assuming that, for the nodes located on the boundaries between blocks, the second– and third–order derivatives relative to different blocks are treated as independent unknowns. This technique is here validated by applications to simple domains, artificially divided in

---

[1] Provided, of course, that the gradient is continuous: for isotropic elastic materials this is true whenever the elastic coefficients (*i.e.*, the Young modulus E and the Poisson ratio ν) are continuous; this is the only case considered here.

different blocks (details of the formulation are provided in Section 2.4 whereas the obtained results are discussed in Section 7.5).

Next, a second approach has been introduced which is very convenient to circumvent the block–boundary problem. This enhances considerably the user–friendliness of the methodology and it is the key innovation of this work. The new scheme is obtained by combining the one–dimensional Hermite interpolation with a three–dimensional extension of the *Coons' Patch* technique, with edges generated by Hermite interpolation. The new element will be referred to as the *Hybrid* element.

To explain such an approach, consider a topologically quadrilateral surface. Given the four edge lines, the Coons patch is obtained as: (1) the sum of the two linear interpolations between opposite boundary lines, minus (2) a bilinear interpolation through the four corner points (for details see Chapter 4). From this interpolation technique stems the basic idea for the new Hybrid elements, whose edges are generated using the 3rd order Hermite interpolation. In addition, the number of unknowns of the related Hybrid (*i.e.*, that of the same order) is reduced by a factor two with respect to the Hermite scheme of order 3(and the computational time by an order of magnitude), without any reduction on the accuracy of the scheme, which remains of order 3. It is worth noting that this element, like the Hermite element, provides a solution that is continuous with its gradient (class C^1). However, the most important improvement introduced by this scheme is the fact that only the values of the unknown function and of its gradient are required at the node of each brick. This impies that the block–boundary problem has been eliminated since for the first order derivatives one can use the Cartesian components (that are continuous).

Extension to higher orders have been investigated. Specifically, Hybrid and Hermite elements of orders from three to seven have been extensively validated and assessed and a general formulation for generating one–dimensional high–order shape functions has been developed, having distinguished two families of elements: the WIP elements(*i.e.*, With Internal Points) and the WEP elements (*i.e.*, With End Nodes). This distinction is crucial because each class of elements presents specific advantages.

In particular, if one adopts a $\mathcal{C}^1$ WIP interpolation, whose order is defined by the quantity of nodes utilized, being the nodal unknowns only the function and the first derivative (for details see Chapter 3), the block–boundary problem can be eliminated also for the higher–order elements (that is, the elements of order higher than three).

In summary, combining the various possibility of interpolation, one obtains effective elements based on a Hermite approach with the key advantage to be not affected by the block–boundary nodes problem and thereby to be used for an effective analysis of complicated topologies.

Finally, the advantages of the formulations affordable by using quasi–static reduction are outlined. As far as an eight–noded high–order element is conceived (for example, the Hermite element of order p), a large percentage of the unknowns is related to the derivatives (to be specific, if $[(p+1)/2]^3$ is the total amount of unknowns per node – or unknown vectors per node – of a Hermite element, one has $[(p+1)/2-1]^3$ unknowns related to the derivatives). These unknowns can therefore be eliminated using a model order reduction scheme, such as a Guyan's quasi–static reduction. This results in a highly efficient scheme that has a high accuracy even though the retained unknowns in the final reduced model are relatively few.

The validations cosidered are related to the modal analysis of the air vibrating inside a cavity without considering the structure that surronds it (interior acoustics in absence of the structure) as well as to the modal analysis of a vibrating elastic thin–plate, using various kinds of constraint (specifically, free; clamped and hinged boundary conditions have been considered).

On the basis of the results obtained, the resulting methodology that is most efficient is the one based upon a combination of three important ingredients: (1) high–order extension of the Hermite interpolation, (2) the three–dimensional extension of Coons' Patch technique, and (3) model order reduction. This combination is very powerful and yields a methodology with the distinguishing feature of a very high accuracy, with the possibility to capture effectively high spacial frequencies, as required in aeroacoustics applications. Indeed, the first two items (Hermite and Coons) yield a finite element that is very accurate. The third item is related to the efficiency, since it is possible to largely reduce the order of the scheme while preserving a high level of accuracy.

1.3 Structure of the thesis

This thesis consists of two parts. **Part I** is dedicated to the mathematical formulation. In this part the Hermite elements and the Hybrid elements are introduced along with their higher–order extensions. The chapters are structured following the chronological–logical development of the activity. The mathematical background for the algorithms used to reduce the order of the finite element matrices is given in appendix (see Appendix E). **Part II** is related to results and assessments. A preliminary chapter is dedicated to the mass and stiffness matrices definition for interior acoustics as well as for structural dynamics. This final chapter contains the concluding remarks.

Chapter 2 describes the starting point of the activity: the Hermite element. Specifically, the basics of the classical third–order Hermite interpolation are presented with the aim to introduce the three–dimensional Hermite brick element. The so called block–boundary problem is addressed in Section 2.3 to put in evidence the limits of the basic formulation. The remedy proposed is described in Section 2.4.

Chapter 3 addresses the extension to higher orders, along with the extension of the block–boundary problem.

Chapter 4 introduces the Hybrid element in its third order formulation. In order to put the thesis in the proper perspective, Section 4.1 describes the works produced in the literature about finite element techniques based on the Coons Patch for three–dimensional interior acoustics. The aim is to put in evidence the differences between the proposed formulation and the closer elements available in the literature (whereas the comparison of the results obtained is presented in Part Two). Sections from 4.2 to 4.4 illustrate the mathematics of the innovative Hybrid element, that is conceived as an extension of the bi–dimensional Coons Patch. A final section (Section 4.5) to comment the differencies between the Hermite and the Hybrid elements closes Chapter 4.

Chapter 5 addresses the extension to higher orders.

Chapter 6 consists of two sections (Sections 6.1 and 6.2) for the definition of the mass and stiffness matrices in both the problem considered: that of the air vibrating inside a cavity and that of the elastic structure. Relatively to Section 6.1, a subsection has been dedicated to the one–dimensional Helmholtz problem (in practice, a second–order derivative operator), since this is used in the next to assess the elements for very simple domains.

Chapter 7 opens with a section of definitions (Section 7.1), in which the main expressions of the errors, used for the assessment of the modes as well as of the eigenvalues are given. Section 7.2 is related to mono–dimensional problems, for which an exact solution is available; since no bricks are here defined, the results are limited to the basic WEP and the WIP formulations, whitout mention to the Hermite and Hybrid elements. Comparisons between the two formulations are presented, throughout a $h-$ and $p-$convergence study. Next, the three–dimensional Helmholtz equation has been considered with simple geometries (cubes and parallelepipeds), for which, again, an exact solution is available. This has been addressed in Section 7.3. Subsection 7.3.9 regards the analysis of the results obtained for interior acoustics using the IRS reduced formulation. Section 7.4 regards the modal analysis of plates with various kind of constraints (specifically: free plate; clamped plate and hinged plate). Finally, Section 7.5 is that related to the block–boundary problem. It has been studied for thin square plates (structural dynamics) and for cubic cavities (interior acoustics).

Chapter 8 contains examples of application of the proposed methodology. To begin with, Section 8.1 wants to quantify the effectiveness of the Hybrid methodology through a comparison with the Provatidis' Coons Macroelement.[1] Next, Section 8.2.1 regards the application of the methodology to curved domains. The results are assessed through those obtained with Ansys. Finally, Section 8.3.1 is related to the structural modal analysis for a wing–box. The wing–box considered here is very simple, is conceived as a thin–walled beam and has not a technical meainig: the aim is to test the methodology for a quite complex domain (in this case generated by 8 blocks).

Finally, **Chapter 9** contains some concluding considerations about the results achieved and about the activities to be done in the future.

Chapter 2

Hermite brick elements

In this chapter, the third–order 8−node Hermite element is described, so as to provide the appropriate background for the introduction of the higher–order Hermite and Hybrid elements described in the next. The Hermite element consists in a third–order *brick* element which nodes are placed at the vertices. Since the three-dimensional extension derives from the classical one–dimensional third–order Hermite interpolation (to be considered in each direction), this formulation is introduced first. After describing the Hermite brick element, the last two sections are dedicated to the problems that arise for complex structures and the remedies proposed.

2.1 Classical Hermite interpolation

The classical one–dimensional Hermite interpolation is also referred to as the Bogner-Fox-Schmit element.[2] This interpolation, that is of class $\mathcal{C}^1$, is given by

$$f(x) = f_-^{(0)} M_-(x) + f_+^{(0)} M_+(x) + f_-^{(1)} N_-(x) + f_+^{(1)} N_+(x) \tag{2.1}$$

(for $x \in [-1, 1]$), where $f_\pm^{(0)}$ denotes the values of $f(x)$ at $x = \pm 1$, and $f_\pm^{(1)}$ denotes the values of df/dx also at $x = \pm 1$. The Hermite interpolation polynomials $M_\pm(x)$ and $N_\pm(x)$ are given by (also for $x \in [-1, 1]$)

$$M_\pm(x) = \frac{1}{4}(2 \pm 3x \mp x^3) \quad \text{and} \quad N_\pm(x) = \frac{1}{4}(\mp 1 - x \pm x^2 + x^3). \tag{2.2}$$

Note that, for instance, $M_+(x)$ is (uniquely) determined by the conditions $M_+(1) = 1$, $M_+(-1) = 0$ and $dM_+/dx = 0$ for $x = \pm 1$. Similarly, we have that $M_-(-1) = 1$, $M_-(1) = 0$ and $dM_-/dx = 0$ for $x = \pm 1$. For the other two polynomials one has that $N_{\pm}(\pm 1) = 0$ whereas $dN_{-}/dx = 1$ for $x = -1$ and $dN_{+}/dx = 1$ for $x = 1$.

Figure 2.1 shows the $M_{\pm}(x)$ Hermite interpolators whereas Fig. 2.2 depicts the $N_{\pm}(x)$ Hermite polynomials.

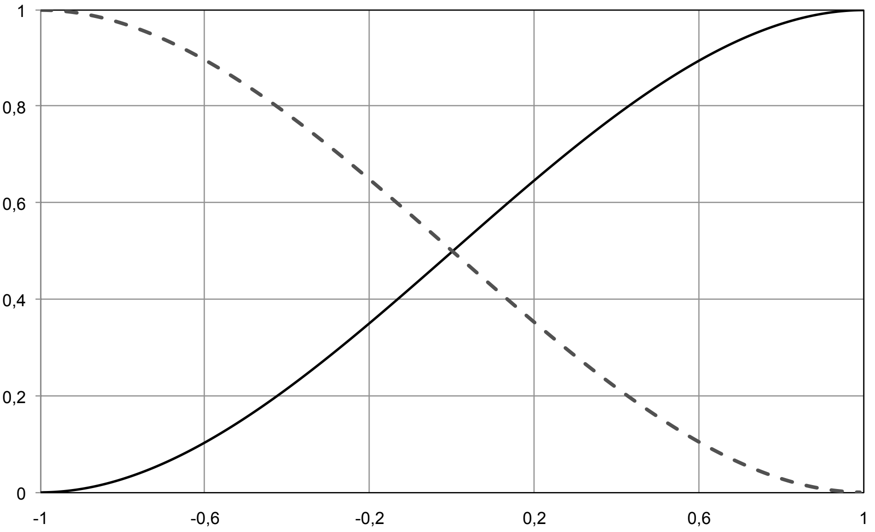

Figure 2.1: Hermite polynomials: M_{-} (dashed line) and M_{+} (continuous line)

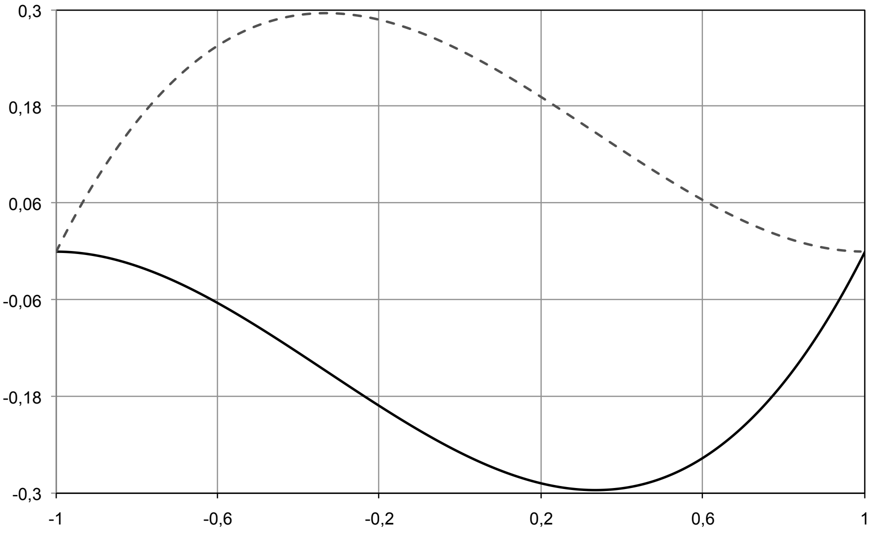

Figure 2.2: Hermite polynomials: N_{-} (dashed line) and N_{+} (continuous line)

2.2 The Hermite 3rd order 8−node element

In order to extend the concept to the three–dimensional case, introduce the curvilinear coordinates ξ^α and consider a brick element, which by definition corresponds to a cube in the ξ^α–space ($\xi^\alpha \in [-1,1]$). Using the Hermite interpolation in all three directions yields an interpolated function $f(\xi^\alpha)$ (*e.g.*, the components of $\mathbf{x}(\xi^\alpha)$ for the geometry, and the velocity potential $\varphi(\xi^\alpha)$ for interior acoustics, as well as the components of the displacement $\mathbf{u}(\xi^\alpha)$ for structural dynamics) given by

$$f(\xi^\alpha) = \\ \sum_{\mathbf{s}} \left(P_{\mathbf{s}}(\xi^\alpha) f_{\mathbf{s}} + \sum_{\beta=1}^{3} P_{\mathbf{s}}^{\beta}(\xi^\alpha) f_{\mathbf{s},\beta} + \sum_{\beta\gamma\in I_2} P_{\mathbf{s}}^{\beta\gamma}(\xi^\alpha) f_{\mathbf{s},\beta\gamma} + P_{\mathbf{s}}^{123}(\xi^\alpha) f_{\mathbf{s},123} \right),$$

where $\mathbf{s} := (s_1, s_2, s_3)$, with $s_k = 1, 2$, defines the eight nodes of the brick element ($\sum_{\mathbf{s}}$ is understood to span over all the eight values of $\mathbf{s}$); moreover, noting that the second–derivative summation spans only over the mixed derivatives, we have that $I_2 := \{(1,2); (2,3); (3,1)\}$, whereas the term 123 is the only mixed derivative of order three. In addition, $P_{\mathbf{s}}(\xi^\alpha)$, $P_{\mathbf{s}}^{\beta}(\xi^\alpha)$, $P_{\mathbf{s}}^{\beta\gamma}(\xi^\alpha)$, and $P_{\mathbf{s}}^{123}(\xi^\alpha)$ are suitable products of the Hermite polynomials in Eq. 2.2; for instance,

$$\begin{aligned} P_{\mathbf{s}}(\xi^\alpha) &= M_{s_1}(\xi^1) M_{s_2}(\xi^2) M_{s_3}(\xi^3), \\ P_{\mathbf{s}}^{1}(\xi^\alpha) &= N_{s_1}(\xi^1) M_{s_2}(\xi^2) M_{s_3}(\xi^3), \\ P_{\mathbf{s}}^{13}(\xi^\alpha) &= N_{s_1}(\xi^1) M_{s_2}(\xi^2) N_{s_3}(\xi^3), \\ P_{\mathbf{s}}^{123}(\xi^\alpha) &= N_{s_1}(\xi^1) N_{s_2}(\xi^2) N_{s_3}(\xi^3). \end{aligned} \tag{2.3}$$

Finally, "$_{,\beta}$" denotes the partial derivative with respect to ξ^β (for instance $f(\xi^\alpha)_{,\beta\gamma} = \partial^2 f(\xi^\alpha)/\partial\xi^\beta\partial\xi^\gamma$).

The expressions above provide the desired local interpolation procedure for any function, in particular, for the unknown itself whenever this is a scalar function $u(\xi^\alpha)$, as in acoustics. These may be combined to yield a global interpolation as

$$u(\xi^\alpha) = \sum_{p=1}^{P} z_p \chi_p(\xi^\alpha), \tag{2.4}$$

where the z_p's comprise the nodal values of u, $u_{,\alpha}$ ($\alpha = 1,2,3$), $u_{,\beta\gamma}$ ($\beta, \gamma \in I_2$), and $u_{,123}$ (hence $P = 64$), whereas $\chi_p(\xi^\alpha)$ are the global shape functions, defined locally by Eq. 2.3.

If the unknown is a vector function $\mathbf{u}(\xi^\alpha)$, as in structural dynamics, we have

$$\mathbf{u}(\xi^\alpha) = \sum_{p=1}^{P} z_p \boldsymbol{\chi}_p(\xi^\alpha), \tag{2.5}$$

where now the z_p's comprise the nodal values of the Cartesian components of $\mathbf{u}$, $\mathbf{u}_{,\alpha}$ ($\alpha = 1, 2, 3$), $\mathbf{u}_{,\beta\gamma}$ ($\beta, \gamma \in I_{\beta\gamma}$), and $\mathbf{u}_{,123}$, whereas $\boldsymbol{\chi}_p(\xi^\alpha)$ are vector global shape functions, obtained from the $\chi_p(\xi^\alpha)$'s in Eq. 2.4 through multiplication by the appropriate base vector. The same interpolation is used for the geometry (isoparametric representation).

2.3 The block–boundary problem

In the following, the domain is conceived as a collection of topologically hexahedral subdomains (*blocks*), which are described by equations of the type $\mathbf{x} = \mathbf{x}(\xi^\alpha)$, with $\xi^\alpha \in [-1, 1]$ ($\alpha = 1, 2, 3$). Each block is divided into $N_1 \times N_2 \times N_3$ elements (*bricks*).

The scheme presented in Section 2.2, hereby referred to as *Scheme A*, presents no problems as long as the geometry of the problem is topologically hexahedral (that is, a rectangular parallelepiped in the ξ^α-space). In this case, in fact, all the partial derivatives assume the same value for all the bricks that share a node. Major problems arise for more complicated structures, even for geometries that may be obtained as combinations of topologically hexahedral blocks.

Using the same global curvilinear coordinates for all the elements, the domain may be divided into elements that are themselves topologically hexahedral, with continuous covariant base vectors (tangents to the coordinate lines), defined by

$$\mathbf{g}_\alpha := \frac{\partial \mathbf{x}}{\partial \xi^\alpha} \tag{2.6}$$

However, if the base vectors are discontinuous, then the partial derivatives of any function $f(\xi^\alpha)$ with respect to ξ^α,[1]

$$\frac{\partial f}{\partial \xi^\alpha} = \frac{\partial f}{\partial x_k} \frac{\partial x_k}{\partial \xi^\alpha} = \operatorname{grad} f \cdot \mathbf{g}_\alpha, \tag{2.7}$$

---

[1] The Einstein summation convention for repeated indices is used throughout the present paper. The indices always range from 1 to 3. Also, Latin indices denote Cartesian coordinates, and Greek ones curvilinear coordinates.

are also discontinuous, even when grad u is continuous. Then, the method becomes complicated to use. Specifically, the main obstacle is the fact that, for instance, the second mixed derivatives $\partial^2 f/\partial\xi^1\partial\xi^2$ at a node assume different meaning for the eight elements that share that node. The same holds true for the third–order one.

For topologically complicated geometries is not possible to introduce a coordinate system such that the base vectors are continuous everywhere and this is one of the most important reason why the use of the Hermite element has been limited to topologically hexahedral geometries. On the other hand, the method appears to be quite powerful and hence deserve further attention. For this reason, in the past few years, this issue have been addressed, so as to render the Hermite element useful for complex geometries as well.[3] The approach proposed is presented below.

It should be emphasized that, for the first–order derivatives, the problem may be removed by assuming as unknowns the values of the Cartesian coordinates of grad f ($f_{,h} := \partial f/\partial x_h$), provided, of course, that the gradient is continuous, a condition always satisfied in linear acoustics and in structural dynamics under the assumption of continuity for the Young modulus E and the Poisson ratio ν. The partial derivatives may then be obtained using Eq. 2.7. The problem, however, remains for the second–order mixed derivatives, because, in order to express them in terms of Cartesian components, one needs all the second–order derivatives, not just the mixed ones, which are the only ones utilized in the three–dimensional Hermite interpolation (the derivatives $\partial^2 f/\partial{\xi^\alpha}^2$ are in fact not included in the unknowns). Similar considerations hold for the third–order derivatives.[2]

The following section illustrates the two methods proposed to solve the problem.

2.4 Remedy: Schemes B and C

The above–mentioned problems arise when the base vectors, $\mathbf{g}_\alpha = \partial\mathbf{x}/\partial\xi^\alpha$, of two adjacent blocks present a discontinuity. It is apparent that resolving this issue is crucial to the usefulness of the Hermite element.

---

[2] Of course, for simple topologically hexahedral geometries (*i.e.*, single–block domain), the formulation presents no problems; indeed, in this case, each partial derivative assumes the same value for all the eight elements that share a node.

For the sake of completeness, consider first the somewhat disappointing results obtained in Morino et al.[4] The first approach tried in[4] consists of expressing the second– and third–order derivatives, via suitable finite differences, in terms of the function at the nodes (akin to the approach used by Gennaretti et al.[5] in a related boundary–element method for aerodynamics). The results for a topologically hexahedral domain, were much worse that those obtained with the basic Scheme A discussed above, and even worse than those obtained with the NASTRAN CHEXA element (Ref.[6]). In another approach used in Ref.,[4] the second– and third–order derivatives were set equal to zero. The results were even worse. Then, still in Ref.,[4] a fifth–order Hermite interpolation was considered, because in this case all the second–order derivatives are available, and hence they as well may be expressed in terms of Cartesian second–order derivatives (for, the second–order derivatives are the covariant components of the Hessian tensor). This shifted the problem from the mixed second– and third–order derivatives into those of order 3, 4, and 5. As expected, the results obtained (still in Ref.[4]) with the complete fifth–order scheme (*i.e.*, retaining all the unknowns) were much better than the corresponding third–order ones. However, those obtained with the "reduced" fifth–order scheme (*i.e.*, obtained by setting to zero the derivatives of order 3, 4, and 5) were worse than the "full" third-order *Scheme A*.

On the basis of these somewhat disappointing results, two new schemes have been explored in Ref.[3] In the first (hereby referred to as *Scheme B*), the second– and third–order derivatives are treated as independent variables for each element of a given node (*i.e.*, for each node, the second– and third–order derivatives are allowed to assume eight different values). Of course, Scheme B requires many more unknowns than Scheme A. Hence, as a compromise, a third scheme, hereby referred to as *Scheme C*, has been introduced. This is a combination of Schemes A and B, in the sense that Scheme B is used for the block–boundary nodes (*i.e.*, nodes that are common to two or more blocks), whereas Scheme A is used for all the interior nodes (*i.e.*, for the large majority of the nodes). The first results, presented in Ref.[3] and further analyses presented here in Section 7.5, are revealed extremely encouraging.

However, Scheme C requires a major quantity of unknowns with respect to Scheme A, even though much less than Scheme B. This additional quantity of unknowns is related to the amount of interface nodes (and complicated geometries could require a quite large number of interface nodes). Moreover, the complexity of the block-boundary node problem increases as one increases the order of the scheme (the higher the order, the higher the amount of nodal unknowns needed). Hence, a more effective solution (not affected by such a limitation) has also been developed (see Section 7.5 for a complete discussion of the results).

In addition, an innovative solution has been developed(an approach that was introduced for the first time in Ref.[7]), which enhances considerably the user–friendliness of the methodology. The objective was to avoid the block–boundary node problem, even maintaining a high order of the scheme. It is possible to do this by adopting a hybrid formulation, that involves different interpolation schemes, so as to have only the function and its first derivative as nodal unknowns. In such a scheme, in fact, one eliminates the issue of incomplete information on the Hessian (there are not higher–order derivatives) and can always use the Cartesian components of the gradient, that are continuous across the interface between different blocks. Chapter 4 is extensively dedicated to this approach.

Chapter 3

Higher–order Hermite elements

In this chapter, an extension to higher–orders for the scheme presented in Chapter 2 (the Hermite brick element) is proposed.

As far as the Hermite interpolation is conceived, the extension to higher–orders will be addressed considering again the nodes only at the end–points and by adding higher nodal derivatives. The mathematical formulation for the one–dimensional case is presented in Sections 3.1. Next, the three–dimensional formulation for the orders 5 and 7 is presented in Section 3.2.

3.1 General $1-$D Hermite interpolation

In this section, a scheme which nodes are placed only at end–points is used. This scheme will be treated as an extension of the classical Hermite interpolation, since it is obtained simply by adding higher nodal derivatives.

Hence, if one has a total number of parameters per node equal to n (the function and its $n-1$ derivatives), the degree of the interpolating polynomial is $r = 2n - 1$.

This formulation, which is general, is an extension to the order r of the classical Hermite interpolation. In fact, for $n = 2$ one has $r = 3$, that is the classical Hermite interpolation of Section 2.1.

Accordingly, the aim of this section is to define a general interpolation formula of order r for a function $u = u(x)$ $(x \in [-1, 1])$, when the node are placed at $x = -1$ (this node will be referred to with the use of the superscript "$_-$") and $x = 1$ (we will be refer to it using the superscript "$_+$"). In order to accomplish this, assume that

$$u(x) = \sum_{p=0}^{n-1} u_p^+ \; M_p^+(x) + \sum_{p=0}^{n-1} u_p^- \; M_p^-(x) \tag{3.1}$$

where n is the total number of the parameters per each of the two nodes (the value of the function itself along with the value of its $n-1$ derivatives) and u^+, u^- are the unknowns at the first and at the second node respectively. Denote with p and q two integers such that $p+q = n-1$ and $p = 0, \ldots, n-1$ (therefore, p refers to the order of the nodal derivatives). The order r is related to the nodal unknowns by the equation $r = 2n-1 = (p+q)+n$. Indicates with $M_p^\pm(x)$ $(p = 0, \ldots, n-1)$ the polynomials of order r of the kind:

$$M_p^\pm(x) = \sum_{j=0}^{q} a_{p_j}^\pm (1 \mp x)^{p+j} \left(\frac{1 \pm x}{2}\right)^n \tag{3.2}$$

where $a_{p_j}^+$ and $a_{p_j}^-$ are sets of $q+1$ coefficients, such that the following conditions be satisfied:

$$\begin{aligned}
&\frac{d^k M_p^\pm}{dx^k}(\mp 1) = 0 \qquad \text{for} \qquad k = 0, \ldots, n-1 \;\; \text{and} \;\; k \neq p \\
&\frac{d^k M_p^\pm}{dx^k}(\pm 1) = \delta_{kp}
\end{aligned}$$

In the following we determine the $a_{p_j}^\pm$ coefficients (for $j = 0, \ldots, q$). In view of the following use of Eq. 3.2, and referring to the p polynomial assume that:

$$F_\pm(x) = \sum_{j=0}^{q} a_{p_j}^\pm (1 \mp x)^{p+j} \qquad \text{and} \qquad G_\pm(x) = \left(\frac{1 \pm x}{2}\right)^n$$

where the subscripts $_\pm$ refer to polynomials $M^\pm(x)$. It can be easily verified that the functions $F_\pm$ and $G_\pm$ satisfy the following properties:

$$\begin{aligned}
&G_\pm(\mp 1) = G_\pm^{(1)}(\mp 1) = \ldots = G_\pm^{(n-1)}(\mp 1) = 0 \\
&G_\pm(\pm 1) = 1; \;\; G_\pm^{(1)}(\pm 1) = \pm\frac{n}{2}; \ldots ; G_\pm^{(k)}(\pm 1) = (\pm 1)^k \frac{n!}{2^k (n-k)!} \\
&F_\pm(\pm 1) = F_\pm^{(1)}(\pm 1) = \ldots = F_\pm^{(p-1)}(\pm 1) = 0 \\
&F_\pm^{(p)}(\pm 1) = (\mp 1)^p \; p! a_{p_0}^\pm \;\; ; \ldots ; \;\; F_\pm^{(p+q)}(\pm 1) = (\mp 1)^{p+q} \; (p+q)! a_{p_q}^\pm
\end{aligned}$$

so as the following $n+p$ conditions are immediately satisfied:

$$\left.\frac{d^k M_p^\pm}{dx^k}\right|_{\mp 1} = 0 \quad \text{for} \quad k = 0, \ldots, n-1$$
$$\left.\frac{d^k M_p^\pm}{dx^k}\right|_{\pm 1} = 0 \quad \text{for} \quad k = 0, \ldots, p-1$$

whereas it is wanted that

$$\left.\frac{d^p M_p^\pm}{dx^p}\right|_{\pm 1} = 1$$

Then, it results:[1]

$$\left.\frac{d^p M_p^\pm}{dx^p}\right|_{\pm 1} = F_\pm^{(p)} G_\pm = (\mp 1)^p \; p! a_{p_0}^\pm = 1$$

that is verified for:

$$a_{p_0}^\pm = (\mp 1)^p \; \frac{1}{p!} \tag{3.3}$$

The first coefficients are thus determined. The further q conditions should be imposed to determine the remaining coefficients ($a_{p_j}^\pm$ for $j = 1, \ldots, q$):

$$\left.\frac{d^{p+j} M_p^\pm}{dx^{p+j}}\right|_{\pm 1} =$$
$$F_{\pm 1}^{(p+j)} G_{\pm 1} + (p+j) F_{\pm 1}^{(p+j-1)} G_{\pm 1}^{(1)} + \frac{(p+j)(p+j-1)}{2} F_{\pm 1}^{(p+j-2)} G_{\pm 1}^{(2)} + \ldots = 0$$

In particular,

$$\left.\frac{d^{p+1} M_p^\pm}{dx^{p+1}}\right|_{\pm 1} = F_{\pm 1}^{(p+1)} G_{\pm 1} + (p+1) F_{\pm 1}^{(p)} G_{\pm 1}^{(1)} = (\mp 1) \; a_{p_1}^\pm + a_{p_0}^\pm (\pm 1) \frac{n}{2} = 0$$

---

[1] Given two generic function $f = f(x)$, $g = g(x)$, one has the following rule for the k–th derivative of the product

$$\frac{d^k}{dx^k} fg = f^{(k)} g + \binom{k}{1} f^{(k-1)} g^{(1)} + \ldots + \binom{k}{k-1} f^{(1)} g^{(k-1)} + f g^{(k)} =$$
$$f^{(k)} g + k f^{(k-1)} g^{(1)} + \frac{k(k-1)}{2} f^{(k-2)} g^{(2)} + \ldots + k f^{(1)} g^{(k-1)} + f g^{(k)}$$

may be used to obtain:

$$a^{\pm}_{p_1} = (\mp 1)^p \, \frac{1}{2} \frac{n}{p!} \tag{3.4}$$

Similarly:

$$a^{\pm}_{p_k} = (\mp 1)^p \binom{n+k-1}{k} \frac{1}{2^k p!} \tag{3.5}$$

where $k = 2, \ldots, q$.

Once the coefficients are determined, the polynomials defined in Eq. 3.2 are also determined. Hence, Eq. 3.1 can be used to interpolate the function $u = u(x)$.

To validate the interpolation formula given above, Hermite polynomials for $x \in [-1, 1]$ up to order seven have been used. In Tabs. 3.1, 3.2, 3.3 the coefficients a_j and b_j are given for each polynomial (and hence for each value of p available for each order of interpolation). Using the coefficients of the tables and combining Eqs. 3.1 and 3.2 one obtains the classical Hermite interpolation formula and the two–node higher order interpolation formulae (fifth and seventh order) given in Subsections 3.1.1 and 3.1.2.

	p	
$n = 2$	0	1
a_0^+; a_0^-	1; 1	−1; 1
a_1^+; a_1^-	1; 1	

Table 3.1: 3rd order Hermite polynomials' coefficients

	p		
$n = 3$	0	1	2
a_0^+; a_0^-	1; 1	−1; 1	1; 1
a_1^+; a_1^-	3/2; 3/2	−3/2; 3/2	
a_2^+; a_2^-	3/2; 3/2		

Table 3.2: 5th order Hermite polynomials' coefficients

	p			
$n = 3$	0	1	2	3
a_0^+; a_0^-	1; 1	−1; 1	1/2; 1/2	−1/6; 1/6
a_1^+; a_1^-	2; 2	−2; 2	1; 1	
a_2^+; a_2^-	5/2; 5/2	−5/2; 5/2		
a_3^+; a_3^-	5/2; 5/2			

Table 3.3: 7th order Hermite polynomials' coefficients

3.1.1 5th order $2-$node interpolation

Consider now the fifth–order extension of the classical Hermite interpolation. As stated in 2.1, the third–order Hermite interpolation, of class $\mathcal{C}^1$, yields the cubic polynomial that is determined by the values of the function, and of its first–order derivative at the two end points. The third–order polynomials, accordingly to the notation used in Eq. 3.1, are given by

$$M_{0\pm}(x) = \frac{1}{4}(2 \pm 3x \mp x^3) \quad \text{and} \quad M_{1\pm}(x) = \frac{1}{4}(\mp 1 - x \pm x^2 + x^3).$$

Similarly, the fifth–order Hermite interpolation, of class $\mathcal{C}^2$, yields the quintic polynomial that is determined by the values of the function, first–order derivative, and second–order derivative, at the two end points, $x = \pm 1$,

$$\begin{aligned} f(x) &= f_-^{(0)} M_{0-}(x) + f_+^{(0)} M_{0+}(x) \\ &+ f_-^{(1)} M_{1-}(x) + f_+^{(1)} M_{1+}(x) \\ &+ f_-^{(2)} M_{2-}(x) + f_+^{(2)} M_{2+}(x) \end{aligned} \tag{3.6}$$

(for $x \in [-1, 1]$), where $f_\pm^{(k)}$ $(k = 0, 1, 2)$ denote the values, at $x = \pm 1$, of respectively $f(x)$, df/dx, and d^2f/dx^2, whereas the Hermite interpolation polynomials $M_{k\pm}(x)$ $(k = 0, 1, 2)$ are now given by

$$\begin{aligned} M_{0\pm}(x) &= \frac{1}{16}\left(8 \pm 15x \mp 10x^3 \pm 3x^5\right), \\ M_{1\pm}(x) &= \frac{1}{16}\left(\mp 5 - 7x \pm 6x^2 + 10x^3 \mp x^4 - 3x^5\right), \\ M_{2\pm}(x) &= \frac{1}{16}\left(1 \pm x - 2x^2 \mp 2x^3 + x^4 \pm x^5\right). \end{aligned} \tag{3.7}$$

with $x \in [-1, 1]$. For instance $M_{0+}(x)$ is (uniquely) determined by the conditions $M_{0+}(1) = 1$, $M_{0+}(-1) = 0$ and $dM_{0+}/dx = d^2M_{0+}/dx^2 = 0$ for $x = \pm 1$.

Note that, the polynomials in Eqs. 3.7 can be rewritten in the form:

$$\begin{aligned}
M_{0_\pm}(x) &= \frac{1}{2}\left(8 \mp 9x + 3x^2\right)\left(\frac{1 \pm x}{2}\right)^3, \\
M_{1_\pm}(x) &= \frac{1}{2}\left(\mp 5 + 8x \mp 3x^2\right)\left(\frac{1 \pm x}{2}\right)^3, \\
M_{2_\pm}(x) &= \frac{1}{2}\left(\mp 1 + x\right)^2\left(\frac{1 \pm x}{2}\right)^3.
\end{aligned}$$

In fact, according to Eqs. 3.2, the first factors can be obtained using the appropriate coefficients of Tab. 3.2. For instance, one has, for the polynomial $M_{0_+}(x)$ (in this case: $p = 0$, $q = 2$ whereas $a_0^+ = 1$ and $a_1^+ = a_2^+ = 3/2$):

$$\begin{aligned}
&M_{0_\pm}(x) \\
&= \left[1 + \frac{3}{2}(1-x) + \frac{3}{2}(1-x)^2\right]\left(\frac{1+x}{2}\right)^3 \\
&= \left(4 - \frac{9}{2}x + \frac{3}{2}x^2\right)\left(\frac{1 \pm x}{2}\right)^3 = \frac{1}{2}\left(8 - 9x + 3x^2\right)\left(\frac{1+x}{2}\right)^3
\end{aligned}$$

Figure 3.1 shows the $M_{0_\pm}(x)$ fifth–order interpolators whereas Figs. 3.2 and 3.3 depict the functions $M_{1_\pm}(x)$ and $M_{2_\pm}(x)$.

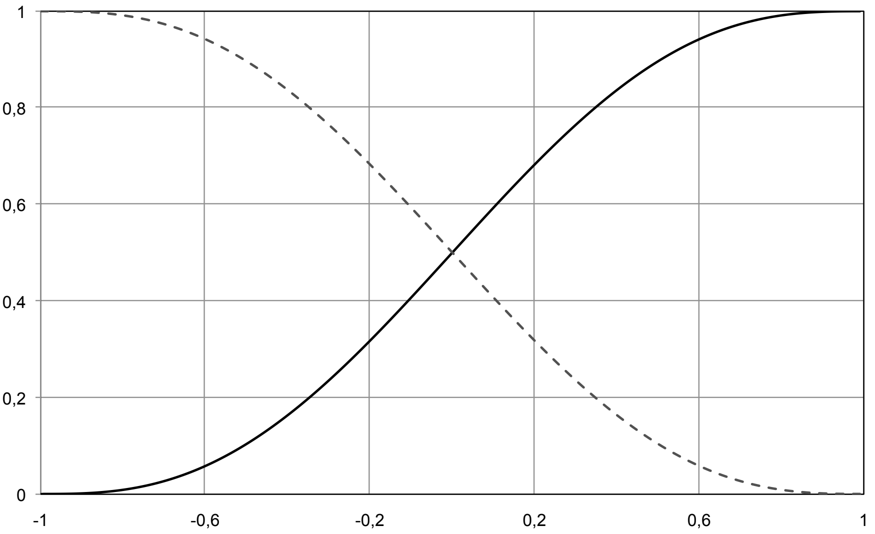

Figure 3.1: 5th order Hermite polynomials: M_{0_-} (dashed line) and M_{0_+} (continuous line)

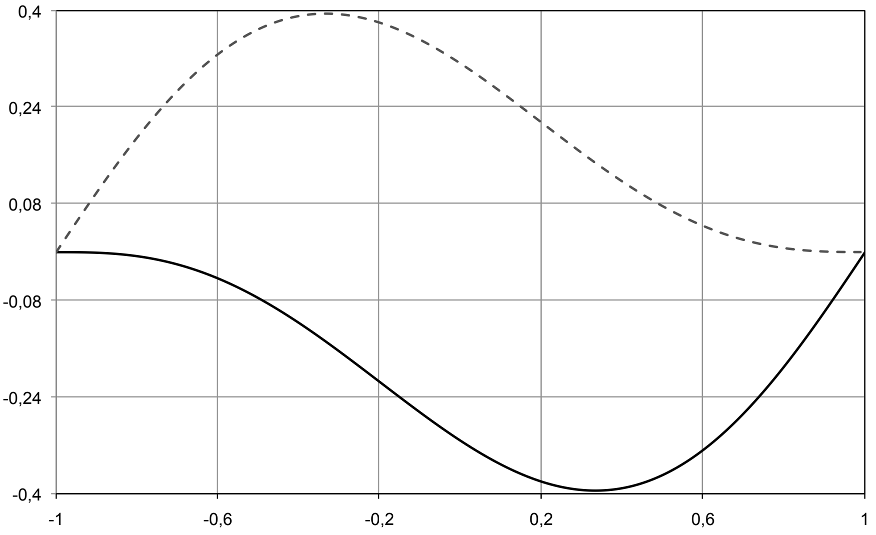

Figure 3.2: 5th order Hermite polynomials: M_{1_-} (dashed line) and M_{1_+} (continuous line)

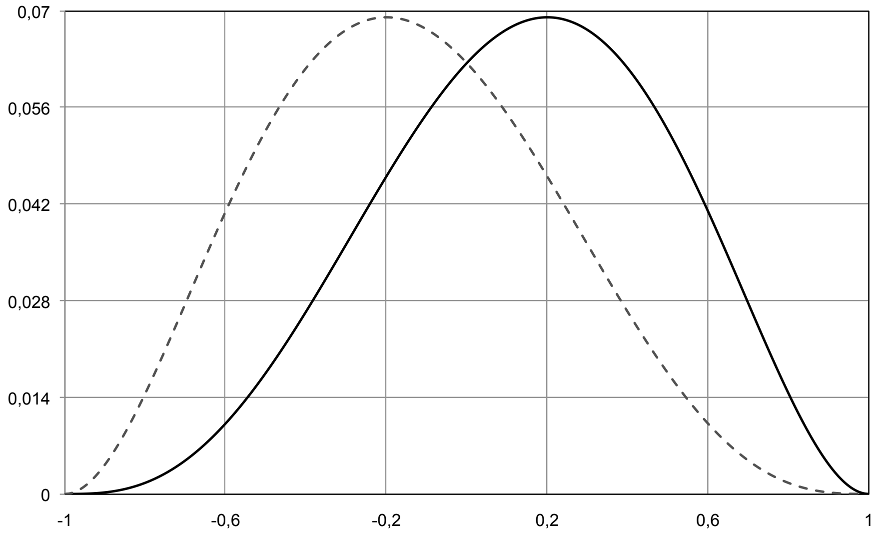

Figure 3.3: 5th order Hermite polynomials: M_{2_-} (dashed line) and M_{2_+} (continuous line)

3.1.2 7th order $2-$node interpolation

The seventh–order Hermite interpolation, of class $\mathcal{C}^3$, yields the polynomial of order seven that is determined by the values of the function, first–order derivative, second–order derivative and third–order derivative, at the two end points, $x = \pm 1$,

$$\begin{aligned} f(x) = {} & f_-^{(0)} M_{0_-}(x) + f_+^{(0)} M_{0_+}(x) \\ & + f_-^{(1)} M_{1_-}(x) + f_+^{(1)} M_{1_+}(x) \\ & + f_-^{(2)} M_{2_-}(x) + f_+^{(2)} M_{2_+}(x) \\ & + f_-^{(3)} M_{3_-}(x) + f_+^{(3)} M_{3_+}(x) \end{aligned}$$

(for $x \in [-1, 1]$), where $f_\pm^{(k)}$ $(k = 0, 1, 2, 3)$ denote the values, at $x = \pm 1$, of respectively $f(x)$, df/dx, d^2f/dx^2 and d^3f/dx^3, whereas the Hermite interpolation polynomials $M_{k\pm}(x)$ $(k = 0, 1, 2, 3)$ are now given by

$$\begin{aligned}
M_{0\pm}(x) &= \frac{1}{32}\left(\mp 5x^7 \pm 21x^5 \mp 35x^3 \pm 35x + 16\right), \\
M_{1\pm}(x) &= \frac{1}{32}\left(5x^7 \pm x^6 - 21x^5 \mp 5x^4 + 35x^3 \pm 15x^2 - 19x \mp 11\right), \\
M_{2\pm}(x) &= \frac{1}{32}\left(\mp 2x^7 - x^6 \pm 8x^5 + 5x^4 \mp 10x^3 - 7x^2 \pm 4x + 3\right), \\
M_{3\pm}(x) &= \frac{1}{32}\left[\frac{1}{3}\left(x^7 \pm x^6 - 3x^5 \mp 3x^4 + 3x^3 \pm 3x^2 - x \mp 1\right)\right].
\end{aligned} \tag{3.8}$$

with $x \in [-1, 1]$. For instance $M^{(0)}_{+}(x)$ is (uniquely) determined by the conditions $M^{(0)}_{+}(1) = 1$, $M^{(0)}_{+}(-1) = 0$ and $dM^{(0)}_{+}/dx = d^2M^{(0)}_{+}/dx^2 = d^3M^{(0)}_{+}/dx^3 = 0$ for $x = \pm 1$.

Note that, the polynomials in Eqs. 3.7 can be rewritten in the form:

$$\begin{aligned}
M_{0\pm}(x) &= \frac{1}{2}\left(16 \mp 29x + 20x^2 \mp 5x^3\right)\left(\frac{1 \pm x}{2}\right)^4, \\
M_{1\pm}(x) &= \frac{1}{2}\left(\mp 11 + 25x \mp 19x^2 + 5x^3\right)\left(\frac{1 \pm x}{2}\right)^4, \\
M_{2\pm}(x) &= \frac{1}{2}\left(3 \mp 8x + 7x^2 \mp 2x^3\right)\left(\frac{1 \pm x}{2}\right)^4, \\
M_{3\pm}(x) &= \frac{1}{6}\left(\mp 1 + x\right)^3\left(\frac{1 \pm x}{2}\right)^4.
\end{aligned}$$

In fact, according to Eqs. 3.2, the first factors can be obtained using the appropriate coefficients of Tab. 3.3. For instance, one has, for the polynomial $M_{0+}(x)$ (in this case: $p = 0$, $q = 3$ whereas $a_0^+ = 1$, $a_1^+ = 2$ and $a_2^+ = a_3^+ = 5/2$):

$$\begin{aligned}
&M_{0\pm}(x) \\
&= \left[1 + 2\left(1 - x\right) + \frac{5}{2}\left(1 - x\right)^2 + \frac{5}{2}\left(1 - x\right)^3\right]\left(\frac{1 + x}{2}\right)^4 \\
&= \left(8 - \frac{29}{2}x + \frac{20}{2}x^2 - \frac{5}{2}x^3\right)\left(\frac{1 \pm x}{2}\right)^3 = \frac{1}{2}\left(16 - 29x + 20x^2 - 5x^3\right)\left(\frac{1 + x}{2}\right)^4
\end{aligned}$$

Figure 3.4 shows the $M_{0\pm}(x)$ seventh–order interpolators whereas Figs. from 3.5 to 3.7 depict the functions $M_{1\pm}(x)$, $M_{2\pm}(x)$ and $M_{3\pm}(x)$.

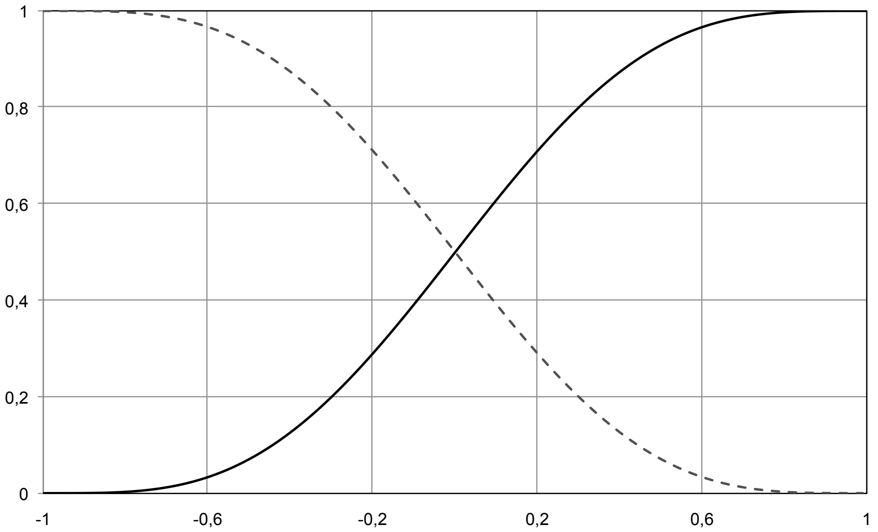

Figure 3.4: 7th order Hermite polynomials: M_{0_-} (dashed line) and M_{0_+} (continuous line)

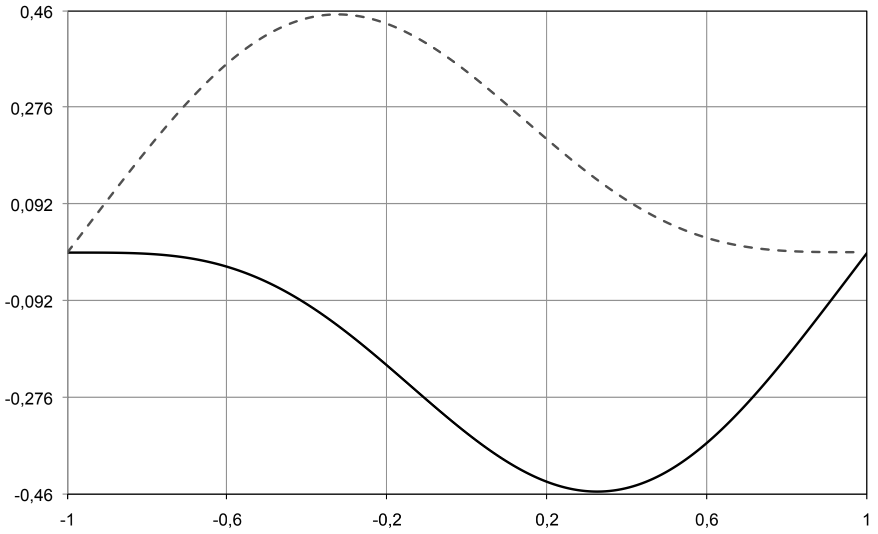

Figure 3.5: 7th order Hermite polynomials: M_{1_-} (dashed line) and M_{1_+} (continuous line)

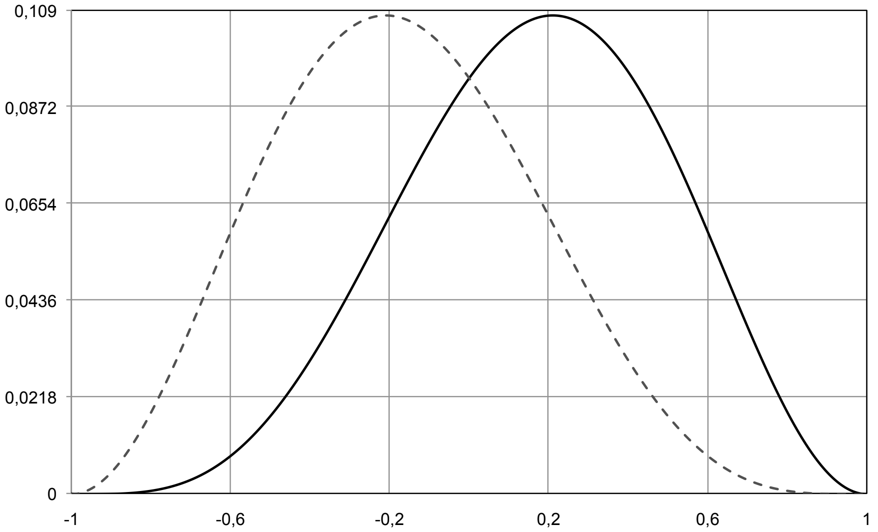

Figure 3.6: 7th order Hermite polynomials: M_{2_-} (dashed line) and M_{2_+} (continuous line)

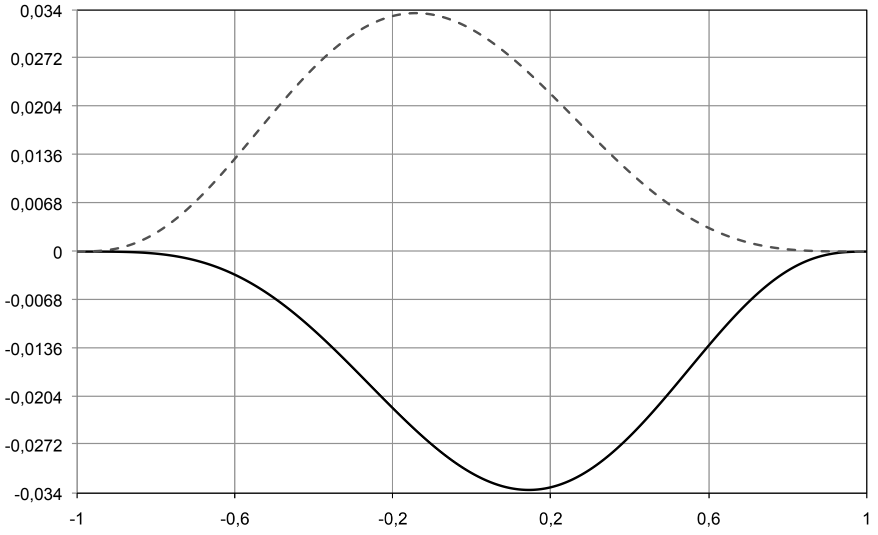

Figure 3.7: 7th order Hermite polynomials: M_{3_-} (dashed line) and M_{3_+} (continuous line)

3.2 Higher–order Hermite bricks

Here, the mathematical formulations for the three–dimensional Hermite brick elements of order 5 and 7 is addressed.

3.2.1 The Hermite 5th order 8–node element

In order to increase the accuracy of the basic third–order Hermite element, higher–orders have been explored. A first step is the extension to order 5.

In Subsection 3.1.1, the fifth–order polynomials for a two nodes interpolation have been obtained. Such a technique can be considered as a Hermite interpolation technique, since it could be seen as an extension of the third–order classical Hermite interpolation (of class $\mathcal{C}^1$), by including a higher nodal derivative. Specifically, the classical Hermite interpolation needs the function and the first derivative at end–nodes whereas the fifth-order Hermite interpolation needs the function, the first derivative end the second derivative at end–nodes (class $\mathcal{C}^2$).

The quintic polynomials obtained in Subsection 3.1.1 (for $x \in [-1,1]$), are:

$$\begin{aligned} M_{0\pm}(x) &= \frac{1}{16}\left(8 \pm 15x \mp 10x^3 \pm 3x^5\right), \\ M_{1\pm}(x) &= \frac{1}{16}\left(\mp 5 - 7x \pm 6x^2 + 10x^3 \mp x^4 - 3x^5\right), \\ M_{2\pm}(x) &= \frac{1}{16}\left(1 \pm x - 2x^2 \mp 2x^3 + x^4 \pm x^5\right). \end{aligned}$$

If one considers the extension to the three–dimensional case, one has

$$\begin{aligned} &f(\xi^\alpha) \\ &= \sum_{\mathbf{s}} \left(P_{\mathbf{s}}(\xi^\alpha) f_{\mathbf{s}} + \sum_{\beta=1}^{3} P_{\mathbf{s}}^{\beta}(\xi^\alpha) f_{\mathbf{s},\beta} + \sum_{\beta\gamma\in I_2} P_{\mathbf{s}}^{\beta\gamma}(\xi^\alpha) f_{\mathbf{s},\beta\gamma} + \sum_{\beta\gamma\lambda\in I_3} P_{\mathbf{s}}^{\beta\gamma\lambda}(\xi^\alpha) f_{\mathbf{s},\beta\gamma\lambda} \right. \\ &\left. + \sum_{\beta\gamma\lambda\mu\in I_4} P_{\mathbf{s}}^{\beta\gamma\lambda\mu}(\xi^\alpha) f_{\mathbf{s},\beta\gamma\lambda\mu} + \sum_{\beta\gamma\lambda\mu\nu\in I_5} P_{\mathbf{s}}^{\beta\gamma\lambda\mu\nu}(\xi^\alpha) f_{\mathbf{s},\beta\gamma\lambda\mu\nu} + P_{\mathbf{s}}^{112233}(\xi^\alpha) f_{\mathbf{s},112233} \right), \end{aligned} \tag{3.9}$$

where $\mathbf{s} := (s_1, s_2, s_3)$, with $s_k = 1, 2$, defines the eight nodes of the brick element ($\sum_{\mathbf{s}}$ is understood to span over all the eight values of $\mathbf{s}$); moreover, noting that the mixed derivatives include at most the second derivative with respect to each variable, we have that

$$\begin{aligned}
&I_2 := \{(1,1);(2,2);(3,3);(1,2);(2,3);(3,1)\},\\
&I_3 := \{(1,2,3);(1,1,2);(1,1,3);(2,2,1);(2,2,3);(3,3,1);(3,3,2)\},\\
&I_4 := \{(1,1,2,2);(2,2,3,3);(3,3,1,1);(1,1,2,3);(2,2,3,1);(3,3,1,2)\},\\
&I_5 := \{(1,1,2,2,3);(2,2,3,3,1);(3,3,1,1,2)\},
\end{aligned} \tag{3.10}$$

whereas the term 112233 is the only pertinent the sixth–order derivative. In addition, $P_{\mathbf{s}}(\xi^\alpha)$, $P_{\mathbf{s}}^{\beta}(\xi^\alpha)$, $P_{\mathbf{s}}^{\beta\gamma}(\xi^\alpha)$, $P_{\mathbf{s}}^{\beta\gamma\lambda}(\xi^\alpha)$, $P_{\mathbf{s}}^{\beta\gamma\lambda\mu}(\xi^\alpha)$, $P_{\mathbf{s}}^{\beta\gamma\lambda\mu\nu}(\xi^\alpha)$, and $P_{\mathbf{s}}^{112233}(\xi^\alpha)$ are suitable products of the Hermite polynomials in Eq. 3.7; for instance,

$$\begin{aligned}
P_{\mathbf{s}}(\xi^\alpha) \quad &= M_{0_{s_1}}(\xi^1)M_{0_{s_2}}(\xi^2)M_{0_{s_3}}(\xi^3),\\
P_{\mathbf{s}}^{1}(\xi^\alpha) \quad &= M_{1_{s_1}}(\xi^1)M_{0_{s_2}}(\xi^2)M_{0_{s_3}}(\xi^3),\\
P_{\mathbf{s}}^{11}(\xi^\alpha) \quad &= M_{2_{s_1}}(\xi^1)M_{0_{s_2}}(\xi^2)M_{0_{s_3}}(\xi^3),\\
P_{\mathbf{s}}^{13}(\xi^\alpha) \quad &= M_{1_1}(\xi^1)M_{0_{s_2}}(\xi^2)M_{1_{s_3}}(\xi^3),\\
P_{\mathbf{s}}^{123}(\xi^\alpha) \quad &= M_{1_{s_1}}(\xi^1)M_{1_{s_2}}(\xi^2)M_{1_{s_3}}(\xi^3)\\
P_{\mathbf{s}}^{11223}(\xi^\alpha) \quad &= M_{2_{s_1}}(\xi^1)M_{2_{s_2}}(\xi^2)M_{1_{s_3}}(\xi^3).
\end{aligned} \tag{3.11}$$

The expressions above provide the desired local interpolation procedure for any function $f(\xi^\alpha)$. Similarly to Section 2.2 (Eq. 2.4), whenever the unknown function is a scalar $u = u(\xi^\alpha)$ (as in acoustics), these may be combined to yield a global interpolation as

$$u(\xi^\alpha) = \sum_{p=1}^{P} z_p \chi_p(\xi^\alpha),$$

where now the z_p's comprise the nodal values of u, $u_{,\alpha}$ $(\alpha = 1,2,3)$, $u_{,\beta\gamma}$ $(\beta\gamma \in I_2)$, $u_{,\beta\gamma\lambda}$ $(\beta\gamma\lambda \in I_3)$, $u_{,\beta\gamma\lambda\mu}$ $(\beta\gamma\lambda\mu \in I_4)$, $u_{,\beta\gamma\lambda\mu\nu}$ $(\beta\gamma\lambda\mu\nu \in I_5)$, as well as $u_{,112233}$, whereas $\chi_p(\xi^\alpha)$ are the global shape functions (considered the eight nodes, $P = 216$), defined locally by Eqs. 3.11.

If the unknown is a vector function, as in structural dynamics, we have

$$\mathbf{u}(\xi^\alpha) = \sum_{p=1}^{P} z_p \boldsymbol{\chi}_p(\xi^\alpha),$$

where now the z_p's comprise the nodal values of the Cartesian components of $\mathbf{u}$, $\mathbf{u}_{,\alpha}$ $(\alpha = 1,2,3)$, $\mathbf{u}_{,\beta\gamma}$ $(\beta\gamma \in I_2)$, $\mathbf{u}_{,\beta\gamma\lambda}$ $(\beta\gamma\lambda \in I_3)$, $\mathbf{u}_{,\beta\gamma\lambda\mu}$ $(\beta\gamma\lambda\mu \in I_4)$, $\mathbf{u}_{,\beta\gamma\lambda\mu\nu}$ $(\beta\gamma\lambda\mu\nu \in I_5)$, as well as $\mathbf{u}_{,112233}$, whereas $\boldsymbol{\chi}_p(\xi^\alpha)$ are vector global shape functions, obtained from the $\chi_p(\xi^\alpha)$'s in Eqs. 3.11, through multiplication by the appropriate base vector. The same interpolation is used for the geometry (isoparametric representation).

3.2.2 The Hermite 7th order 8–node element

A further improvement in accuracy is given by shifting the order of the element from five to seven.

In Subsection 3.1.2, the seventh–order Hermite polynomials have been given. They are related to the function, the first derivative, the second derivative and the third derivative, evaluated in correspondence of each of the two nodes; the interpolation is indeed of class $\mathcal{C}^3$, and is described (for $x \in [-1, 1]$) by the shape functions:

$$\begin{aligned}
M_{0\pm}(x) &= \frac{1}{32}\left(\mp 5x^7 \pm 21x^5 \mp 35x^3 \pm 35x + 16\right), \\
M_{1\pm}(x) &= \frac{1}{32}\left(5x^7 \pm x^6 - 21x^5 \mp 5x^4 + 35x^3 \pm 15x^2 - 19x \mp 11\right), \\
M_{2\pm}(x) &= \frac{1}{32}\left(\mp 2x^7 - x^6 \pm 8x^5 + 5x^4 \mp 10x^3 - 7x^2 \pm 4x + 3\right), \\
M_{3\pm}(x) &= \frac{1}{32}\left[\frac{1}{3}\left(x^7 \pm x^6 - 3x^5 \mp 3x^4 + 3x^3 \pm 3x^2 - x \mp 1\right)\right].
\end{aligned}$$

As above, if one considers the extension to the three–dimensional case, one has

$$\begin{aligned}
&f(\xi^\alpha) \\
&= \sum_{\mathbf{s}} \Bigg(P_{\mathbf{s}}(\xi^\alpha) f_{\mathbf{s}} + \sum_{\beta=1}^{3} P_{\mathbf{s}}^{\beta}(\xi^\alpha) f_{\mathbf{s},\beta} + \sum_{\beta\gamma\in I_2} P_{\mathbf{s}}^{\beta\gamma}(\xi^\alpha) f_{\mathbf{s},\beta\gamma} + \sum_{\beta\gamma\lambda\in I_3} P_{\mathbf{s}}^{\beta\gamma\lambda}(\xi^\alpha) f_{\mathbf{s},\beta\gamma\lambda} \\
&+ \sum_{\beta\gamma\lambda\mu\in I_4} P_{\mathbf{s}}^{\beta\gamma\lambda\mu}(\xi^\alpha) f_{\mathbf{s},\beta\gamma\lambda\mu} + \sum_{\beta\gamma\lambda\mu\nu\in I_5} P_{\mathbf{s}}^{\beta\gamma\lambda\mu\nu}(\xi^\alpha) f_{\mathbf{s},\beta\gamma\lambda\mu\nu} \\
&+ \sum_{\beta\gamma\lambda\mu\nu\omega\in I_6} P_{\mathbf{s}}^{\beta\gamma\lambda\mu\nu\omega}(\xi^\alpha) f_{\mathbf{s},\beta\gamma\lambda\mu\nu\omega} + \sum_{\beta\gamma\lambda\mu\nu\omega\tau\in I_7} P_{\mathbf{s}}^{\beta\gamma\lambda\mu\nu\omega\tau}(\xi^\alpha) f_{\mathbf{s},\beta\gamma\lambda\mu\nu\omega\tau} \\
&+ \sum_{\beta\gamma\lambda\mu\nu\omega\tau\iota\in I_8} P_{\mathbf{s}}^{\beta\gamma\lambda\mu\nu\omega\tau\iota}(\xi^\alpha) f_{\mathbf{s},\beta\gamma\lambda\mu\nu\omega\tau\iota} + P_{\mathbf{s}}^{111222333}(\xi^\alpha) f_{\mathbf{s},111222333} \Bigg),
\end{aligned} \tag{3.12}$$

where $\mathbf{s} := (s_1, s_2, s_3)$, with $s_k = 1, 2$, defines the eight nodes of the brick element ($\sum_{\mathbf{s}}$ is understood to span over all the eight values of $\mathbf{s}$); moreover, noting that the mixed derivatives include now at most the third derivative with respect to each variable, we have that

$$
\begin{aligned}
&I_2 := \\
&\{(1,1);(2,2);(3,3);(1,2);(2,3);(3,1)\}, \\
&I_3 := \\
&\{(1,1,1);(2,2,2);(3,3,3);(1,2,3);(1,1,2); \\
&(1,1,3);(2,2,1);(2,2,3);(3,3,1);(3,3,2)\}, \\
&I_4 := \\
&\{(1,1,2,2);(2,2,3,3);(3,3,1,1);(1,1,2,3);(2,2,3,1);(3,3,1,2); \\
&(1,3,3,3);(2,3,3,3);(1,2,2,2);(3,2,2,2);(2,1,1,1);(3,1,1,1)\}, \\
&I_5 := \\
&\{(1,1,3,3,3);(2,2,3,3,3);(1,1,2,2,2);(3,3,2,2,2);(2,2,1,1,1);(3,3,1,1,1); \\
&(1,2,3,3,3);(1,3,2,2,2);(2,3,1,1,1);(1,1,2,2,3);(2,2,3,3,1);(3,3,1,1,2)\}, \\
&I_6 := \\
&\{(1,2,2,3,3,3);(1,1,2,3,3,3);(1,3,3,2,2,2);(3,1,1,2,2,2);(2,3,3,1,1,1); \\
&(3,2,2,1,1,1);(1,1,1,2,2,2);(1,1,1,3,3,3);(2,2,2,3,3,3);(1,1,2,2,3,3)\}, \\
&I_7 := \\
&\{(1,1,1,2,2,2,3);(1,1,1,2,3,3,3);(1,2,2,2,3,3,3); \\
&(1,1,2,2,3,3,3);(1,1,2,2,2,3,3);(1,1,1,2,2,3,3)\}, \\
&I_8 := \\
&\{(1,1,1,2,2,2,3,3);(1,1,1,2,2,3,3,3);(1,1,2,2,2,3,3,3)\},
\end{aligned}
\tag{3.13}
$$

whereas the term 111222333 is the only pertinent the ninth–order derivative.

In addition, $P_{\mathbf{s}}(\xi^\alpha)$, $P_{\mathbf{s}}^{\beta}(\xi^\alpha)$, $P_{\mathbf{s}}^{\beta\gamma}(\xi^\alpha)$, $P_{\mathbf{s}}^{\beta\gamma\lambda}(\xi^\alpha)$, $P_{\mathbf{s}}^{\beta\gamma\lambda\mu}(\xi^\alpha)$, $P_{\mathbf{s}}^{\beta\gamma\lambda\mu\nu}(\xi^\alpha)$, $P_{\mathbf{s}}^{\beta\gamma\lambda\mu\nu\omega}(\xi^\alpha)$, $P_{\mathbf{s}}^{\beta\gamma\lambda\mu\nu\omega\tau}(\xi^\alpha)$, $P_{\mathbf{s}}^{\beta\gamma\lambda\mu\nu\omega\tau\iota}(\xi^\alpha)$, and $P_{\mathbf{s}}^{111222333}(\xi^\alpha)$ are suitable products of the Hermite polynomials in Eq. 3.7; for instance,

$$\begin{aligned}
P_{\mathbf{s}}(\xi^\alpha) &= M_{0_{s_1}}(\xi^1)M_{0_{s_2}}(\xi^2)M_{0_{s_3}}(\xi^3),\\
P_{\mathbf{s}}^{1}(\xi^\alpha) &= M_{1_{s_1}}(\xi^1)M_{0_{s_2}}(\xi^2)M_{0_{s_3}}(\xi^3),\\
P_{\mathbf{s}}^{11}(\xi^\alpha) &= M_{2_{s_1}}(\xi^1)M_{0_{s_2}}(\xi^2)M_{0_{s_3}}(\xi^3),\\
P_{\mathbf{s}}^{13}(\xi^\alpha) &= M_{1_1}(\xi^1)M_{0_{s_2}}(\xi^2)M_{1_{s_3}}(\xi^3),\\
P_{\mathbf{s}}^{111}(\xi^\alpha) &= M_{3_{s_1}}(\xi^1)M_{0_{s_2}}(\xi^2)M_{0_{s_3}}(\xi^3),\\
P_{\mathbf{s}}^{1122}(\xi^\alpha) &= M_{2_{s_1}}(\xi^1)M_{2_{s_2}}(\xi^2)M_{0_{s_3}}(\xi^3),\\
P_{\mathbf{s}}^{11333}(\xi^\alpha) &= M_{2_{s_1}}(\xi^1)M_{0_{s_2}}(\xi^2)M_{3_{s_3}}(\xi^3),\\
P_{\mathbf{s}}^{122333}(\xi^\alpha) &= M_{1_{s_1}}(\xi^1)M_{2_{s_2}}(\xi^2)M_{3_{s_3}}(\xi^3),\\
P_{\mathbf{s}}^{1112223}(\xi^\alpha) &= M_{3_{s_1}}(\xi^1)M_{3_{s_2}}(\xi^2)M_{1_{s_3}}(\xi^3),\\
P_{\mathbf{s}}^{111222333}(\xi^\alpha) &= M_{3_{s_1}}(\xi^1)M_{3_{s_2}}(\xi^2)M_{3_{s_3}}(\xi^3),
\end{aligned} \tag{3.14}$$

The expressions above provide the desired local interpolation procedure for any function $f(\xi^\alpha)$. Similarly to Section 2.2 (Eq. 2.4), whenever the unknown function is a scalar $u = u(\xi^\alpha)$ (as in acoustics), these may be combined to yield a global interpolation as

$$u(\xi^\alpha) = \sum_{p=1}^{P} z_p \chi_p(\xi^\alpha),$$

where now the z_p's comprise the nodal values of u, $u_{,\alpha}$ $(\alpha = 1, 2, 3)$, $u_{,\beta\gamma}$ $(\beta\gamma \in I_2)$, $u_{,\beta\gamma\lambda}$ $(\beta\gamma\lambda \in I_3)$, $u_{,\beta\gamma\lambda\mu}$ $(\beta\gamma\lambda\mu \in I_4)$, $u_{,\beta\gamma\lambda\mu\nu}$ $(\beta\gamma\lambda\mu\nu \in I_5)$, $u_{,\beta\gamma\lambda\mu\nu\omega}$ $(\beta\gamma\lambda\mu\nu\omega \in I_6)$, $u_{,\beta\gamma\lambda\mu\nu\omega\tau}$ $(\beta\gamma\lambda\mu\nu\omega\tau \in I_7)$, $u_{,\beta\gamma\lambda\mu\nu\omega\tau\iota}$ $(\beta\gamma\lambda\mu\nu\omega\tau\iota \in I_8)$, as well as $u_{,111222333}$, whereas $\chi_p(\xi^\alpha)$ are the global shape functions (considered the eight nodes, $P = 512$), defined locally by Eqs. 3.14.

If the unknown is a vector function $\mathbf{u}(\xi^\alpha)$, as in structural dynamics, we have

$$\mathbf{u}(\xi^\alpha) = \sum_{p=1}^{P} z_p \boldsymbol{\chi}_p(\xi^\alpha),$$

where now the z_p's comprise the nodal values of the Cartesian components of $\mathbf{u}$, $\mathbf{u}_{,\alpha}$ $(\alpha = 1, 2, 3)$, $\mathbf{u}_{,\beta\gamma}$ $(\beta\gamma \in I_2)$, $\mathbf{u}_{,\beta\gamma\lambda}$ $(\beta\gamma\lambda \in I_3)$, $\mathbf{u}_{,\beta\gamma\lambda\mu}$ $(\beta\gamma\lambda\mu \in I_4)$, $\mathbf{u}_{,\beta\gamma\lambda\mu\nu}$ $(\beta\gamma\lambda\mu\nu \in I_5)$, $\mathbf{u}_{,\beta\gamma\lambda\mu\nu\omega}$ $(\beta\gamma\lambda\mu\nu\omega \in I_6)$, $\mathbf{u}_{,\beta\gamma\lambda\mu\nu\omega\tau}$ $(\beta\gamma\lambda\mu\nu\omega\tau \in I_7)$, $\mathbf{u}_{,\beta\gamma\lambda\mu\nu\omega\tau\iota}$ $(\beta\gamma\lambda\mu\nu\omega\tau\iota \in I_8)$, as well as $\mathbf{u}_{,111222333}$, whereas $\boldsymbol{\chi}_p(\xi^\alpha)$ are vector global shape functions, obtained from the $\chi_p(\xi^\alpha)$'s in Eqs. 3.14, through multiplication by the appropriate base vector. The same interpolation is used for the geometry (isoparametric representation).

3.3 Block–boundary problem

The block–boundary problem discussed in Section 2.3 persists in higher–order formulations, once having shifted on higher–order derivatives the issue of incomplete informations.

In fact, for the fifth–order scheme one has the complete set of derivatives of the function up to order two (in fact, for each node we have all the 3 first derivatives and all the 6 second derivatives) whereas incomplete set of derivatives from order three to order six (we have only a mixed sixth–order derivative).

Similarly, for the 7th order $8-$node Hermite element one has all the derivatives up to order three (*i.e.*, the 3 first derivatives, the 6 second derivatives and the 10 third derivatives) whereas incomplete information for the derivatives of order from four to nine (we have only a mixed ninth–order derivative).

Results for a *Scheme C* formulation introduced in Section 2.4, applied also to higher orders, are presented in Section 7.5. They show that, as a rule of thumb, the higher the order of the element (and thus the higher the quantity of derivatives for which incomplete information is available), the greater the loss in accuracy highlighted. In addition, the complexity of a *Scheme C* implementation increases as the order of the element increases.

This leads to the idea of an element for which the order is reached with less unknowns then the Hermite element, thus reducing the complexity of the scheme with advantages for the *Scheme C* implementation.

Chapter 4

Hybrid brick elements

The approach presented here, has been introduced in the past years.[7] The interpolation scheme is obtained by combining the one–dimensional Hermite interpolation with a three–dimensional extension of the Coons' Patch technique, introduced for the first time in '60s by S. A. Coons .[8]–[10]

4.1 State of the art

The interpolation technique presented here is quite different from related schemes available in the literature, known as Coons Macroelement (see, in particular, the paper of Provaditis,[1] which presents a review of past work in the subject). In order to explain the difference with respect to the work of Provaditis, a few words regarding the Coons patch and its three–dimensional extensions appears to be in order. In order to put the present thesis in the proper perspective, it is important to emphasize that, if the interpolation method is used as a finite–element basis, the order of accuracy of the resulting Coons element cannot reach the value four, no matter how accurate the description of the boundary line is.[1] The same is true for three–dimensional extensions which utilize only nodes along the boundary edges of a macroelement (as in the work of Provatidis): no matter how accurate the description of the unknown is along these edges, the order of the scheme is at most equal to three (this applies in particular, to the work of Provaditis).

In the approach introduced in,[7] the unknown is described by a third–order Hermite interpolation. It should be emphasize that the edge lines are

---

[1] For, the term $\left(\xi^1\,\xi^2\right)^2$ would be missing.

not arbitrary, but are described by a Hermite interpolation. The three–dimensional element generated following this scheme is referred to as *Hybrid element*.

4.2 The Coons Patch

Consider a topologically quadrilateral surface; given the four edge lines, the Coons Patch is obtained as: (1) the sum of the two linear interpolations between opposite boundary lines, minus (2) a bilinear interpolation through the four corner points (see Eq. 4.2). Let $\mathbf{x}_0(\xi,\eta)$, with $\xi,\eta \in [-1;1]$, describe a generic topologically quadrilateral surface patch. Let

$$\mathbf{x} = \mathbf{x}_{1,3}(\eta) = \mathbf{x}_0(\pm 1,\eta) \quad \text{and} \quad \mathbf{x} = \mathbf{x}_{2,4}(\xi) = \mathbf{x}_0(\xi,\pm 1)$$

with $\xi,\eta \in [-1;1]$, be the equations that describe the four edges of the patch, and let

$$\begin{aligned} \mathbf{x}_{++} &= \mathbf{x}_0(+1,+1) = \mathbf{x}_1(+1) = \mathbf{x}_2(+1) \\ \mathbf{x}_{+-} &= \mathbf{x}_0(+1,-1) = \mathbf{x}_4(+1) = \mathbf{x}_1(-1) \\ \mathbf{x}_{-+} &= \mathbf{x}_0(-1,+1) = \mathbf{x}_2(-1) = \mathbf{x}_3(+1) \\ \mathbf{x}_{--} &= \mathbf{x}_0(-1,-1) = \mathbf{x}_3(-1) = \mathbf{x}_4(-1) \end{aligned} \tag{4.1}$$

denote the four corner points.

As indicated above, we assume the functions $\mathbf{x}_1(\eta)$, $\mathbf{x}_2(\xi)$, $\mathbf{x}_3(\eta)$, $\mathbf{x}_4(\xi)$ to be prescribed. One wants to approximate $\mathbf{x}_0(\xi,\eta)$ with a surface $\mathbf{x}_{\mathsf{C}}(\xi,\eta)$ that has these lines as edges. The surface $\mathbf{x}_{\mathsf{C}}(\xi,\eta)$ thereby obtained is known as a Coons' Patch.[8]–[10] As mentioned above, the Coons' Patch is obtained as a sum of the two linear interpolations between opposite boundary lines, minus a bilinear interpolation through the four corner points. This yields, being $L_\pm(x)$ the linear interpolation functions (that should be seen also as the low–order interpolation within the scheme) such that $L_\pm(x) := (1 \pm x)/2$

$$\begin{aligned} &\mathbf{x}_{\mathsf{C}}(\xi,\eta) \\ &= L_+(\xi)\,\mathbf{x}_1(\eta) + L_+(\eta)\,\mathbf{x}_2(\xi) + L_-(\xi)\,\mathbf{x}_3(\eta) + L_-(\eta)\,\mathbf{x}_4(\xi) \\ &- L_+(\xi)\,L_+(\eta)\,\mathbf{x}_{++} - L_+(\xi)\,L_-(\eta)\,\mathbf{x}_{+-} - L_-(\xi)\,L_+(\eta)\,\mathbf{x}_{-+} - L_-(\xi)\,L_-(\eta)\,\mathbf{x}_{--} \end{aligned} \tag{4.2}$$

The four edges of this surface indeed coincide with the four generating lines. For instance, we have, using Eq. 4.1,

$$\begin{aligned} &\mathbf{x}_{\mathsf{C}}(1,\eta) \\ &= \mathbf{x}_1(\eta) + L_+(\eta)\,\mathbf{x}_2(1) + L_-(\eta)\,\mathbf{x}_4(1) - L_+(\eta)\,\mathbf{x}_{++} - L_-(\eta)\,\mathbf{x}_{+-} = \mathbf{x}_1(\eta), \end{aligned}$$

since $\mathbf{x}_2(1) = \mathbf{x}_{++}$ and $\mathbf{x}_4(1) = \mathbf{x}_{+-}$ (see Eq. 4.1). Similarly, $\mathbf{x}_{\mathsf{C}}(\xi, 1) = \mathbf{x}_2(\xi)$, $\mathbf{x}_{\mathsf{C}}(-1, \eta) = \mathbf{x}_3(\eta)$, and $\mathbf{x}_{\mathsf{C}}(\xi, -1) = \mathbf{x}_4(\xi)$.

4.3 The three–dimensional extension

Next, consider the extension to the three–dimensional case, as suggested in.[7] Specifically, we want to obtain a block starting from its six prescribed generating faces. In analogy with what is done to obtain Eq. 4.2, the function $\mathbf{x}(\xi, \eta, \zeta)$, which describes the block, is obtained as: (1) the sum of the three linear interpolations between opposite faces, minus (2) the sum of three bilinear interpolations through four "parallel" edges, plus (3) a trilinear interpolation through the eight vertices. This yields

$$
\begin{aligned}
&\mathbf{x}(\xi, \eta, \zeta) \\
&= L_+(\xi)\, \check{\mathbf{x}}(+1, \eta, \zeta) + L_+(\eta)\, \check{\mathbf{x}}(\xi, +1, \zeta) + L_+(\zeta)\, \check{\mathbf{x}}(\xi, \eta, +1) \\
&+ L_-(\xi)\, \check{\mathbf{x}}(-1, \eta, \zeta) + L_-(\eta)\, \check{\mathbf{x}}(\xi, -1, \zeta) + L_-(\zeta)\, \check{\mathbf{x}}(\xi, \eta, -1) \\
&- L_+(\xi)\, L_+(\eta)\, \check{\mathbf{x}}(+1, +1, \zeta) - L_+(\xi)\, L_+(\zeta)\, \check{\mathbf{x}}(+1, \eta, +1) - L_+(\eta)\, L_+(\zeta)\, \check{\mathbf{x}}(\xi, +1, +1) \\
&- L_+(\xi)\, L_-(\eta)\, \check{\mathbf{x}}(+1, -1, \zeta) - L_+(\xi)\, L_-(\zeta)\, \check{\mathbf{x}}(+1, \eta, -1) - L_+(\eta)\, L_-(\zeta)\, \check{\mathbf{x}}(\xi, +1, -1) \\
&- L_-(\xi)\, L_+(\eta)\, \check{\mathbf{x}}(-1, +1, \zeta) - L_-(\xi)\, L_+(\zeta)\, \check{\mathbf{x}}(-1, \eta, +1) - L_-(\eta)\, L_+(\zeta)\, \check{\mathbf{x}}(\xi, -1, +1) \\
&- L_-(\xi)\, L_-(\eta)\, \check{\mathbf{x}}(-1, -1, \zeta) - L_-(\xi)\, L_-(\zeta)\, \check{\mathbf{x}}(-1, \eta, -1) - L_-(\eta)\, L_-(\zeta)\, \check{\mathbf{x}}(\xi, -1, -1) \\
&+ L_+(\xi)\, L_+(\eta)\, L_+(\zeta)\, \check{\mathbf{x}}(+1, +1, +1) + L_+(\xi)\, L_+(\eta)\, L_-(\zeta)\, \check{\mathbf{x}}(+1, +1, -1) \\
&+ L_+(\xi)\, L_-(\eta)\, L_+(\zeta)\, \check{\mathbf{x}}(+1, -1, +1) + L_+(\xi)\, L_-(\eta)\, L_-(\zeta)\, \check{\mathbf{x}}(+1, -1, -1) \\
&+ L_-(\xi)\, L_+(\eta)\, L_+(\zeta)\, \check{\mathbf{x}}(-1, +1, +1) + L_-(\xi)\, L_+(\eta)\, L_-(\zeta)\, \check{\mathbf{x}}(-1, +1, -1) \\
&+ L_-(\xi)\, L_-(\eta)\, L_+(\zeta)\, \check{\mathbf{x}}(-1, -1, +1) + L_-(\xi)\, L_-(\eta)\, L_-(\zeta)\, \check{\mathbf{x}}(-1, -1, -1)
\end{aligned}
\tag{4.3}
$$

where $\check{\mathbf{x}}(\xi, \eta, \zeta)$ denotes the function prescribed at the six faces (for instance, $\check{\mathbf{x}}(1, \eta, \zeta)$ denotes the face at $\xi = 1$, $\check{\mathbf{x}}(1, 1, \zeta)$ the edge for $\xi = \eta = 1$, and $\check{\mathbf{x}}(1, 1, 1)$ the vertex for $\xi = \eta = \zeta = 1$). The block thereby generated does indeed have the prescribed faces; for instance,

$$
\begin{aligned}
&\mathbf{x}(\xi, \eta, 1) \\
&= L_+(\xi)\, \check{\mathbf{x}}(1, \eta, 1) + L_+(\eta)\, \check{\mathbf{x}}(\xi, 1, 1) + L_-(\xi)\, \check{\mathbf{x}}(-1, \eta, 1) + L_-(\eta)\, \check{\mathbf{x}}(\xi, -1, 1) \\
&- L_+(\xi)\, \check{\mathbf{x}}(1, \eta, 1) - L_+(\eta)\, \check{\mathbf{x}}(\xi, 1, 1) - L_-(\xi)\, \check{\mathbf{x}}(-1, \eta, 1) - L_-(\eta)\, \check{\mathbf{x}}(\xi, -1, 1) \\
&- L_+(\xi)\, L_+(\eta)\, \check{\mathbf{x}}(1, 1, 1) \quad - L_+(\xi)\, L_-(\eta)\, \check{\mathbf{x}}(1, -1, 1) \\
&- L_-(\xi)\, L_+(\eta)\, \check{\mathbf{x}}(-1, 1, 1) - L_-(\xi)\, L_-(\eta)\, \check{\mathbf{x}}(-1, -1, 1) \\
&+ L_+(\xi)\, L_+(\eta)\, \check{\mathbf{x}}(1, 1, 1) \quad + L_+(\xi)\, L_-(\eta)\, \check{\mathbf{x}}(1, -1, 1) \\
&+ L_-(\xi)\, L_+(\eta)\, \check{\mathbf{x}}(-1, 1, 1) + L_-(\xi)\, L_-(\eta)\, \check{\mathbf{x}}(-1, -1, 1) + \ \check{\mathbf{x}}(\xi, \eta, 1)
\end{aligned}
$$

or,

$$\mathbf{x}(\xi,\eta,1)=\check{\mathbf{x}}(\xi,\eta,1).$$

It should be emphasized that combining the above procedure with that in Section 4.2, that is, assuming that the six generating faces of the block are provided as Coons patches, allows one to generate a block simply from the equations of its twelve edge lines.

4.4 The Hybrid 3rd order $8-$node element

Next, consider what happens to the three–dimensional extension of the Coons patch technique, when the twelve generating edge lines are obtained by using the Hermite interpolation technique.

In the simplest version of the Hybrid element, the third–order Hermite interpolation is used to define each edge. Hence, it is sufficient to provide the location, $\mathbf{x}$, and the covariant base vectors, $\partial\mathbf{x}/\partial\xi$, at each of the two end points of each edge. Extending this to three dimensions, and still using the Hermite interpolation to define the twelve edge lines, one obtains an interpolation technique that requires only the location and the three covariant base vectors at the eight corners of each block (as well as each brick), for a total of 32 parameters (instead of the 64 required by the Hermite interpolation). The same scheme is used for the unknowns (isoparametric scheme). The result is that, with respect to the Hermite scheme, the number of unknowns is reduced by a factor two (and the computational time by an order of magnitude), without any reduction on the accuracy of the scheme, which remains of order three. It is worth noting that this element, like the Hermite element, provides a solution that is continuous with its gradient (class C^1).

However, the most important improvement introduced by this scheme is the fact that now the block–boundary node problem discussed at the end of Subsection 2.3 can be eliminated: only the values of the unknown function and of its gradient are required at the node of each brick (if a brick has block–boundary nodes, the problem is resolved using the Cartesian components of the gradient).

Returning to the Coons patch interpolation, Eq. 4.2, we assume that the four edge lines of the patch be described by a Hermite interpolation of the type given in Eq. 2.2, that is,

$$\begin{aligned}\mathbf{x}_{1,3}(\eta)=\mathbf{x}(\pm1,\eta)&=\mathbf{x}_{\pm+}\,M_+(\eta)+\mathbf{x}_{\pm-}\,M_-(\eta)+\mathbf{x}^{\eta}_{\pm+}\,N_+(\eta)+\mathbf{x}^{\eta}_{\pm-}\,N_-(\eta)\\ \mathbf{x}_{2,4}(\xi)=\mathbf{x}(\xi,\pm1)&=\mathbf{x}_{+\pm}\,M_+(\xi)+\mathbf{x}_{-\pm}\,M_-(\xi)+\mathbf{x}^{\xi}_{+\pm}\,N_+(\xi)+\mathbf{x}^{\xi}_{-\pm}\,N_-(\xi)\end{aligned} \tag{4.4}$$

where $\mathbf{x}_{\pm\pm}$ denote the four corner points of the patch, $\mathbf{x}^{\xi}_{+\pm} := \partial\mathbf{x}/\partial\xi|_{\mathbf{x}_{+\pm}}$ and $\mathbf{x}^{\eta}_{+\pm} := \partial\mathbf{x}/\partial\eta|_{\mathbf{x}_{+\pm}}$ denote the corresponding base vectors, whereas $M_{\pm}(x), N_{\pm}(x)$ denote the one–dimensional Hermite shape functions (see again Eq. 2.2).

Combining Eqs. 4.2 and 4.4 yields

$$\begin{aligned}
&\mathbf{x}(\xi,\eta)\\
&= \mathbf{x}_{++}[L_{+}(\xi)M_{+}(\eta) + M_{+}(\xi)L_{+}(\eta) - L_{+}(\xi)L_{+}(\eta)]\\
&+ \mathbf{x}_{+-}[L_{+}(\xi)M_{-}(\eta) + M_{+}(\xi)L_{-}(\eta) - L_{+}(\xi)L_{-}(\eta)]\\
&+ \mathbf{x}_{-+}[L_{-}(\xi)M_{+}(\eta) + M_{-}(\xi)L_{+}(\eta) - L_{-}(\xi)L_{+}(\eta)]\\
&+ \mathbf{x}_{--}[L_{-}(\xi)M_{-}(\eta) + M_{-}(\xi)L_{-}(\eta) - L_{-}(\xi)L_{-}(\eta)]\\
&+ \mathbf{x}^{\xi}_{++}N_{+}(\xi)L_{+}(\eta) + \mathbf{x}^{\xi}_{+-}N_{+}(\xi)L_{-}(\eta) + \mathbf{x}^{\xi}_{-+}N_{-}(\xi)L_{+}(\eta) + \mathbf{x}^{\xi}_{--}N_{-}(\xi)L_{-}(\eta)\\
&+ \mathbf{x}^{\eta}_{++}L_{+}(\xi)N_{+}(\eta) + \mathbf{x}^{\eta}_{+-}L_{+}(\xi)N_{-}(\eta) + \mathbf{x}^{\eta}_{-+}L_{-}(\xi)N_{+}(\eta) + \mathbf{x}^{\eta}_{--}L_{-}(\xi)N_{-}(\eta),
\end{aligned} \tag{4.5}$$

Introducing the function

$$P_{s_1 s_2}(\xi,\eta) = L_{s_1}(\xi)\, M_{s_2}(\eta) + M_{s_1}(\xi)\, L_{s_2}(\eta) - L_{s_1}(\xi)\, L_{s_2}(\eta) \tag{4.6}$$

Eq. 4.5 may be rewritten as

$$\begin{aligned}
\mathbf{x}(\xi,\eta) =& \sum_{s_1,s_2=1}^{2} \mathbf{x}_{s_1 s_2} P_{s_1 s_2}(\xi,\eta)\\
&+ \sum_{s_1,s_2=1}^{2} \mathbf{x}^{\xi}_{s_1 s_2} N_{s_1}(\xi) L_{s_2}(\eta) + \sum_{s_1,s_2=1}^{2} \mathbf{x}^{\eta}_{s_1 s_2} L_{s_1}(\xi) N_{s_2}(\eta)
\end{aligned} \tag{4.7}$$

Next, let us turn to the three–dimensional extension (*i.e.*, the expression for a hexahedral block). Combining Eqs. 4.3 and 4.7, one obtains

$$\mathbf{x}_{\mathsf{block}}(\xi,\eta,\zeta) = \mathbf{x}_{\mathsf{faces}}(\xi,\eta,\zeta) - \mathbf{x}_{\mathsf{edges}}(\xi,\eta,\zeta) + \mathbf{x}_{\mathsf{vertices}}(\xi,\eta,\zeta),$$

where, setting $\mathbf{s} := (s_1, s_2, s_3)$, with $s_k = 1,2$, $\mathbf{x}_{\mathbf{s},1} := \partial\mathbf{x}/\partial\xi|_{\mathbf{x}_{\mathbf{s}}}$, $\mathbf{x}_{\mathbf{s},2} := \partial\mathbf{x}/\partial\eta|_{\mathbf{x}_{\mathbf{s}}}$, and $\mathbf{x}_{\mathbf{s},3} := \partial\mathbf{x}/\partial\zeta|_{\mathbf{x}_{\mathbf{s}}}$, the contribution from the three linear interpolations between the opposite faces is given by ($\sum_{\mathbf{s}}$ is understood to span over the eight values of $\mathbf{s}$)

$$
\begin{aligned}
&\mathbf{x}_{\mathsf{faces}}(\xi,\eta,\zeta)\\
&= \sum_{\mathbf{s}} \mathbf{x}_{\mathbf{s}}\, P_{s_1 s_2}(\xi,\eta)\, L_{s_3}(\zeta) + \sum_{\mathbf{s}} \mathbf{x}_{\mathbf{s}}\, P_{s_2 s_3}(\eta,\zeta)\, L_{s_1}(\xi) + \sum_{\mathbf{s}} \mathbf{x}_{\mathbf{s}}\, P_{s_3 s_1}(\zeta,\xi)\, L_{s_2}(\eta)\\
&+ \sum_{\mathbf{s}} \mathbf{x}_{\mathbf{s},1}\, N_{s_1}(\xi)\, L_{s_2}(\eta)\, L_{s_3}(\zeta) + \sum_{\mathbf{s}} \mathbf{x}_{\mathbf{s},2}\, L_{s_1}(\xi)\, N_{s_2}(\eta)\, L_{s_3}(\zeta)\\
&+ \sum_{\mathbf{s}} \mathbf{x}_{\mathbf{s},2}\, L_{s_1}(\xi)\, N_{s_2}(\eta)\, L_{s_3}(\zeta) + \sum_{\mathbf{s}} \mathbf{x}_{\mathbf{s},3}\, L_{s_1}(\xi)\, L_{s_2}(\eta)\, N_{s_3}(\zeta)\\
&+ \sum_{\mathbf{s}} \mathbf{x}_{\mathbf{s},3}\, L_{s_1}(\xi)\, L_{s_2}(\eta)\, N_{s_3}(\zeta) + \sum_{\mathbf{s}} \mathbf{x}_{\mathbf{s},1}\, N_{s_1}(\xi)\, L_{s_2}(\eta)\, L_{s_3}(\zeta)
\end{aligned}
$$

whereas the contribution from three bilinear interpolations through “parallel” edges is given by

$$
\begin{aligned}
\mathbf{x}_{\mathsf{edges}}(\xi,\eta,\zeta) \quad &= \sum_{\mathbf{s}} \left[\mathbf{x}_{\mathbf{s}}\, M_{s_1}(\xi) + \mathbf{x}_{\mathbf{s},1}\, N_{s_1}(\xi)\right]\, L_{s_2}(\eta)\, L_{s_3}(\zeta)\\
&+ \sum_{\mathbf{s}} \left[\mathbf{x}_{\mathbf{s}}\, M_{s_2}(\eta) + \mathbf{x}_{\mathbf{s},2}\, N_{s_2}(\eta)\right]\, L_{s_1}(\xi)\, L_{s_3}(\zeta)\\
&+ \sum_{\mathbf{s}} \left[\mathbf{x}_{\mathbf{s}}\, M_{s_3}(\zeta) + \mathbf{x}_{\mathbf{s},3}\, N_{s_3}(\zeta)\right]\, L_{s_1}(\xi)\, L_{s_2}(\eta)
\end{aligned}
$$

and finally the trilinear interpolation through the eight vertices is given by

$$
\mathbf{x}_{\mathsf{vertices}}(\xi,\eta,\zeta) = \sum_{\mathbf{s}} \mathbf{x}_{\mathbf{s}}\, L_{s_1}(\xi)\, L_{s_2}(\eta)\, L_{s_3}(\zeta)
$$

Combining these expressions, one obtains

$$
\mathbf{x}_{\mathsf{block}}(\xi,\eta,\zeta) = \sum_{\mathbf{s}} \mathbf{x}_{\mathbf{s}}\, R_{\mathbf{s}}(\xi,\eta,\zeta) + \sum_{\mathbf{s}} \sum_{\alpha=1}^{3} \mathbf{x}_{\mathbf{s},\alpha}\, S_{\mathbf{s}}^{\alpha}(\xi,\eta,\zeta), \tag{4.8}
$$

where

$$
\begin{aligned}
&R_{\mathbf{s}}(\xi,\eta,\zeta)\\
&= P_{s_1 s_2}(\xi,\eta)\, L_{s_3}(\zeta) + P_{s_2 s_3}(\eta,\zeta)\, L_{s_1}(\xi) + P_{s_3 s_1}(\zeta,\xi)\, L_{s_2}(\eta)\\
&- M_{s_1}(\xi)\, L_{s_2}(\eta)\, L_{s_3}(\zeta) - L_{s_1}(\xi)\, M_{s_2}(\eta)\, L_{s_3}(\zeta) - L_{s_1}(\xi)\, L_{s_2}(\eta)\, M_{s_3}(\zeta)\\
&+ L_{s_1}(\xi)\, L_{s_3}(\eta)\, L_{s_3}(\zeta)
\end{aligned}
$$

hence, considering Eq. 4.6

$$
\begin{aligned}
&R_{\mathbf{s}}(\xi,\eta,\zeta)\\
&= M_{s_1}(\xi)\, L_{s_2}(\eta)\, L_{s_3}(\zeta) + L_{s_1}(\xi)\, M_{s_2}(\eta)\, L_{s_3}(\zeta)\\
&+ L_{s_1}(\xi)\, L_{s_2}(\eta)\, M_{s_3}(\zeta) - 2\, L_{s_1}(\xi)\, L_{s_2}(\eta)\, L_{s_3}(\zeta)
\end{aligned} \tag{4.9}
$$

whereas

$$\begin{aligned} S^1_{\mathbf{s}}(\xi,\eta,\zeta) &= N_{s_1}(\xi)\, L_{s_2}(\eta)\, L_{s_3}(\zeta) \\ S^2_{\mathbf{s}}(\xi,\eta,\zeta) &= L_{s_1}(\xi)\, N_{s_2}(\eta)\, L_{s_3}(\zeta) \\ S^3_{\mathbf{s}}(\xi,\eta,\zeta) &= L_{s_1}(\xi)\, L_{s_2}(\eta)\, N_{s_3}(\zeta) \end{aligned} \tag{4.10}$$

The expressions above provide the desired local interpolation procedure for the geometry $\mathbf{x} = \mathbf{x}(\xi,\eta,\zeta)$. The same interpolation can be used to interpolate any function $f = f(\xi^\alpha)$ (similarly to Chapter 2, ξ^α with $\alpha = 1, 2, 3$ refers to the three coordinates ξ, η, ζ) in the volume defined by the block. One obtains

$$f(\xi^\alpha) = \sum_{\mathbf{s}} f_{\mathbf{s}}\, R_{\mathbf{s}}(\xi^\alpha) + \sum_{\mathbf{s}} \sum_{\alpha=1}^{3} f_{\mathbf{s},\alpha}\, S^\alpha_{\mathbf{s}}(\xi^\alpha), \tag{4.11}$$

Accordingly to Section 2.2 (Eq. 2.4), whenever the unknown function is a scalar $u = u(\xi^\alpha)$ (as in acoustics), these may be combined to yield a global interpolation as

$$u(\xi^\alpha) = \sum_{p=1}^{P} z_p \chi_p(\xi^\alpha), \tag{4.12}$$

where now the z_p's comprise the nodal values of u and $u_{,\alpha}$ ($\alpha = 1, 2, 3$) (considered the eight nodes, $P = 32$), whereas $\chi_p(\xi^\alpha)$ are the global shape functions, defined locally by Eqs. 4.9, 4.10.

If the unknown is a vector function $\mathbf{u}$, as in structural dynamics, we have

$$\mathbf{u}(\xi^\alpha) = \sum_{p=1}^{P} z_p \boldsymbol{\chi}_p(\xi^\alpha), \tag{4.13}$$

where now the z_p's comprise the nodal values of the Cartesian components of $\mathbf{u}$ and $\mathbf{u}_{,\alpha}$ ($\alpha = 1, 2, 3$) whereas $\boldsymbol{\chi}_p(\xi^\alpha)$ are vector global shape functions, obtained from the $\chi_p(\xi^\alpha)$'s in Eqs. 4.9, 4.10 through multiplication by the appropriate base vector. The same interpolation is used for the geometry (isoparametric representation).

4.5 Comments

In this Chapter a new element, whose geometry and unknown function are completely defined by only their nodal values and their nodal values of the three first–order partial derivatives, has been introduced and referred to as the Hybrid 3rd order 8−node brick. As in the case of the Hermite 3rd order 8–nodes element, the local interpolation, Eq. 4.8, may be recast as a global interpolation, as in Eq. 2.4 and the same expression may be used to interpolate, still within each brick element, any function. Thus, Eq. 4.8 provides an isoparametric finite–element interpolation function.

An important advantage of the 3rd order 8−nodes Hybrid element over the Hermite one, is that it is exempt from the block–boundary nodes problem that arise in the Hermite element for non hexhedral geometries (see Section 2.3).

In addition, in the case of the Hybrid third–order 8–nodes element, the 32 local shape functions are linear combinations of monomials of the type $\xi^p \eta^q \zeta^r$ (with $p = 0, 1, 2, 3,\ q, r = 0, 1$; or $q = 0, 1, 2, 3,\ p, r = 0, 1$; or $r = 0, 1, 2, 3,\ p, q = 0, 1$), also numbering 32 in total. Both sets of functions are linearly independent and thus they span the same subspace. Hence, either one may be used as a basis for this subspace.

Finally, note that all the monomials with $p + q + r \leq 3$ are included in this subspace. Hence, the scheme is of order three and an h^3−convergence is expected, as it is for the Hermite scheme, even though half nodal unknowns are required (recall that, for the Hermite brick, 64 unknowns per brick are needed).

Chapter 5

Higher–order Hybrid element

In this chapter the problem of how to improve the accuracy of the Hybrid element is discussed. In particular, an extension to order 7 of the Hybrid element presented in Chapter 4 is proposed. This is based upon Hermite interpolations, that will be hereafter referred to as *WEP interpolations*, to indicate an interpolation method *With End–Points* (only).

On the contrary, *WIP interpolation* will refer to an interpolation method *With Intermediate–Points.*

5.1 Higher–order WEP Hybrid elements

In order to describe the extension to higher–orders of the WEP Hybrid scheme (that is a brick consisting of only 8 nodes), it is convenient to rephrase the Hybrid element formulation of Section 4.4 as follows: the scheme consists of a combination of a high–accuracy and a low–accuracy interpolation scheme. For instance, for the two–dimensional case (specifically, for a quadrilateral surface in space) the scheme consists of (1) a *low–accuracy* (linear) interpolation of two opposite lines which are described by a *high–accuracy* (third–order) interpolation, plus (2) a similar process for two other opposite lines, minus (3) a double low–accuracy (bilinear) interpolation of the four corners.

In order to increase the accuracy, one is forced to increase the order of the low–accuracy interpolation. In general, the order of the accurate interpolation requires twice as many parameters as the low order one. For instance, if the accurate interpolation is of the eleventh order, the other would be of the fifth order. It is easy to see that, except for the third order, the issue of the patch–boundary nodes represents itself.

In this thesis two different Hybrid elements of order higher than three have been addressed. Specifically, one of them is related to a Hermite interpolation scheme (and hence a WEP interpolation for the definition given at the beginning of the Chapter); it is of order seven and has been addressed in Subsection 5.1.1. This element will be referred to as the *Hybrid* $7th$ *order* $8-$*nodes*.

A quite different approach stems from an internal node formulation (that is a WIP formulation), is of order five and has been addressed in Subsection 5.4.1. This formulation, despite a lower order of the element with respect to the former one, presents the key advantage of eliminating the block–boundary problem also for higher–order elements. This element will be referred to as the *Hybrid* $5th$ *order* $27-$*nodes*.

5.1.1 The Hybrid 7th order $8-$node element

In this subsection, a WEP formulation is adopted. Specifically, the 3rd–order Hermite interpolation is used for the low–accuracy interpolation whereas the 7th order WEP interpolation is used for the high–accuracy interpolation. Specifically, a seventh–order hybrid scheme extension is considered: this may be obtained from Eq. 4.3, by replacing the low–accuracy (linear) interpolation with a third–order Hermite interpolation, and the high–accuracy (third–order) interpolation with a seventh–order WEP interpolation.[1]

For each of the eight nodes, this requires the use of the values of the function and its first, second and third derivatives, along with the first derivative of each one of these quantities in the other two directions. To be precise, the unknowns at each node are: (i) the function, u, (ii) the three first–order derivatives ($u_{,1}$, $u_{,2}$, $u_{,3}$), (iii) the six second–order derivatives ($u_{,11}$, $u_{,22}$, $u_{,33}$; $u_{,12}$, $u_{,23}$, $u_{,31}$), (iv) ten third–order derivatives ($u_{,111}$, $u_{,222}$, $u_{,333}$; $u_{,112}$, $u_{,113}$, $u_{,221}$, $u_{,223}$, $u_{,331}$, $u_{,332}$; $u_{,123}$), (v) nine fourth–order derivatives ($u_{,1123}$, $u_{,2213}$, $u_{,3312}$; $u_{,1112}$, $u_{,1113}$, $u_{,2221}$, $u_{,2223}$, $u_{,3331}$, $u_{,3332}$), and (vi) three fifth–order derivatives ($u_{,11123}$, $u_{,22213}$, $u_{,33312}$). Thus, the total of unknowns is 32 for each node.

To begin with, both the third–order Hermite shape functions of Eq. 2.2 and the seventh–order Hermite shape functions of Eq. 3.1.2 that, for convenience, are repeated hereafter. To avoid misleadings in the meaning of symbols, the third–order polynomials are now referred to as $M_k(x)$ (for

---

[1] Note that, within the Hybrid elements family, the overall accuracy cannot reach the order eight: as it is easy to verify, the term $\left(\xi^1\,\xi^2\right)^4$ would always be missing.

$k = 0, 1$) whereas the seventh–order ones are now referred to as $N_k(x)$ (for $k = 0, 1, 2, 3$). Thus, one has for $x \in [-1, 1]$:

$$
\begin{aligned}
M_{0\pm}(x) &= \frac{1}{4}(2 \pm 3x \mp x^3), \\
M_{1\pm}(x) &= \frac{1}{4}(\mp 1 - x \pm x^2 + x^3)
\end{aligned}
$$

and

$$
\begin{aligned}
N_{0\pm}(x) &= \frac{1}{32}\left(\mp 5x^7 \pm 21x^5 \mp 35x^3 \pm 35x + 16\right), \\
N_{1\pm}(x) &= \frac{1}{32}\left(5x^7 \pm x^6 - 21x^5 \mp 5x^4 + 35x^3 \pm 15x^2 - 19x \mp 11\right), \\
N_{2\pm}(x) &= \frac{1}{32}\left(\mp 2x^7 - x^6 \pm 8x^5 + 5x^4 \mp 10x^3 - 7x^2 \pm 4x + 3\right), \\
N_{3\pm}(x) &= \frac{1}{32}\left[\frac{1}{3}\left(x^7 \pm x^6 - 3x^5 \mp 3x^4 + 3x^3 \pm 3x^2 - x \mp 1\right)\right].
\end{aligned}
$$

Equation 4.11 of Section 4.4 may be rewritten for a seventh–order scheme and for a generic function $f = f(\xi^\alpha)$ to give

$$
\begin{aligned}
&f(\xi^\alpha) = \\
&\sum_{\mathbf{s}} \left(R_{\mathbf{s}}(\xi^\alpha)\, f_{\mathbf{s}} + \sum_{\beta=1}^{3} R_{\mathbf{s}}^{\beta}(\xi^\alpha)\, f_{\mathbf{s},\beta} + \sum_{\beta\gamma\in=I_2} R_{\mathbf{s}}^{\beta\gamma}(\xi^\alpha)\, f_{\mathbf{s},\beta\gamma} + R_{\mathbf{s}}^{123}\, f_{\mathbf{s},123}(\xi^\alpha) \right) \\
&+ \sum_{\mathbf{s}} \left(\sum_{\beta=1}^{3} S_{\mathbf{s}}^{\beta\beta}(\xi^\alpha)\, f_{\mathbf{s},\beta\beta} + \sum_{\beta\gamma\lambda\in I_3} S_{\mathbf{s}}^{\beta\gamma\lambda}(\xi^\alpha) f_{\mathbf{s},\beta\gamma\lambda} \right. \\
&\qquad \left. + \sum_{\beta\gamma\lambda\mu\in I_4} S_{\mathbf{s}}^{\beta\gamma\lambda\mu}(\xi^\alpha) f_{\mathbf{s},\beta\gamma\lambda\mu} + \sum_{\beta\gamma\lambda\mu\nu\in I_5} S_{\mathbf{s}}^{\beta\gamma\lambda\mu\nu}(\xi^\alpha) f_{\mathbf{s},\beta\gamma\lambda\mu\nu} \right)
\end{aligned}
\tag{5.1}
$$

where $\mathbf{s} := (s_1, s_2, s_3)$, with $s_k = 1, 2$, defines the eight nodes of the brick element ($\sum_{\mathbf{s}}$ is understood to span over all the eight values of $\mathbf{s}$); moreover, noting that the mixed derivatives include now at most the third derivative in a direction when a first derivative is present upon the others, one obtains

$$
\begin{aligned}
&I_2 := \\
&\{(1,2);(1,3);(2,3)\}, \\
&I_3 := \\
&\{(1,1,1);(2,2,2);(3,3,3); \\
&(1,1,2);(1,2,2);(1,1,3);(3,3,1);(2,2,3);(3,3,2)\}, \\
&I_4 := \\
&\{(1,1,2,3);(2,2,3,1);(3,3,1,2); \\
&(1,3,3,3);(2,3,3,3);(1,2,2,2);(3,2,2,2);(2,1,1,1);(3,1,1,1)\}, \\
&I_5 := \\
&\{(1,2,3,3,3);(1,3,2,2,2);(2,3,1,1,1)\},
\end{aligned}
\tag{5.2}
$$

In addition, $R_{\mathbf{s}}(\xi^\alpha)$, $R_{\mathbf{s}}^{\beta}(\xi^\alpha)$, $R_{\mathbf{s}}^{\beta\gamma}(\xi^\alpha)$, $R_{\mathbf{s}}^{123}(\xi^\alpha)$ and $S_{\mathbf{s}}^{\beta\beta}(\xi^\alpha)$, $S_{\mathbf{s}}^{\beta\gamma\lambda}(\xi^\alpha)$, $S_{\mathbf{s}}^{\beta\gamma\lambda\mu}(\xi^\alpha)$, $S_{\mathbf{s}}^{\beta\gamma\lambda\mu\nu}(\xi^\alpha)$, are suitable products of the Hermite polynomials of order seven and three. Specifically, we have

$$
\begin{aligned}
&R_{\mathbf{s}}(\xi^\alpha) \\
&= N_{0s_1}(\xi^1)\,M_{0s_2}(\xi^2)\,M_{0s_3}(\xi^3) + M_{0s_1}(\xi^1)\,N_{0s_2}(\xi^2)\,M_{0s_3}(\xi^3) \\
&+ M_{0s_1}(\xi^1)\,M_{0s_2}(\xi^2)\,N_{0s_3}(\xi^3) - 2\,N_{0s_1}(\xi^1)\,N_{0s_2}(\xi^2)\,N_{0s_3}(\xi^3)
\end{aligned}
\tag{5.3}
$$

$$
\begin{aligned}
&R_{\mathbf{s}}^1(\xi^\alpha) \\
&= N_{1s_1}(\xi^1)\,M_{0s_2}(\xi^2)\,M_{0s_3}(\xi^3) + M_{1s_1}(\xi^1)\,N_{0s_2}(\xi^2)\,M_{0s_3}(\xi^3) \\
&+ M_{1s_1}(\xi^1)\,M_{0s_2}(\xi^2)\,N_{0s_3}(\xi^3) - 2\,N_{1s_1}(\xi^1)\,N_{0s_2}(\xi^2)\,N_{0s_3}(\xi^3)
\end{aligned}
\tag{5.4}
$$

$$
\begin{aligned}
&R_{\mathbf{s}}^{12}(\xi^\alpha) \\
&= N_{1s_1}(\xi^1)\,M_{1s_2}(\xi^2)\,M_{0s_3}(\xi^3) + M_{1s_1}(\xi^1)\,N_{1s_2}(\xi^2)\,M_{0s_3}(\xi^3) \\
&+ M_{1s_1}(\xi^1)\,M_{1s_2}(\xi^2)\,N_{0s_3}(\xi^3) - 2\,N_{1s_1}(\xi^1)\,N_{1s_2}(\xi^2)\,N_{0s_3}(\xi^3)
\end{aligned}
\tag{5.5}
$$

$$
\begin{aligned}
&R_{\mathbf{s}}^{123}(\xi^\alpha) \\
&= N_{1s_1}(\xi^1)\,M_{1s_2}(\xi^2)\,M_{1s_3}(\xi^3) + M_{1s_1}(\xi^1)\,N_{1s_2}(\xi^2)\,M_{1s_3}(\xi^3)
\end{aligned}
\tag{5.6}
$$

whereas

$$
\begin{aligned}
S_{\mathbf{s}}^{11}(\xi^\alpha) &= N_{2s_1}(\xi^1)\,M_{0s_2}(\xi^2)\,M_{0s_3}(\xi^3) \\
S_{\mathbf{s}}^{111}(\xi^\alpha) &= N_{3s_1}(\xi^1)\,M_{0s_2}(\xi^2)\,M_{0s_3}(\xi^3) \\
S_{\mathbf{s}}^{1123}(\xi^\alpha) &= N_{2s_1}(\xi^1)\,M_{1s_2}(\xi^2)\,M_{1s_3}(\xi^3) \\
S_{\mathbf{s}}^{11123}(\xi^\alpha) &= N_{3s_1}(\xi^1)\,M_{1s_2}(\xi^2)\,M_{1s_3}(\xi^3)
\end{aligned}
\tag{5.7}
$$

The expressions above provide the desired local interpolation procedure for any function $f(\xi^\alpha)$. Similarly to Section 2.2 (Eq. 2.4), whenever the unknown function is a scalar $u = u(\xi^\alpha)$ (as in acoustics), these may be combined to yield a global interpolation as

$$u(\xi^\alpha) = \sum_{p=1}^{P} z_p \chi_p(\xi^\alpha),$$

where now the z_p's comprise the nodal values of u, $u_{,\alpha}$ $(\alpha = 1, 2, 3)$, $u_{,\beta\gamma}$ $(\beta\gamma \in I_2)$, $u_{,\beta\gamma\lambda}$ $(\beta\gamma\lambda \in I_3)$, $u_{,\beta\gamma\lambda\mu}$ $(\beta\gamma\lambda\mu \in I_4)$, $u_{,\beta\gamma\lambda\mu\nu}$ $(\beta\gamma\lambda\mu\nu \in I_5)$, $u_{,\beta\gamma\lambda\mu\nu\omega}$ $(\beta\gamma\lambda\mu\nu\omega \in I_6)$, $u_{,\beta\gamma\lambda\mu\nu\omega\tau}$ $(\beta\gamma\lambda\mu\nu\omega\tau \in I_7)$, $u_{,\beta\gamma\lambda\mu\nu\omega\tau\iota}$ $(\beta\gamma\lambda\mu\nu\omega\tau\iota \in I_8)$, as well as $u_{,111222333}$, whereas $\chi_p(\xi^\alpha)$ are the global shape functions (considered the eight nodes, $P = 512$), defined locally by Eqs. 3.14.

If the unknown is a vector function, as in structural dynamics, we have

$$\mathbf{u}(\xi^\alpha) = \sum_{p=1}^{P} z_p \boldsymbol{\chi}_p(\xi^\alpha),$$

where now the z_p's comprise the nodal values of the Cartesian components of $\mathbf{u}$, $\mathbf{u}_{,\alpha}$ $(\alpha = 1, 2, 3)$, $\mathbf{u}_{,\beta\gamma}$ $(\beta\gamma \in I_2)$, $\mathbf{u}_{,\beta\gamma\lambda}$ $(\beta\gamma\lambda \in I_3)$, $\mathbf{u}_{,\beta\gamma\lambda\mu}$ $(\beta\gamma\lambda\mu \in I_4)$, $\mathbf{u}_{,\beta\gamma\lambda\mu\nu}$ $(\beta\gamma\lambda\mu\nu \in I_5)$, $\mathbf{u}_{,\beta\gamma\lambda\mu\nu\omega}$ $(\beta\gamma\lambda\mu\nu\omega \in I_6)$, $\mathbf{u}_{,\beta\gamma\lambda\mu\nu\omega\tau}$ $(\beta\gamma\lambda\mu\nu\omega\tau \in I_7)$, $\mathbf{u}_{,\beta\gamma\lambda\mu\nu\omega\tau\iota}$ $(\beta\gamma\lambda\mu\nu\omega\tau\iota \in I_8)$, as well as $\mathbf{u}_{,111222333}$, whereas $\boldsymbol{\chi}_p(\xi^\alpha)$ are vector global shape functions, obtained from the $\chi_p(\xi^\alpha)$'s in Eqs. 3.14, through multiplication by the appropriate base vector. The same interpolation is used for the geometry (isoparametric representation).

5.2 Block–boundary problem

Note that, the block–boundary problem discussed in Section 2.3 appears again. In fact, for the seventh–order scheme, we have all the derivative of order 1, 2 and 3; however, we do not have all the derivatives of order 4 and 5.

This comment leads to the idea of creating a Hybrid element of order higher then three with the distinguishing feature of being not affected by the block–boundary problem. This is obtained using a WIP formulation.

The formulation developed is addressed in Subsection 5.4.1.

5.3 One–dimensional WIP interpolation

In this section a high–order internal–node scheme is addressed. This scheme will be shortly referred to as a *WIP scheme* to indicate an interpolation method *With Intermediate–Points*. The main intent here is to introduce a new hybrid scheme, in which for the Hermitian interpolation scheme, instead of prescribing the function and its derivatives at the end points, one prescribes the values of the function and of its first derivative at n points within the interval of interest, two of which being the end points.

Specifically, let $M_k(x)$ and $N_k(x)$, with $k = 1, \dots, n$ (the total number of nodes is here assumed to be n), the polynomials related to the function and the derivative respectively of the $k - th$ node, we have

$$u(x) = \sum_{k=1}^{n} u_k M_k(x) + \sum_{k=1}^{n} u'_k N_k(x)$$

where the polynomials $M_k(x)$ and $N_k(x)$ satisfy the conditions

$$M_k(x_j) = \delta_{kj}; \qquad M'_k(x_j) = 0; \qquad N_k(x_j) = 0; \qquad N'_k(x_j) = \delta_{kj}. \tag{5.8}$$

For any value of n, these polynomials are given by

$$\begin{aligned} M_k(x) &= \frac{x-a}{x_k-a} \prod_{k \neq j=1}^{n} \frac{(x-x_j)^2}{(x_k-x_j)^2} \\ N_k(x) &= (x-x_k) \prod_{k \neq j=1}^{n} \frac{(x-x_j)^2}{(x_k-x_j)^2} \end{aligned} \tag{5.9}$$

with a obtained from

$$\frac{1}{x_k - a} + 2 \sum_{k \neq j=1}^{n} \frac{1}{x_k - x_j} = 0 \tag{5.10}$$

Indeed, it is apparent that the polynomials $M_k(x)$ and $N_k(x)$ vanish with their derivatives at $x = x_j$, with $k \neq j$. In addition, for $k = j$, we have $N_k(x_k) = 0$, as well as $M'_k(x_k) = 0$ since, using Eq. 5.10, the logarithmic derivative of $M_k(x)$ at $x = x_k$ is given by

$$\frac{M'_k(x_k)}{M_k(x_k)} = \left[\frac{1}{x-a} + 2 \sum_{k \neq j=1}^{n} \frac{1}{x - x_j} \right]_{x=x_k} = 0.$$

Finally, it is apparent that $M_k(x_k) = 1$, whereas

$$N'_k(x_k) = \left[\prod_{k \neq j=1}^{n} \frac{(x-x_j)^2}{(x_k-x_j)^2} + (x - x_k) \frac{\mathrm{d}}{\mathrm{d}x} \prod_{k \neq j=1}^{n} \frac{(x-x_j)^2}{(x_k-x_j)^2} \right]_{x=x_k} = 1$$

Thus, all the interpolation conditions in Eq. 5.8 are satisfied.

5.3.1 5th order $3-$node interpolation

As an application of Eqs. 5.9 and 5.10, the fifth–order shape functions for a three point interpolation are given here.

In Subsection 3.1.1 the quintic polynomials for an interpolation that uses only the two end–nodes has been given. In this Subsection the quintic polynomials are those for a three nodes interpolation, obtained with the nodal values of the function and the first derivative at $x = -1, 0, 1$,

$$\begin{aligned} f(x) &= f_-^{(0)} M_-(x) + f_+^{(0)} M_0(x) + f_+^{(0)} M_+(x) \\ &\quad + f_-^{(1)} N_-(x) + f_+^{(1)} N_0(x) + f_+^{(1)} N_+(x) \end{aligned}$$

(for $x \in [-1, 1]$), where $f_\pm^{(k)}$ $(k = 0, 1, 2, 3)$ denote the values, at $x = \pm 1$, of respectively $f(x)$, df/dx, d^2f/dx^2 and d^3f/dx^3, whereas the Hermite interpolation polynomials related to the external points (*i.e.*, for $x = -1, 1$), $M_\pm(x)$ and $N_\pm(x)$, and those related to the interior point (*i.e.*, for $x = 0$) $M_0(x)$ and $N_0(x)$, are given by

$$\begin{aligned} M_\pm(x) &= \frac{1}{4}\left(\mp 3x^5 - 2x^4 \pm 5x^3 + 4x^2\right), \\ M_0(x) &= x^4 - 2x^2 + 1, \\ N_\pm(x) &= \frac{1}{4}\left(x^5 \pm x^4 - x^3 \mp x^2\right), \\ N_0(x) &= x^5 - 2x^3 + x. \end{aligned} \tag{5.11}$$

with $x \in [-1, 1]$. For instance $M_0(x)$ is (uniquely) determined by the six conditions $M_0(0) = 1$, $M_0(\pm 1) = 0$ and $dM_0/dx = 0$ for $x = -1, 0, 1$.

Figure 5.1 shows the three $M_\pm(x)$ and $M_0(x)$ fifth–order interpolators, whereas Fig. 5.2 depicts the three functions $N_\pm(x)$ and $N_0(x)$.

5.4 Higher–order WIP Hybrid elements

A second approach for the Hybrid scheme stems from an internal node formulation (that is a WIP formulation). The case studied here is of order five and has been addressed in Subsection 5.4.1. This formulation, despite a lower order of the element with respect to the former one, presents the advantage of eliminating the block–boundary problem. This element will be referred to as the *Hybrid* 5*–th order* 27*–nodes.*

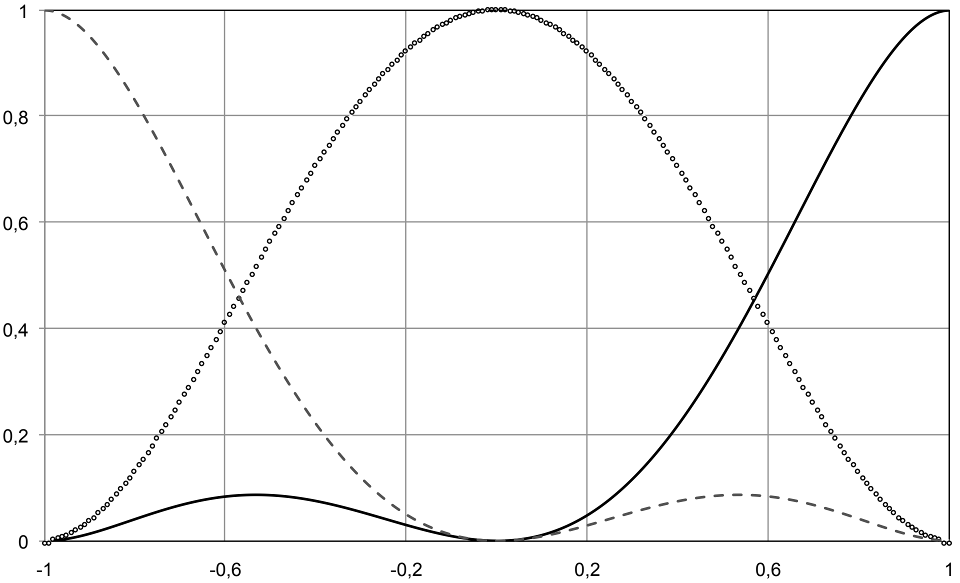

Figure 5.1: 5th order WIP polynomials: M_- (dashed line), M_+ (continuous line) and M_0 (points)

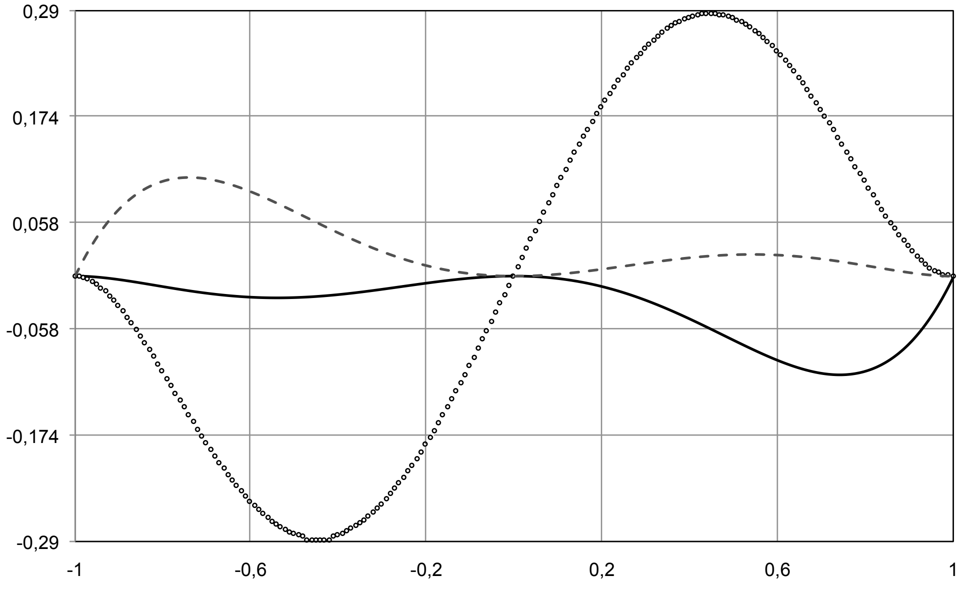

Figure 5.2: 5th order WIP polynomials: N_- (dashed line), N_+ (continuous line) and N_0 (points)

5.4.1 The Hybrid 5th order 27–node element

This subsection is dedicated to the fifth–order Hybrid element, obtained using a WIP formulation. To formulate such a scheme, one starts with the three–dimensional Coons interpolation, Eq. 4.11, and replaces the high–accuracy (third order) interpolation functions, with the corresponding polynomial given in Eq. 5.9, whereas the low–accuracy (linear) interpolation functions are replaced by Lagrangian interpolation polynomials

$$L_k(x) = \sum_{k \neq j=1}^{n} \frac{x - x_j}{x_k - x_j} \tag{5.12}$$

which satisfy the condition $L_k(x_j) = \delta_{kj}$ (again, n is the number of nodes for each dimension). It should be noted that the scheme requires points that are internal not only to the edges but also to the element itself.

Specifically, a number of nodes n equal to 3 is considered. Thus, one has a brick of 27 nodes. Within the element, a second–order interpolation is used for the low–accuracy interpolation (instead of a linear one) whereas a fifth–order interpolation has been used for the high–accuracy interpolation (instead of a third–order). Equation 4.11 is hereafter repeated:

$$f(\xi^\alpha) = \sum_{\mathbf{s}} f_{\mathbf{s}}\, R_{\mathbf{s}}(\xi^\alpha) + \sum_{\mathbf{s}} \sum_{\alpha=1}^{3} f_{\mathbf{s},\alpha}\, S_{\mathbf{s}}^\alpha(\xi^\alpha),$$

Again, one has

$$\begin{aligned}
&R_{\mathbf{s}}(\xi,\eta,\zeta) \\
&= M_{s_1}(\xi)\, L_{s_2}(\eta)\, L_{s_3}(\zeta) + L_{s_1}(\xi)\, M_{s_2}(\eta)\, L_{s_3}(\zeta) \\
&+ L_{s_1}(\xi)\, L_{s_2}(\eta)\, M_{s_3}(\zeta) - 2\, L_{s_1}(\xi)\, L_{s_2}(\eta)\, L_{s_3}(\zeta)
\end{aligned}$$

and

$$\begin{aligned}
S_{\mathbf{s}}^1(\xi,\eta,\zeta) &= N_{s_1}(\xi)\, L_{s_2}(\eta)\, L_{s_3}(\zeta) \\
S_{\mathbf{s}}^2(\xi,\eta,\zeta) &= L_{s_1}(\xi)\, N_{s_2}(\eta)\, L_{s_3}(\zeta) \\
S_{\mathbf{s}}^3(\xi,\eta,\zeta) &= L_{s_1}(\xi)\, L_{s_2}(\eta)\, N_{s_3}(\zeta)
\end{aligned}$$

as in the basic third–order Hybrid scheme. The first difference is in the definition of $\mathbf{s}$: now, one has $\mathbf{s} := (s_1, s_2, s_3)$, with $s_k = 1, 2, 3$ (hence, $\mathbf{s}$ is understood to span over 27 nodes). The second difference regards the interpolation polynomials: now the high–accuracy interpolators are given by

Eqs. 5.3.1:

$$
\begin{aligned}
M_\pm(x) &= \frac{1}{4}\left(\mp 3x^5 - 2x^4 \pm 5x^3 + x^2\right) \qquad \text{and} \qquad M_0(x) = x^4 - 2x^2 + 1, \\
N_\pm(x) &= \frac{1}{4}\left(x^5 \pm x^4 - x^3 \mp x^2\right) \qquad \text{and} \qquad N_0(x) = x^5 - 2x^3 + x.
\end{aligned}
$$

whereas the low-accuracy interpolation, no longer linear, is given by the quadratic polynomials

$$
L_\pm(x) = \frac{1}{2}x\,(x \pm 1) \qquad \text{and} \qquad L_0(x) = -x^2 + 1.
$$

where "$_\pm$" refers to the nodes placed in $x = \pm 1$ and "$_0$" is related to the node at $x = 0$.

5.5 Comments

It is interesting to make a comparison with the Hybrid elements obtained using a WEP formulation and the Hybrid elements obtained through a WIP scheme.

Firstly, note that, for the third–order case, the internal–point and the end–point hybrid schemes coincide.

You may easily convince yourself that a fifth–order formulation is possible for the WIP element, but not for the WEP element.

Thus, the lowest order for which a comparison is meaningful is the seventh–order scheme. In this case in fact, the WEP element requires 32 unknowns for each of the 8 nodes, for a total of 256 unknowns. In the seventh–order WIP brick, for each finite element we have 4^3 nodes, with 4 unknowns for each node, also for a total of 256 unknowns.[2] Thus, for the seventh–order formulation, the number of unknowns in each element are the same for the two types of elements.

---

[2] In general, for the n–th order scheme, we have $\left(\frac{n+1}{2}\right)^3$ nodes, with 4 unknowns per node, for a total of $\frac{1}{2}(n+1)^3$ unknowns.

Part II

Part two

Chapter 6

Mass and Stiffness matrices

The objective of this Chapter is to define the mass and stiffness matrices for the two problems under consideration in this thesis: evaluation of the natural modes of vibration of the air inside a cavity (interior acoustics, see Section 6.1) and those of an elastic structure (structural dynamics, see Section 6.2).

Variational formulations will be used. As for any variational formulation, the boundary conditions in general may be divided into two types (see for instance, the works of Brenner and Scott[11] and Braess[12]): essential or geometrical boundary conditions (*e.g.*, Dirichlet boundary conditions for the Laplacian), which must be satisfied by the shape functions used for the discretization (for instance, Eqs. 2.3 for the Hermite 3rd order 8−node brick of Chapter 2, or Eqs. 4.9 and 4.10 for the Hybrid 3rd order 8−node of Chapter 4), and natural boundary conditions (*e.g.*, Neumann boundary conditions for the Laplacian), which require no action, in the sense that they are automatically satisfied.

6.1 Mass and stiffness matrices in acoustics

The first problem under consideration is the evaluation of the natural modes of vibration for the air inside a given cavity, that is governed by the wave equation for the velocity potential φ, such that $\mathbf{v} = \operatorname{grad}\varphi$. The problem has been formulated in terms of the velocity potential, as this simplifies the boundary condition of a rigid wall, that is, zero normal component of the velocity, *i.e.*, a zero normal derivative of φ: $\partial\varphi/\partial n = 0$; the pressure equals $i\omega\varphi/\rho$, ρ being the density of the air. This problem may be stated in variational form as

$$\frac{1}{2}\frac{\omega^2}{c_s^2}\int_{\mathcal{V}}\varphi^2 d\mathcal{V} - \frac{1}{2}\int_{\mathcal{V}}\|\text{grad}\,\varphi\|^2 d\mathcal{V} = \text{stationary}_{\varphi(\xi^\alpha)}, \tag{6.1}$$

where c_s is the speed of sound.

The only type of boundary conditions considered in this work for the acoustics problem are those of a rigid boundary wall, which as mentioned above requires that $\partial\varphi/\partial n = 0$. This is a natural boundary condition and therefore no action is required.

Substituting the approximation for φ of Eq. 2.4, Eq. 6.1 yields

$$\mathsf{Kz} = \frac{\omega^2}{c_s^2}\mathsf{Mz} \tag{6.2}$$

where $\mathsf{z} = \{z_n\}$ is the vector of the unknowns, whereas the mass and stiffness matrices are respectively given by $\mathsf{M} = [m_{mn}]$ and $\mathsf{K} = [k_{mn}]$, with

$$\begin{aligned} m_{mn} &= \int_{\mathcal{V}} \chi_m(\xi^\alpha)\chi_m(\xi^\alpha) d\mathcal{V} \\ k_{mn} &= \int_{\mathcal{V}} \text{grad}\,\chi_m(\xi^\alpha)\cdot\text{grad}\,\chi_n(\xi^\alpha) d\mathcal{V}, \end{aligned} \tag{6.3}$$

6.1.1 One–dimensional eigenvalue problem

The above results can be used to implement the one–dimensional eigenvalue problem, (*i.e.*, that related, from a physical point of view, to the dynamic of the air vibrating inside a closed–end pipe). One has:

$$L\Phi(\xi) = \lambda\Phi(\xi) \tag{6.4}$$

where Φ is the eigenfunction whereas $\lambda = \omega^2/c^2$ denotes the eigenvalue. L is the second–order ordinary differential operator: $L = -d^2/dx^2$ so as $-\phi''(\xi) = \lambda\phi(\xi)$ (ξ being the local coordinate such that $\xi \in [-1, 1]$). Using a Galerkin approximation one has

$$\Phi(\xi) = \sum_n z_n \chi_n(\xi)$$

and

$$-\sum_n \langle \chi_m, \chi_n'' \rangle z_n = \sum_n \langle \chi_m', \chi_n' \rangle z_n = \lambda \sum_n \langle \chi_m, \chi_n \rangle z_n$$

or

$$\mathsf{Kz} = \lambda\mathsf{Mz}$$

where $\mathsf{z} = \{z_n\}$ is the vector of the unknowns, whereas the mass and stiffness matrices are respectively given by

$$\begin{aligned} m_{mn} &= \int \chi_m \chi_n d\xi \\ k_{mn} &= \int \chi'_m \chi'_n d\xi \end{aligned} \tag{6.5}$$

6.2 Mass and stiffness matrices in structural dynamics

The second problem considered in this thesis is the evaluation of the natural modes of vibration of an isotropic elastic material, with continuous material properties. This may be stated in variational form as[1]

$$\frac{1}{2}\omega^2 \int_{\mathcal{V}} \rho \|\mathbf{u}\|^2 d\mathcal{V} - \frac{1}{2}\int_{\mathcal{V}} \sigma^{\alpha\beta}\epsilon_{\alpha\beta} d\mathcal{V} = extr[\mathbf{u}(\xi^\alpha)], \tag{6.6}$$

where

$$\sigma^\beta_\alpha = 2G[\epsilon^\beta_\alpha + \epsilon^\gamma_\gamma \delta^\beta_\alpha \nu/(1-2\nu)] \tag{6.7}$$

and

$$\epsilon_{\alpha\beta} = (u_{\alpha/\beta} + u_{\beta/\alpha})/2 = \mathbf{g}_\alpha \cdot \frac{\partial \mathbf{u}}{\partial \xi^\beta} + \mathbf{g}_\beta \cdot \frac{\partial \mathbf{u}}{\partial \xi^\alpha}, \tag{6.8}$$

with $..._{/\alpha}$ denoting covariant differentiation.

The boundary conditions considered are either those for a free–surface boundary (that is a natural boundary condition, which require no action), or those for a clamped–surface boundary, for which the values of the nodal displacements (and their tangential derivatives) vanish. The study has been extended to the validation of the formulation for the case of a shell hinged at the boundary.

Substituting the approximation for u proposed in Eq. 2.4 (again, see Section 2.2), where now the interpolating functions are vector functions $\boldsymbol{\chi}(\xi^\alpha)$, yields

$$\mathsf{Kz} = \omega^2 \mathsf{Mz} \tag{6.9}$$

where again $\mathsf{z} = \{z_n\}$ is the vector of the unknown nodal values, whereas the mass and stiffness matrices are respectively given by $\mathsf{M} = [m_{mn}]$ and

---

[1] The most general linear stress–strain relationship is given by $\sigma^{\alpha\beta} = c^{\alpha\beta\gamma\delta}\epsilon_{\gamma\delta}$. where in $c^{\alpha\beta\gamma\delta}$ there are only twenty one independent coefficients, because of the symmetry of the stress and strain tensors, as well as from energy considerations. For the sake of simplicity, this general expression is not included in this work, since all the numerical results are limited to isotropic homogeneous material.

$\mathsf{K} = [k_{mn}]$, with

$$
\begin{aligned}
m_{mn} &= \int_{\mathcal{V}} \rho\, \boldsymbol{\chi}_m(\xi^\alpha) \cdot \boldsymbol{\chi}_n(\xi^\alpha) d\mathcal{V} \\
k_{mn} &= \sum_{\alpha,\gamma} \int_{\mathcal{V}} 2G \left(P_\alpha^\gamma P_\gamma^\alpha + \frac{\nu}{1-2\nu} P_\alpha^\alpha P_\gamma^\gamma \right) d\mathcal{V},
\end{aligned}
\tag{6.10}
$$

where

$$
P_\alpha^\gamma(\xi^\rho) = \sum_\beta \left[\boldsymbol{\chi}_{m,\alpha} \cdot \mathbf{g}_\beta + \boldsymbol{\chi}_{n,\beta} \cdot \mathbf{g}_\alpha \right] g^{\beta\gamma} \tag{6.11}
$$

$g^{\beta\gamma}$ being the contravariant metric tensor components, in the undeformed configuration.

Chapter 7

Validation and assessment

In this Chapter, a validation of the proposed methodology is addressed, both in interior acoustic and structural applications. This Chapter consists of five sections of results, before of which an introduction section (Section 7.1) is intended to introduce the fundamental definitions of the errors that will be used throughout the Chapter to assess the schemes and qualitative considerations about the following analysis..

The first part consists of preliminary results obtained for a one-dimensional problem (Section 7.2). Test cases are very simple and the main intention is to pre–assess the skills of the methodology itself, without introducing any complexities in the geometry or in the constraints application.

The second one (Section 7.3) includes three-dimensional interior acoustic analysis for quite simple domains. In particular, the modes and the eigenvalues of the air vibrating inside a cavity are explored; the cavities considered are either a parallelepiped or a cube.

Next, the third part concerns the application of the quais–static reduction procedures (Guyan's and IRS, see Appendix E for details) for thin geometries (such as those used here for structural applications) and for solid domains (such as the cavities used in interior acoustics applications).

The fourth part (Section 7.4) is dedicated to structural problems; the geometries considered include rectangular-cross-section beam, rectangular plates and spherical shells, all treated as three-dimensional structures (whereas the analysis in Section 7.2 is for a one-dimensional domain). Results are obtained with and without quasi-static reduction.

Finally, the last part (Section 7.4) regards an assessment of *Scheme C*, used as a remedy for the bloc–boundary problem.

7.1 Preliminary definitions

Consider the expression of the error introduced in the evaluation of the eigenfunctions. Let us begin with the least-square definition, given by

$$\epsilon_k = \left[\int_{\mathcal{V}} \rho \big(\Phi_k - \Phi_k^{\mathsf{A}} \big)^2 \, \mathrm{d}\mathcal{V} \right]^{1/2} \tag{7.1}$$

where Φ_k and $\Phi_k^{\mathsf{A}}(\xi^\alpha)$ denote, respectively, the exact and the approximate th eigenfunction. In general we may define

$$\epsilon_{jk} = \left[\int_{\mathcal{V}} \rho \big(\Phi_j - \Phi_j^{\mathsf{A}} \big) \big(\Phi_k - \Phi_k^{\mathsf{A}} \big) \, \mathrm{d}\mathcal{V} \right]^{1/2} \tag{7.2}$$

Note that, according to Eq. 2.4

$$\Phi_k^{\mathsf{A}}(\xi^\alpha) = \sum_j z_{jk} \chi_j(\xi^\alpha) \tag{7.3}$$

where z_{kj} denotes the $j-$th component of the $k-$th eigenvector of Eq. 6.2; the vectors z_k satisfies the orthonormality relation $\mathsf{z}_j^{\mathsf{T}} \mathsf{M} \, \mathsf{z}_k = \delta_{jk}$, which corresponds to the condition $\int_{\mathcal{V}} \Phi_j^{\mathsf{A}} \, \Phi_k^{\mathsf{A}} \mathrm{d}\mathcal{V} = \delta_{jk}$, as easily verified. In addition, for convenience, the exact eigenfunctions $\Phi_k(\xi^\alpha)$ are approximated with the same interpolation formula that is, using the same shape functions $\chi_j(\xi^\alpha)$, as

$$\Phi_k(\xi^\alpha) = \sum_q y_{qk} \chi_j(\xi^\alpha), \tag{7.4}$$

where y_{qk} denotes the q–th component of the k–th vectors y_k which is defined as follows: the components y_{qk} are those nodal values corresponding to z_{qk}, that are obtained from the exact k–th eigenfunction $\Phi_k(\xi^\alpha)$, and are also normalized by $\mathsf{y}_k^{\mathsf{T}} \mathsf{M} \, \mathsf{y}_k = 1$. Combining Eqs. 7.2, 7.3, 7.4, and using Eq. 6.3 as well as $\mathsf{z}_k^{\mathsf{T}} \mathsf{M} \, \mathsf{z}_k = \mathsf{y}_k^{\mathsf{T}} \mathsf{M} \, \mathsf{y}_k = 1$, one obtains

$$\begin{aligned} \epsilon_{jk}^2 &= \sum_{qr} \big(y_{qk} - z_{qk} \big) \big(y_{rk} - z_{rk} \big) \int_{\mathcal{V}} \chi_q \, \chi_r \, \mathrm{d}\mathcal{V} = \left(\mathsf{y}_j - \mathsf{z}_j \right)^{\mathsf{T}} \mathsf{M} \left(\mathsf{y}_k - \mathsf{z}_k \right) \\ &= 2 \, - \mathsf{z}_j^{\mathsf{T}} \mathsf{M} \mathsf{y}_k - \mathsf{z}_k^{\mathsf{T}} \mathsf{M} \mathsf{y}_j \end{aligned} \tag{7.5}$$

The error on the eigenvalues is instead referred to as e_k and is given by :

$$e_k = \big| \lambda_k - \mu_k \big|. \tag{7.6}$$

The above definitions of the errors regarding eigenfunctions (modes) and eigenvalues (frequencies squared) are utilized throughout the entire validation process. The above definition of e_k is particularly useful in presenting h–convergences; the further definition of the relative error will be used

$$e_{r_k} = \frac{\left|\lambda_k - \mu_k\right|}{\mu_k}. \tag{7.7}$$

A final comment before presenting the results pertains the difference in the order of magnitude of the eigenvalue error as compared to that of the eigenfunction error. Specifically, let Φ be an exact eigenfunction of the selfadjoint operator $\mathcal{L}$, with

$$\|\Phi\|^2 = \big\langle \Phi, \Phi \big\rangle := \int_{\mathcal{V}} \Phi^2 \mathrm{d}\mathcal{V} = 1.$$

Consider an approximate eigenfunction $\Phi_\varepsilon = \Phi + \varepsilon \Phi'$, with $\big\langle \Phi, \Phi' \big\rangle = 0$; we have

$$\|\Phi_\varepsilon\|^2 = 1 + \varepsilon^2 \big\langle \Phi', \Phi' \big\rangle.$$

Using $\mathcal{L}\Phi = \mu\Phi$, we have $\mu = \big\langle \mathcal{L}\Phi, \Phi \big\rangle$ and

$$\begin{aligned} \mu_\varepsilon &:= \frac{\big\langle \mathcal{L}\Phi_\varepsilon, \Phi_\varepsilon \big\rangle}{\big\langle \Phi_\varepsilon\, , \Phi_\varepsilon \big\rangle} = \frac{\big\langle \mathcal{L}(\Phi + \varepsilon\Phi'), \Phi + \varepsilon\Phi' \big\rangle}{\big\langle\ \Phi + \varepsilon\Phi'\ ,\ \Phi + \varepsilon\Phi'\ \big\rangle} \\ &= \frac{\big\langle \mathcal{L}\Phi, \Phi \big\rangle + \varepsilon \big\langle \mathcal{L}\Phi', \Phi' \big\rangle}{\big\langle \Phi, \Phi \big\rangle + \varepsilon \big\langle \Phi', \Phi' \big\rangle} = \frac{\mu + \varepsilon^2 \big\langle \mathcal{L}\Phi', \Phi' \big\rangle}{1 + \varepsilon^2 \big\langle \Phi', \Phi' \big\rangle} = \mu + \mathcal{O}\big(\varepsilon^2\big) \end{aligned} \tag{7.8}$$

7.2 One–dimensional case

The objective of this subsection is to provide a preliminary assessment for the WEP and the WIP schemes, in terms of both the mesh size (h–convergences) and the order of the scheme (p–convergences). In order to accomplish this, it is sufficient to address one-dimensional problems. The main advantages are the simplicity of implementation along with a lower computational effort with respect to a three–dimensional analysis, especially in case of refined meshes.

The assessment is not limited to low-order modes (that is modes related to low spatial frequencies).

Specifically, the problem of a closed-end pipe of length ℓ has been considered. This is mathematically equivalent to the solution of the one-dimensional Helmholtz equation with Neumann boundary conditions, that is, setting $\mu = \omega^2/c_s^2$ (c_s is the speed of sound),

$$\frac{\mathrm{d}^2\Phi}{\mathrm{d}x^2} + \mu\,\Phi = 0 \qquad \text{with} \qquad \left.\frac{\mathrm{d}\Phi}{\mathrm{d}x}\right|_{x=0,\ell} = 0,$$

for which the eigensolutions are given by

$$\Phi_k = \cos\frac{k\pi x}{\ell} \qquad \text{and} \qquad \mu_k = \frac{\omega_k^2}{c_s^2} = \frac{k^2\pi^2}{\ell^2}$$

In the applications that follow, a length $\ell = \pi$ has been chosen along with a speed of sound $c_s = 1$, so as to have $\mu_k = k^2$.

7.2.1 h–convergence

This Subsection is dedicated to the $h-$convergence analyses for a closed-end pipe, for various schemes. Specifically, the schemes considered are:

1. the classical Hermite third-order scheme, here referred to also as "WEP III" (see Subsection 2.2);
2. the 5th order WEP scheme, here referred to also as "WEP V" (see Subsection 3.1.1);
3. the WIP scheme of order five and class $\mathcal{C}^1$ (see Subsection 5.3.1);
4. the 7th order WEP scheme, here referred to also as "WEP VII"(see Subsection 3.1.2);
5. the WIP scheme of order seven and class $\mathcal{C}^1$ (therefore obtained with four nodes, with the function and the first derivative as nodal unknowns).

For each scheme, the convergence is studied by increasing the number of elements; thus, we talk about h–convergence. The expected convergence rate is based upon the order of the polynomial within each element. For example, in case of scheme 1. that uses a polynomial of order 3, the expected convergence for ϵ_k is like $h^3 = \ell^3/N^3$, where N is the number of elements used. Thus, for this scheme a convergence rate equal to 3 for modes is expected. Similarly, for the other schemes, which use polynomials of order 5 and 7, the expected convergence rates are equal to 5 and 7.

On the other hand, it is known that the error on the eigenvalue is like the square of that on the eigenfunction (see Eq. 7.8). Hence, the convergence rate for the eigenvalues is expected to be twice as large as that for the eigenfunctions, that is, 6 for scheme 1., 10 for schemes 2. and 3. (order 5) and 14 for schemes 4. and 5. (order 7).

To begin with, h–convergence analyses for the first ten eigenfunctions and eigenvalues are presented in Figs. from 7.1 to 7.10 with the aim of assessing and comparing the convergence properties of the five schemes, both in terms of modes and eigenvalues, for a relatively wide range of frequencies. In this set of figures, those on the left side pertain the convergence for the eigenfunctions ($\log \epsilon_k$ with $k = 1, \ldots, 10$), whereas those on the right side pertain the convergence for the corresponding eigenvalues ($\log e_k$ with $k = 1, \ldots, 10$) as functions of $-\log N$. Indeed, since the convergence is expected to be like $h^n = \ell^n / N^n$ (for a scheme of order n), the results are conveniently presented in a log–log diagram. The dashed lines in those diagrams represent the 'expected trends'.

Below each image, an additional supporting figure is presented. This shows only the linear trend (that is obtained for sufficiently refined meshes), along with the equation that best fit the data, so that to give additional informations about the 'obtained trend'. Some of the obtained values are not present for the first two eigenfunctions and eigenvalues because the corresponding errors are too small and thus not considered for the determination of the rate of convergence ($\log \epsilon \geq -8$ and $\log e \geq -12$ have been considered realistic with respect to the round–off errors).

In this group of images, the obtained trends present the following aspect: the k–th mode (and eigenvalue) h–convergence has a minimum for a mesh of $N = k$. This has been associated to the subdivision itself that, in this case, presents nodes on stationary points.[1]

The WIP scheme denotes a better accuracy. It is expected, since the comparison is give for the same N. In fact, the WIP approach uses a greater number of DOFS than the WEP scheme (for a WIP scheme one has $N_{DOF} = 2[(n_{node} - 1)N + 1]$ whereas for a WEP scheme $N_{DOF} = 1/2(p + 1)(N + 1)$, being p the order of the scheme and n_{node} the number of nodes of the element).

Tables 7.1 and 7.2 concern the obtained convergence rates (for eigenvalues and eigenfunctions respectively). The expected values (*i.e.*, for a n–order scheme, n for the eigenfunctions and $2n$ for the eigenvalues) are given in the first line of each table.

The convergence rate is always close to that expected, confirming that lower element–boundary continuity of the internal–point scheme does not decrease the convergence rate (in addition, in the figures the internal–point error appears to be generally lower than the end–point error). It appears that best results, in terms of rate of convergence, are obtained with order five, especially using the WEP configuration (the numerical rate overruns that expected of 40% for the eigenfunctions 5, 6, 7). However, the main

---

[1] The zero frequency mode is excluded from this analysis, so that, for the numeration used, k holds the k–frequency mode. Hence, one has, for the i–th node ($\ell = \pi$): $x = i/N$ and $\Phi_k = \cos N\pi x/\ell = \cos \pi i = \pm 1$.

expected advantage of a WIP configuration stems from the improved user–friendliness, not from a higher accuracy.

In Subsection 7.2.2 an analysis with the aim to assess the accuracy of both methods is addressed.

	WEP III	WEP V	WIP V	WEP VII	WIP VII
Expected rate	6	10	10	14	14
1	5.7	9.8	-	-	-
2	5.4	10.3	9.7	-	-
3	5.2	10.8	9.6	13	10.7
4	5.1	10.6	9.9	13	13.4
5	5.4	10.6	9.7	12.7	13.4
6	5.3	10.7	9.6	12.6	13.4
7	5.2	10.9	9.5	12.5	13.4
8	5.1	10.9	9.4	12.6	13.4
9	5	11	9.4	12.5	13.4
10	5	11	9.3	12.5	13.4

Table 7.1: Closed–end pipe: convergence rates for eigenvalues

	WEP III	WEP V	WIP V	WEP VII	WIP VII
Expected rate	3	5	5	7	7
1	3.5	6.1	-	-	-
2	3.6	6.3	5.7	-	-
3	3.4	6.6	5.7	7	5.3
4	3.3	6.8	5.6	7.1	7.4
5	3.3	7	5.6	7.1	7.6
6	3.4	7	5.5	7.1	7.7
7	3.3	7	5.5	7.1	7.6
8	3.4	6.9	5.5	7.1	7.7
9	3.4	6.9	5.5	7.1	7.7
10	3.6	6.9	5.5	7	7.5

Table 7.2: Closed–end pipe: convergence rates for eigenfunctions

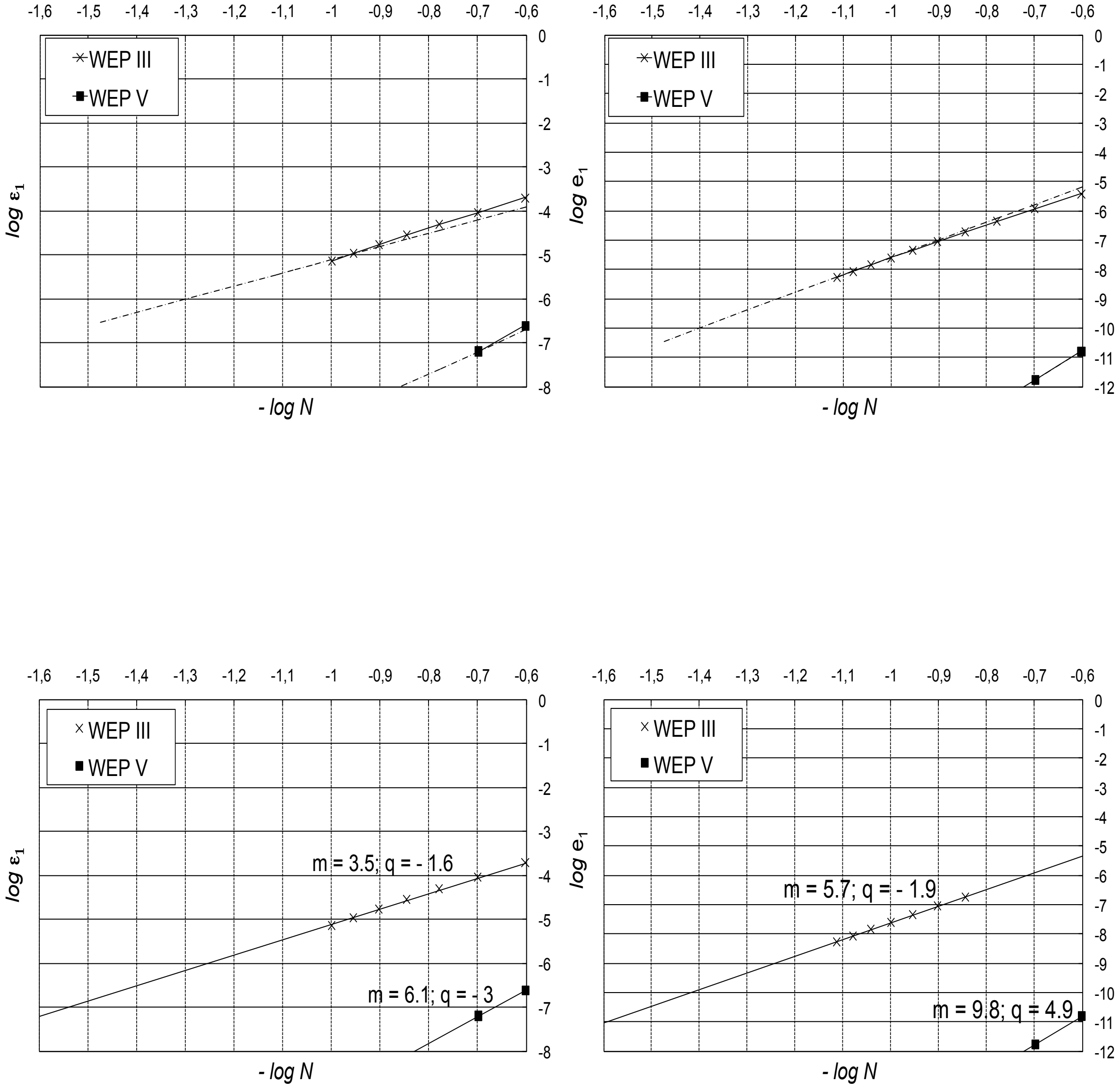

Figure 7.1: Closed–end pipe: 1st mode (left) and eigenvalue (right); expected trend (top) and obtained trend (bottom)

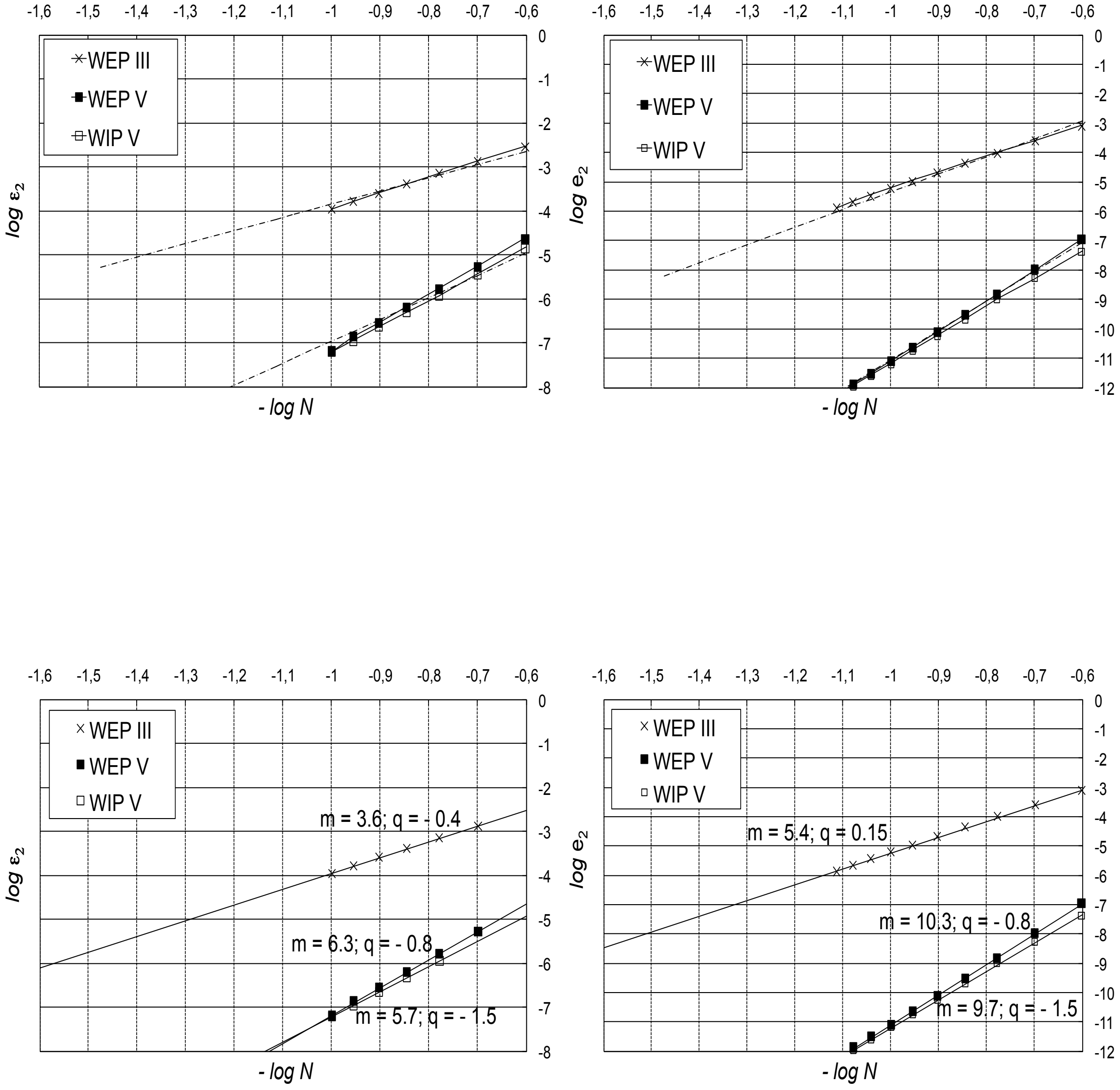

Figure 7.2: Closed–end pipe: 2nd mode (left) and eigenvalue (right); expected trend (top) and obtained trend (bottom)

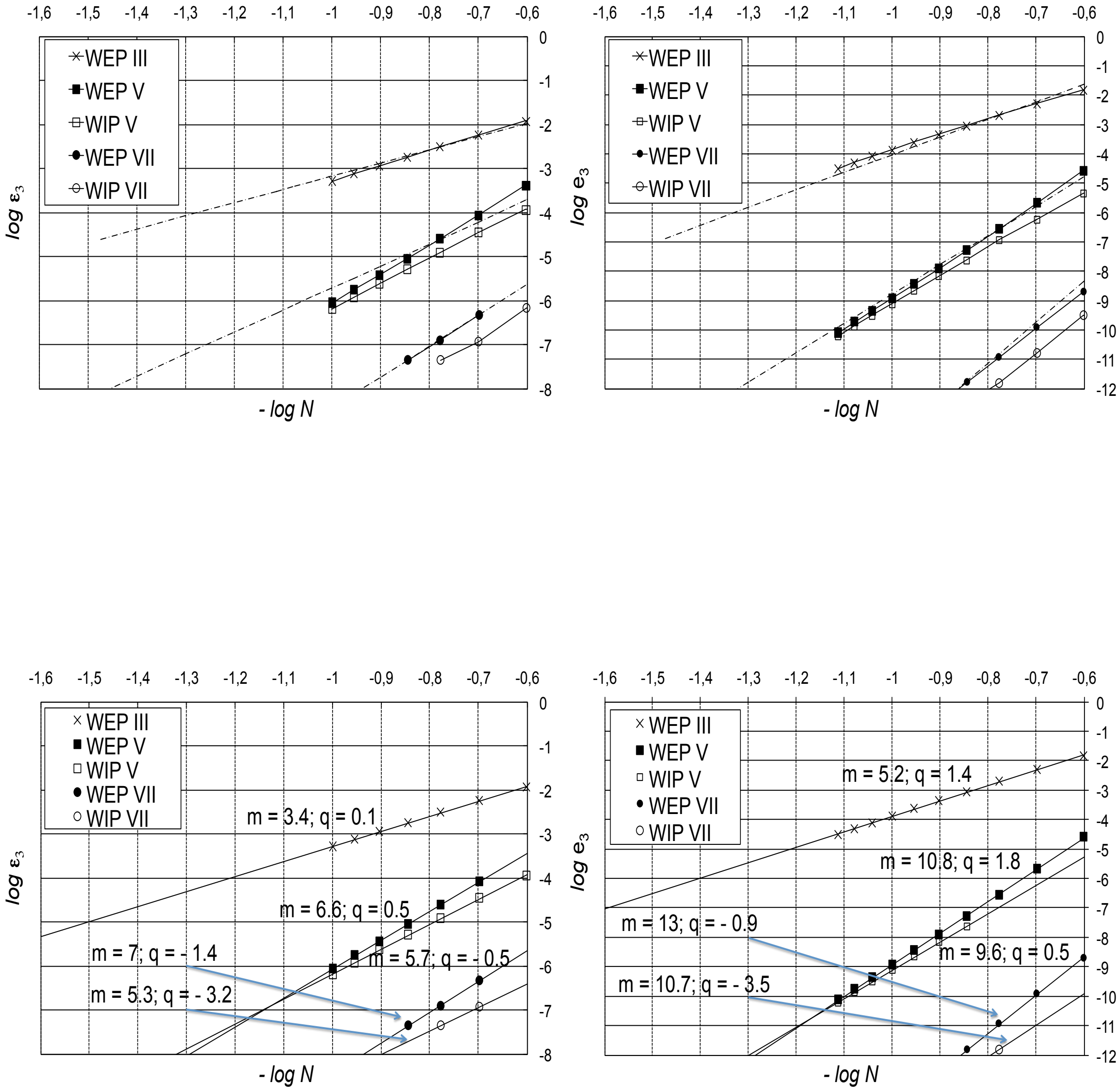

Figure 7.3: Closed–end pipe: 3rd mode (left) and eigenvalue (right); expected trend (top) and obtained trend (bottom)

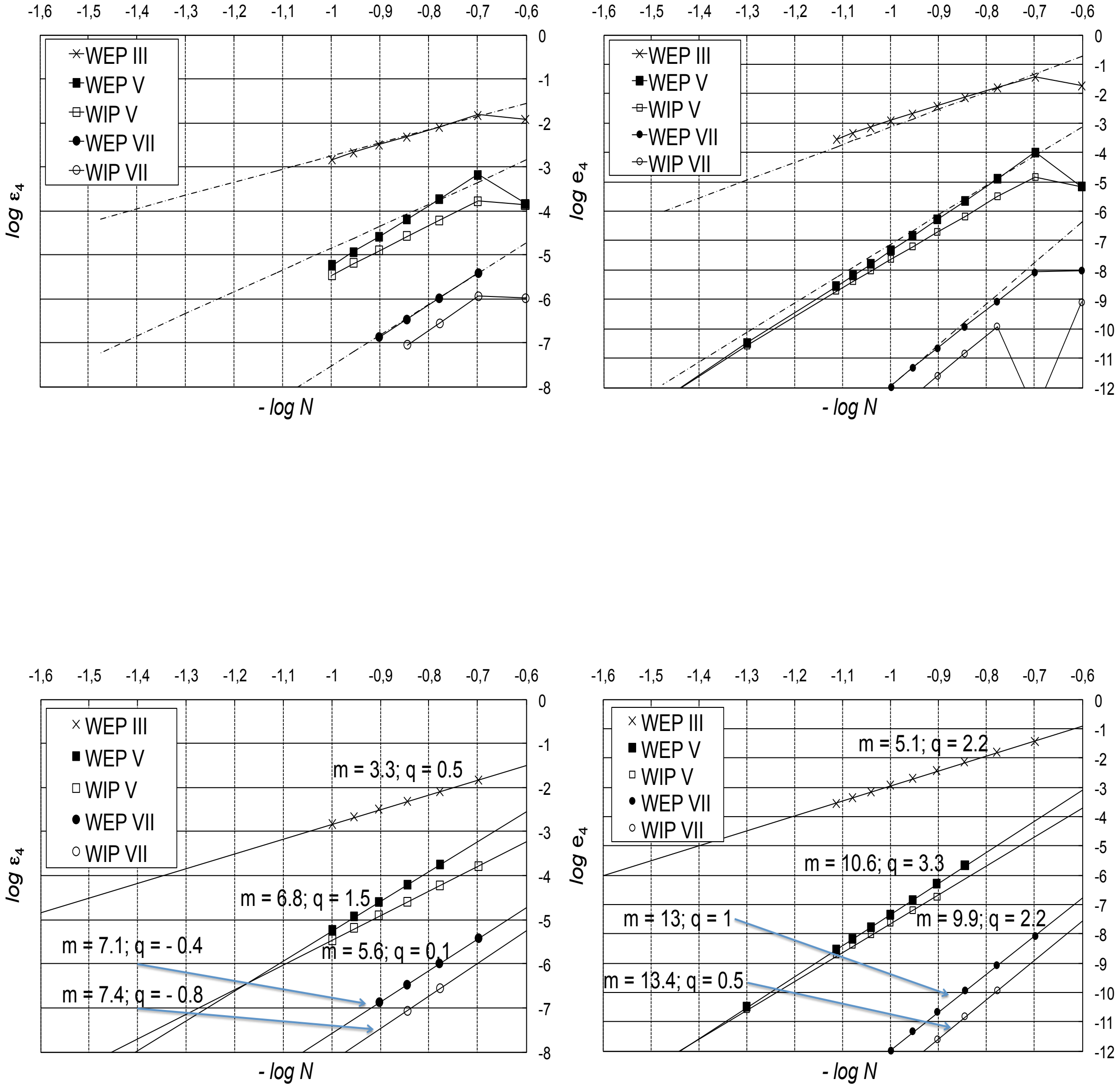

Figure 7.4: Closed–end pipe: 4th mode (left) and eigenvalue (right); expected trend (top) and obtained trend (bottom)

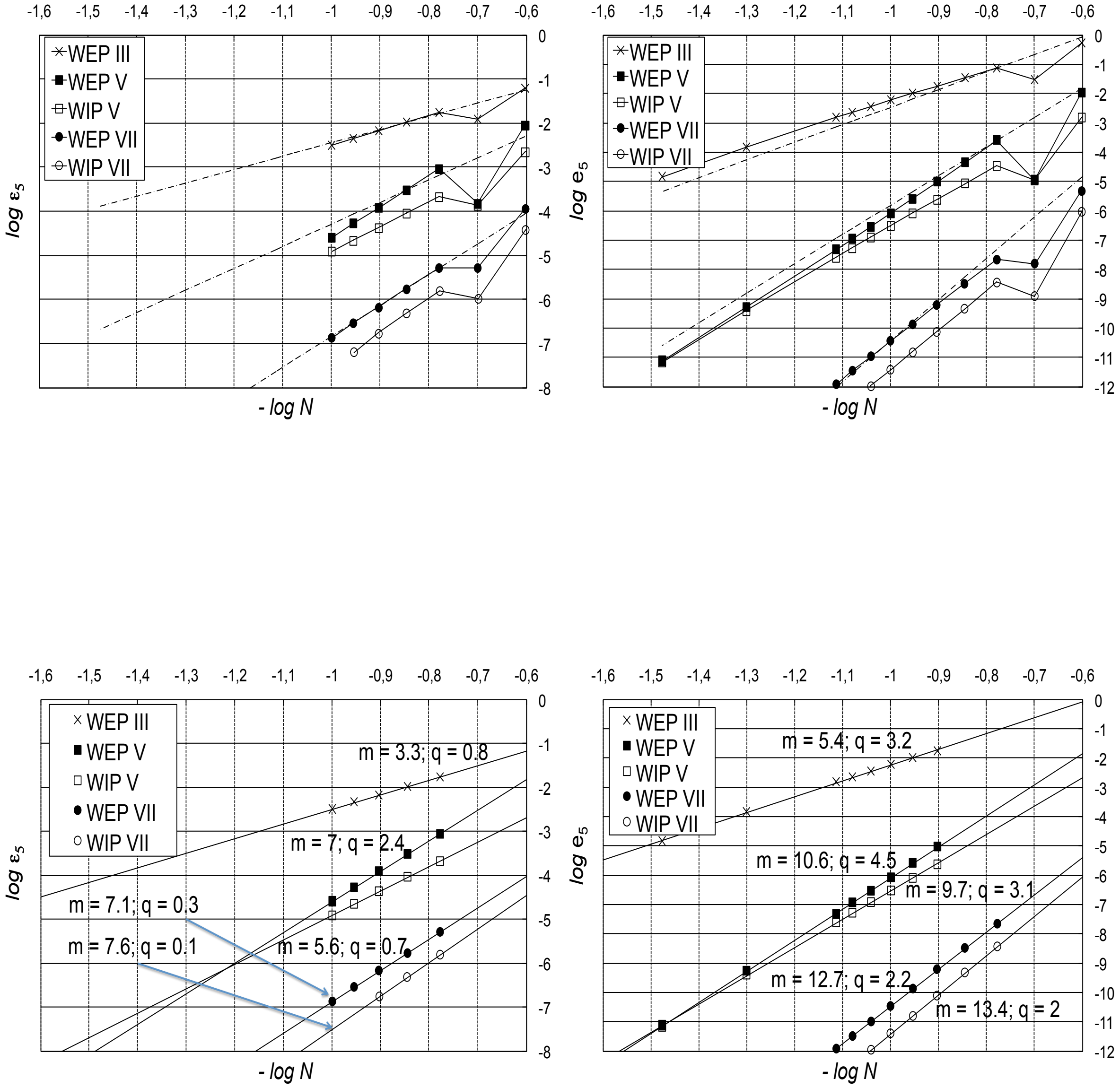

Figure 7.5: Closed–end pipe: 5th mode (left) and eigenvalue (right); expected trend (top) and obtained trend (bottom)

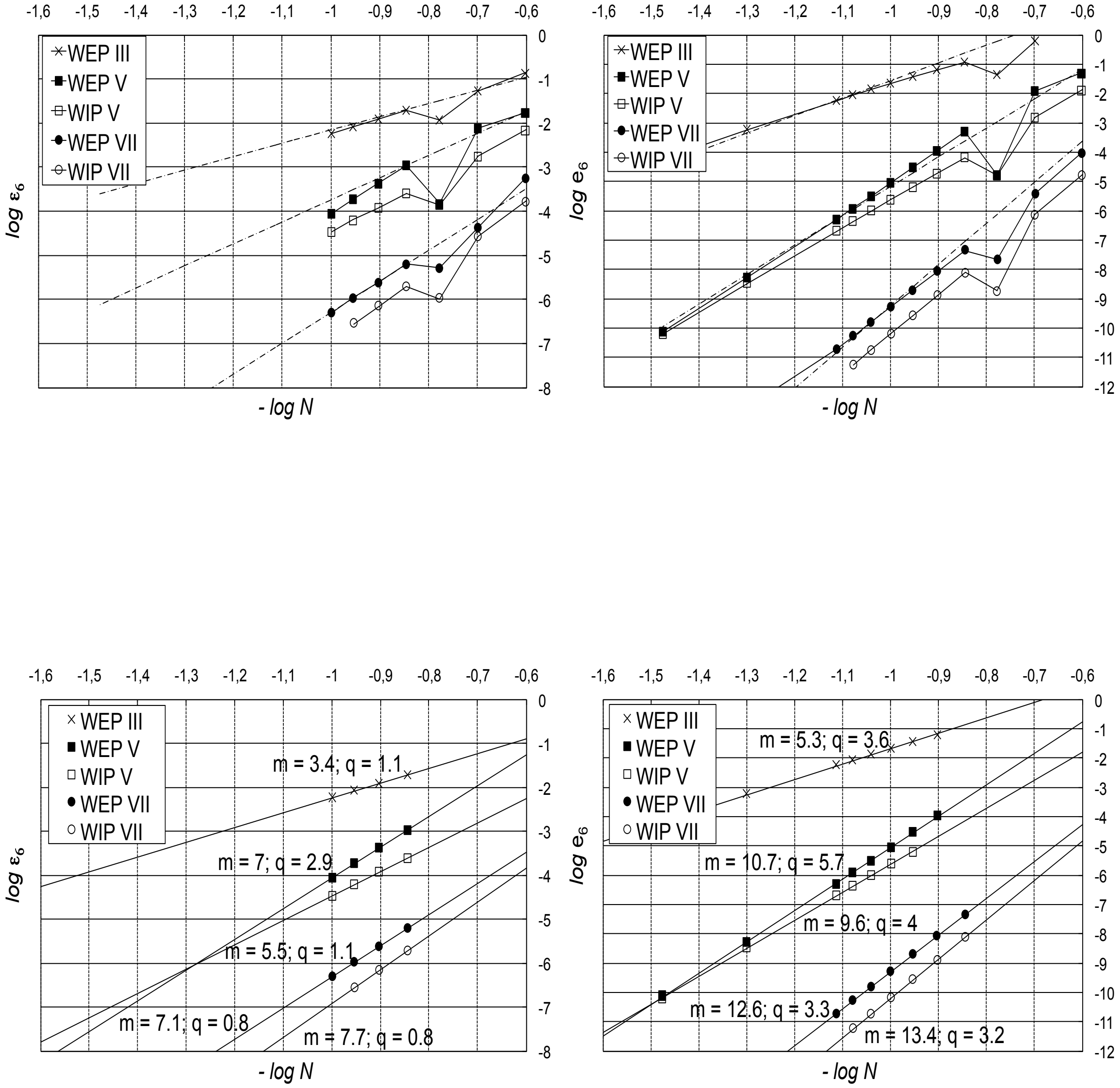

Figure 7.6: Closed–end pipe: 6th mode (left) and eigenvalue (right); expected trend (top) and obtained trend (bottom)

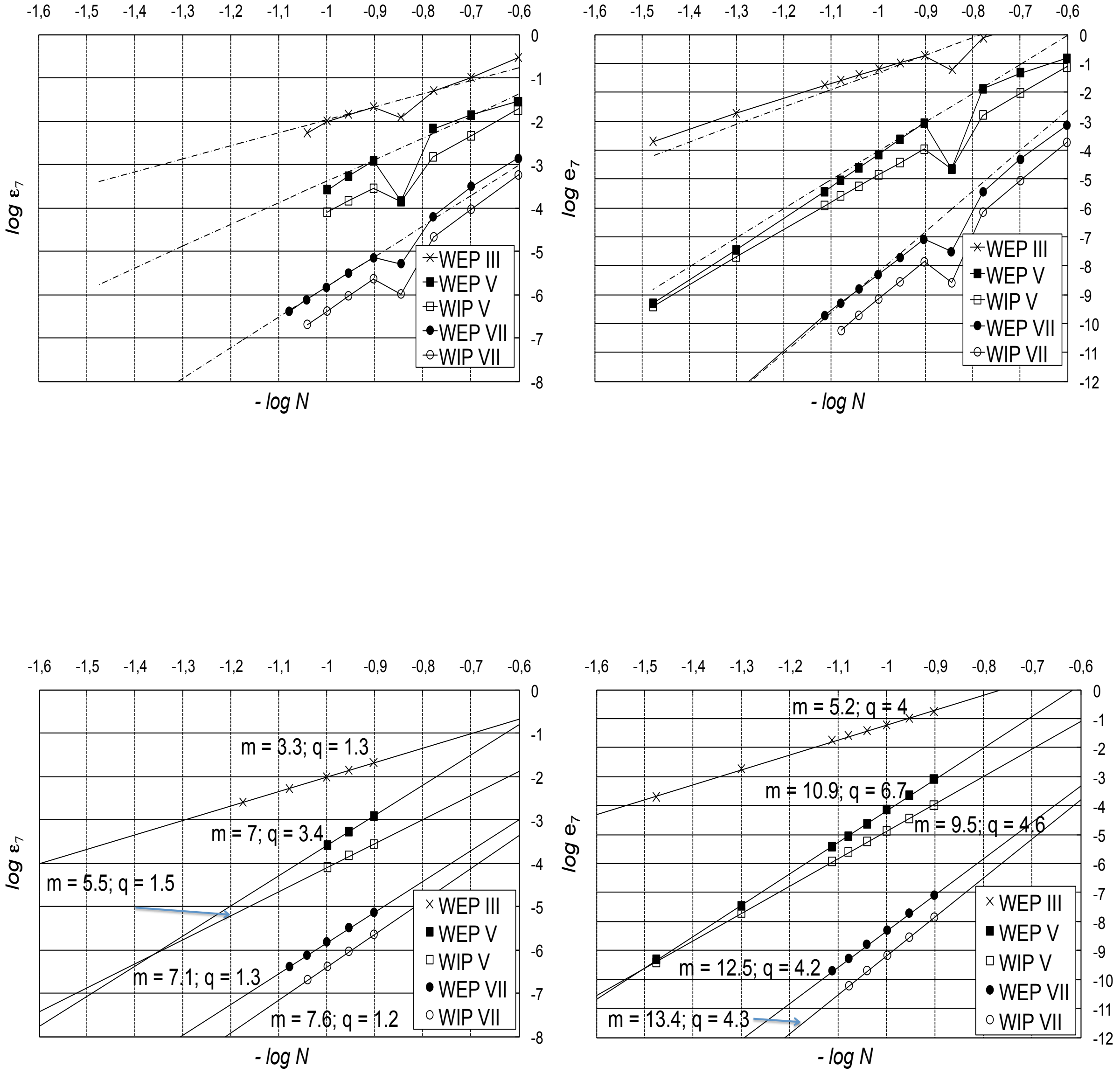

Figure 7.7: Closed–end pipe: 7th mode (left) and eigenvalue (right); expected trend (top) and obtained trend (bottom)

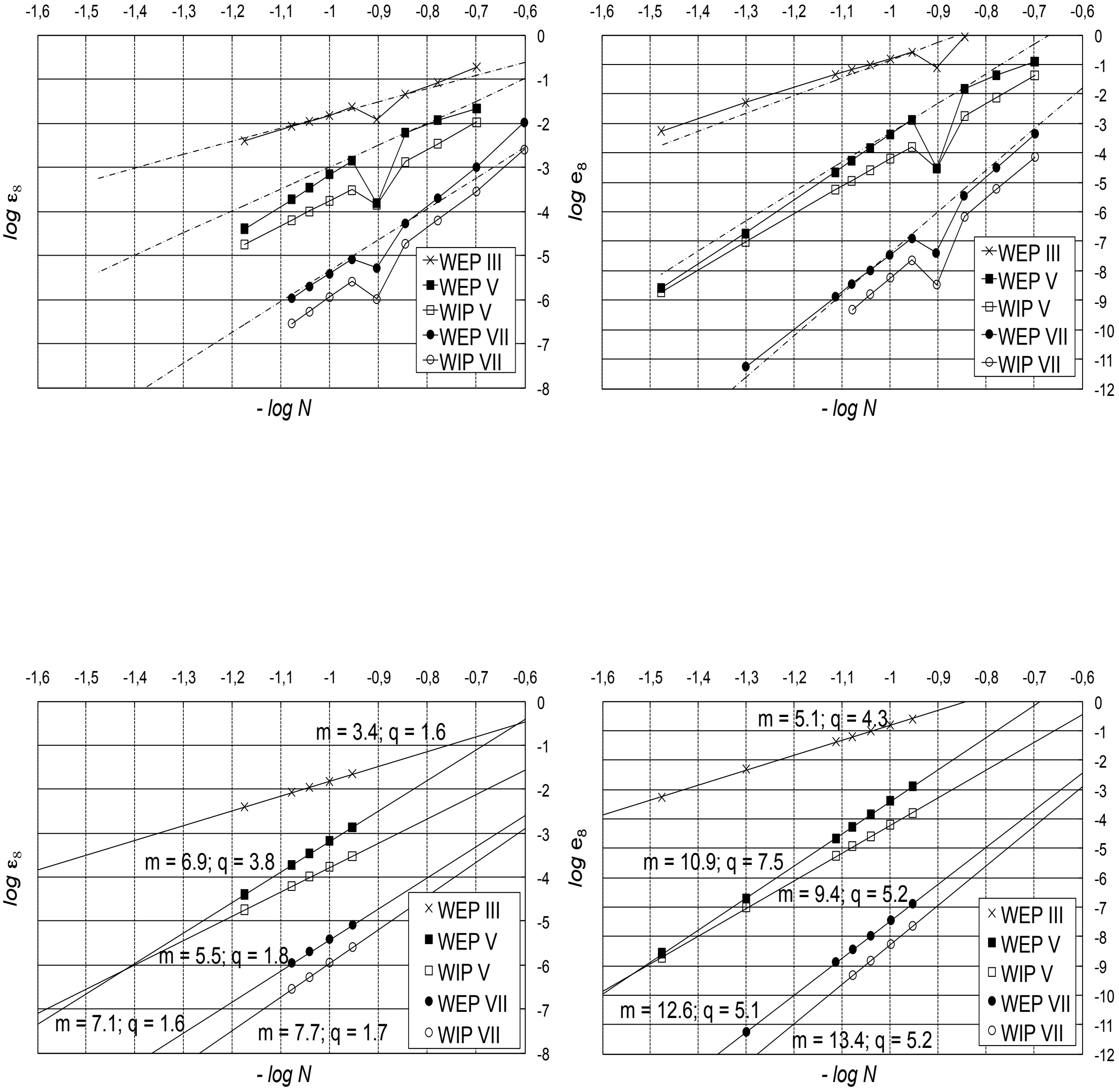

Figure 7.8: Closed–end pipe: 8th mode (left) and eigenvalue (right); expected trend (top) and obtained trend (bottom)

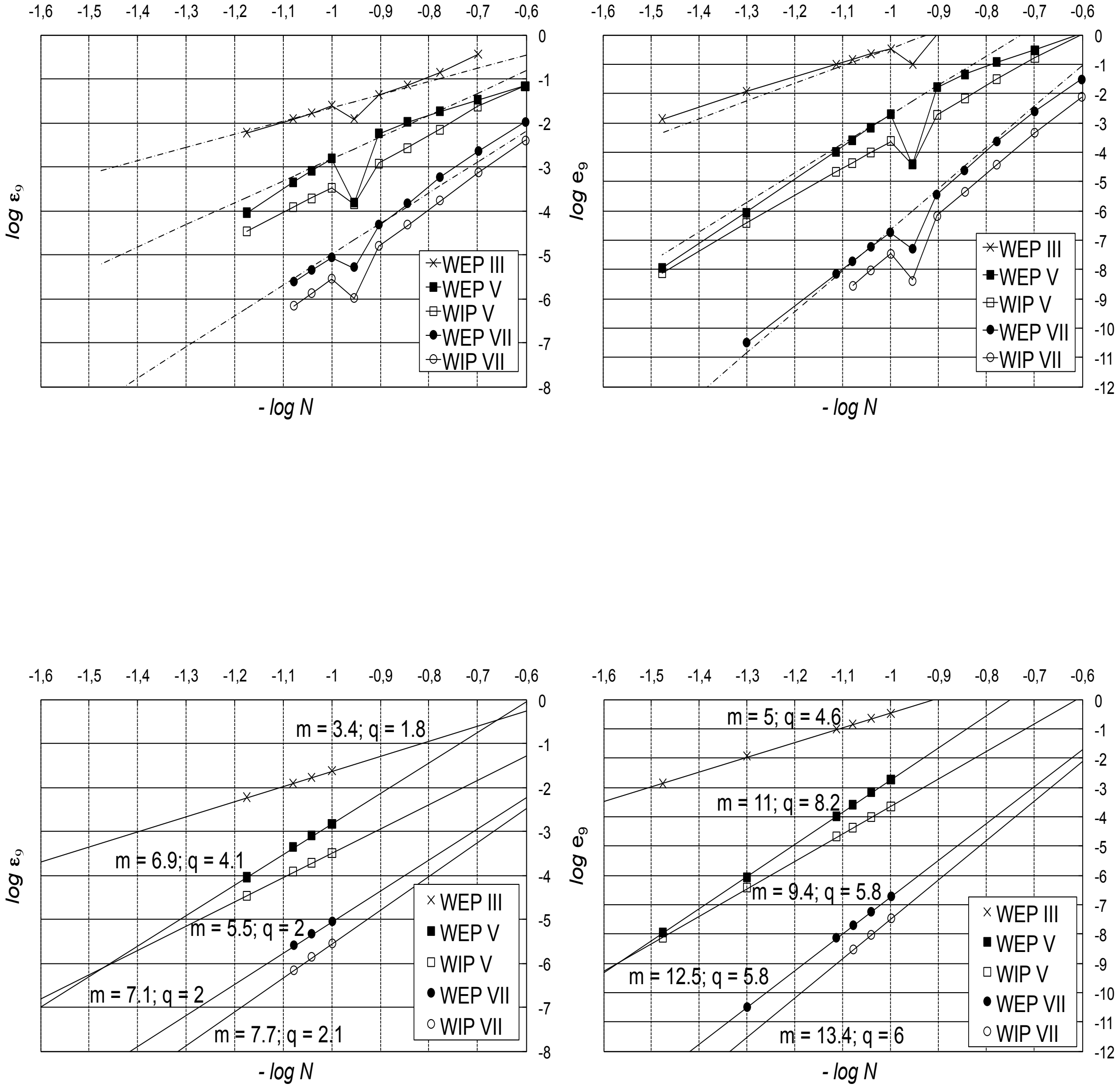

Figure 7.9: Closed–end pipe: 9th mode (left) and eigenvalue (right); expected trend (top) and obtained trend (bottom)

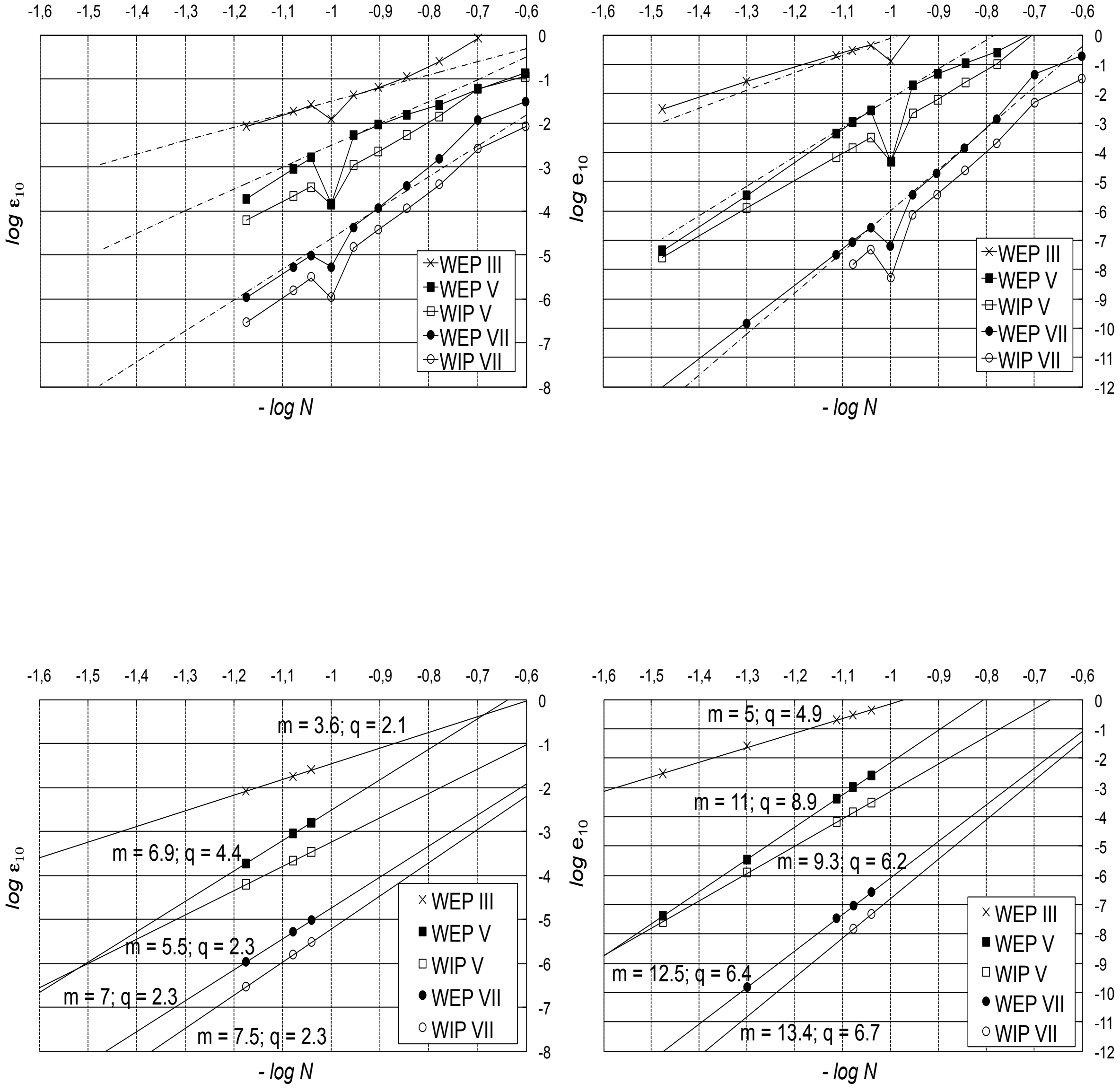

Figure 7.10: Closed–end pipe: 10th mode (left) and eigenvalue (right); expected trend (top) and obtained trend (bottom)

7.2.2 Preliminary WIP p–convergences

This subsection is dedicated to the WIP schemes as the number of nodes increases. The problem under consideration is the same of the preceding Subsection, that is a closed–end pipe of length π, so as to have, for the k–th mode, an eigenvalue equal to k^2 ($c_s = 1m/s$).

The first two figures regard the assessment of the well known Runge's phenomenon, occurring when the number of nodes n becomes too large. Specifically, it is wanted to show how large can be this quantity, before reaching the instability. This is shown in the left part of Fig. 7.11, where the p–convergence for the first eigenvalue is presented. It appears that, within order 27 (obtained with 14 nodes), the solution is accurate and not affected by a round–off error instability. This is obtained using equidistant nodes. On the other hand, the right part of Figure 7.11 is obtained using the Gauss–Chebishev–Lobatto nodes, according to which the nodes are placed with a trigonometric distribution (see, for instance, Ref.[13]): the accuracy of the solution appears to be good up to an order 37 (that corresponds to a 19−node scheme).

Next, the behavior for a low number of nodes (such that results are largely within the stability region defined in Fig. 7.11) is investigated. Figure 7.12 depicts the p–convergence for the eigenvalues from 1 to 5, for WIP schemes, from two to eight nodes (that corresponds to a order 15).

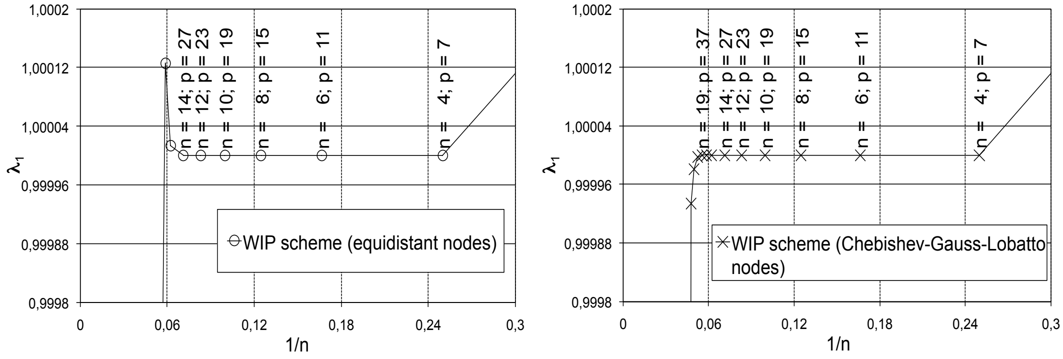

Figure 7.11: Closed end pipe: equidistant (left) and Gauss–Chebishev–Lobatto (right) nodes distribution for WIP schemes

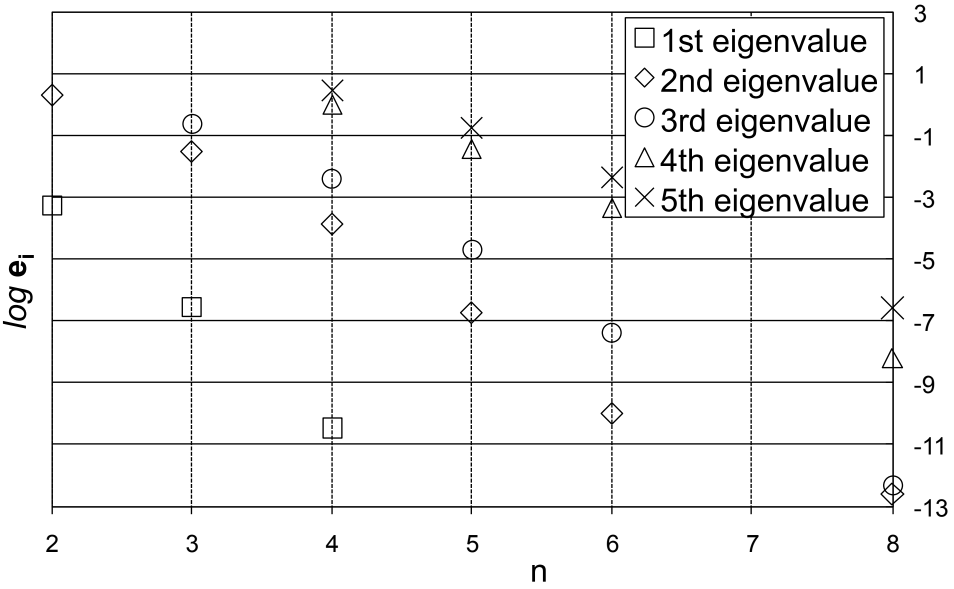

Figure 7.12: Closed end pipe: WIP $p-$convergence for eigenvalues $1-5$

7.2.3 WEP schemes *vs* WIP schemes

Next, the accuracy of the various schemes is assessed, either reducing the mesh size (h–convergences will be depicted) and increasing the order of polynomials (p–convergences will be depicted).

Specifically, Figs. from 7.13 to 7.16 show a h–convergence analysis of the classical third-order Hermite element (that coincides with a WEP scheme of order three), for the whole set of numerical modes and the related eigenvalues obtained. If N is the number of mesh elements, in these figures we have $N = 1, 2, 3, 4, 5$ or $N = 1, 2, 4, 8, 16$. Thus, since the number of total degrees of freedom is given by $N_{DOF} = 2(N+1)$, we have $N_{DOF} = 4, 6, 8, 10, 12$ (first two figures) and $N_{DOF} = 4, 6, 10, 18, 34$ (last two figures). It appears that, even though $2(N + 1)$ modes are generated, a quantity of $N + 1$ modes and related eigenvalues are accurately captured (in summary, the error on modes ϵ has revealed lower than 10^{-1} whereas the relative error on eigenvalues e_r appears to be lower than 10^{-2}). In addition, the last two eigenvalues appear to be not accurate and therefore the results on eigenfunctions (that are even larger) are not presented for them. A minimum for the $1 + N-$mode is obtained. For this modal shape, the nodes and the stationary points coincide.

Figures from 7.17 to 7.20 depict a p–convergence using a WIP configuration, for a mesh of $N = 1$ (first two figures) and $N = 2$ (last two figures).

Specifically, the schemes considered here are those of order $p = 3, 5, 7, 9, 11$. Again, at least a half of the total amount of modes extracted has revealed an error ϵ lower than 10^{-1} and a related relative error on eigenvalues e_r lower than 10^{-2}.

Figures 7.21 and 7.22 depict a p–convergence obtained using a WEP configuration, for $N = 1$. In this case, the orders considered are $p = 5, 7, 9, 17$. Similar considerations hold for the accuracy obtained in these figures.

Figures from 7.23 to 7.26 concern the accuracy of the various WEP elements. In particular, figures 7.23 and 7.24 (that is a zoom of the former one) show results on eigenvalues obtained using the third-order in comparison with those obtained using fifth–order: it appears that, for high frequencies, the fifth–order scheme maintain the accuracy better than three when the same amount of unknowns are utilized (here, a WEP fifth-order with a $N = 5$ subdivision has the same degrees of freedom of a Hermite third-order with $N = 8$ elements).

Similar considerations hold for the other two figures, where a Hermite seventh–order with $N = 5$ is compared to a Hermite third–order with $N = 11$ and to a Hermite fifth–order with $N = 7$. It is easy to convince yourself that the comparison is made for the same amount of degrees of freedom, being $N_{DOF} = 1/2(p + 1)(N + 1)$ (p is the order of the scheme).

Similarly, Figs. from 7.27 to 7.30 concern the accuracy of WIP elements for the complete range of eigenvalues extracted. Specifically, Figs. 7.27 and 7.28 depict the $i-$th eigenvalue λ_i ($i = 1, N_{DOF}$), for various schemes (order from three to eleven has been explored). Figures 7.29 and 7.30 show the logarithm of the relative error e_{r_i} (see eq. 7.7) of the i–th eigenvalue. A phenomenon (considered) similar to that discussed in Subsection 7.2.1 has occurred: the errors have now a minimum or a maximum for $i = 1 + kN$; this is more evident in the last figure, where each trend has been traced with a line.

Next, consider WEP schemes and WIP schemes together. Figures from 7.31 to 7.36 compare these approaches in their fifth and seventh–orders. Specifically, Figs. 7.31 and 7.32 regard order five whereas Figs. 7.33 and 7.34 concern order seven. They depict the eigenvalues λ_i. The last two figures depict $\log e_{r_i}$. It appears that, for the same order p and for the same N_{DOF}, the WEP approach (of class $\mathcal{C}^p$) is generally more accurate than the WIP (of class $\mathcal{C}^1$).

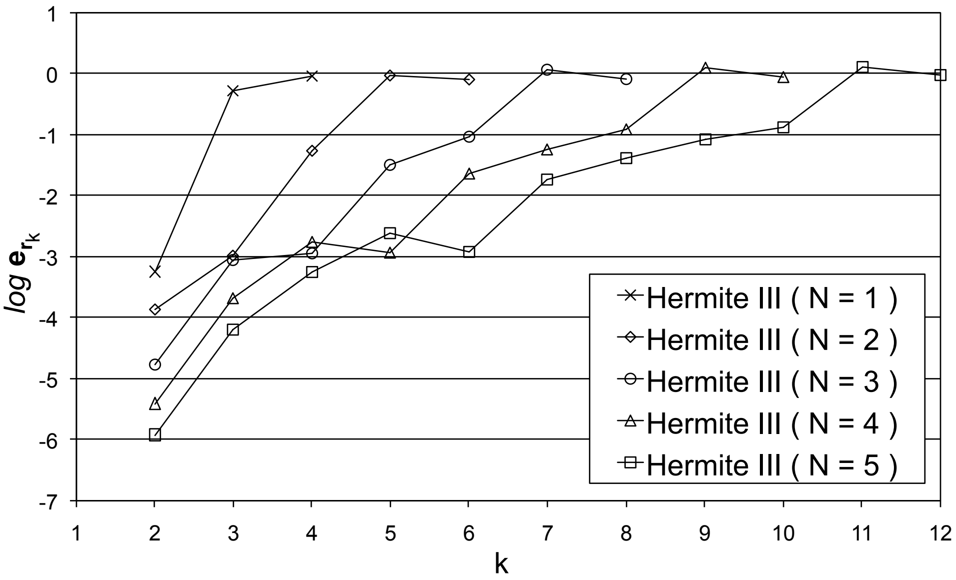

Figure 7.13: Closed end pipe: Hermite h–convergence for eigenvalues ($N = 1, 2, 3, 4, 5$)

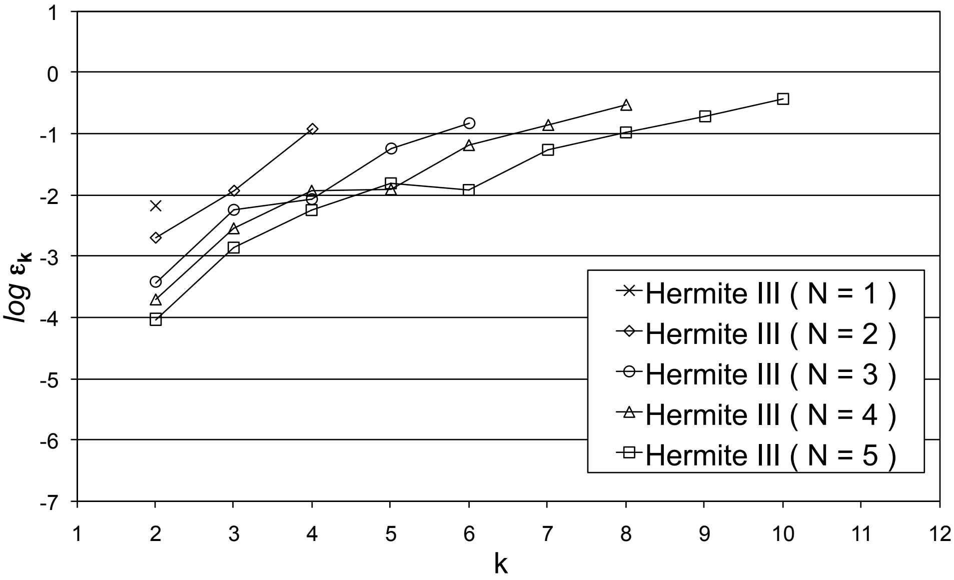

Figure 7.14: Closed end pipe: Hermite h–convergence for eigenfunctions ($N = 1, 2, 3, 4, 5$)

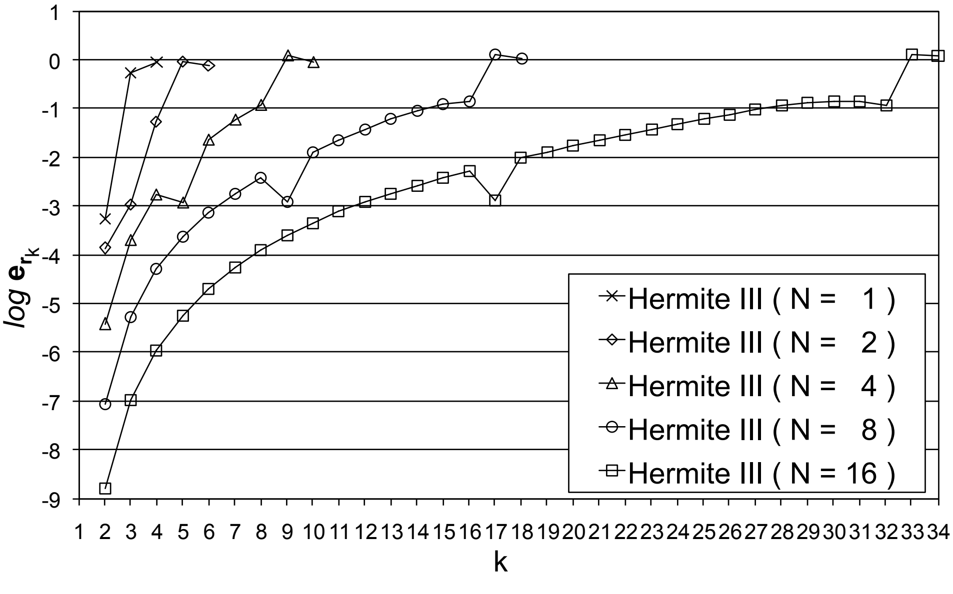

Figure 7.15: Closed end pipe: Hermite h–convergence for eigenvalues ($N = 1, 2, 4, 8, 16$)

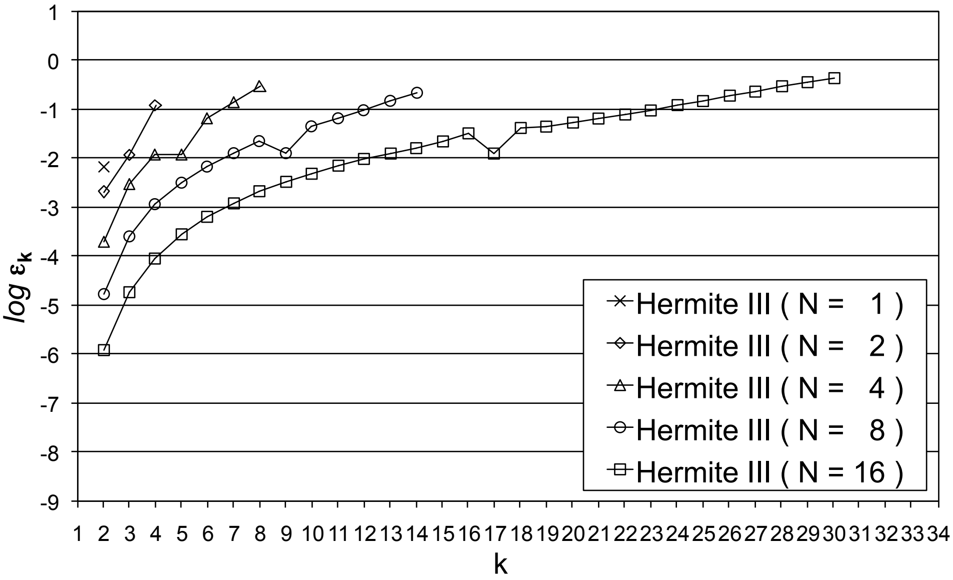

Figure 7.16: Closed end pipe: Hermite h–convergence for eigenfunctions $(N = 1, 2, 4, 8, 16)$

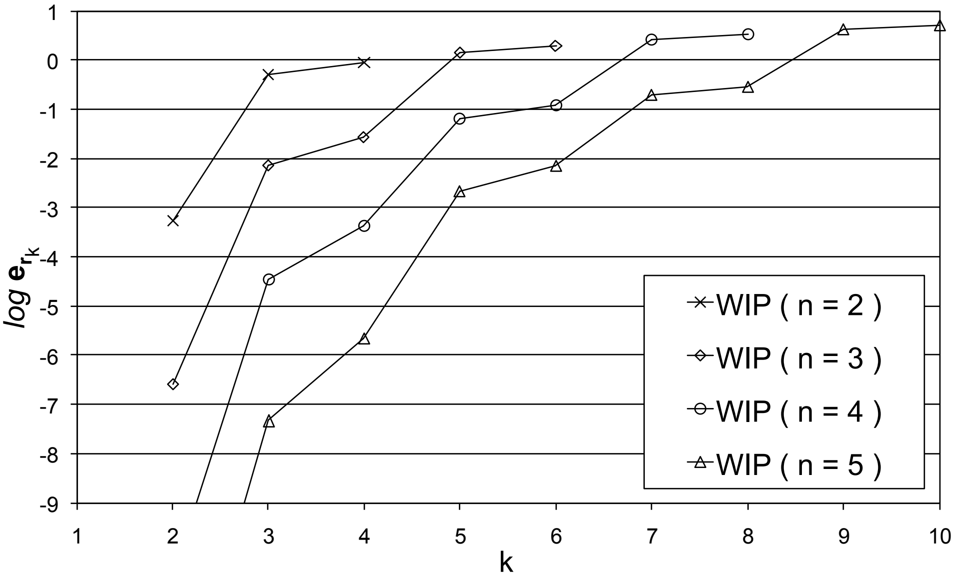

Figure 7.17: Closed end pipe: WIP p–convergence for eigenvalues $(N = 1)$

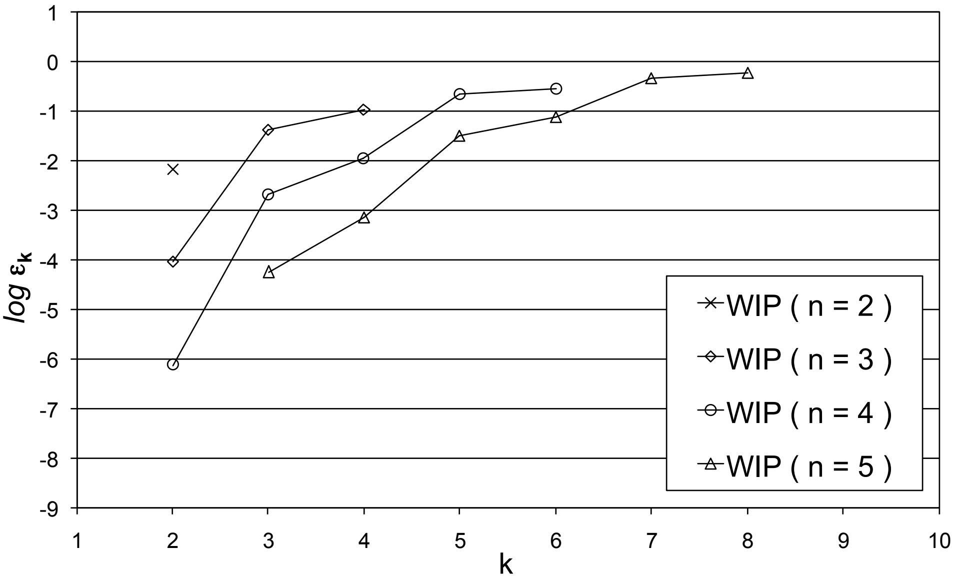

Figure 7.18: Closed end pipe: WIP p–convergence for eigenfunctions $(N = 1)$

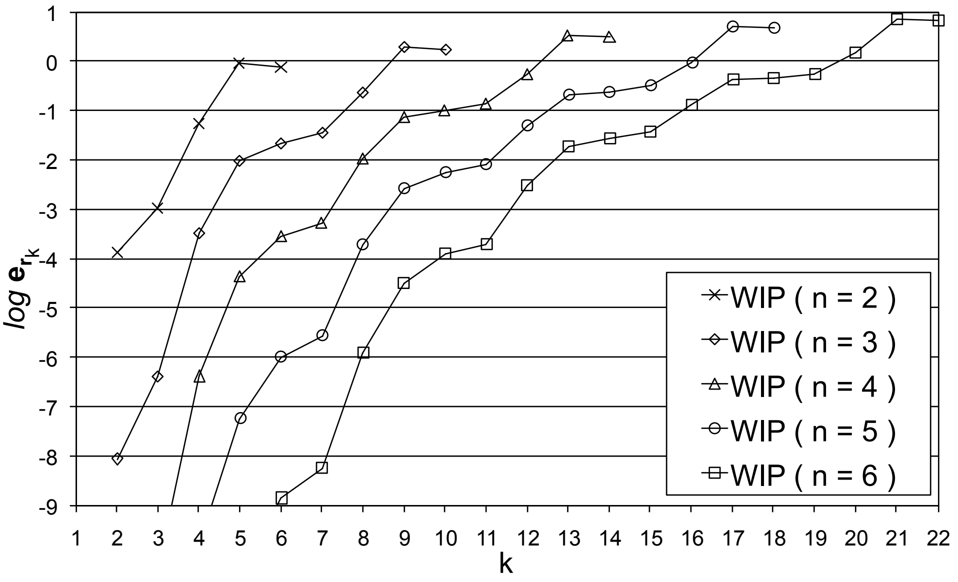

Figure 7.19: Closed end pipe: WIP p–convergence for eigenvalues $(N = 2)$

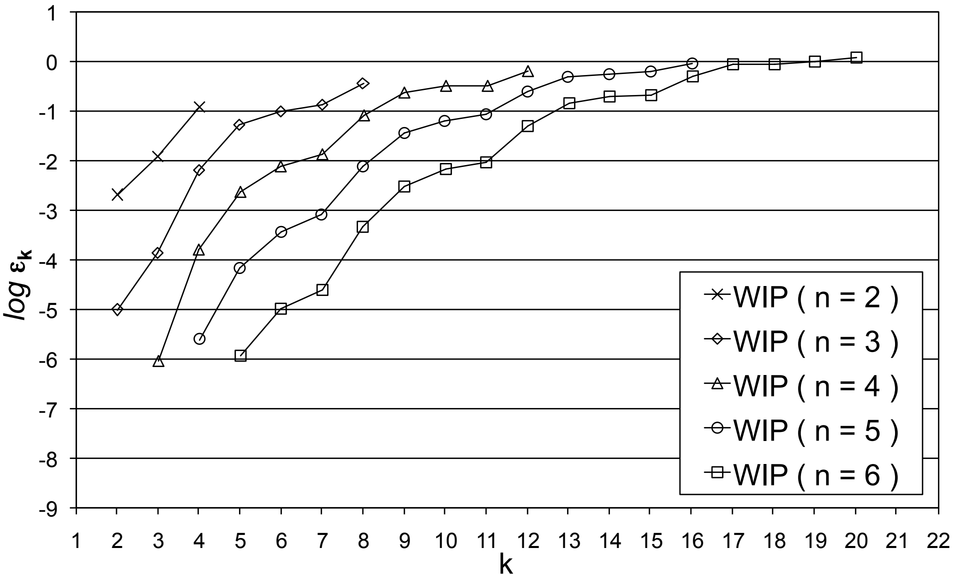

Figure 7.20: Closed end pipe: WIP p–convergence for eigenfunctions $(N = 2)$

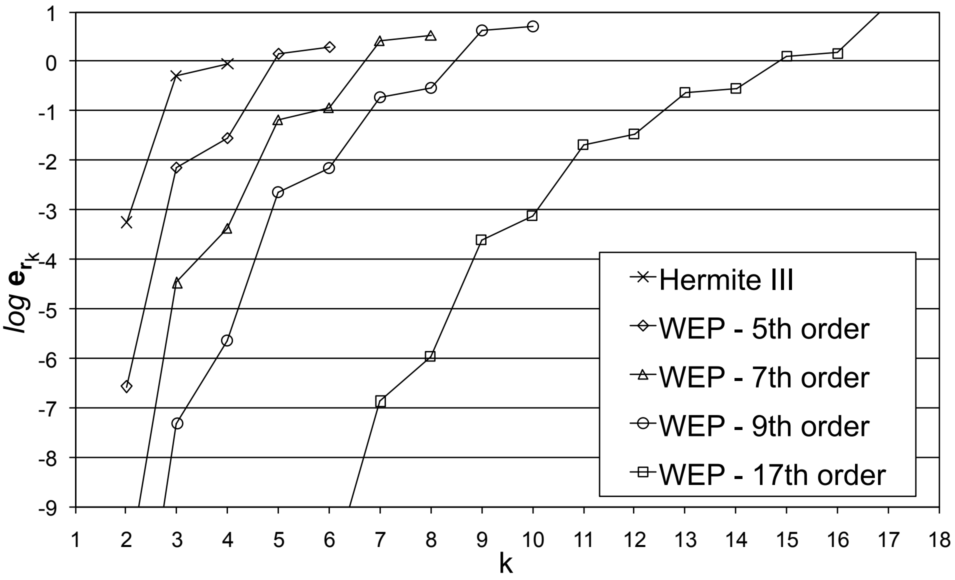

Figure 7.21: Closed end pipe: WEP p–convergence for eigenvalues

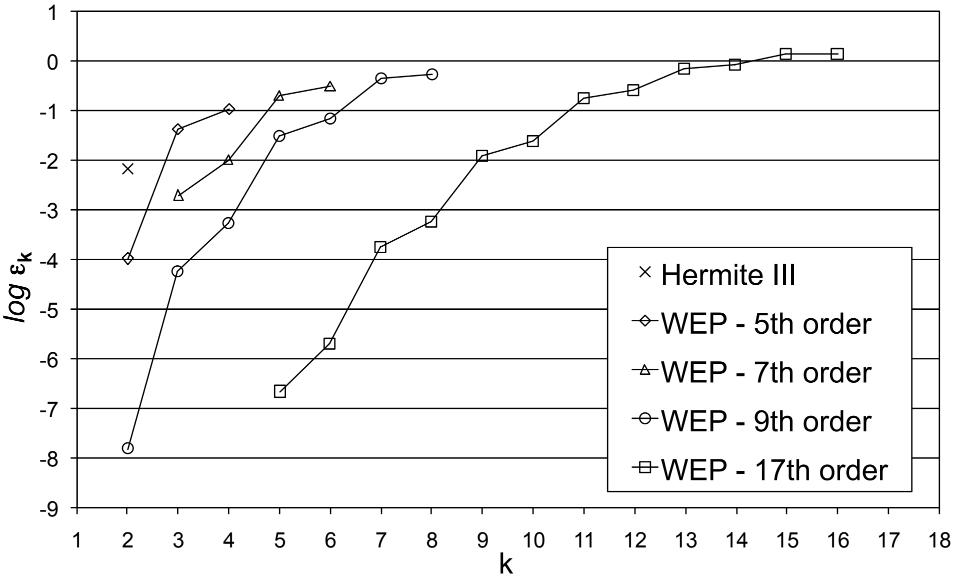

Figure 7.22: Closed end pipe: WEP p–convergence for eigenfunctions

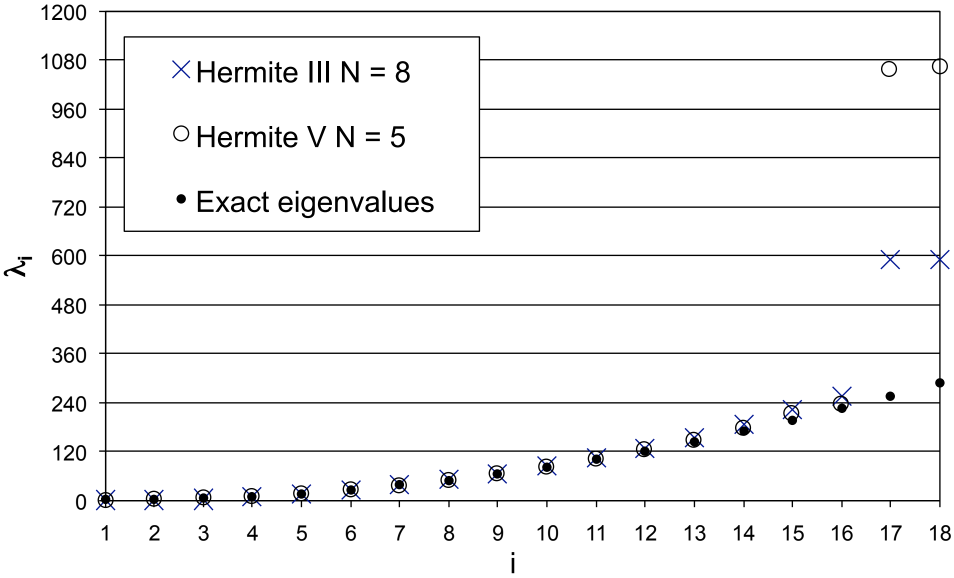

Figure 7.23: Closed end pipe: 3rd *vs* 5th order WEP schemes

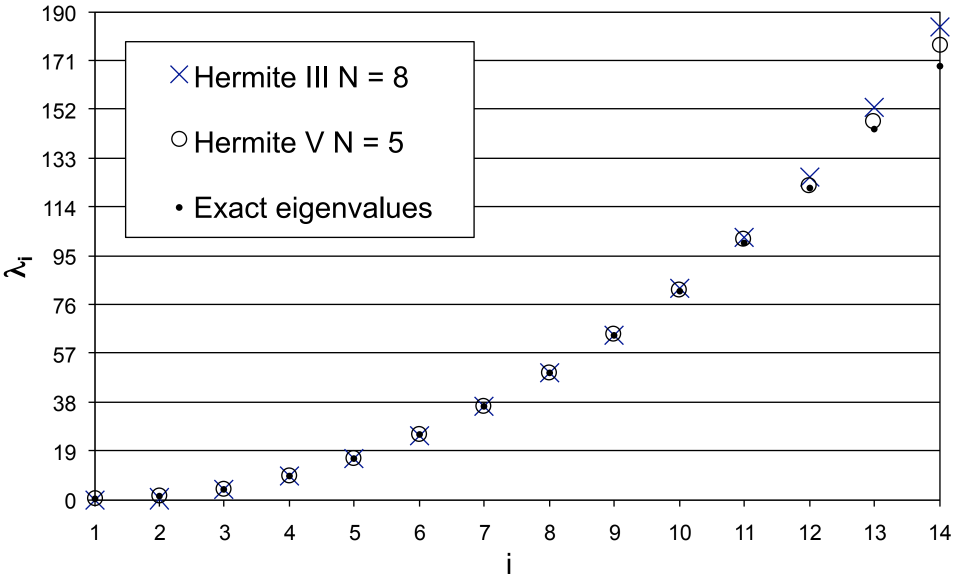

Figure 7.24: Zoom of Fig. 7.23

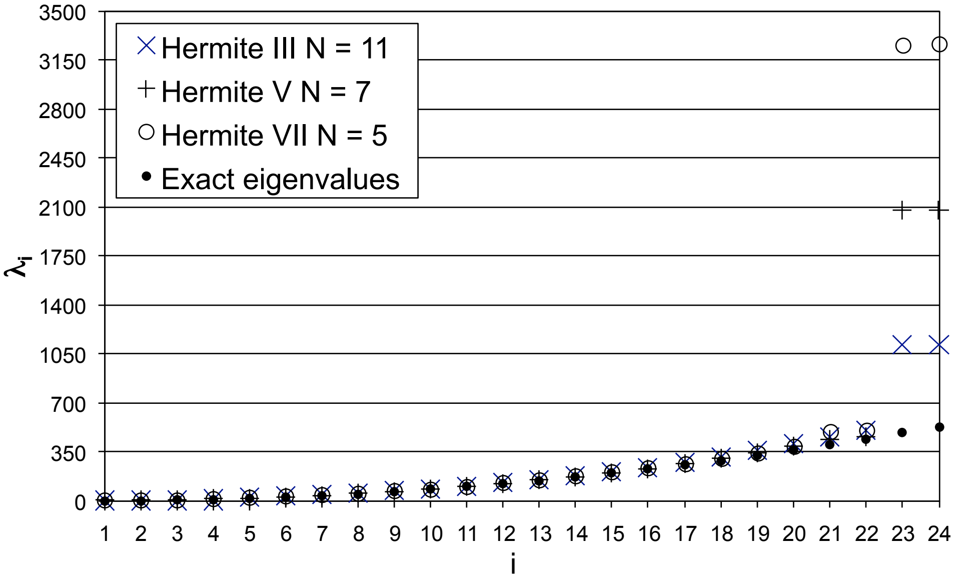

Figure 7.25: Closed end pipe: 3rd *vs* 5th *vs* 7th order WEP schemes

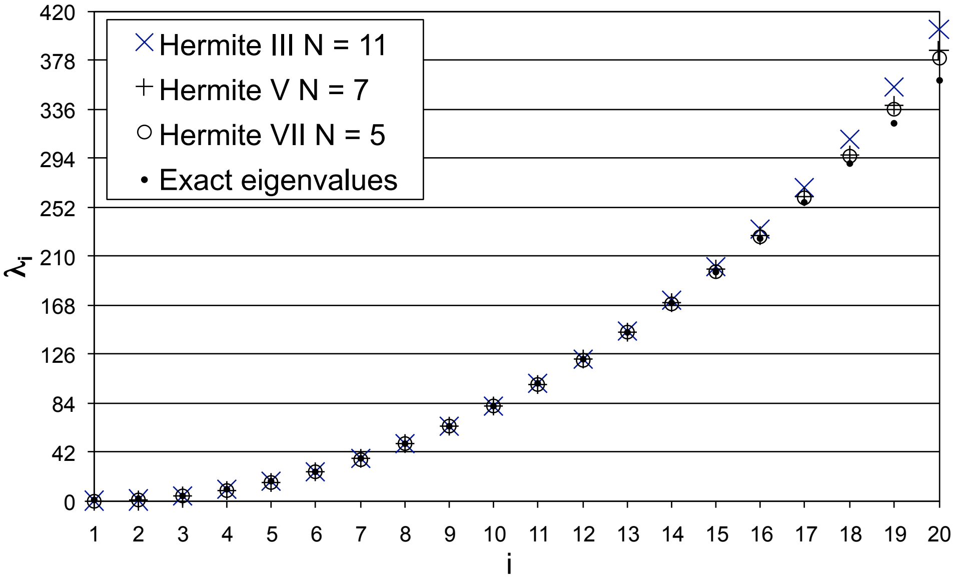

Figure 7.26: Zoom of Fig. 7.25

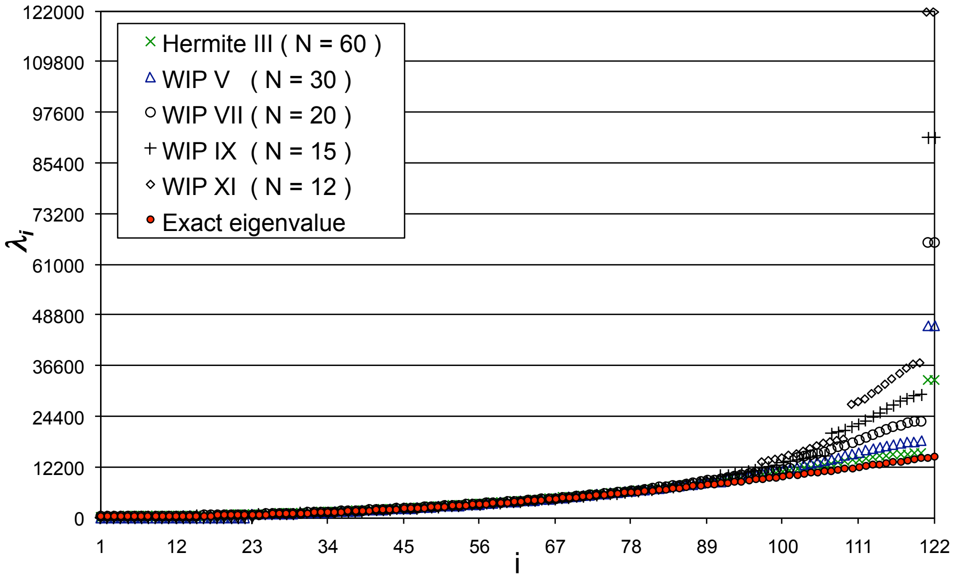

Figure 7.27: Closed end pipe: 3rd *vs* 5th *vs* 7th *vs* 9th *vs* 11th order WIP schemes

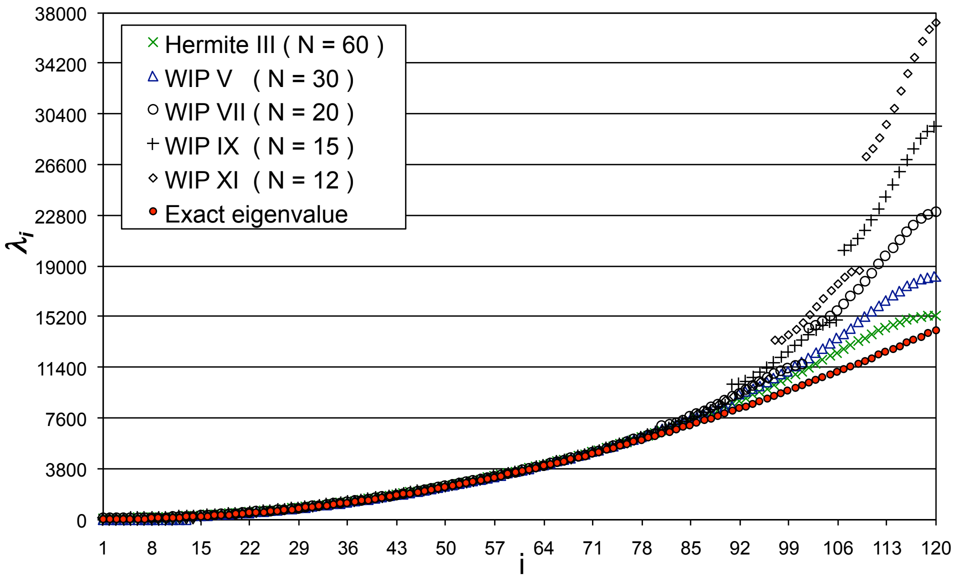

Figure 7.28: Zoom of Fig. 7.27

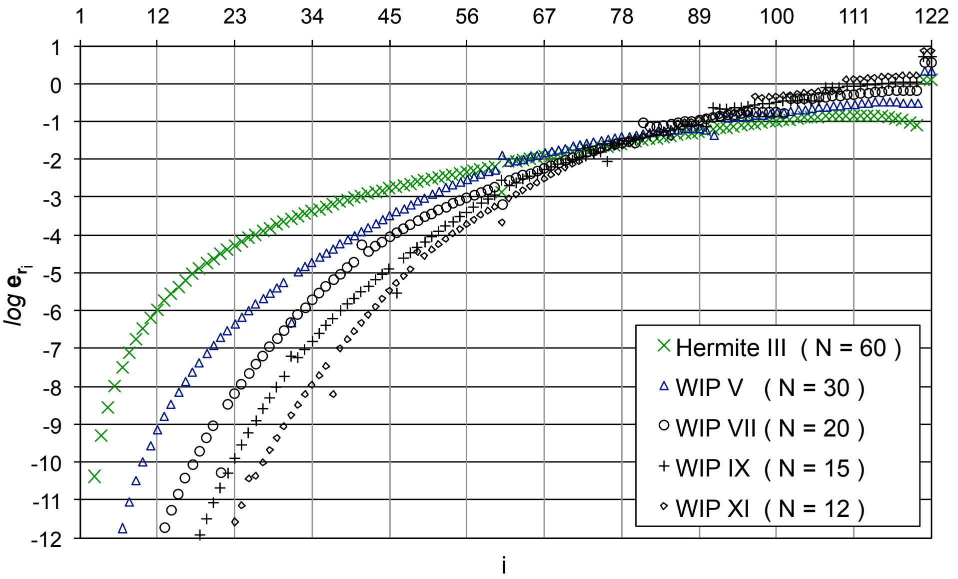

Figure 7.29: Logarithmic errors representation of Fig. 7.27

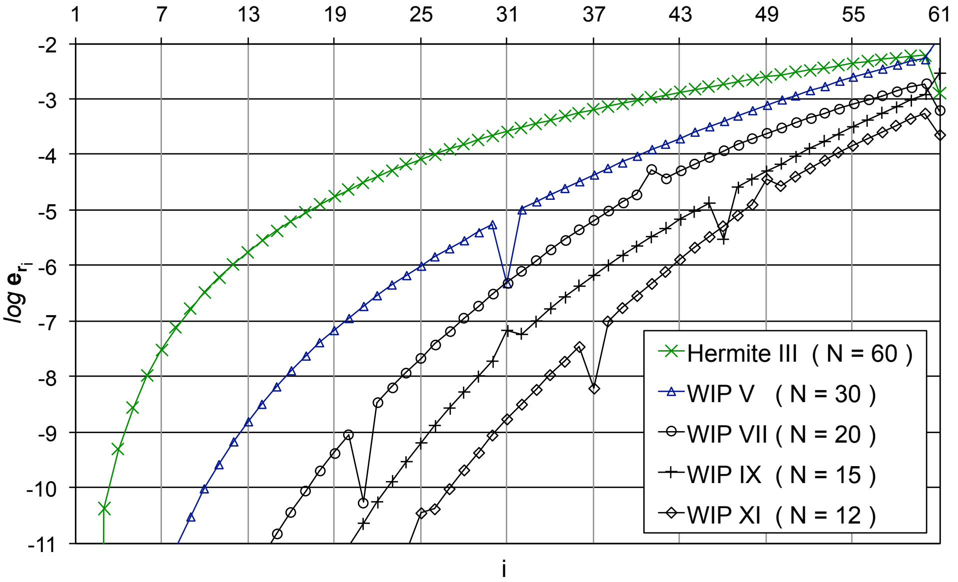

Figure 7.30: Zoom Fig. 7.29

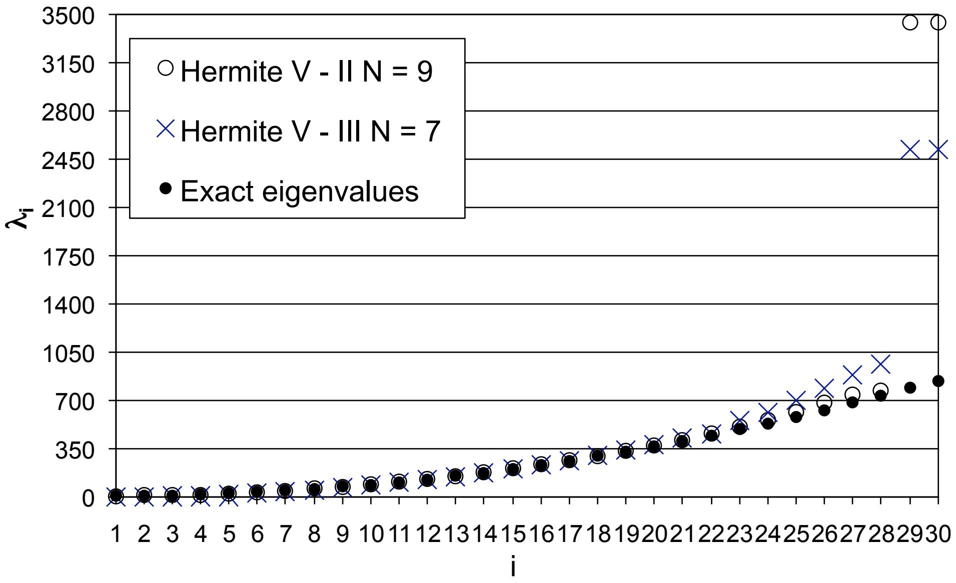

Figure 7.31: Closed end pipe: 5th order WEP *vs* WIP scheme (λ_i *vs* i)

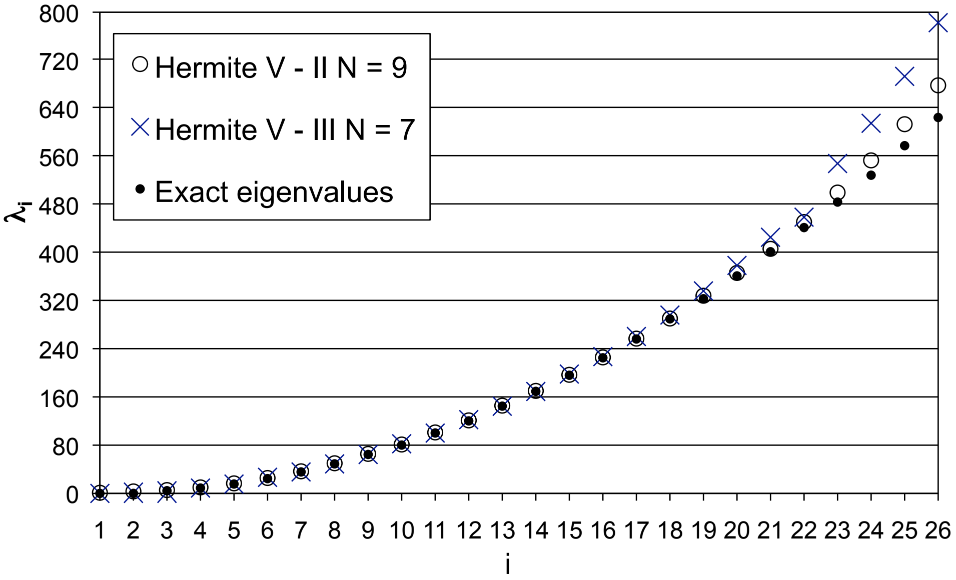

Figure 7.32: Zoom of Fig. 7.31

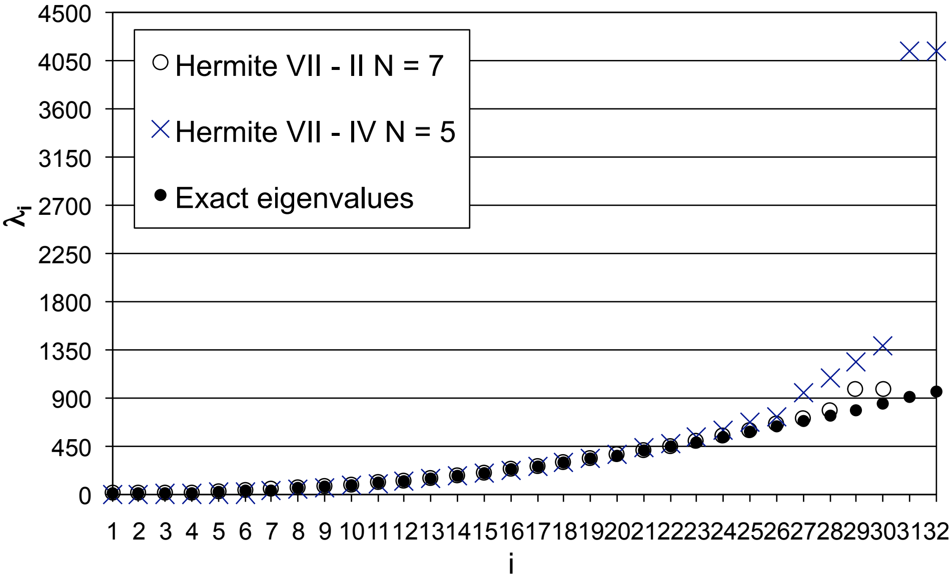

Figure 7.33: Closed end pipe: 7th order WEP vs WIP scheme (λ_i vs i)

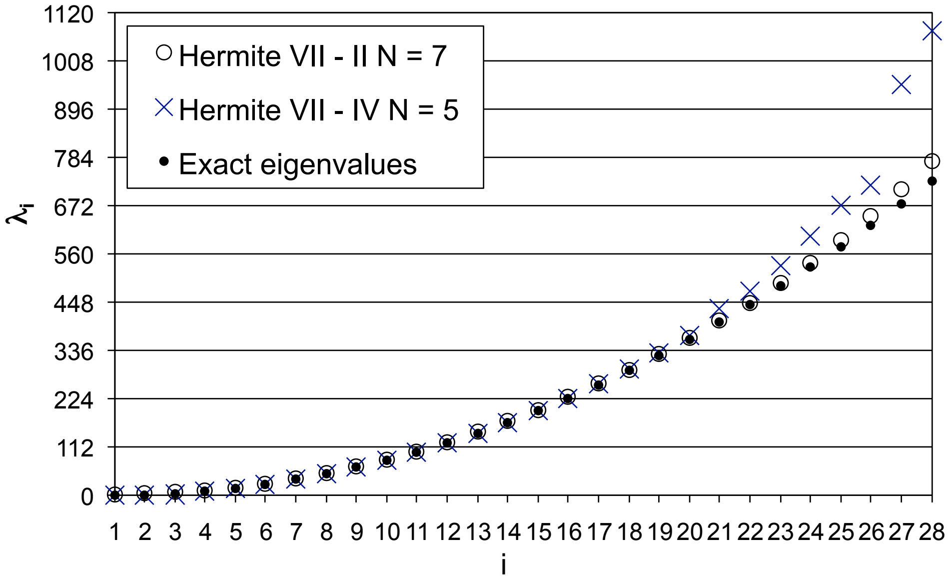

Figure 7.34: Zoom of Fig. 7.33

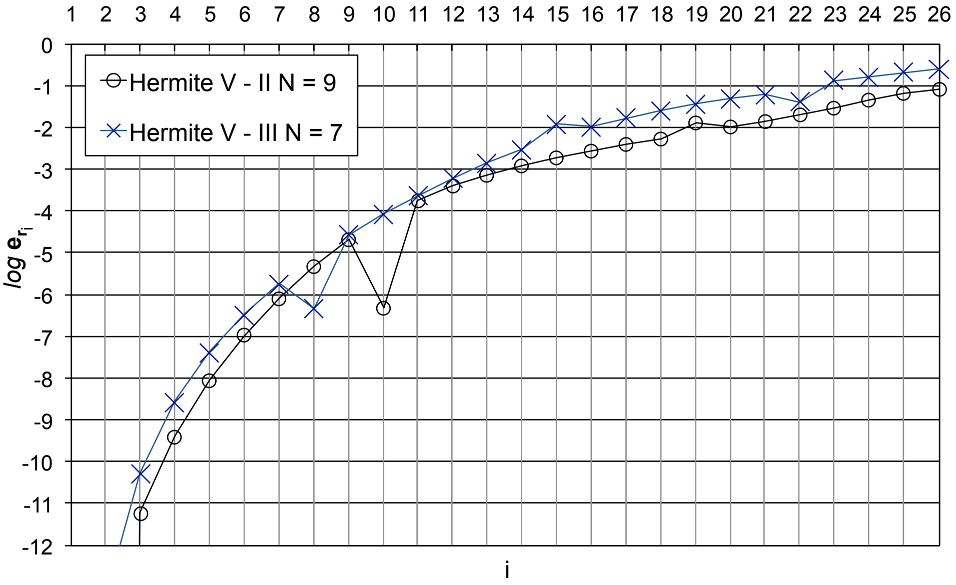

Figure 7.35: Closed end pipe: 5th order WEP *vs* WIP scheme ($\log e_i$ *vs* i)

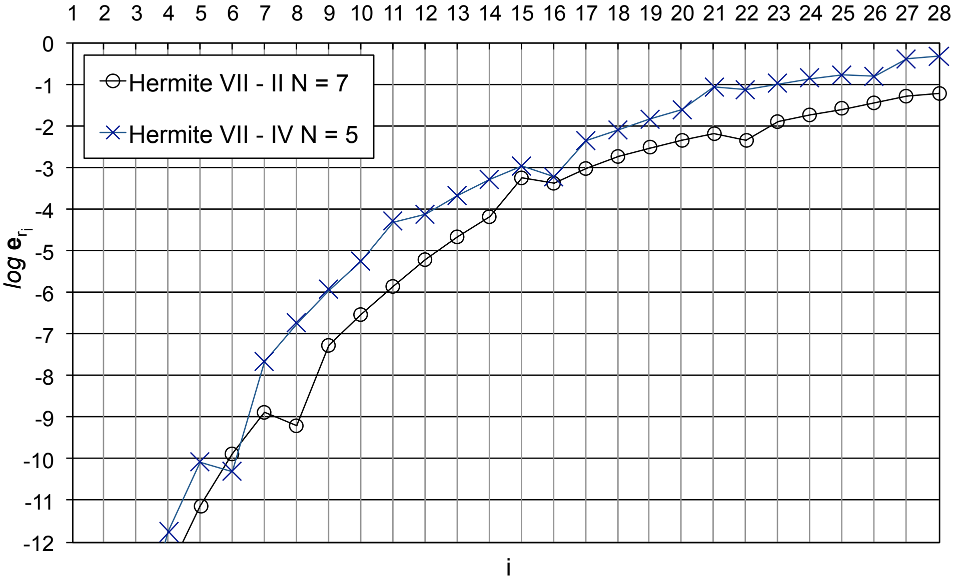

Figure 7.36: Closed end pipe: 7th order WEP *vs* WIP scheme ($\log e_i$ *vs* i)

7.3 Three–dimensional interior acoustics

Next, we want to assess the methodology in three-dimensional internal acoustics, exploring the possibility of using quasi-static reductions in solid geometries (the Guyan procedure introduced in Section E.1 has been considered as well as its extension known as the IRS techniques, introduced in Section E.2).

The problem investigated is the eigenproblem for the Laplacian, because a closed–form solution is available. This corresponds to the evaluation of the natural frequencies and modes of vibration of the air inside a hexahedral cavity, with edges a, b and c; the walls are assumed to be rigid, since this corresponds to the natural boundary condition and no further actions are required in constraints application. The exact solution we have is:

$$\Phi_{mnp} = \cos\frac{m\pi x}{a}\cos\frac{n\pi y}{b}\cos\frac{p\pi z}{c} \tag{7.9}$$

and

$$\mu_{mnp} = \frac{\omega_{mnp}^2}{c_s^2} = \frac{m^2\pi^2}{a^2} + \frac{n^2\pi^2}{b^2} + \frac{p^2\pi^2}{c^2} \tag{7.10}$$

(recall that the rigid wall boundary condition is $\partial u/\partial n = 0$, *i.e.*, a natural boundary condition). For simplicity, a velocity of sound $c_s = 1$ has been choosen. The discretization uses a subdivision into finite elements, with N elements in each direction, for a total of N^3 elements and $(N+1)^3$ nodes.

7.3.1 $h-$convergences

First, we consider a cubic cavity of sides π, so that to have $\mu_{mnp} = \omega_{mnp}^2 = m^2 + n^2 + p^2$.

Figures from 7.37 to 7.42 show a h–convergence study for three eigenvalues (to be specific, those having the exact values of 3, 12 and 27, respectively related to the $[1,1,1]$,$[2,2,2]$ and $[3,3,3]$ modes), using orders up to seven. Results are compared with Ansys (see the Ansys Reference Manual[14]). The element used is Fluid 30, specific for three-dimensional fluid-structure interaction problems. This element is a eight-noded brick that has four nodal unknowns (that is the three components of the displacement and the pressure) when the interaction between the fluid and the structure is taken into account whereas only one (that is the pressure) when the structure is not included in the analysis. Since the structure interaction is not included in this analysis, the option ‘structure absent’ has been applied and a single degree of freedom per node (that is the pressure) has been considered for comparisons (see the Ansys Elements Reference also included in[14]).

Table 7.3 show the numerical value of the convergence rate obtained with such formulations, compared to that expected (i.e., 6, 10 and 14, see Seection 7.1).

Finally, Figs. from 7.43 to 7.45 depict the eigenvalues related to the $[1,1,1]$,$[2,2,2]$ and $[3,3,3]$ modes as functions of $1/N_{DOF}$. In these figures the images on the left contain all the proposed elements and include the Ansys Fluid 30 whereas those on the right are a zoom on the higher order (only orders from 5 to 7 are showed). It appears that, even though the total amount of the unknowns increases within the element as the order of the element increases, the efficiency revealed by the higher orders is better than that showed by the lower–order elements.

	Fluid 30	Hybrid III	Hermite III	Hybrid V-II	Hermite V	Hybrid VII-III	Hermite VII
Exp. rate	2	6	6	10	10	14	14
$[1,1,1]$	1.9	4.9	5.3	9.5	10.3	12.2	-
$[2,2,2]$	2	5.1	5.2	9.1	11.1	13.0	16.6
$[3,3,3]$	1.9	4.8	5.1	8.9	11.4	14.7	14.2

Table 7.3: Cubic cavity: convergence rates for eigenvalues

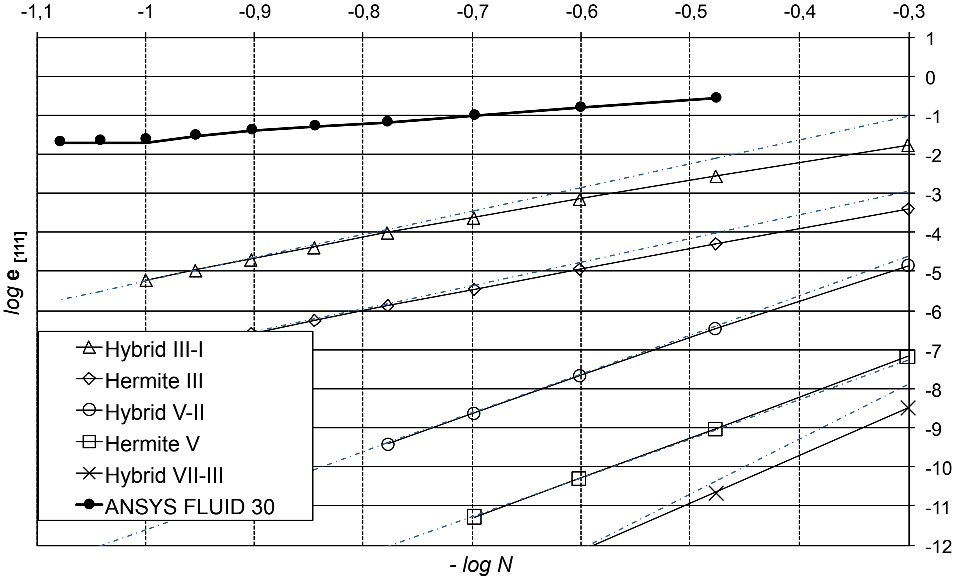

Figure 7.37: Cubic cavity: h–convergence for $\lambda_{[1,1,1]}$

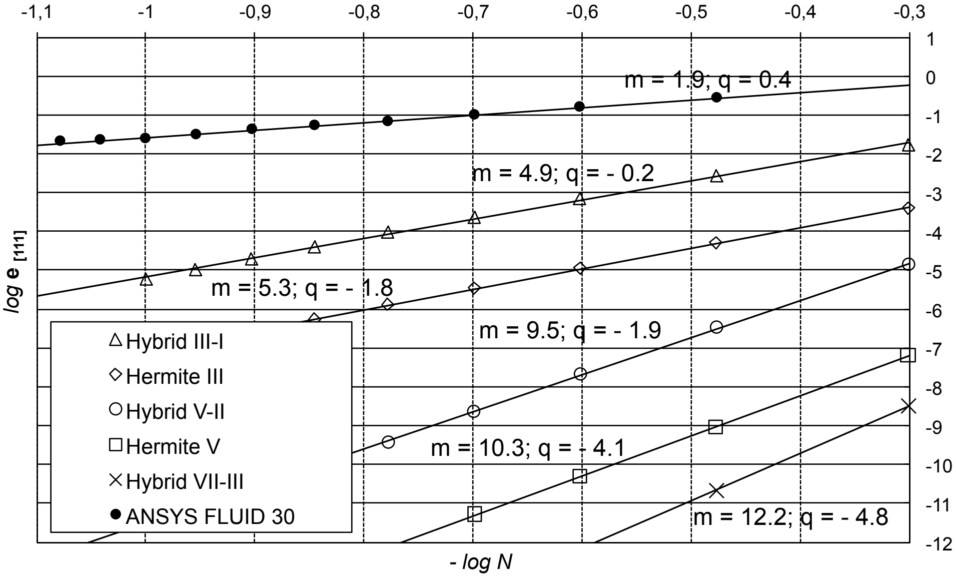

Figure 7.38: Convergence rates of Fig. 7.37

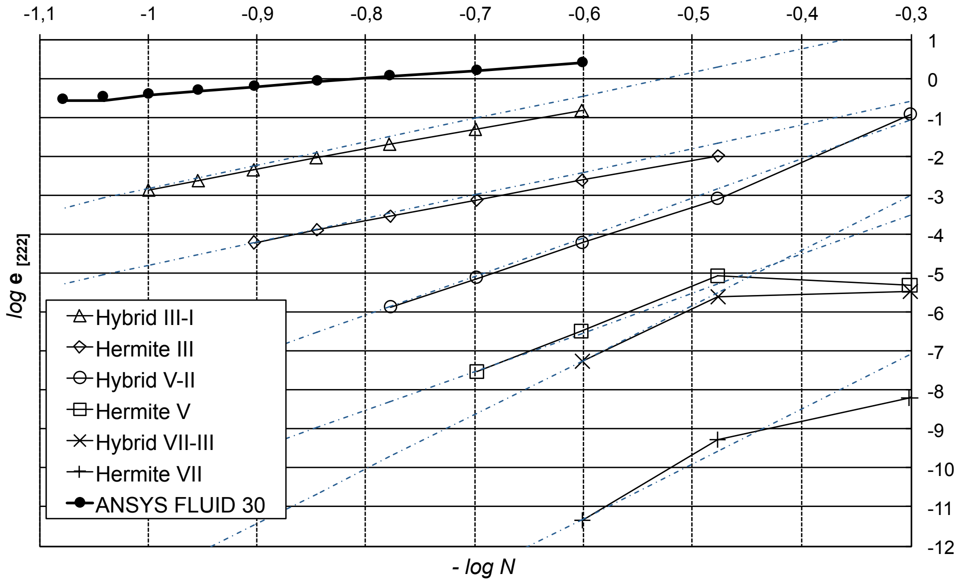

Figure 7.39: Cubic cavity: h–convergence for $\lambda_{[2,2,2]}$

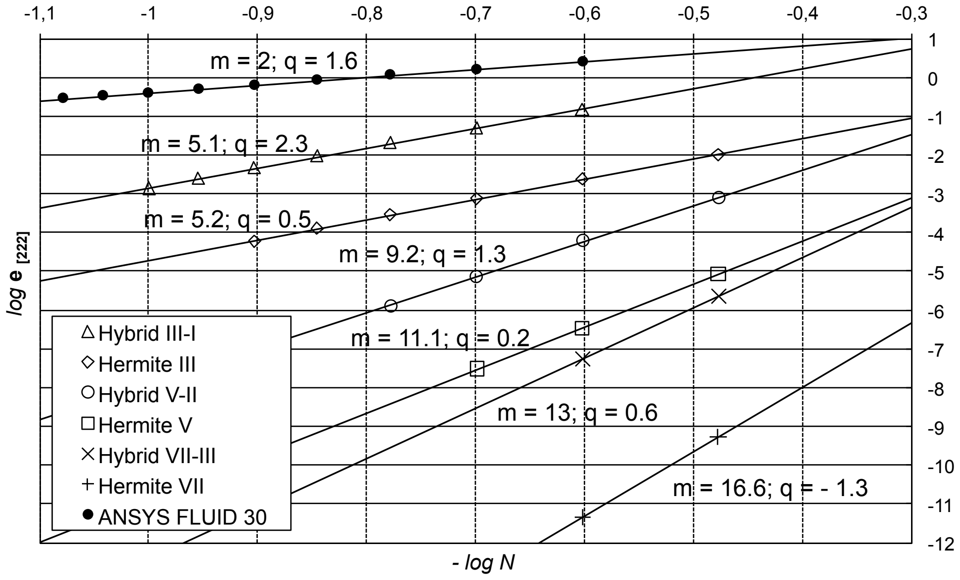

Figure 7.40: Convergence rates of Fig. 7.39

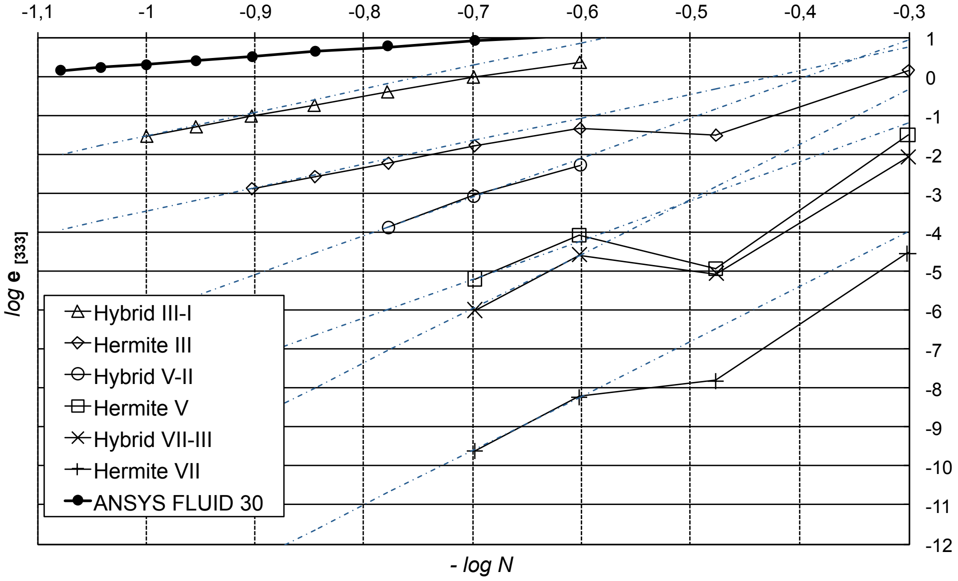

Figure 7.41: Cubic cavity: h–convergence for $\lambda_{[3,3,3]}$

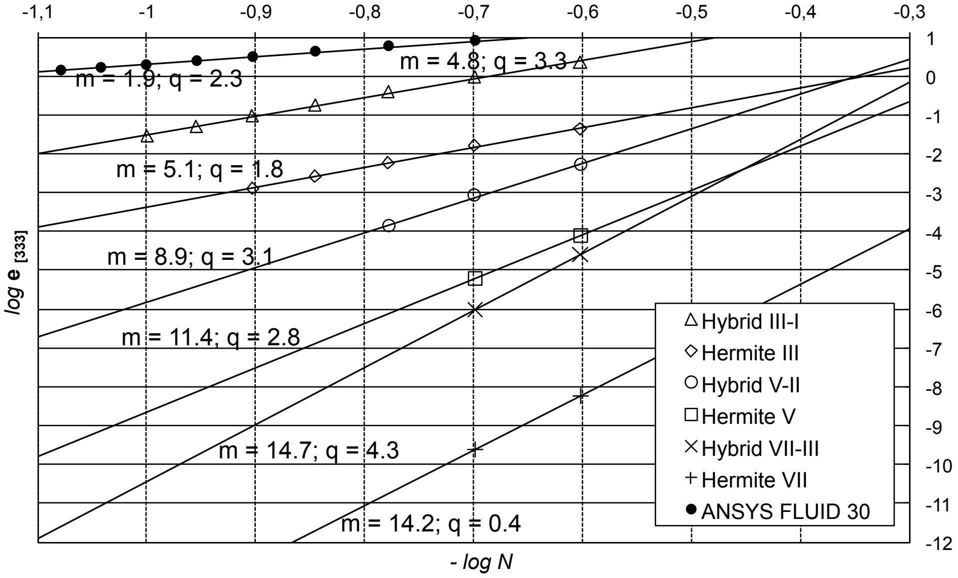

Figure 7.42: Convergence rates of Fig. 7.41

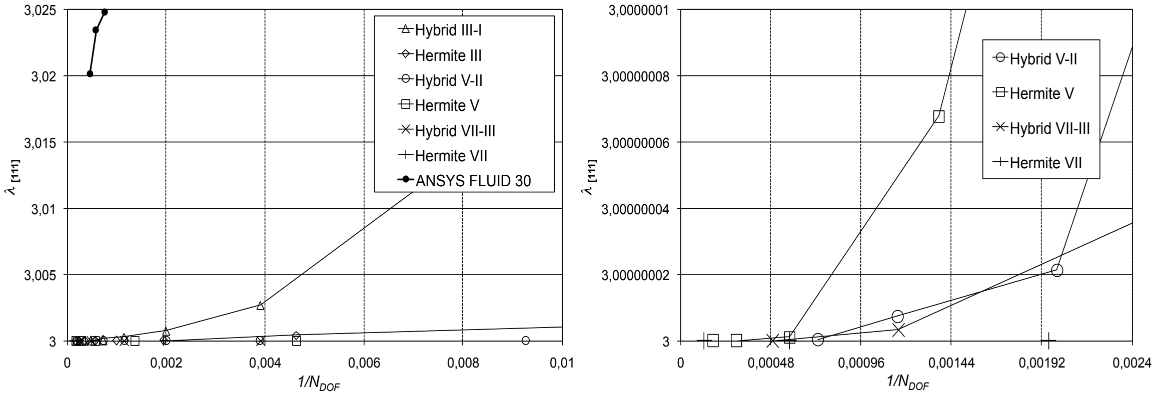

Figure 7.43: Cubic cavity: $\lambda_{[1,1,1]}$ vs $1/N_{DOF}$

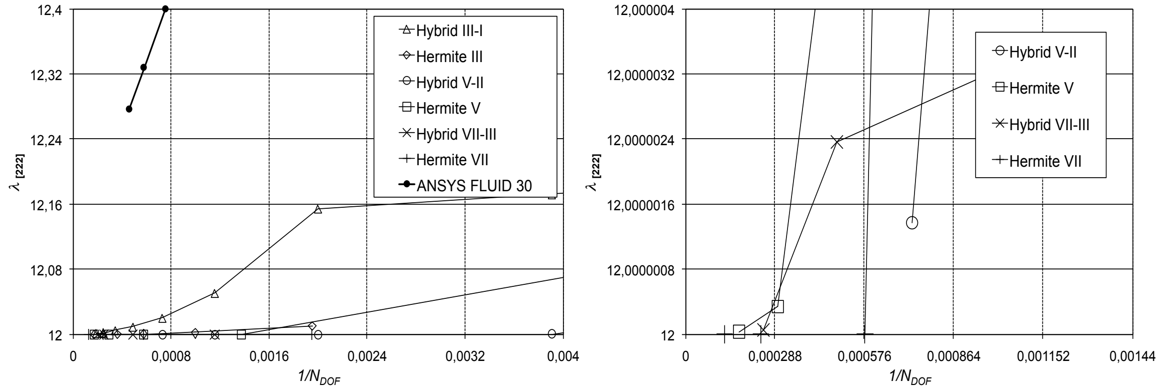

Figure 7.44: Cubic cavity: $\lambda_{[2,2,2]}$ vs $1/N_{DOF}$

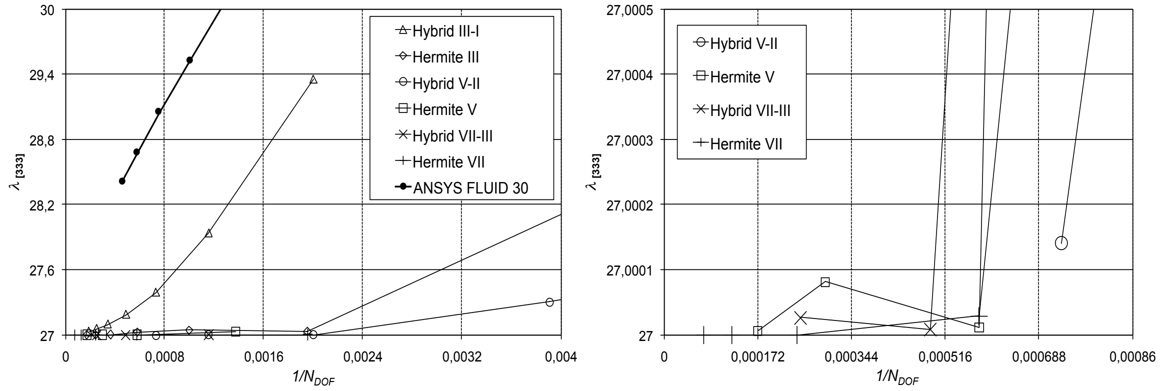

Figure 7.45: Cubic cavity: $\lambda_{[3,3,3]}$ vs $1/N_{DOF}$

7.3.2 High–frequencies analysis

Next, an assessment of the numerical modes obtained is addressed. The objective is to determine how many modes (and how many eigenvalues) are acceptably captured using the basic Hermite (see Section 2.2) and Hybrid bricks (see Section 4.4) along with their higher–order extensions (see Sections 3.2 and 5.1).

The problem under investigation is that of a rectangular cavity of sides $a = \pi$, $b = 1.01\pi$ and $c = 0.99\pi$ or that of a cube cavity of side π. In particular, the analysis of modes is best addressed for a rectangular cavity, since this geometry may be used to minimize the coupling between modes and therefore rendering simpler the evaluation.

The dimensions of the parallelepiped are chosen to avoid the coupling between modes that pertain to the same eigenvalues, as in the case of a cube, while maintaining the eigenvalues related to the same number of waves sufficiently close to each other (thus, the eigenvalue related to $[1, 0, 0]$ is wanted quite close to the $[0, 1, 0]$ and $[0, 0, 1]$ ones). Indeed, in each figure, the modes and the related eigenvalues are sorted per number of waves and $[k, l, m]$ holds the i–th mode to its number of waves per direction. As an example of the above mentioned coupling, see Figures 7.46 and 7.47. In this set of images, Fig. 7.46 depicts the values of $\mathsf{z}_j^T \mathsf{M} \mathsf{y}_i - \delta_{ij}$ (for $i, j = 1, \dots, N_{DOF}$), as obtained for a cube of side π using a Hybrid 3rd order $8-$node brick with $N = 1$, whereas Fig. 7.47 concerns the same analysis for a Hybrid 3rd order $8-$node brick with $N = 1$ and for a Hybrid 5th order $27-$node brick with $N = 1$.

The number of subdivisions, supposed equal for each direction will be referred to as $N = N_1 = N_2 = N_3$ whereas the number of waves will be referred to as n_w.

In the following, the value of $\mathsf{z}_j^T \mathsf{M} \mathsf{y}_i - \delta_{ij}$ is depicted as a two–dimensional mapping using a grey scale from 0 to 0.05 and it is obtained through a modal reconstruction that uses a further subdivision of the N^3 elements (the domain has just been meshed in $NxNxN$ elements for the M and K evaluation) in $n_{div} = 3$.

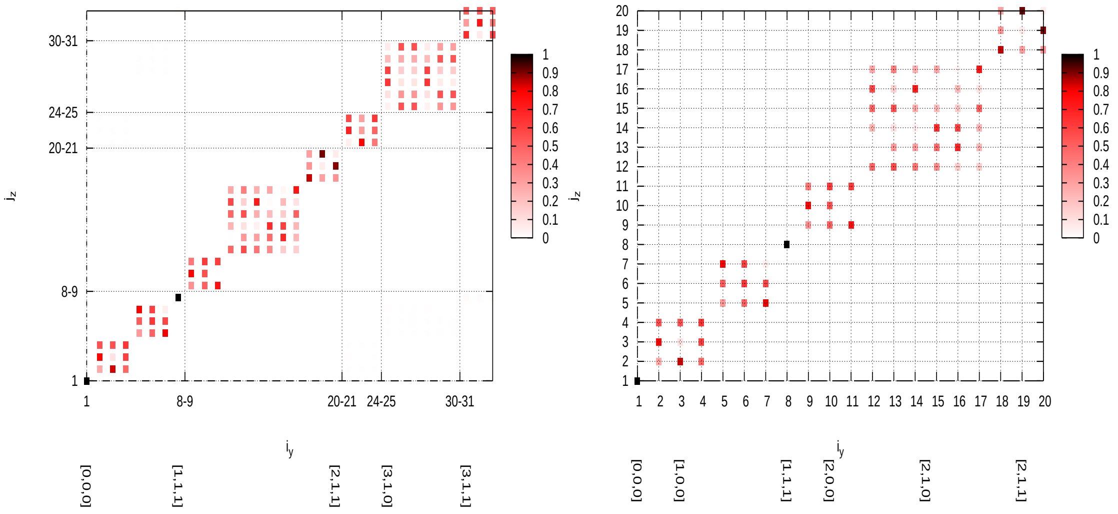

Figure 7.46: Cubic cavity: coupled modes with Hybrid 3rd order ($N = 1$)

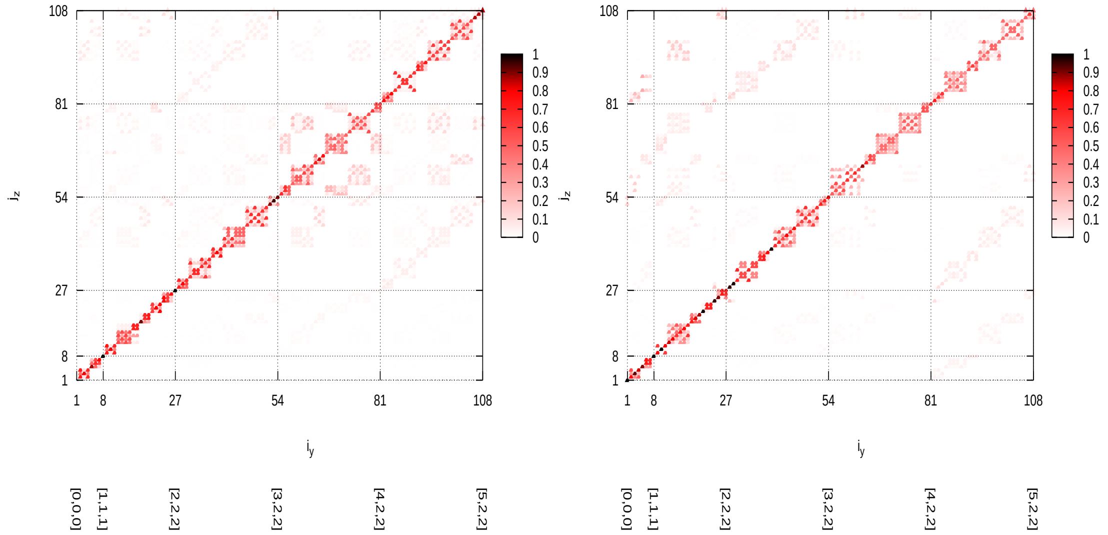

Figure 7.47: Cubic cavity: coupled modes with Hybrid 3rd order ($N = 2$) and Hybrid 5th order ($N = 1$)

7.3.3 Hermite 3rd order $8-$node element

This subsection is dedicated to the Hermite 3rd order 8−node brick introduced in Section 2.2. A preliminary analysis of this element has been addressed throughout the past years, starting from the 2004 International Conference on Computational & Experimental Engineering & Sciences (ICCES'04).[3] The study was limited to very low eigenvalues and frequencies of simple structural problems (plates and shells). Here, an extensive analysis related to both the complete set of eigenvalues and modes extracted is presented.

Figures from 7.48 to 7.53 show a complete set of results concerning modes and eigenvalues for the Hermite 3rd order 8−node brick, obtained with meshes of $N = 1, 2, 3$ elements per direction.

Results for $N = 1$ are presented in Figs. 7.48 and 7.49, where the whole set of modes and eigenvalues (a total of 64) is considered. For the total number of waves one has $N_w = 3$. Results show very good accuracy for the first 8 modes and eigenvalues, the last of them corresponding to 1 wave per direction.

Results for $N = 2$ are presented in Figs. 7.50 and 7.51, where, again, the whole set of modes and eigenvalues (they are 216) is considered. For the total number of waves, now one has $N_w = 5$. Results show very good accuracy for the first 27 modes and eigenvalues, *i.e.*, for $n_w \leq 2$. Acceptable results are obtained also for $2 \leq n_w \leq 3$. Results for $N = 3$ are presented in Figs. 7.52 and 7.53. Even though the maximum number of modes that can be obtained is 512 (and the maximum number of waves is $N_w = 7$), results are plotted only for the first 125 modes and eigenvalues (*i.e.*, for $n_w \leq 4$). Again, results are very good for $n_w \leq 3$.

Looking at Figs. from 7.48 to 7.51, if $N_w = 2N+1$ is the number of waves included using a mesh of N elements in each direction,[2] the quantity of waves per direction captured with very good accuracy appears to be $n_w = N$. Also, an acceptable accuracy seems to be maintained until $(n_w = N + 1)$.

As a rule of thumb, one can assume that, say $N_{DOF} = (2N + 2)^3$ the total number of unknowns, the quantity of modes acceptably captured is $N_0 = (N + 1)^3$. As a consequence, $N_0/N_{DOF} = 1/8$ of the total modes extracted has a good accuracy.

---

[2] This corresponds to the total number of unknowns per direction, $2N + 2$, minus 1 to take into account the presence of a zero frequency.

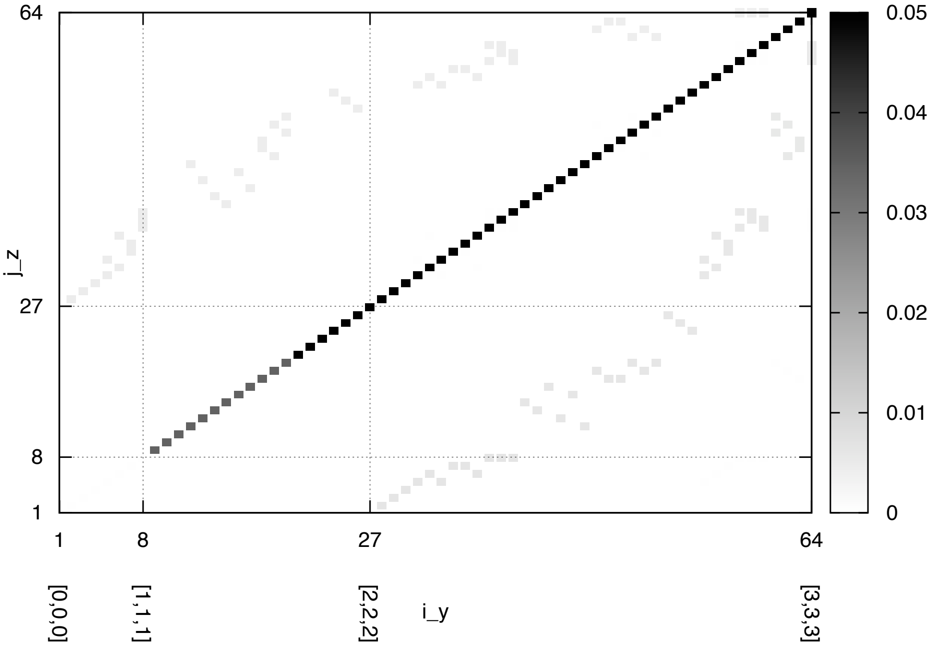

Figure 7.48: Rectangular cavity: eigenfunctions with the Hermite 3rd order 8−node ($N = 1$)

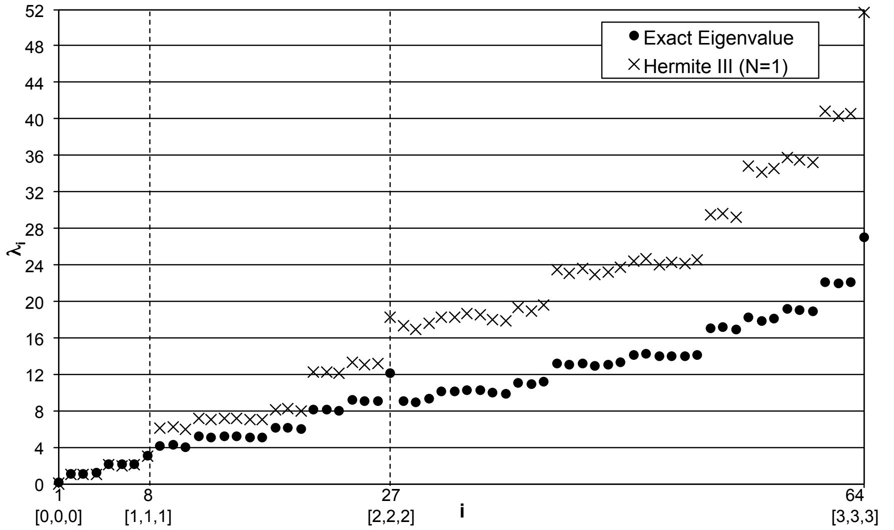

Figure 7.49: Rectangular cavity: eigenvalues with the Hermite 3rd order 8−node ($N = 1$)

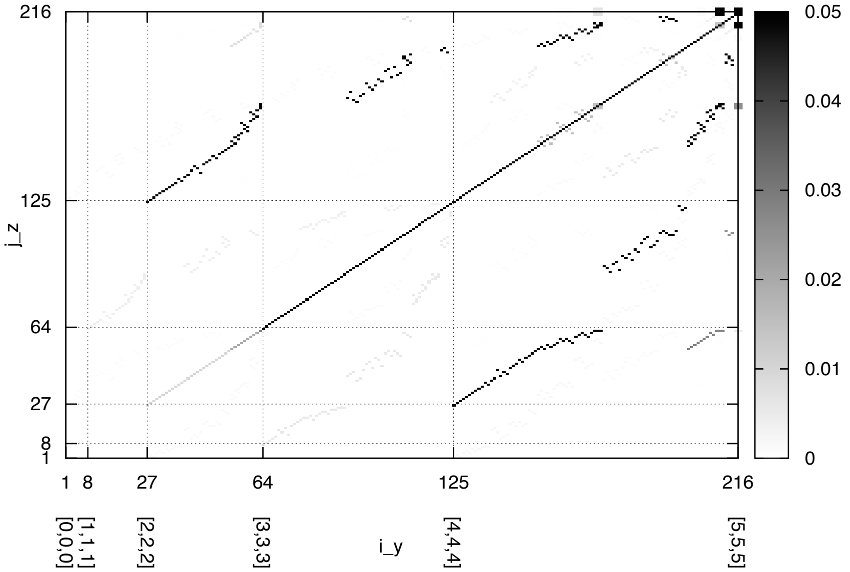

Figure 7.50: Rectangular cavity: eigenfunctions with the Hermite 3rd order 8−node ($N = 2$)

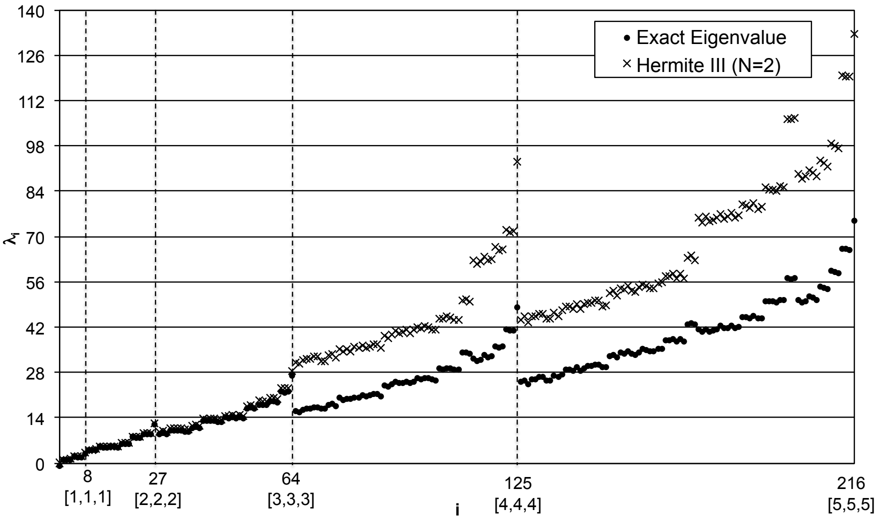

Figure 7.51: Rectangular cavity: eigenvalues with the Hermite 3rd order 8−node ($N = 2$)

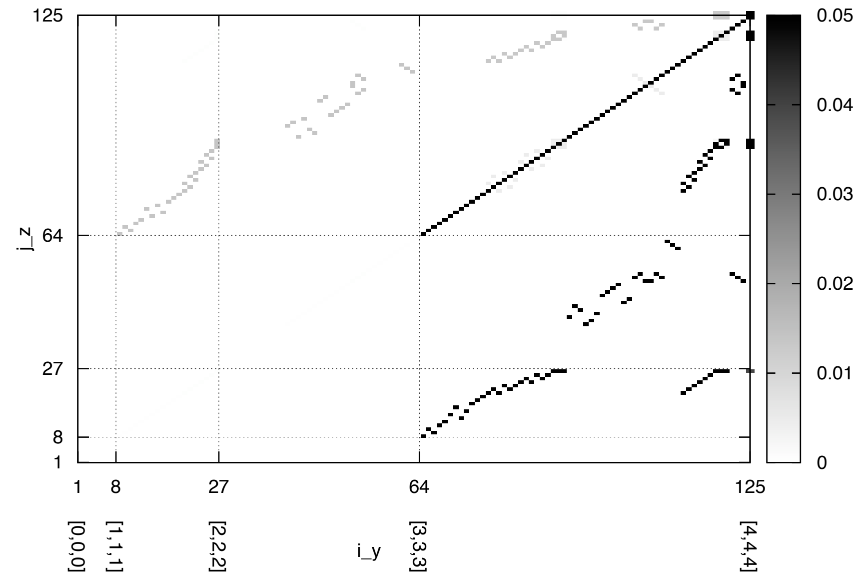

Figure 7.52: Rectangular cavity: eigenfunctions with the Hermite 3rd order 8−node ($N = 3$)

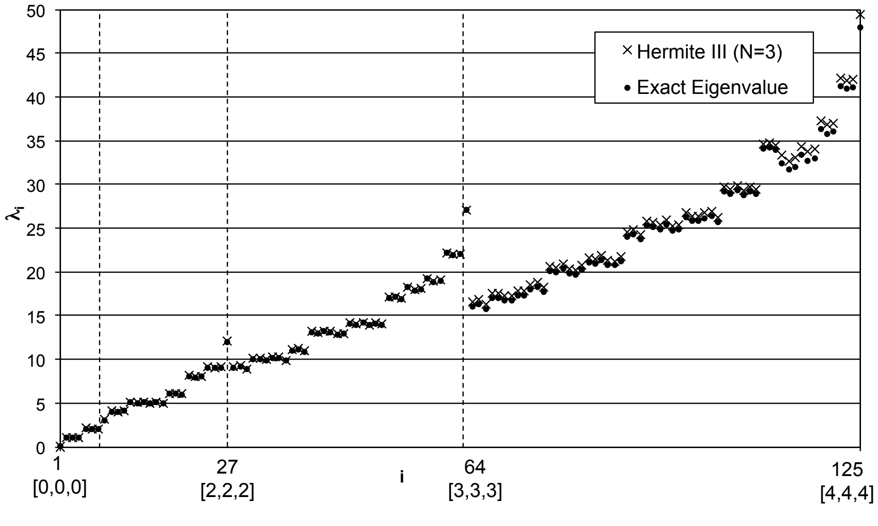

Figure 7.53: Rectangular cavity: eigenvalues with the Hermite 3rd order 8−node ($N = 3$)

7.3.4 Hermite 5th order $8-$node element

This subsection is dedicated to the Hermite 5th order 8−node brick, introduced in Subsection 3.2.1. This element has been preliminarily introduced at the 12th AIAA/CEAS Aeroacoustics Conference.[15] In that case, the analysis was limited to the $h-$convergence analysis for a very small subset of low–frequency eigenvalues. Here the study is extended to modes and to the complete set of eigenvalues and modes extracted.

The following figures pertains the air vibrating inside a rectangular cavity of sides π, 1.01π and 0.99π.

Figures 7.54 and 7.55 show a mode analysis for the element, using a subdivision of $N = 1$. The discretized problem has 216 degrees of freedom (*i.e.*, 27 unknowns per node for each of the 8 nodes; note that for the Hermite 3rd order 8−node element of the preceding subsection, the same number of unknowns is obtained for $N = 2$). Now one has $N_w = 5$ as a maximum number of waves per direction.[3] It appears that good results are obtained for a number of waves $n_w \leq 3$.

Within the same analysis, Fig. 7.55 shows the results for the eigenvalues whereas Fig. 7.56 adds to the preceding figure the results obtained in Subsection 7.3.3 for the Hermite 5th order 8−node with $N = 2$ to have a comparison for the same number of unknowns. In particular, the 5th order element shows a better accuracy than the 3rd order, for frequencies having $n_w \leq 3$ (see also the zoom on the right).

Figure 7.57 show a comparison between the Hermite 3rd order 8−node and the Hermite 5th order 8−node bricks, for the same number of unknowns. Specifically, the blue lines are obtained using $N = 2$ elements for the third order brick and $N = 1$ for the fifth order one whereas the green lines are related to a $N = 5$ elements for the third–order brick and $N = 2$ elements for the fifth order brick. The different colors refer to a specific value of N_{DOF} (*i.e.*, 6^3 for the blue and 12^3 for the green lines), since one has $N_{DOF} = (2N + 2)^3$ for the third–order brick and $N_{DOF} = (3N + 3)^3$ for the fifth–order one.

As expected (see Subsection 7.3.3), results are very good for $n_w \leq 2$ for the blue trend (being $N_w = 5$ the maximum number of waves included in this analysis).

Also, the green trends are extremely accurate for $n_w \leq 5$ (now $N_w = 11$ is the total number of waves for this meshes). A good accuracy is obtained

---

[3] Similarly to Subsection 7.3.3, in this case it results $n_w = 3N + 2$, N being the number of subdivision for each direction.

for $6 \leq n_w \leq 8$

As a rule of thumb, one can assume that, say $N_{DOF} = (3N + 3)^3$ the total number of unknowns, the quantity of modes acceptably captured is (considering also the results obtained in Subsection 7.3.3) $N_0 = [3/2(N+1)]^3$. As a consequence, again $N_0/N_{DOF} = 1/8$ of the total modes extracted has a good accuracy.

Consider the Hermite 5th order 8−node element with $N = 3$ elements. In order to have the same quantity of DOFs, compare it with the Hermite 3rd order with $N = 5$ elements. On the basis of the above results and of the results presented in Subsection 7.3.3, the expected amount of acceptable modes is 6^3. This translates in a maximum number of waves acceptably captured of $n_w = 5$. Figures from 7.58 to 7.60 show the $[k, k, k]$ mode for $k = 1, 2, 3, 4, 5, 6$. The aim is to show the capability of maintaining the accuracy in the modal shape. Specifically, they depict a comparison beetween the numerical modes and the exact ones. On the other hand, Figure 7.61 shows the 'bad' numerical modes (the last two in number of waves to be extracted) in comparison with the exact ones: the loss in accuracy appears to be mainly related to the presence of non–zero first derivatives at the boundaries.

The following figures pertains the air vibrating inside a cubic cavity of side π.

To assess the method in comparison with commercial solutions, some of the preliminary resuts (see Ref.[15]) are reviewed. Figure 7.62 pertains the modal analysis of the air vibrating inside a cubic cavity of side π. In this figure results are limited to the first 27 eigenvalues, obtained using three different approaches: (1) a Hermite 5th order 8−node with $N = 1$; (2) a Hermite 3rd order 8−node with $N = 2$ and (3) an Ansys FLUID 30 element with $N = 5$. For this schemes we have the same quantity of unknowns (to be specific, 216). In fact, one has $N_{DOF} = (3N + 3)^3$ for the fifth order; $N_{DOF} = (2N + 2)^3$ for the third order and $N_{DOF} = (N + 1)^3$ for Ansys Fluid 30, since it uses a single nodal unknown (*i.e.*, the potential velocity) when the 'structure absent' option is active (as in the present case). Results show generally a better accuracy for the Hermite elements, especially for the higher eigenvalues.

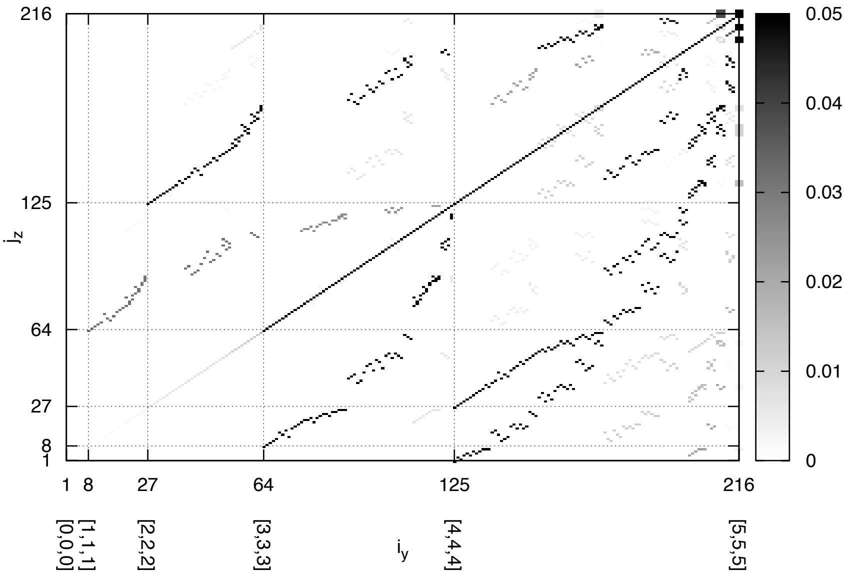

Figure 7.54: Rectangular cavity: eigenfunctions with the Hermite 5th order 8–node ($N = 1$)

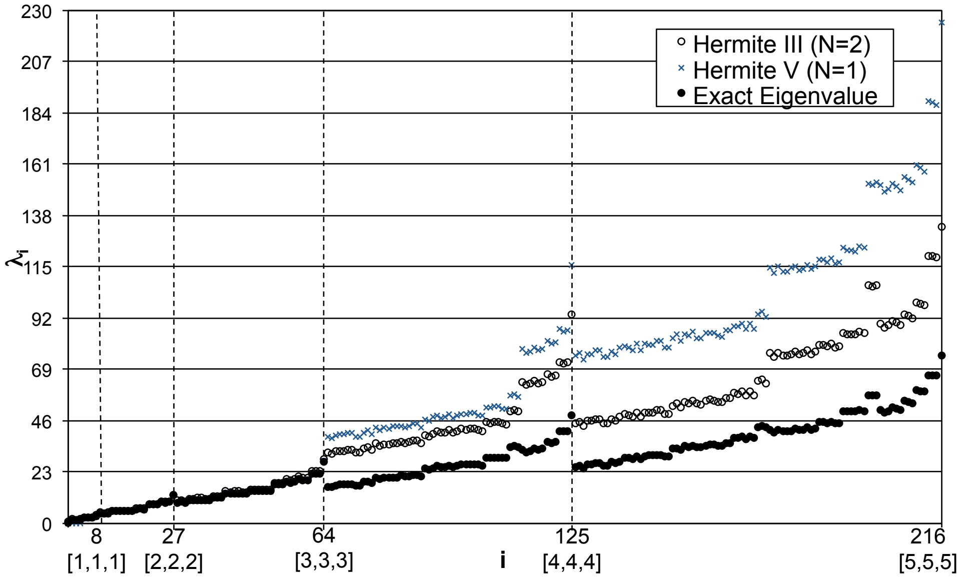

Figure 7.55: Rectangular cavity: eigenvalues with the Hermite 5th order ($N = 1$) and the Hermite 3rd order ($N = 2$)

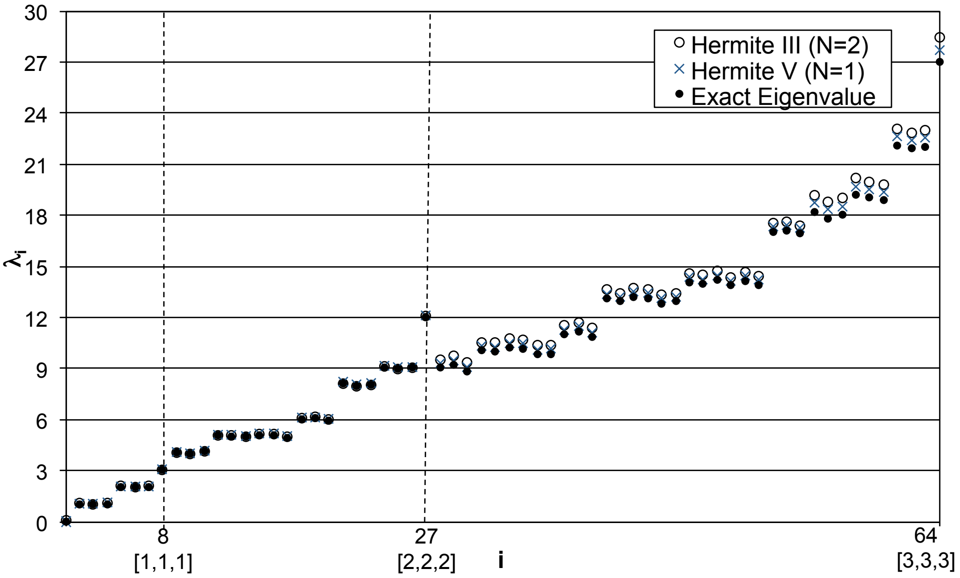

Figure 7.56: Zoom of Fig. 7.55

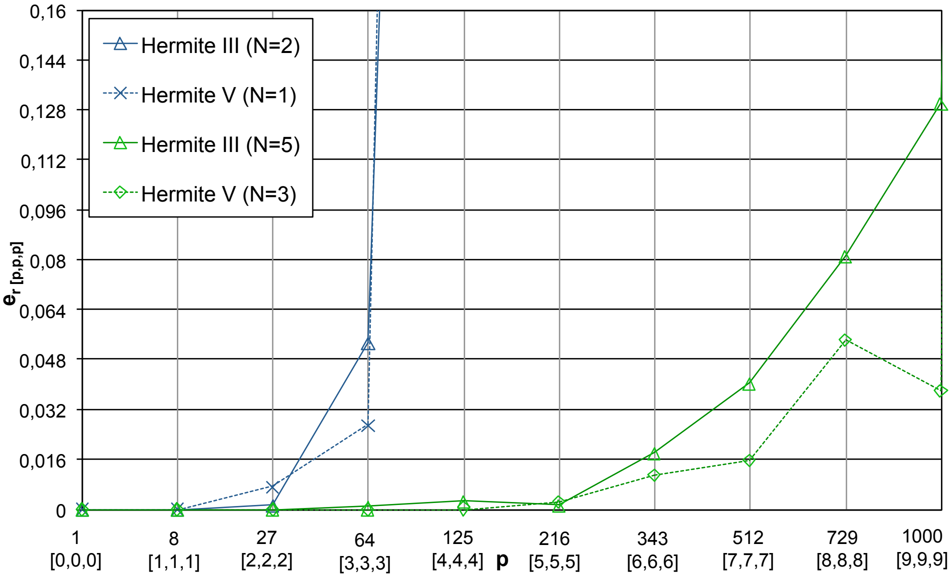

Figure 7.57: Rectangular cavity: Hermite 5th order $(N = 1, 3)$ vs Hermite 3rd order $(N = 2, 5)$

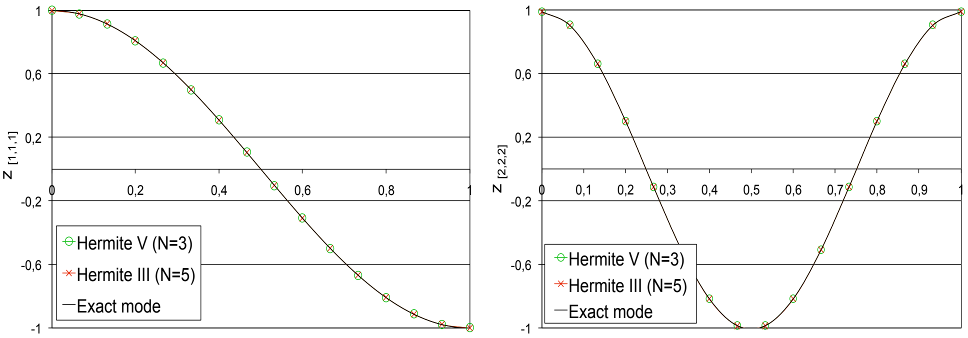

Figure 7.58: Rectangular cavity: modes $[1,1,1]$ and $[2,2,2]$ with Hermite 5th order $(N=3)$ and Hermite 3rd order $(N=5)$

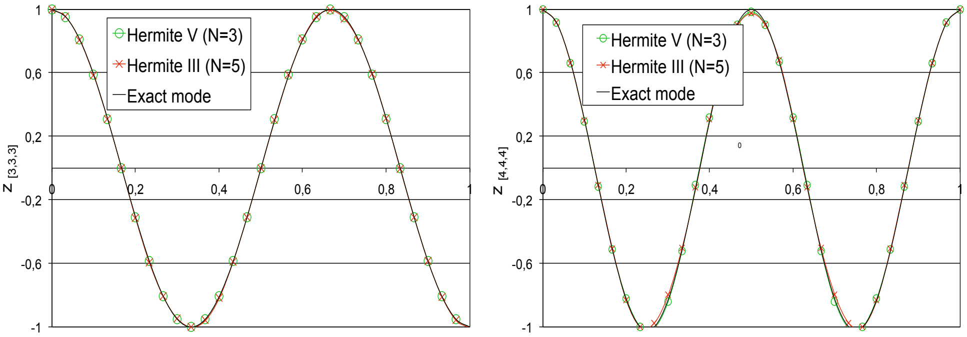

Figure 7.59: Rectangular cavity: modes $[3,3,3]$ and $[4,4,4]$ with Hermite 5th order $(N=3)$ and Hermite 3rd order $(N=5)$

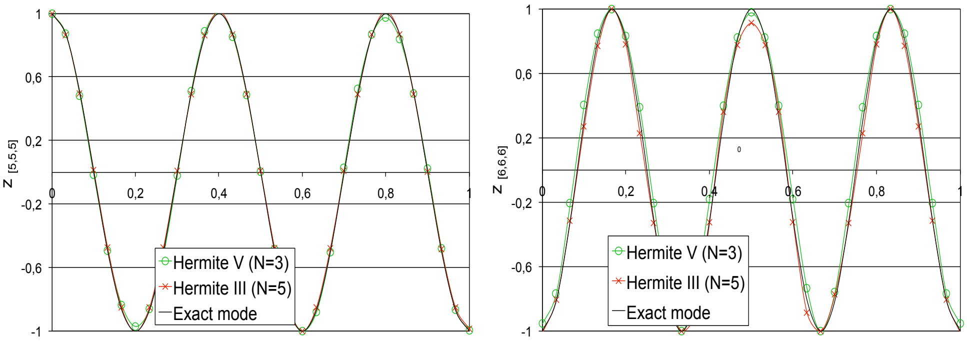

Figure 7.60: Rectangular cavity: modes $[5,5,5]$ and $[6,6,6]$ with Hermite 5th order $(N=3)$ and Hermite 3rd order $(N=5)$

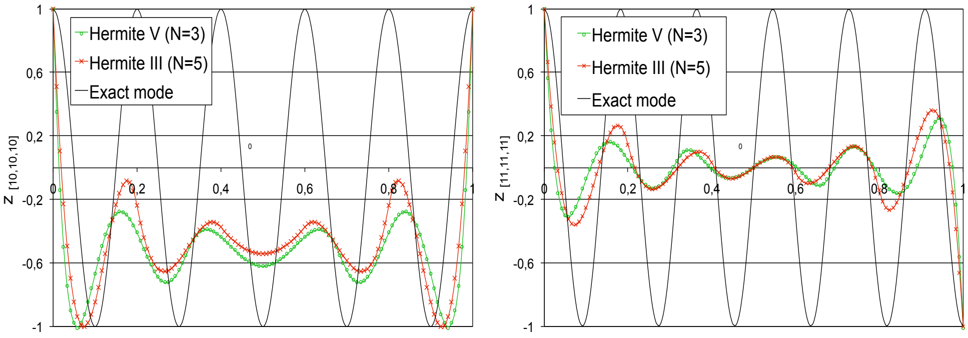

Figure 7.61: Rectangular cavity: modes $[10, 10, 10]$ and $[11, 11, 11]$ with Hermite 5th order ($N = 3$) and Hermite 3rd order ($N = 5$)

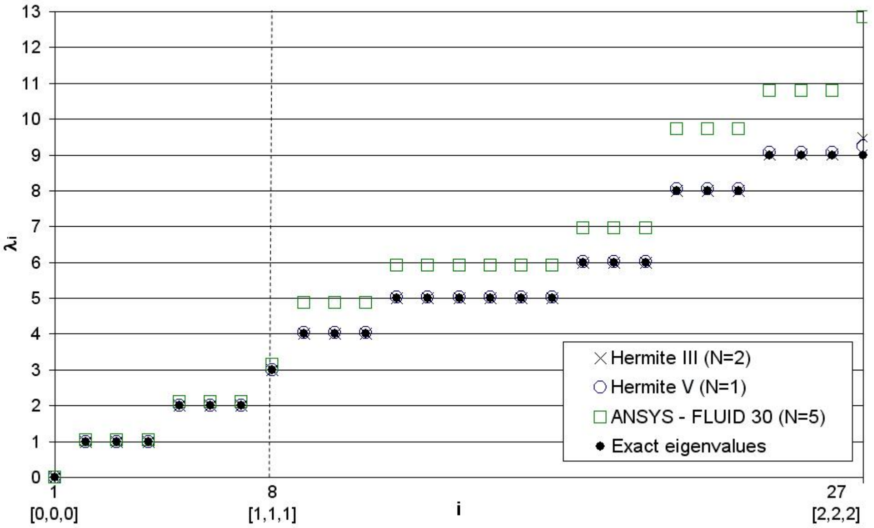

Figure 7.62: Cubic cavity: 5th and 3rd order Hermite elements vs Ansys

7.3.5 Hermite 7th order $8-$node element

The Hermite 7th order 8−node brick has been introduced in Subsection 3.2.2. This element has been preliminarily presented at the 13th AIAA/CEAS Aeroacoustics Conference[16] with an analysis related to a very small subset of low–frequency eigenvalues. In this subsection the analysis has been extended also to eigenfunctions and regards low–frequency modes as well as relatively high–frequency modes.

The following figures pertains the air vibrating inside a parallelepiped cavity of sides π, 1.01π and 0.99π.

Figure 7.63 regards the modes analysis using a subdivision of $N = 1$. Specifically, the figure depicts the value of $\delta_{ij} - \mathsf{y}_i^T \mathsf{M} \mathsf{z}_j$ through a gray–scale mapping. The numerical problem has 512 degrees of freedom (*i.e.*, 64 unknowns per node for each of the 8 nodes) and therefore the whole set of modes (and corresponding eigenvalues) are related to a total number of waves $N_w \leq 7$. However, the figure is related to the first 125 eigenfunctions (*i.e.*, to $n_w \leq 4$), since this subset contains itself all the accurate modes.[4]

Similarly, Fig. 7.64 concerns the first 125 eigenvalues, sorted per number of waves, according to the ordination of the modes presented in Fig. 7.63. Results obtained in Subsection 7.3.3 for $N = 3$ are repeated here for comparison, since the two analysis (order 3 and order 7) pertain the same number of degrees of freedom (in fact, here we have $N_{DOF} = (4N + 4)^3$ with $N = 1$ whereas for the third–order case we have $N_{DOF} = (2N + 2)^3$ with $N = 3$).

As a rule of thumb, one can assume that, say $N_{DOF} = (4N+4)^3$ the total number of unknowns, the quantity of modes acceptably captured is (according to the results of Subsection 7.3.3) $N_0 = [2(N + 1)]^3$. As a consequence, again $N_0/N_{DOF} = 1/8$ of the total modes extracted denotes a good accuracy.

The following figures pertains the air vibrating inside a cubic cavity of sides π.

Figure 7.65 regards a comparison between the three Hermite elements described in this section (*i.e.*, those related to orders 3, 5 and 7), for subdivisions of the domain chosen so as to have the same number of DOFs. It

---

[4] In Subsection 7.3.3 an analysis for the Hermite 3rd order 8 nodes brick having the same DOFs (that for $N = 3$) has been presented: in that case, a set of 125 modes and eigenvalues has been presented. In this range, a subset of 64 modes (that corresponds to $n_w \leq 3$) has denoted good accuracy.

depicts the relative error for the $[k, k, k]$ eigenvalue, for $k \leq 10$. The blue lines concern the Hermite elements in its third order ($N = 3$) and seventh order ($N = 1$) formulation. In each case one has 512 unknowns, that is a total number of waves $N_w = 7$. The subset of modes acceptably captured is related to $n_w \leq 3$. The three green lines are related to the Hermite 3rd order with $N = 5$, as well as to the Hermite 5th order with $N = 3$ and to the Hermite 7th order with $N = 2$. For each of the green line the total number of DOFs is 12^3 whereas the number of eigenvalues acceptably captured is (as expected) related to $n_w \leq 5$. Finally, the two red lines are related to a more refined mesh; specifically, the third order Hermite element is now used with $N = 7$ whereas the seventh order Hermite element is considered with $N = 3$, for a total of 16^3 unknowns and $n_w \leq 7$ waves acceptably captured.

Next, to have a comparison between the present element and those available in commercial softwares, some preliminary set of results (see also the preliminary analysis of[16]) is presented in Fig. 7.66 and pertains the modal analysis of the air vibrating inside a cubic cavity of side π. In this figure results are limited to the first 64 eigenvalues, as obtained with three different approaches: (1) a Hermite 7th order 8−node element with $N = 1$; (2) a Hermite 3rd order 8−node element with $N = 3$ and (3) an Ansys FLUID 30 element with $N = 7$. For these schemes we have the same quantity of unknowns (to be specific, 512). In fact, one has $N_{DOF} = (4N + 4)^3$ for the seventh order Hermite element; $N_{DOF} = (2N + 2)^3$ for the third order Hermite element and $N_{DOF} = (N + 1)^3$ for the Ansys Fluid 30 element (see Subsection 7.3.4). It appears that the Hermite elements show generally a better accuracy than the Ansys one, especially for the higher–frequency eigenvalues.

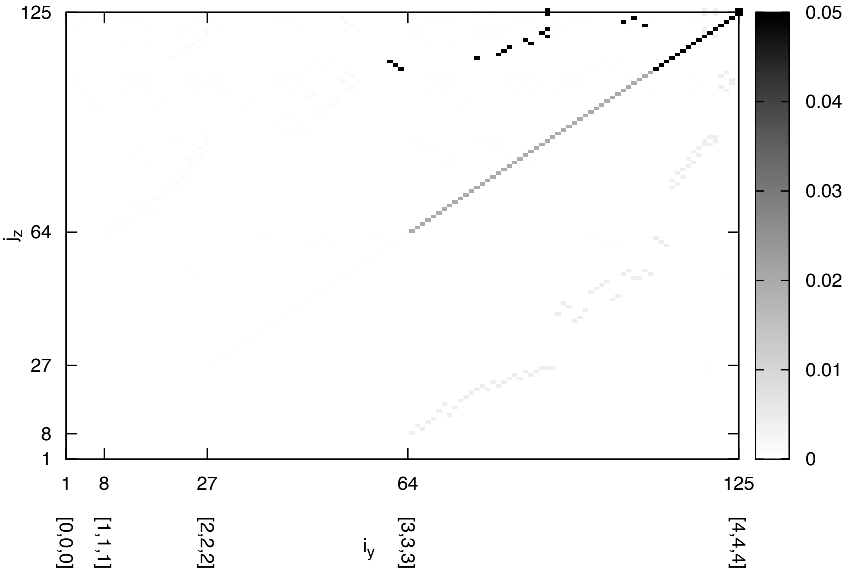

Figure 7.63: Rectangular cavity: eigenfunctions with the Hermite 7th order $(N = 1)$

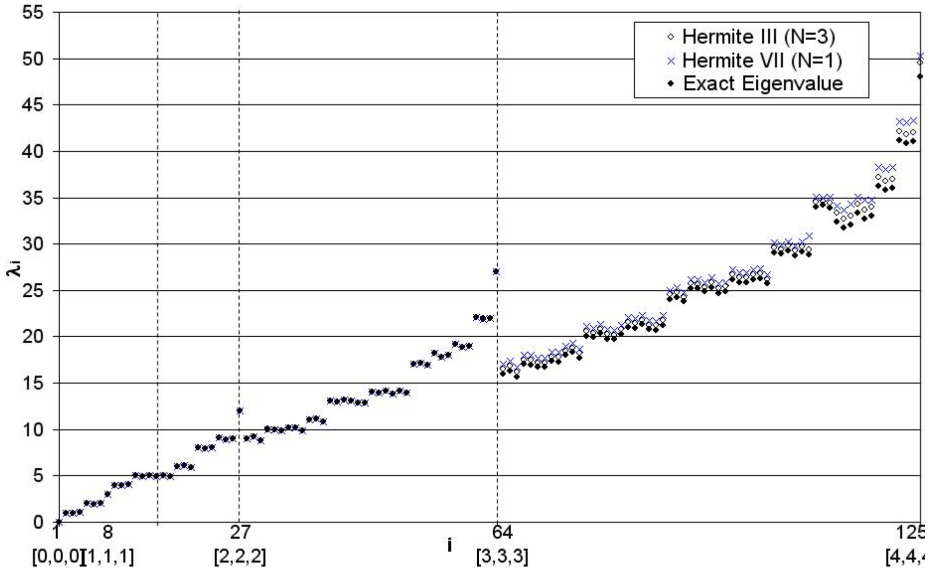

Figure 7.64: Rectangular cavity: eigenvalues with the Hermite 7th order $(N = 1)$ and Hermite 3rd order $(N = 3)$

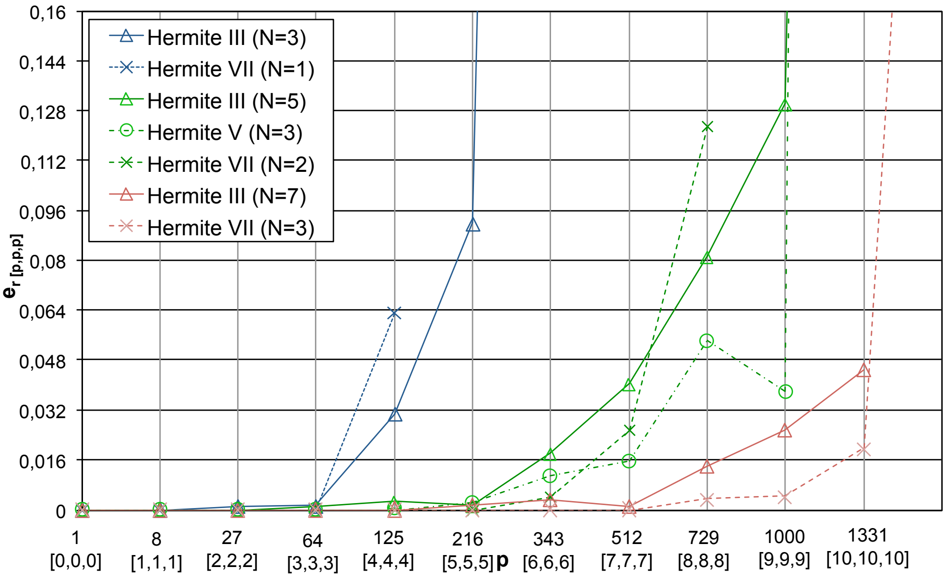

Figure 7.65: Cubic cavity: Hermite elements of orders 3, 5 and 7

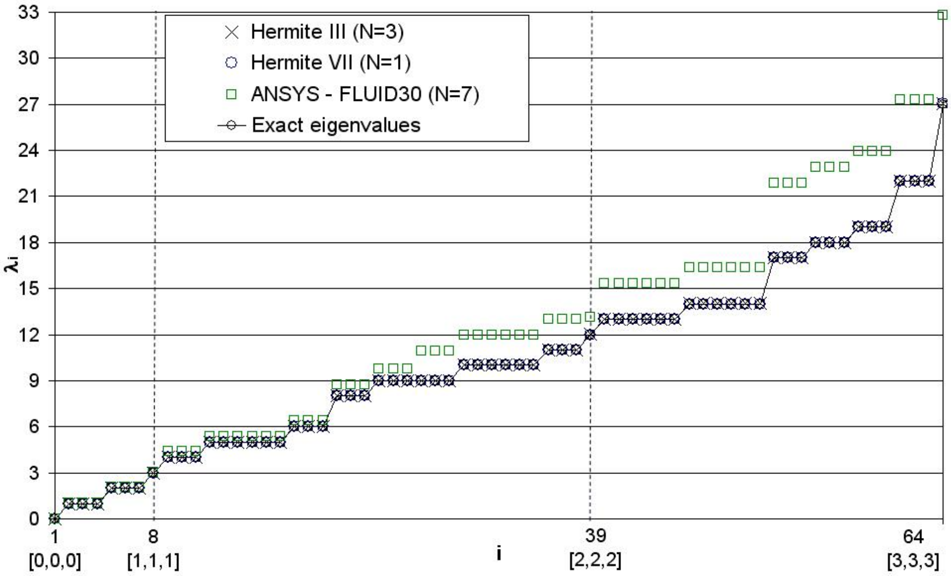

Figure 7.66: Cubic cavity: 7th and 3rd order Hermite elements vs Ansys

7.3.6 Hybrid 3rd order $8-$node element

The Hybrid 3rd order 8−node brick has been introduced in Section 4.4. A preliminary validation of this element has been presented in occasion of the 47th AIAA/ASME/ASCE/AHS/ASC Structures, Structural Dynamics & Materials Conference.[7] In that occasion, the assessment was limited to simple structural applications and to a restricted number of eigenvalues. Here, the analysis is extended to interior acoustics and the assessment is related to eigenvalues as well as to eigenfunctions, with extension to relatively high–frequency modes.

Figures from 7.67 to 7.72 concern an analysis of the modes and eigenvalues, as obtained with a subdivision of $N = 1, 2, 3$ elements per direction. In particular, Figs. 7.67 and 7.68 depict the results for $N = 1$. In this case a total of 32 modes and eigenvalues are obtained (in fact, one has 4 unknowns for each of the 8 nodes of the brick element). According to the order of the element and to the results obtained for the 3rd order Hermite brick in Subsection 7.3.3, a maximum of $n_w = 1$ number of waves per direction is expected to be accurate. This is confirmed in the figures, for modes as well as for eigenvalues. Similar considerations hold for the other four figures, related in couples to $N = 2$ and $N = 3$. In general, as expected, the same amount of modes and eigenvalues that are accurate using a Hermite 3rd order brick (those related to a number of waves $n_w \leq N$), is also very accurate using a Hybrid 3rd order element.

One of the main advantages above the Hermite formulation is that, in this case, only half unknowns are needed, reducing of 50% the size of the problem without reducing accuracy. Therefore, as a rule of thumb, one can say that a quantity of modes and eigenvalues equal to 1/4 of the total DOFs is acceptably captured.

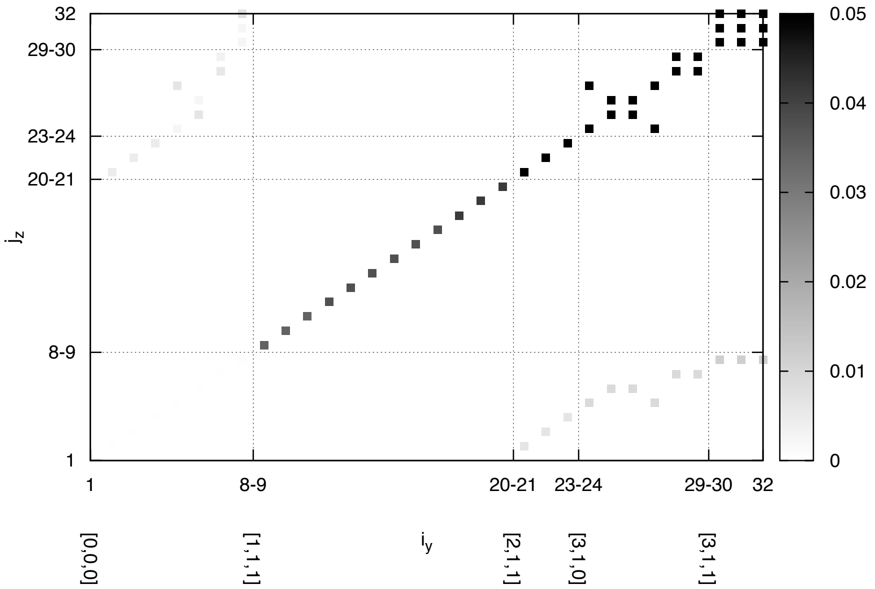

Figure 7.67: Rectangular cavity: eigenfunctions with the Hybrid 3rd order $8-$node element $(N = 1)$

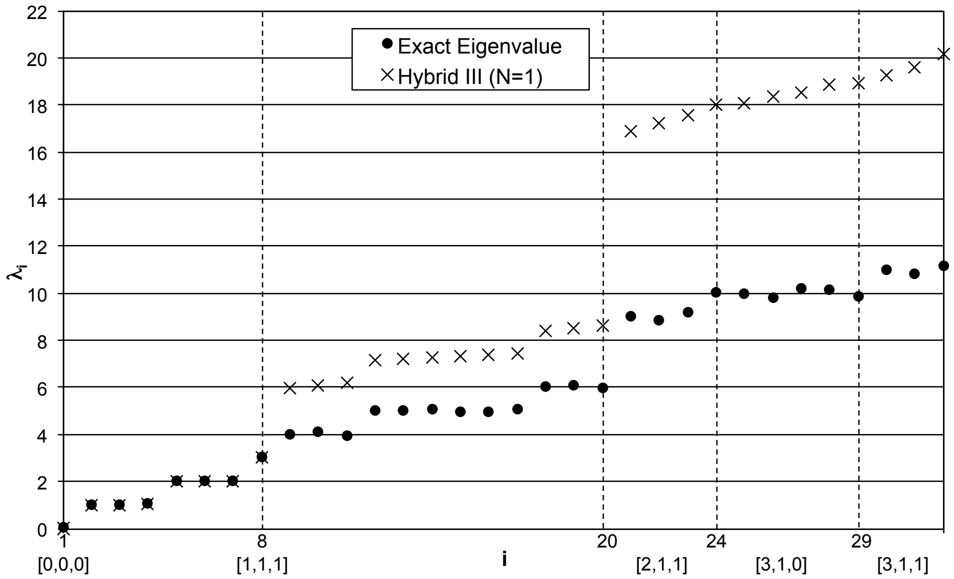

Figure 7.68: Rectangular cavity: eigenvalues with the Hybrid 3rd order $8-$node element $(N = 1)$

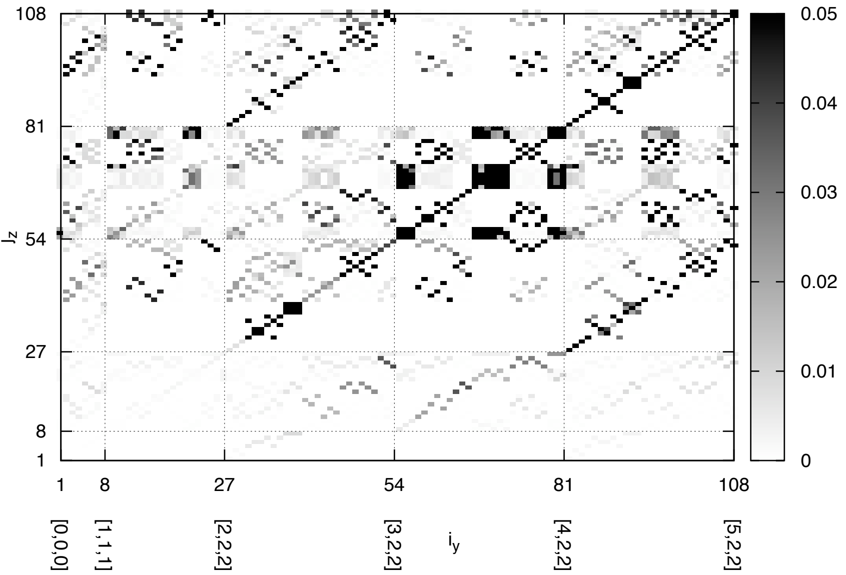

Figure 7.69: Rectangular cavity: eigenfunctions with the Hybrid 3rd order 8–node element ($N = 2$)

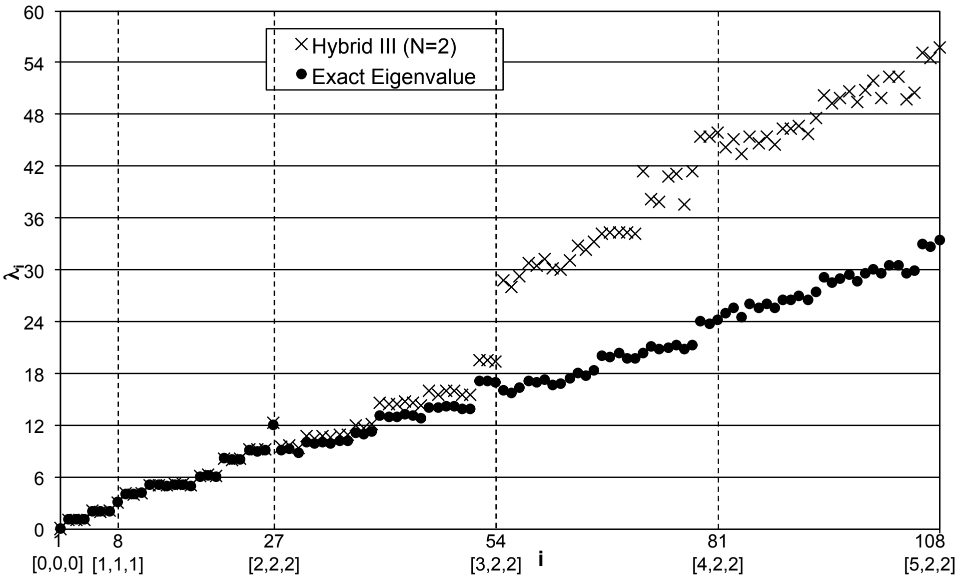

Figure 7.70: Rectangular cavity: eigenvalues with the Hybrid 3rd order 8–node element ($N = 2$)

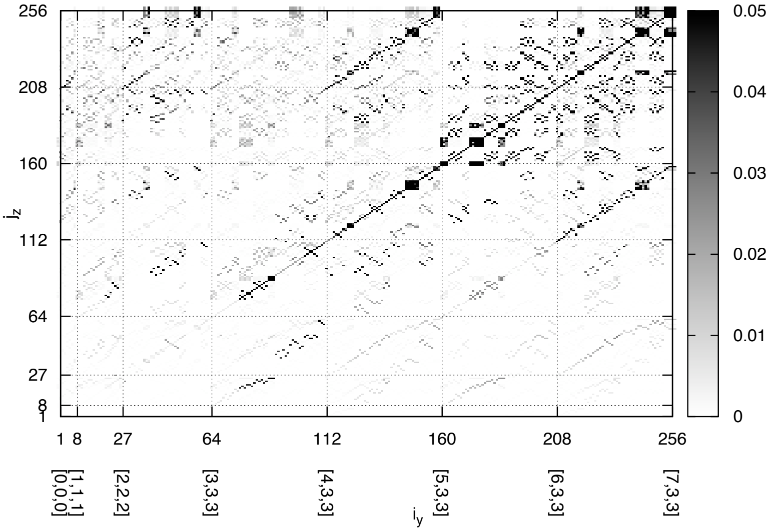

Figure 7.71: Rectangular cavity: eigenfunctions with the Hybrid 3rd order 8−node element ($N = 3$)

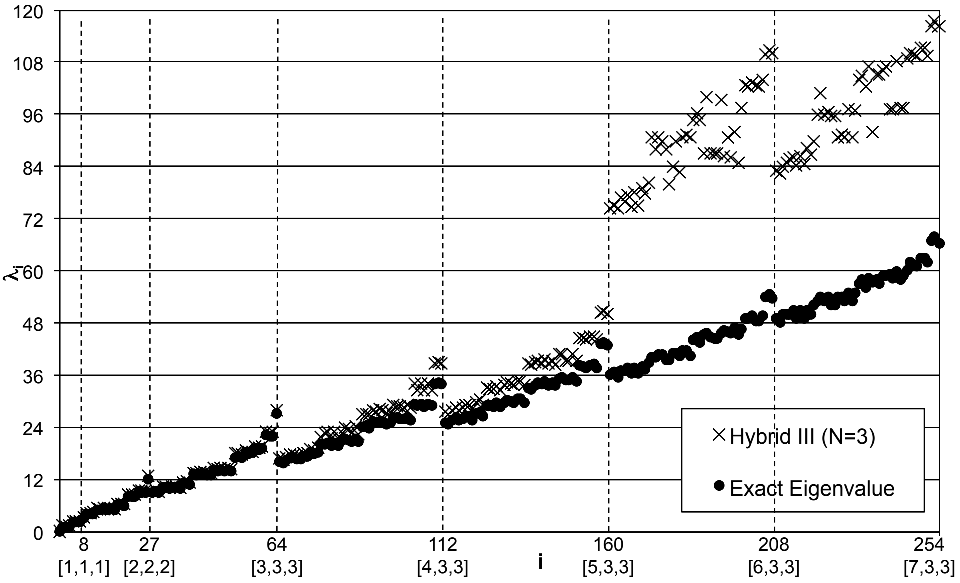

Figure 7.72: Rectangular cavity: eigenvalues with the Hybrid 3rd order 8−node element ($N = 3$)

7.3.7 Hybrid 7th order $8-$node element

This Subsection regards the results obtained for interior acoustics (modal analyses) with the Hybrid 7th order $8-$node element introduced in Subsection 5.1.1. A preliminary analysis concerning this element has been presented at the 13th AIAA/CEAS Aeroacoustics Conference.[16] In that occasion, the analyses were limited to the first eigenvalues of a cubic cavity and to a preliminary assessment for relatively high frequencies. Recent developments pertain the modal analyses of the air vibrating inside a rectangular cavity and the validation regards the eigenvalues as well as the eigenfunctions.

Figure 7.73 regards the mapping of the projections between the numerical modes z_j (for $j = 1, \ldots, N_{DOF}$) and the analytical modes y (also, for $i = 1, \ldots, N_{DOF}$). Specifically, they depict the mapping of $\delta_{ij} - \mathsf{z}_j^T \mathsf{M} \mathsf{y}_i$, using a mesh of $N = 1$ (therefore, a total of 256 unknowns are included, since one has 32 nodal unknowns for each of the 8 nodes).

Figures 7.74 and its zoom presented in Fig. 7.75 pertain the whole set of eigenvalues, sorted per number of waves, according to the ordination used for Fig. 7.73.

Figure 7.75 focuses only on the eigenvalues expected to be accurate. The results have been compared with those obtained for the Hybrid 3rd order $8-$node element with $N = 3$, since this presents the same number of DOFs (in fact, one has $N_{DOF} = 4(2N+2)^3$ for the 7th order whereas $N_{DOF} = 4(N+1)^3$ for the 3rd order).

The following analysis pertains the air vibrating inside a cubic cavity of sides π.

Results obtained with a different mesh sizes ($N = 1, 2$) are shown in Figs. 7.76 and 7.77 which are preliminary result presented in 2007 and which pertain the modal analysis of the air vibrating inside a cubic cavity of side π. In these figures results are limited to the first 39 eigenvalues (that correspond to a number of waves $n_w \leq 2$), obtained using three different approaches: (1) a Hybrid 7th order $8-$node element; (2) a Hybrid 3rd order $8-$node element and (3) an Ansys FLUID 30 element with $N = 9$.

The figure on the top is obtained with a mesh of $N = 1$ whereas the figure on the bottom is obtained using a mesh of $N = 2$. For both the Hybrid schemes we have the same quantity of unknowns (to be specific, 256 and 864 respectively). In fact, one has $N_{DOF} = 4(2N + 2)^3$ for the 7th order and $N_{DOF} = 4(N+1)^3$ for the 3rd order. For the Ansys element a subdivision in $N = 6, 9$ elements has been used respectively. These meshes produce $N_{DOF} = (N+1)^3 = 343, 1000$ unknowns (see Subsection 7.3.4).

According to Fig. 7.77, the Hybrid elements show a better accuracy, especially for the higher eigenvalues, even though the unknowns used with Ansys are around 15% more.

Moreover, it appears that the higher order shows a better accuracy for the finer mesh. In fact, the relative error for the last eigenvalue (*i.e.*, $(\lambda_{39_A} - \lambda_{39_N})/\lambda_{39_A} = (12 - \lambda_{39_N})/12)$ is $3 \cdot 10^{-7}$ for the Hybrid 7th order whereas $4 \cdot 10^{-3}$ for the Hybrid 3rd order.

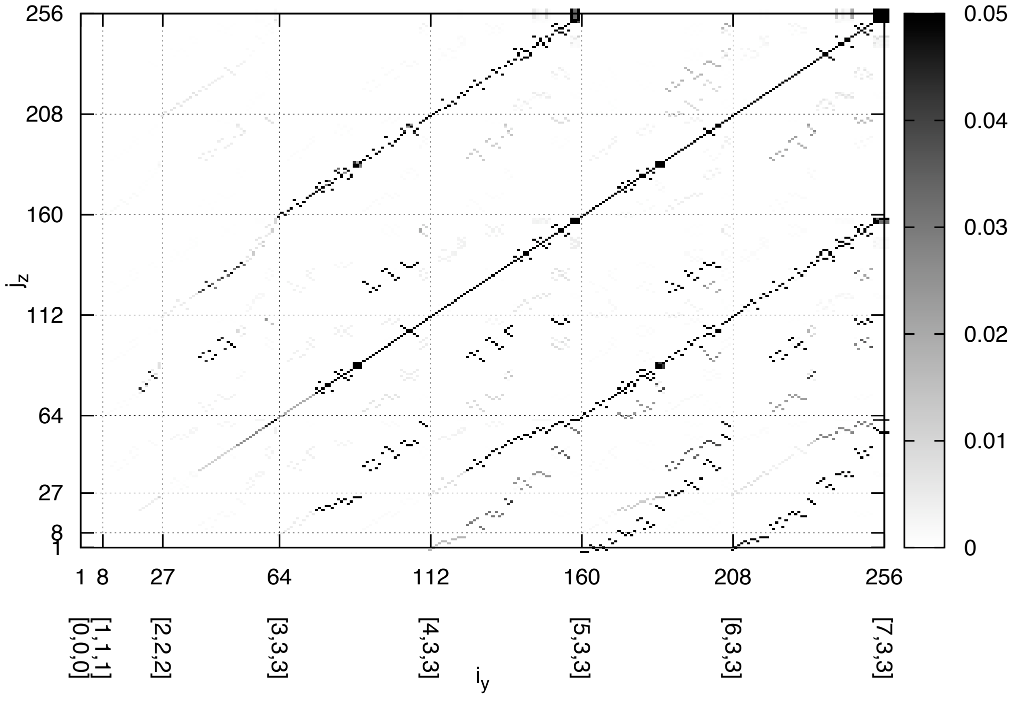

Figure 7.73: Rectangular cavity: eigenfunctions with the Hybrid 7th order 8−node ($N = 1$)

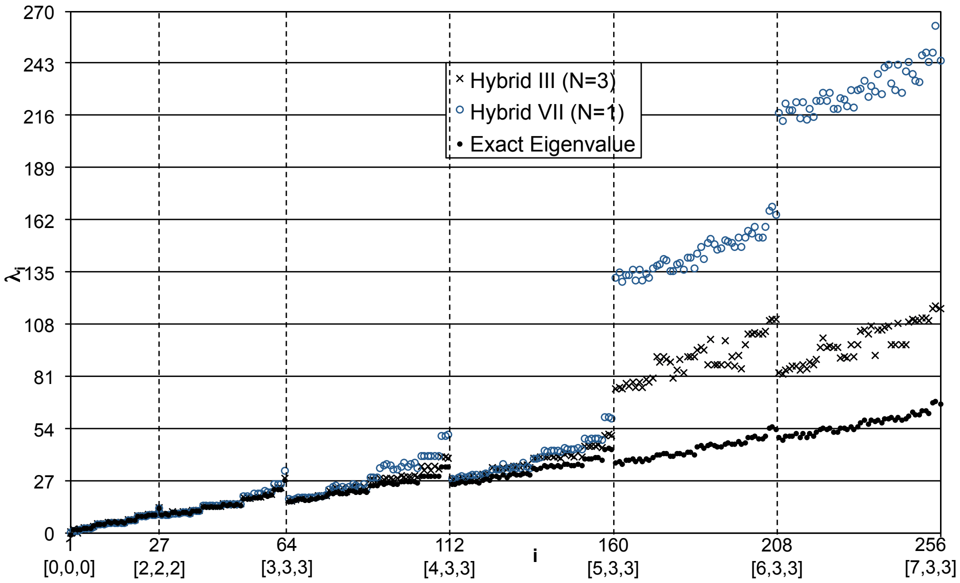

Figure 7.74: Rectangular cavity: eigenvalues with the Hybrid 7th order $8-$node $(N = 1)$

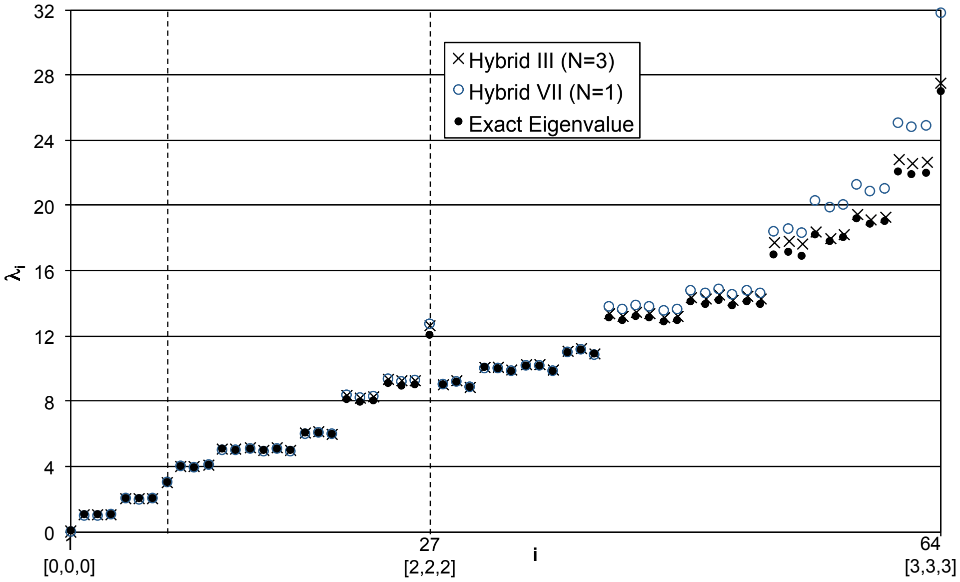

Figure 7.75: Zoom of Fig. 7.74

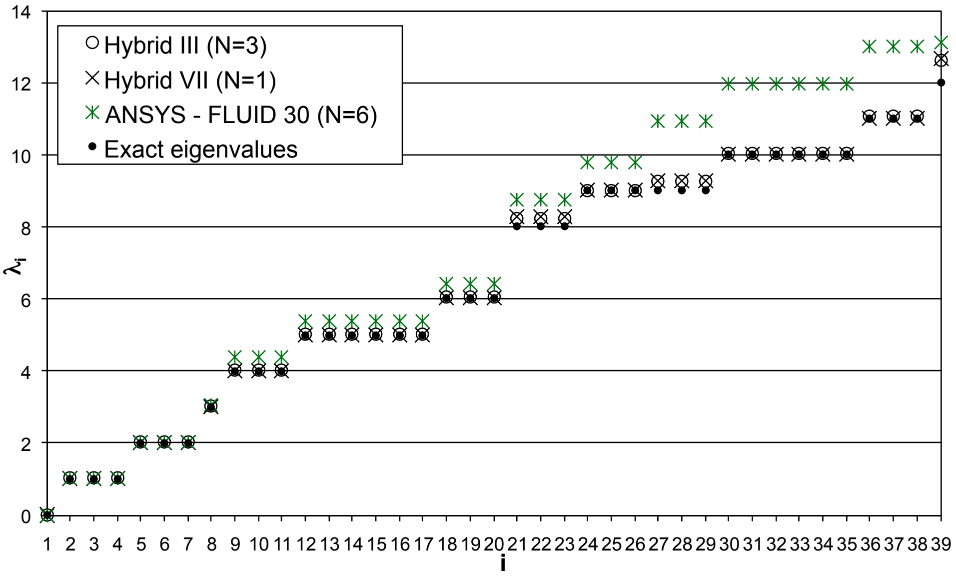

Figure 7.76: Cubic cavity: Hybrid 7th order ($N = 1$) *vs* Hybrid 3rd order ($N = 3$)

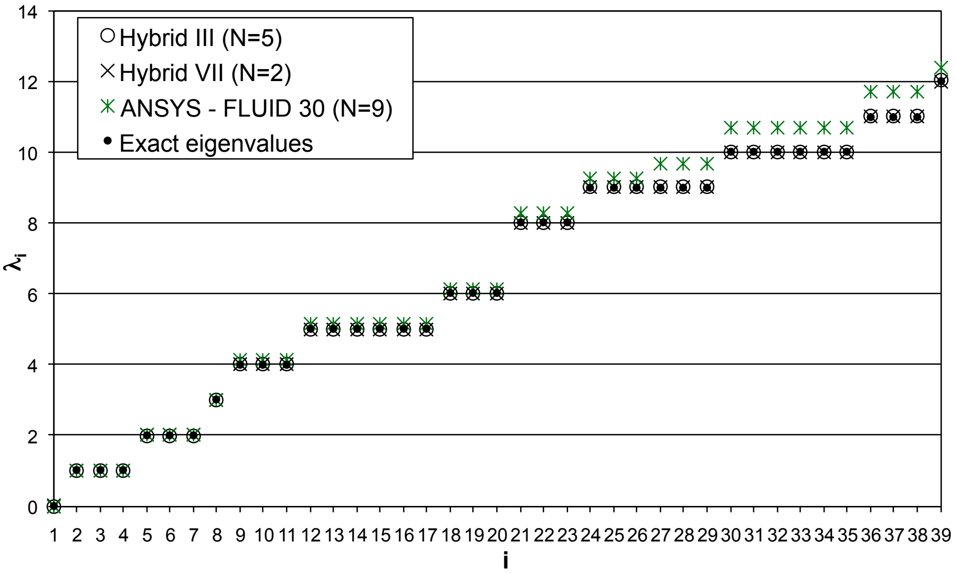

Figure 7.77: Cubic cavity: Hybrid 7th order ($N = 2$) *vs* Hybrid 3rd order ($N = 5$)

7.3.8 Hybrid 5th order $27-$node element

This Subsection regards the Hybrid 5th order 27–node element, that has been introduced in Subsection 5.4.1. A validation of this element has been presented recently, at the 15th AIAA/CEAS Aeroacoustics Conference.[17] Results have been obtained for a rectangular cavity and are here analyzed thoroughly.

Figures from 7.78 to 7.80 concern the analysis of modes and eigenvalues obtained by subdividing the parallelepiped domain in $N = 1$ element per direction. In this case one has a total of 108 modes and eigenvalues, since the element uses 4 unknowns for each of the 27 nodes. The maximum number of waves is $n_w = 5$ for one direction, when it is $n_w \leq 2$ in the other two directions. Results appear extremely good for the first 27 modes and eigenvalues (that correspond to 1/4 of the total modes and eigenvalues extracted and to $n_w \leq 2$).

One can compare the above results with thee Hybrid 3rd order $8-$nodes (see Subsection 7.3.6) with $N = 2$ elements: in fact, one has again $N_{DOF} = 108$, since the element uses 4 nodal unknowns for each of the 27 nodes deriving from the mesh. Such a comparison is shown in Figs. 7.79 and 7.80, were the results obtained in Subsection 7.3.6 for $N = 2$ are repeated.

Again, an advantage above the Hermite scheme of same order (compare the results of Subsection 7.3.4) is that a 50% of unknowns are needed, even though the same quantity of modes and eigenvalues appears to be accurate. Similarly to the results obtained in Subsection 7.3.6 for the Hybrid 3rd order $8-$node element, as a rule of thumb one can say that a quantity of modes and eigenvalues equal to 1/4 of the total DOFs is acceptably captured.

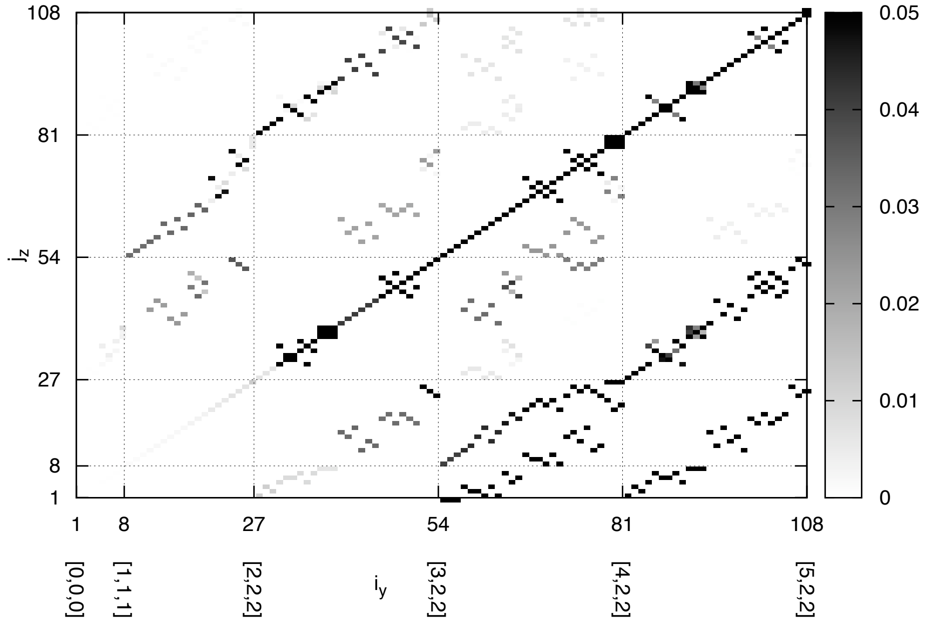

Figure 7.78: Rectangular cavity: eigenfunctions with the Hybrid 5th order $27-$node ($N=1$)

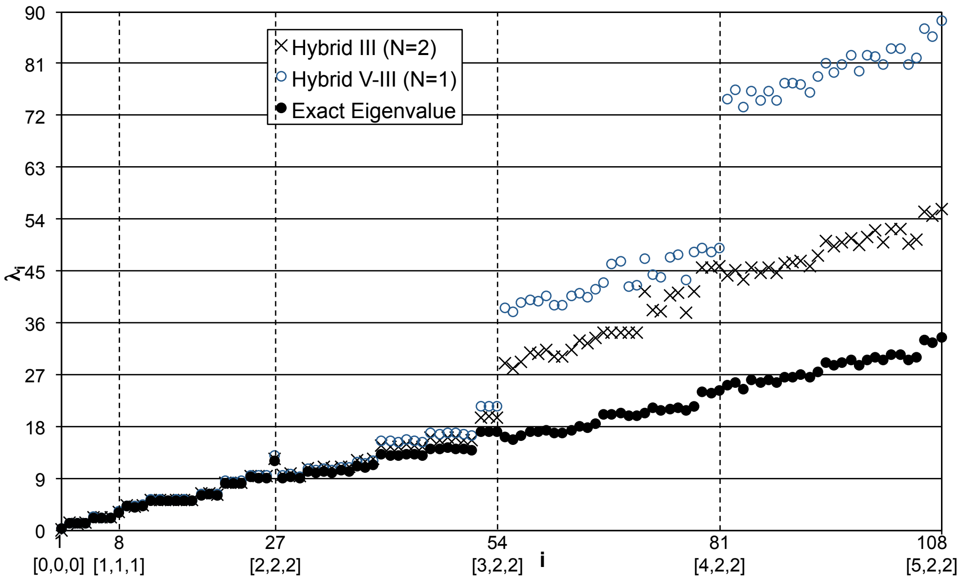

Figure 7.79: Rectangular cavity: eigenvalues with the Hybrid 5th order $27-$node ($N=1$) and Hybrid 3rd order $8-$node ($N=2$)

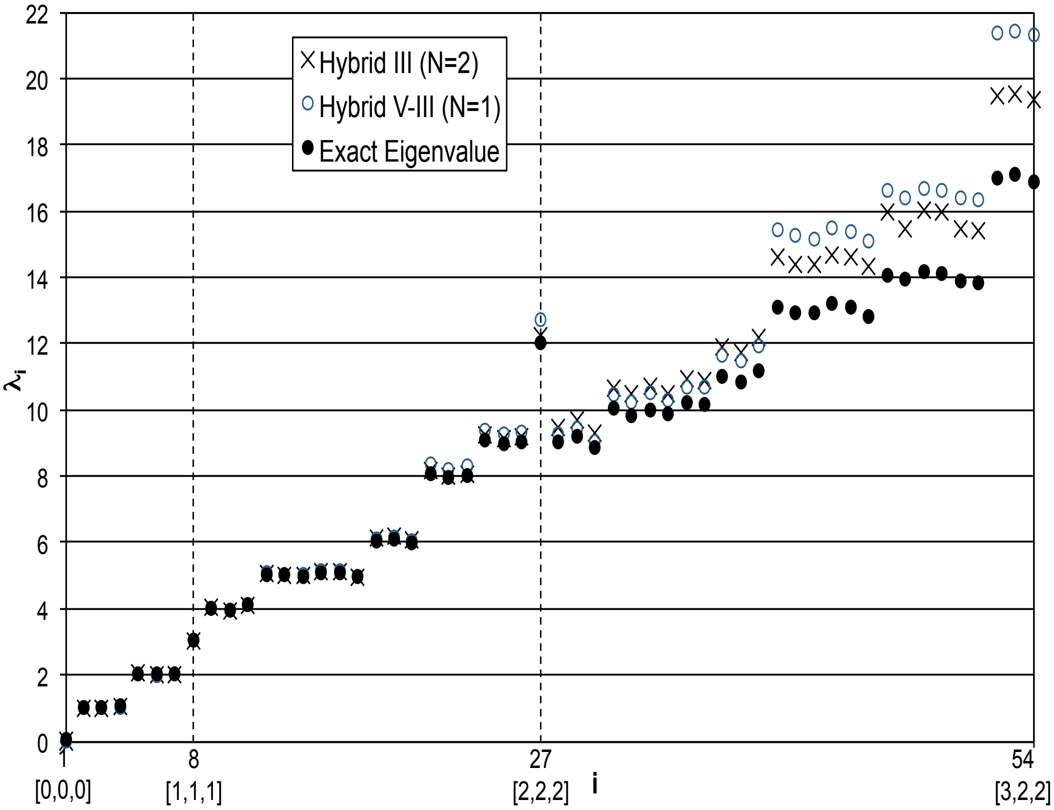

Figure 7.80: Zoom of Fig. 7.79

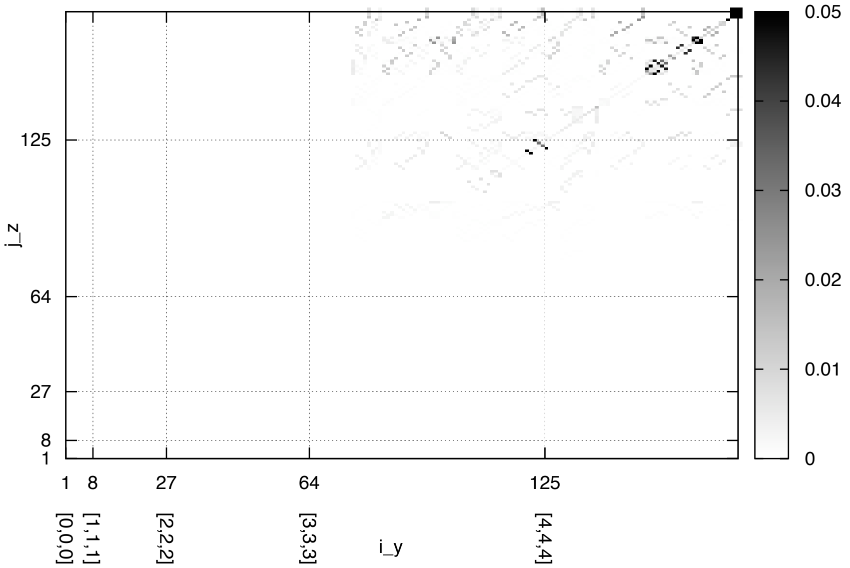

Figure 7.81: Rectangular cavity: eigenfunctions with the Hybrid 5th order $27-$node $(N=2)$

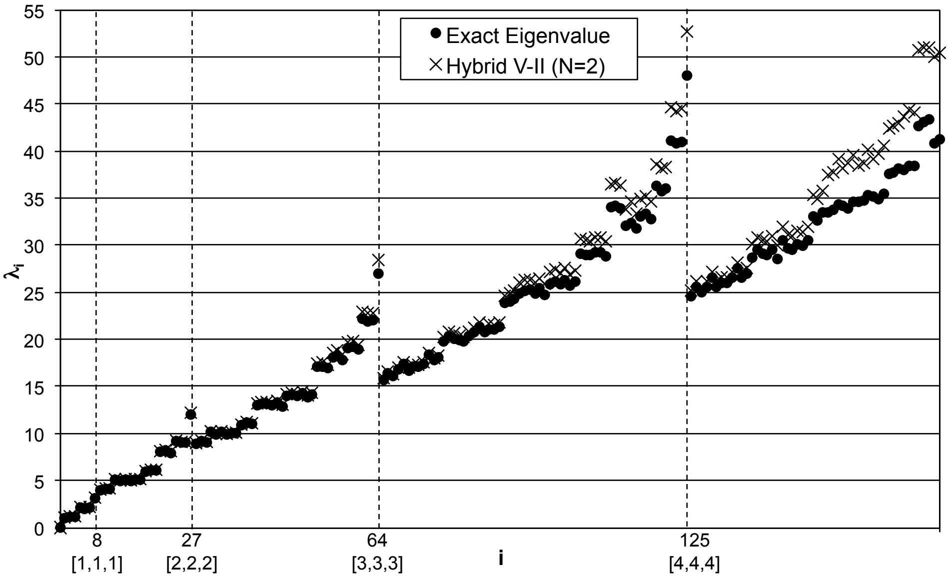

Figure 7.82: Rectangular cavity: eigenvalues with the Hybrid 5th order $27-$node $(N=2)$

7.3.9 IRS for interior acoustics

This section regard the reduced formulations, as obtained by using a quasi–static reduction algorithm. In particular, the applicability of the basic Guyan's reduction and of its extension called IRS (see Appendix E for details about the mathematical formulations) is addressed for acoustic problems in full three dimensional domains. Specifically, the application to three–dimensional acoustic problems of the basic Guyan's procedure is discussed, along with the substantial improvement obtained shifting to the IRS technique.

In the next, results are labelled according to the following criterion. *Complete* means that no reduction technique has been applied. To identify a reduced formulation, the level of Guyan's reduction (*i.e.*, the number of nodal unknown to be retained) is declared. Thus, *Guyan1* means that only the function is retained; *Guyan4* means that the function and the first three derivatives are retained, and so on. The same meaning holds for *IRS1*.

The analyses presented here pertain the air vibrating within a cubic cavity of side π.

Figures 7.83 and 7.84 show a preliminary investigation of the Guyan's reduction technique. Specifically, they depict the $h-$convergences for the Hermite 3rd order and 5th order elements, obtained with various Guyan schemes. The $h-$convergences are presented in function of the total degrees of freedom N_{DOF}, since the various formulations consider different amounts of nodal unknowns (in fact, for *Guyan1* one has $N_{DOF} = (N+1)^3$; for *Guyan4* one has $N_{DOF} = 4(N+1)^3$, etc.). The Ansys Fluid 30 element is included in the analyses as a way of comparison. It appears that, even though results became better than Ansys if a refined mesh is used, the application of the Guyan's procedure shows an important penalization with respect to the complete formulation. In comparison with the Ansys Fluid 30 element, results for the Hermite 5th order are worse even when a 40% of the unknowns is eliminated. This problem has been attributed to the non-negligibility of the inertia effects in case of a cubic domain. Thus, the IRS version of Guyan's procedure (see Section E.2 for mathematical details), that takes into account also the first order inertia terms, has been implemented and results have been compared with Guyan's.

Figures from 7.85 to 7.87 show the convergences obtained for the eigenvalues related to the $[1,0,0]$, $[1,1,0]$ and $[1,1,1]$ modes, using both the Guyan's and the IRS techniques, when only the function is retained (this implies that the scheme has only a single degree of freedom per node). Figures express the results in terms of the number of unknowns (one has $N_{DOF} = (N+1)^3$ for each element used). They show that the use of IRS improves the accuracy, giving results much better than Ansys despite a less computational effort (assumed to be directly related to the amount of degrees of freedom).

Finally, Figs. 7.88 and 7.89 show a comparison between the basic Guyan's reduction and the IRS technique. The first is obtained with a $N = 2$ (image on the left) mesh of the geometry whereas the second is related to a $N = 3$ subdivision of the domain.

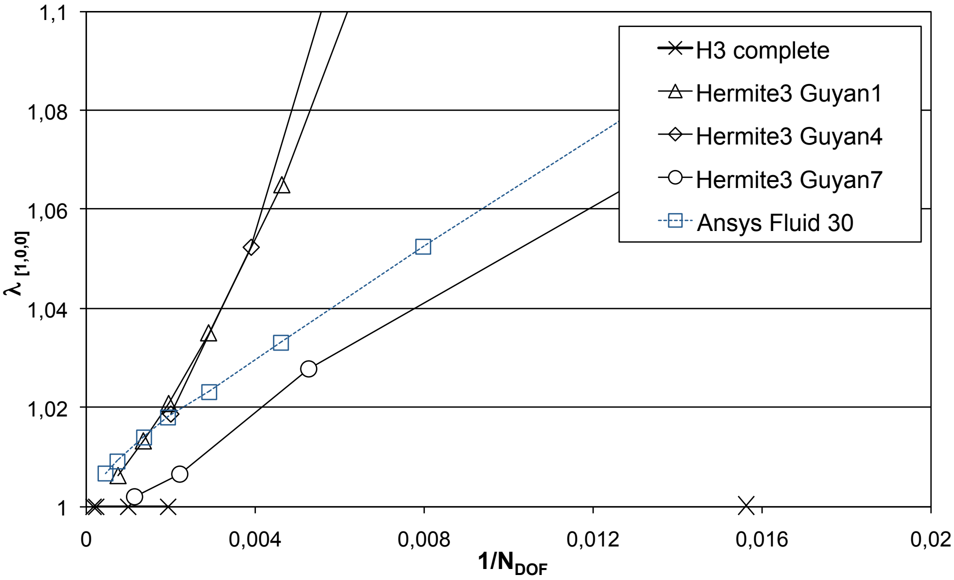

Figure 7.83: Cubic cavity: Hermite 3rd order with Guyan

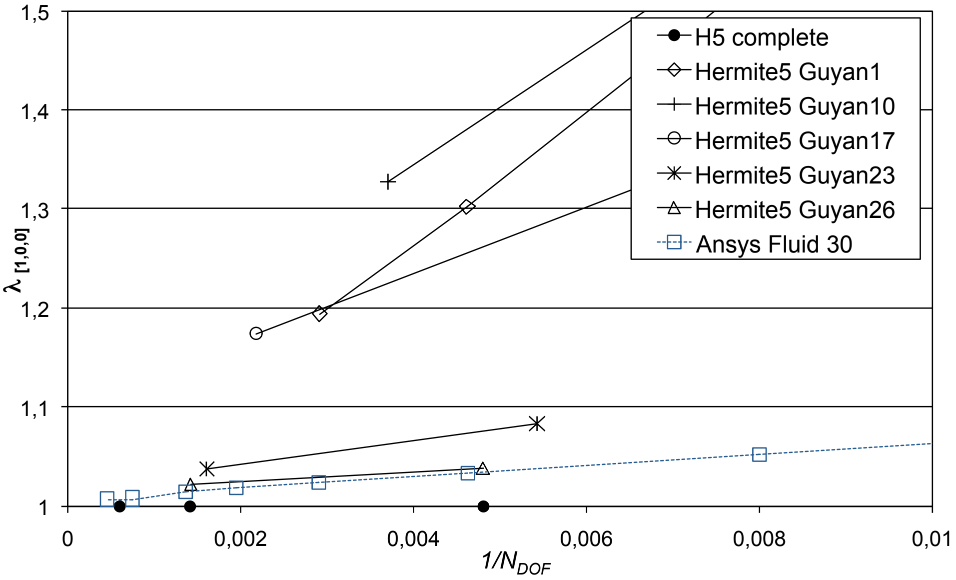

Figure 7.84: Cubic cavity: Hermite 5th order with Guyan

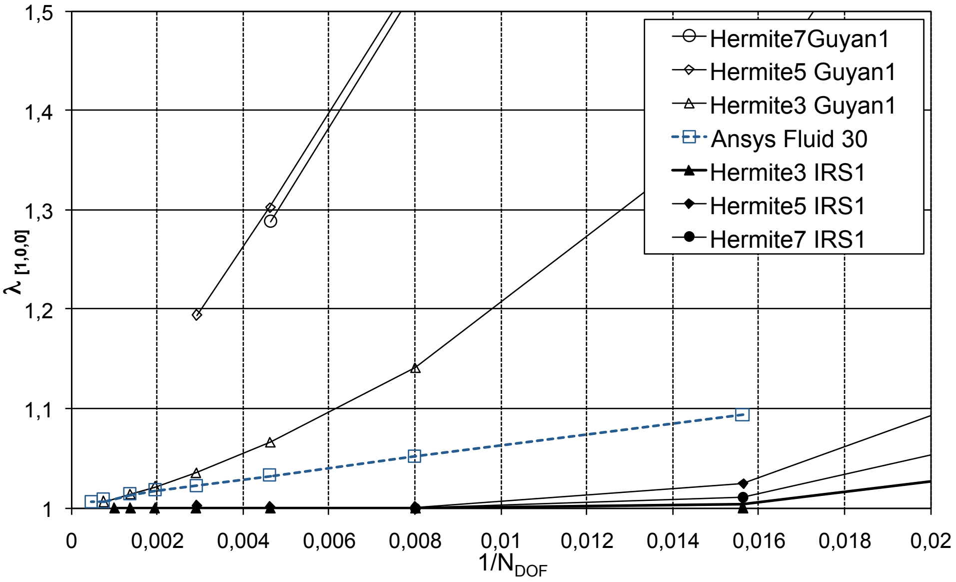

Figure 7.85: Cubic cavity: eigenvalue $[1, 0, 0]$ with Guyan and IRS

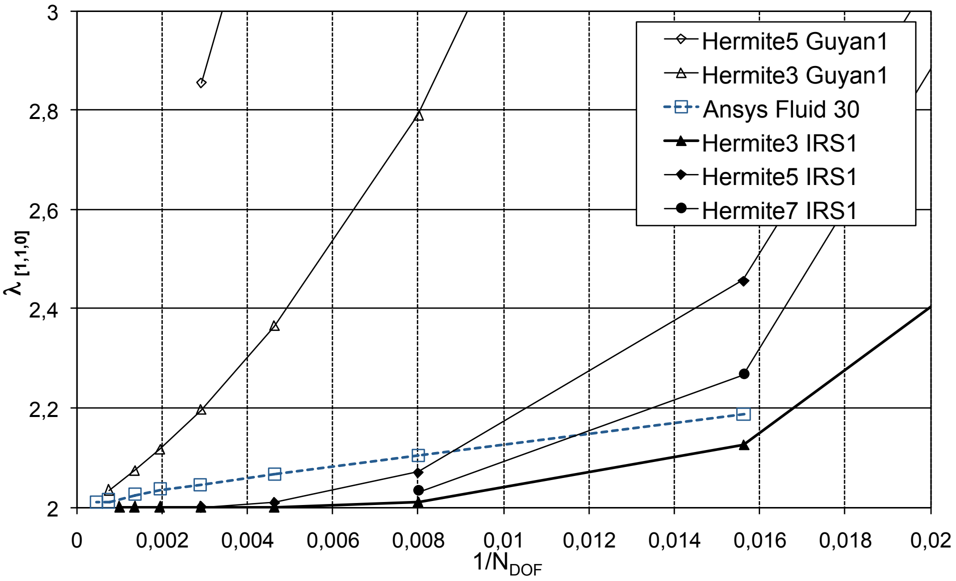

Figure 7.86: Cubic cavity: eigenvalue $[1,1,0]$ with Guyan and IRS

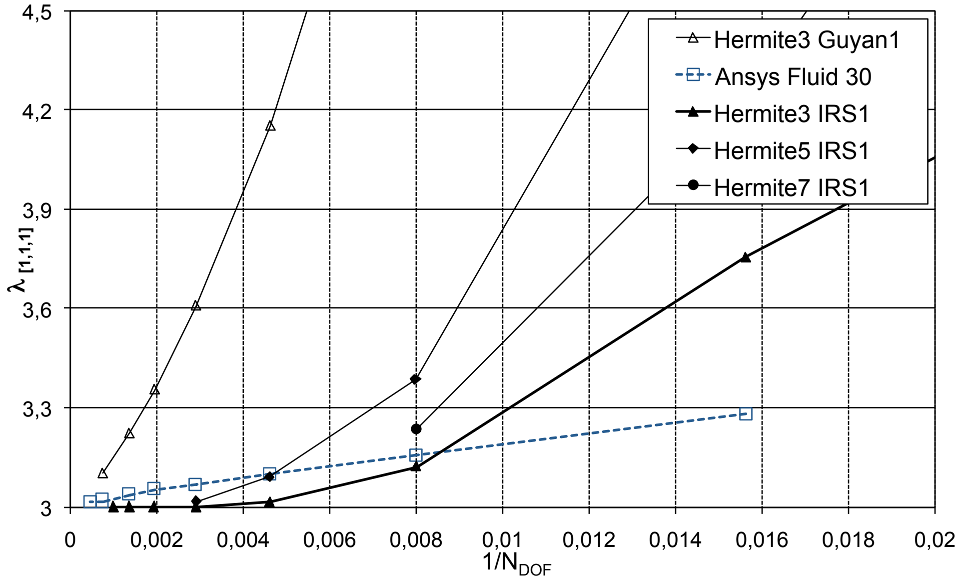

Figure 7.87: Cubic cavity: eigenvalue $[1,1,1]$ with Guyan and IRS

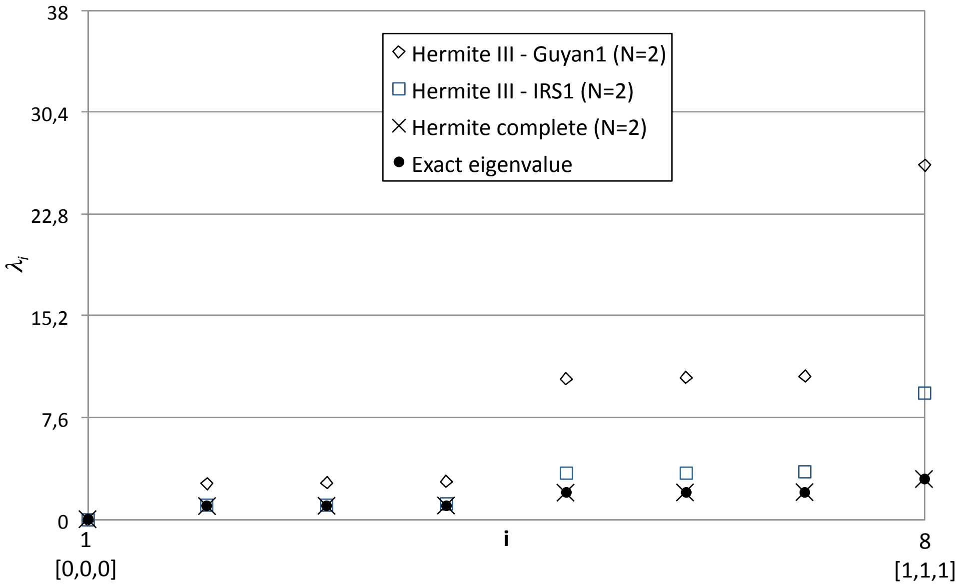

Figure 7.88: Cubic cavity: eigenvalues $1 - 8$ with $N = 2$ (Guyan and IRS)

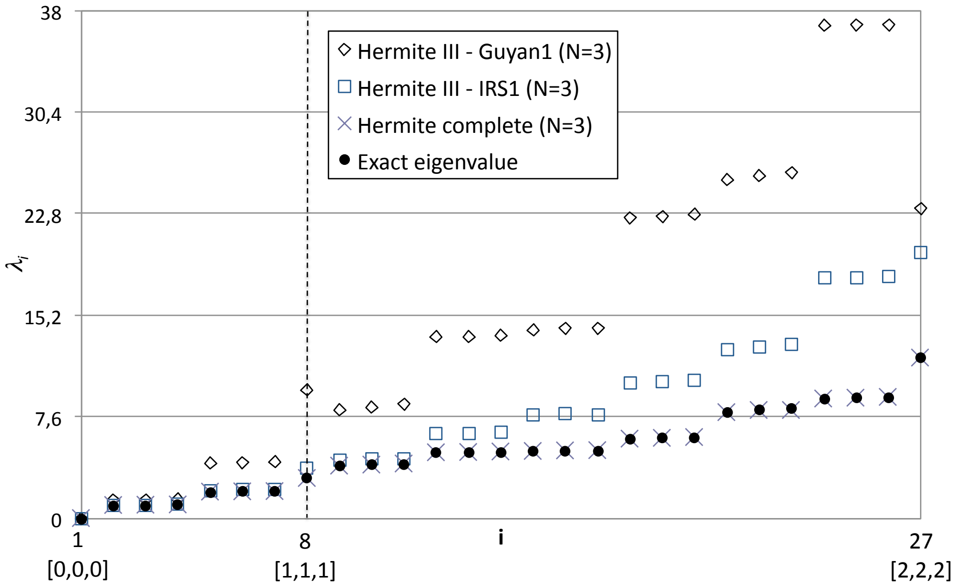

Figure 7.89: Cubic cavity: eigenvalues $1 - 27$ with $N = 3$ (Guyan and IRS)

7.4 Structures

In this section, the results obtained for structural applications are presented (including those obtained with the reduced formulations). For simplicity, for all the test cases, the density ρ and the Young Modulus E are set equal to 1, whereas a Poisson Ratio ν of 0.225 is considered. To have meaningful comparisons, Ansys elements have been used with the 'consistent mass matrix' option for all the results.

In the next, λ_i is used to indicate the $i-$th eigenvalue whereas ω_i is used to indicate the $i-$th natural frequency; accordingly, $\bar{\omega}_i$ is the $i-$th dimensionless frequency.

7.4.1 Guyan for (thin) structures

This subsection is dedicated to a preliminary analysis of the results obtained using a reduction technique in thin structures analysis. Modal analyses for the vibration of a free rectangular cross–section beam of dimensions $\ell = 1$, $h_1 = 0.01$ and $h_2 = 0.015$ are presented. The structure is treated as a three–dimensional object, with a mesh of N elements along the length and 1 element along the other two directions, for a total amount of N subdivisions in the volume itself.

In case of thin structure (beams as well as plates and shells) it is convenient to reduce the number of unknowns up to half the number of nodes: instead of the upper– and lower–side nodal displacements (say, u_u and u_l respectively), one may use their semi–sum and semi–difference, $\mathsf{u}_m = 1/2(\mathsf{u}_u + \mathsf{u}_l)$ and $\mathsf{u}_\Delta = 1/2(\mathsf{u}_u - \mathsf{u}_l)$.

Since u_Δ/τ is related to thickness variations (normal components) and rotations around the mid–surface (in–plane components), the u_Δ variables correspond to high–frequency motions and therefore the Guyan reduction may be applied to remove them and all the derivatives. We refer to this scheme as *Double Guyan* reduction.

Results are compared with those obtained using the Ansys Solid-Shell 190 (optimized for thin–wall structures) and the Ansys Solid 186, that is a twenty-noded element with three degrees of freedom per node (*i.e.*, the three components of the displacement). The results presented regard the first ten eigenvalues.

In the next, results are labelled according to the criterion introduced in

Subsection 7.3.9 or with a 'Double Guyan'.

Figures from 7.90 to 7.99 depict the eigenvalues as a function of the degrees of freedom N_{DOF}, with and without using the Double Guyan reduction procedure.

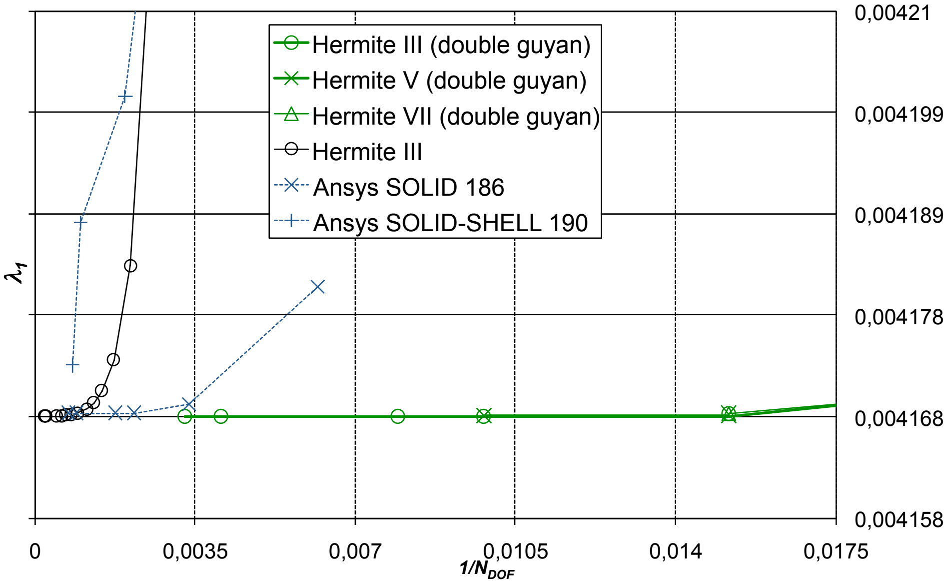

Figure 7.90: Free rectangular cross–section beam: λ_1 with Guyan

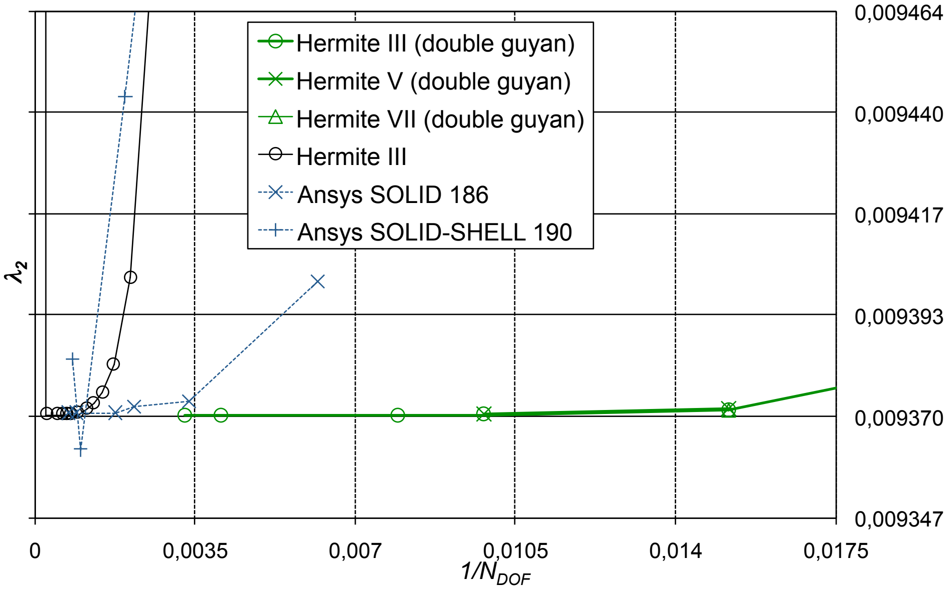

Figure 7.91: Free rectangular cross–section beam: λ_2 with Guyan

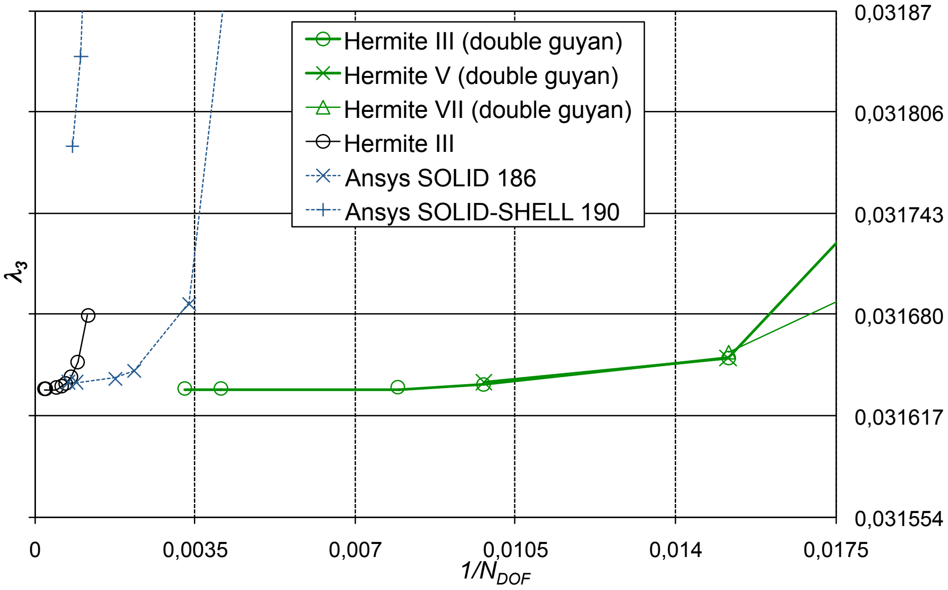

Figure 7.92: Free rectangular cross–section beam: λ_3 with Guyan

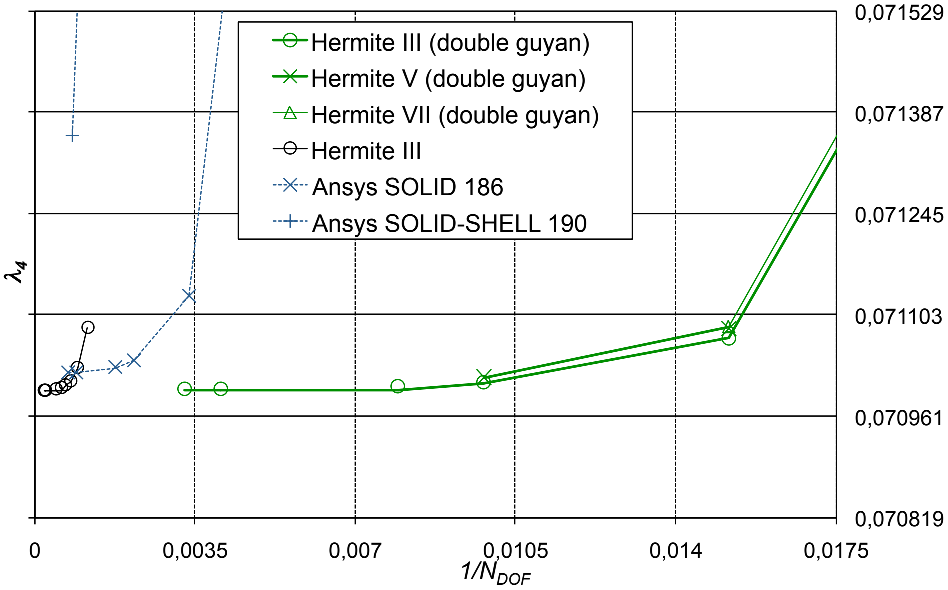

Figure 7.93: Free rectangular cross–section beam: λ_4 with Guyan

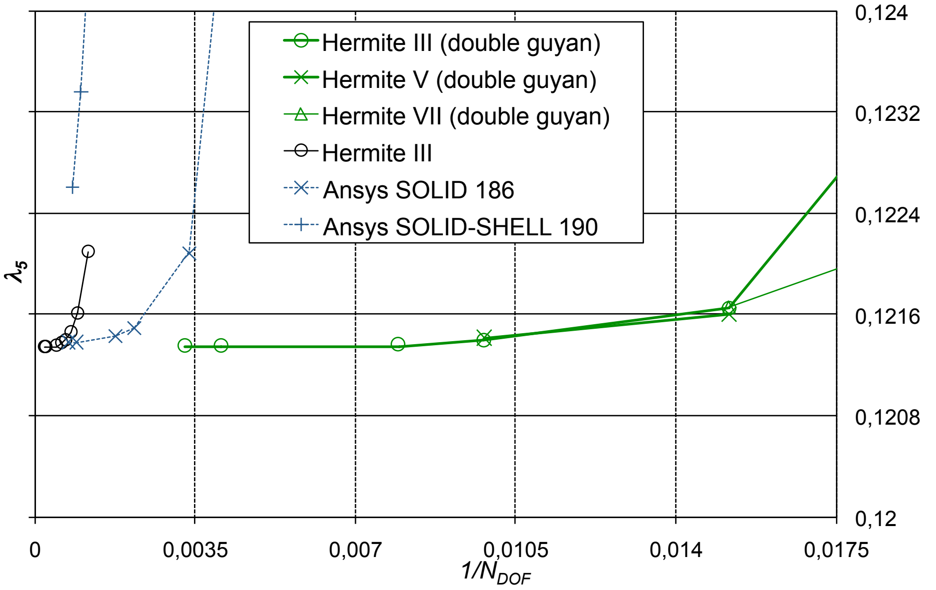

Figure 7.94: Free rectangular cross–section beam: λ_5 with Guyan

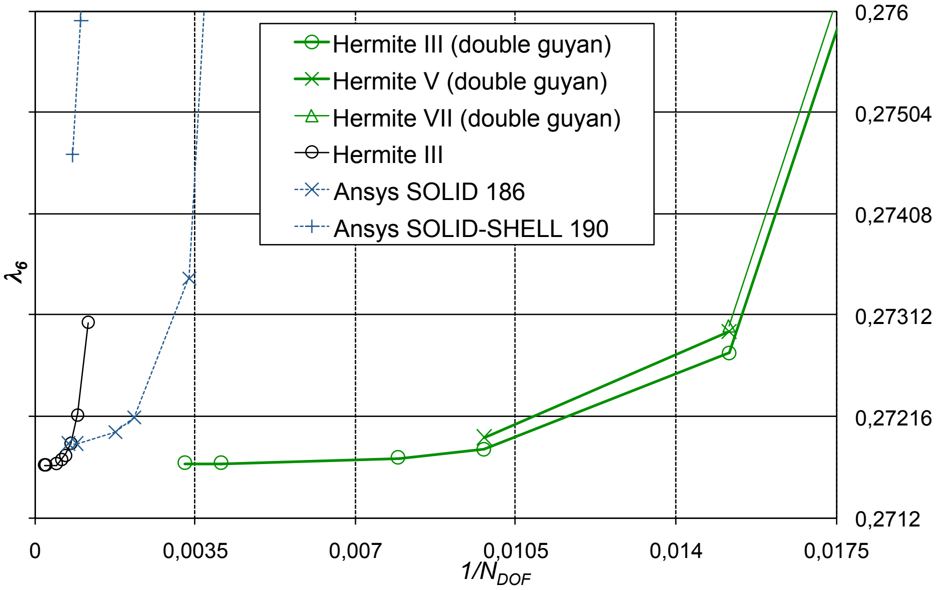

Figure 7.95: Free rectangular cross–section beam: λ_6 with Guyan

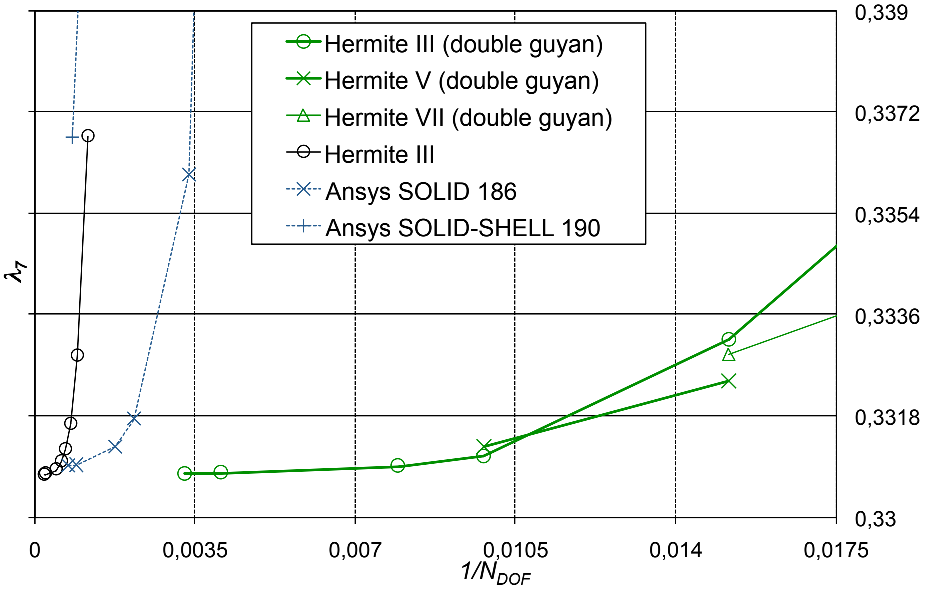

Figure 7.96: Free rectangular cross–section beam: λ_7 with Guyan

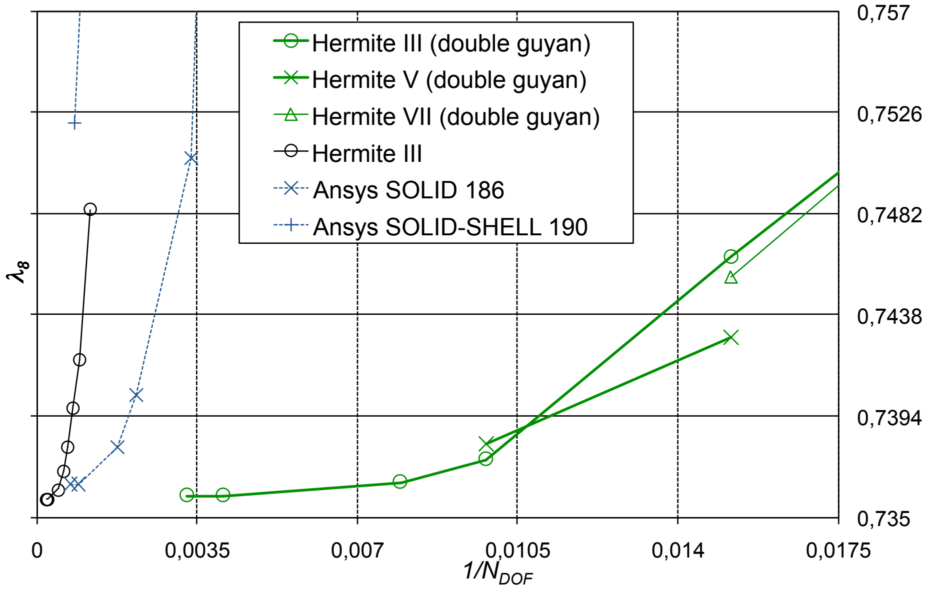

Figure 7.97: Free rectangular cross–section beam: λ_8 with Guyan

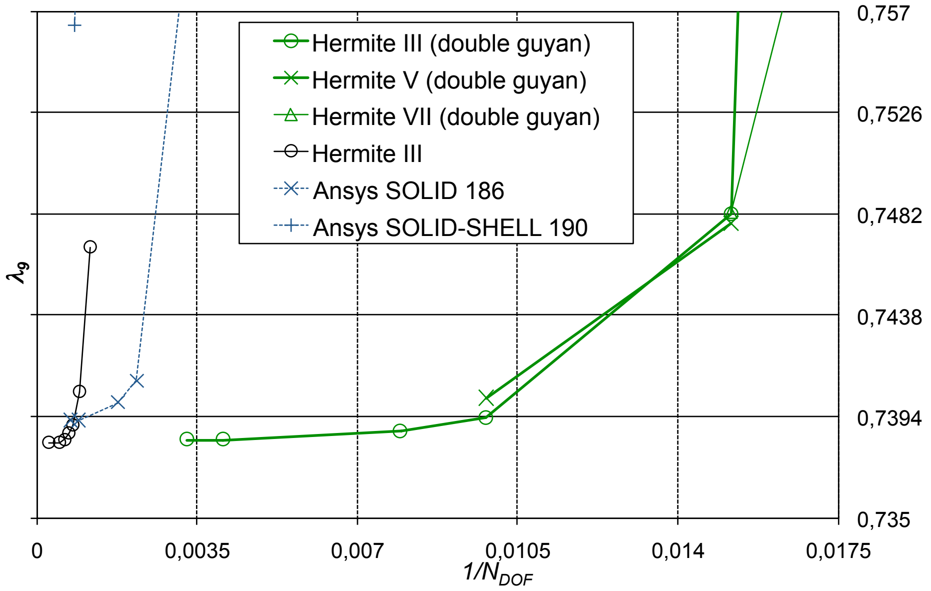

Figure 7.98: Free rectangular cross–section beam: λ_9 with Guyan

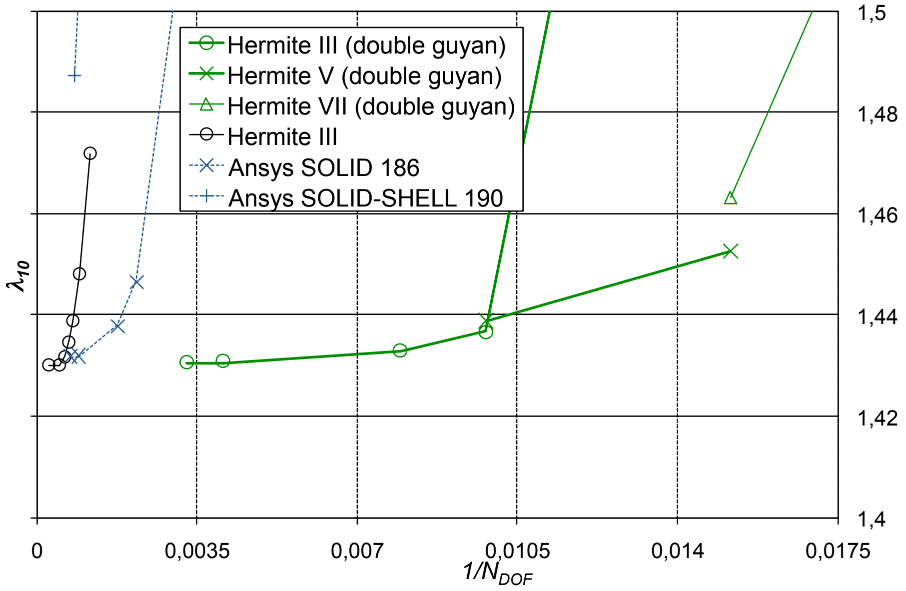

Figure 7.99: Free rectangular cross–section beam: λ_{10} with Guyan

7.4.2 Free and clamped plates

Consider a thin square plate of side $\ell = 1$ and thickness $h = 0.01$. To begin with, assume free boundary conditions.

Figures from 7.100 to 7.107 regard convergence analyses for the relatively high dimensionless frequencies. Results are compared with those obtained using Ansys. Specifically, the comparisons have been done with the Ansys two–dimensional shell element (denoted here by *Ansys 2D*), which is commonly used to analyze plates and shells. Also, the three–dimensional element with 20 nodes (here denoted by *Ansys 3D 20n*) has been used, because it is the most closely related to the present elements. The plate is discretized with N elements along each side and one element in the normal direction.

The images in Figs. from 7.100 to 7.103 concern the results for quite large sets of frequencies. The figures are presented in two couples of images (complete set of frequencies extracted and zoom). Specifically, the first two figures are obtained using the Hermite and the Hybrid elements of order 3 and the Ansys Shell element, each with $N = 6$. Then, they have been compared with the Ansys Shell with $N = 16$ (assumed to give the converged solutions). The second set of images is obtained using the Hermite of orders 3 and 5, using respectively $N = 5$ and $N = 3$ elements and the Ansys Shell with $N = 9$ elements. These meshes give the same number of N_{DOF} for the Hermite elements and a number of DOFs for the Ansys element relatively close to each other (to be specific, we have $N_{DOF} = 5184$ for the Hermites and $N_{DOF} = 6000$ for the Ansys element). The zoom is presented for the first 49 dimensionless frequencies $\bar{\omega}_i = \omega_i \rho / E$. Note that, the first 6 frequencies (that are zero) are related to the first six rigid motions.

Next, the convergence analyses for the first four dimensionless natural frequencies, $\bar{\omega}_i = \omega_i \rho / E$ (for the assumptions made at the beginning of this section $\bar{\omega}_1 = \omega_1$) are shown in Figs. from 7.104 to 7.107. The horizontal lines correspond to the frequency of the thin plate equation (eigenvalue of the bi–Laplacian), as obtained with the Galerkin method (with base functions given by the product of free beam eigenfunctions). The figure on the left presents the value of $\bar{\omega}_i$ as a function of $1/N$ whereas that on the right is obtained as a function of $1/N_{DOF}$.

Results include Guyan's reduction and *Double Guyan* (see Subsection 7.4.1). They are shown in Figs. 7.108 and 7.109. It is apparent that the Guyan reduction plays a key role in the use of Hermite and Hybrid elements in thin structures applications. In fact, it may be introduced with minimal penalization and it gives an accuracy higher than that of the Ansys Shell, even though the Ansys Shell element being specifically designed for shells.

Consider now the same thin square plate with clamped edges.

In Fig. 7.110, the first eigenvalue is presented as a function of $1/N$ and $1/N_{DOF}$ for a clamped plate. Specifically, in the first image, the comparison is made with equal number of elements and the loss in accuracy is insignificant. The advantage of the Guyan 8−to−1 reduction in DOFs is more evident in the second image, where the comparison with the Ansys results is very encouraging (here, the results for the Ansys three–dimensional 20−node element is shown with the Ansys Shell element).

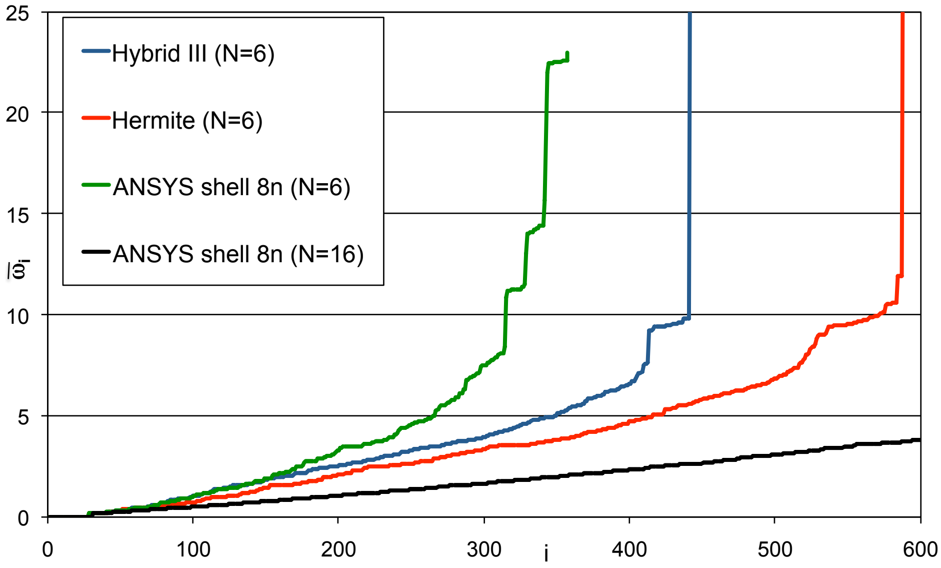

Figure 7.100: Free square plate: Hybrid and Hermite 3rd order ($\bar{\omega}_i$ *vs* i)

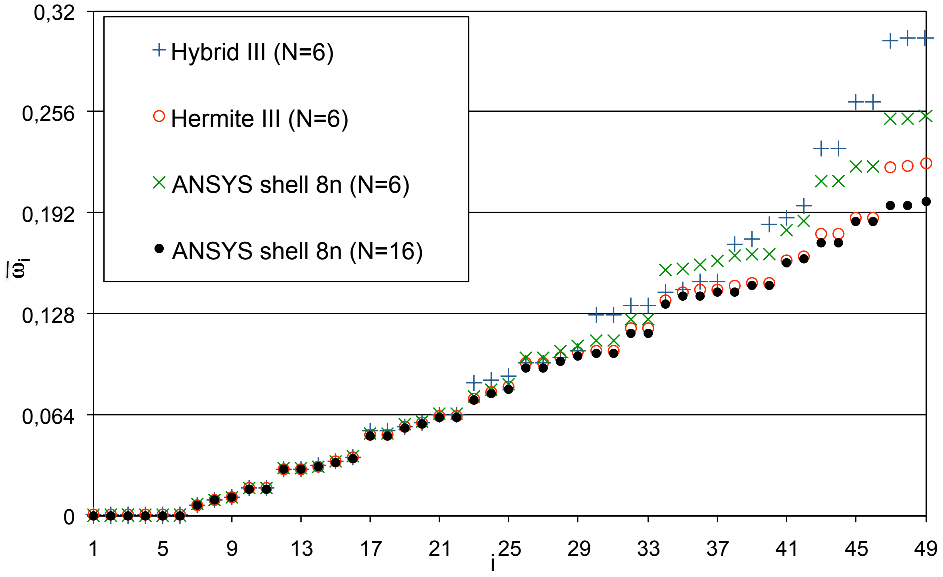

Figure 7.101: Zoom of Fig. 7.100

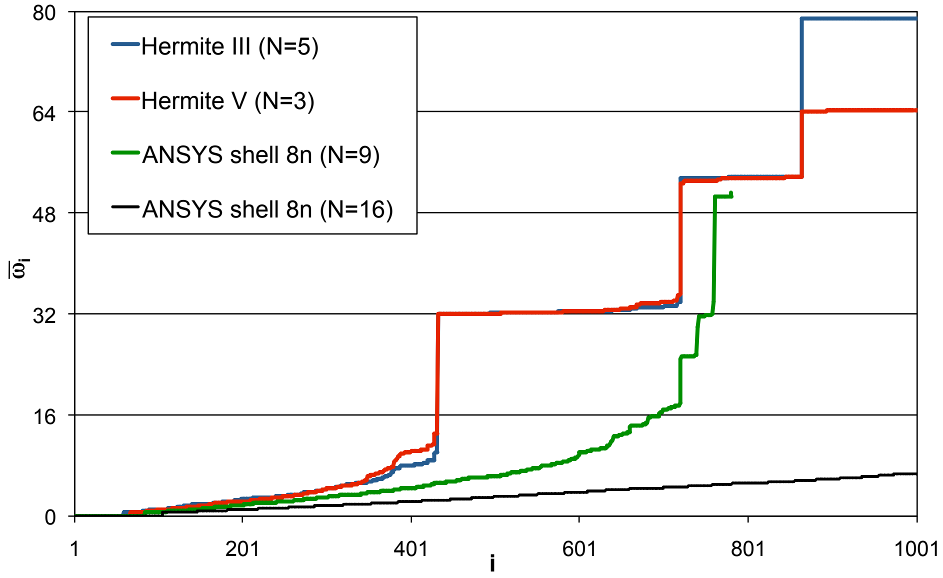

Figure 7.102: Free square plate: Hermite 3rd order and 5th order ($\bar{\omega}_i$ *vs* i)

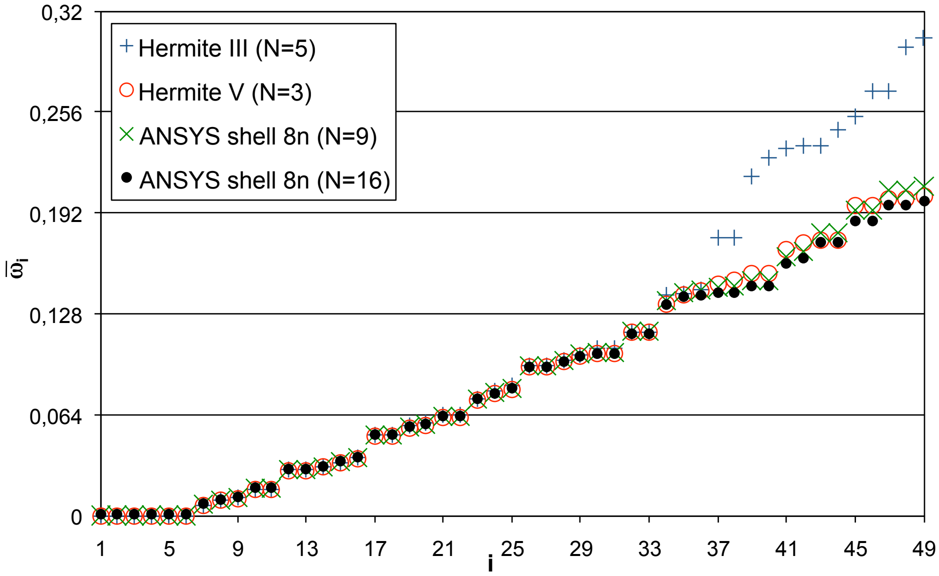

Figure 7.103: Zoom of Fig. 7.102

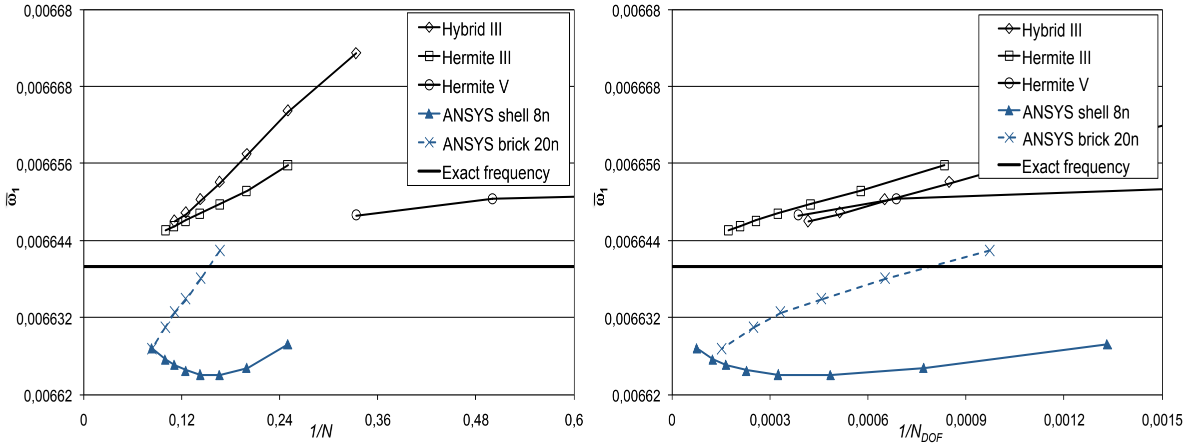

Figure 7.104: Free square plate: $\bar{\omega}_1$ *vs* $1/N$ (left) and *vs* $1/N_{DOF}$ (right)

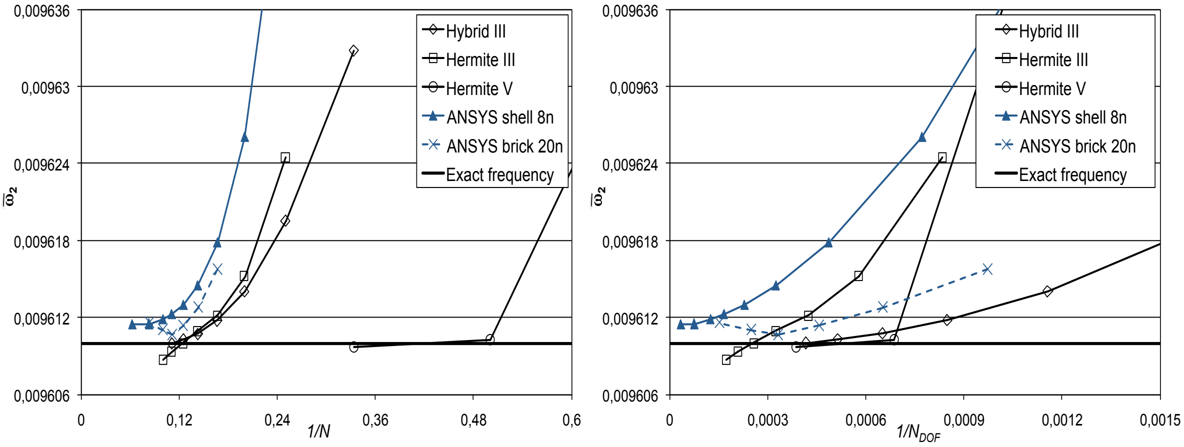

Figure 7.105: Free square plate: $\bar{\omega}_2$ *vs* $1/N$ (left) and *vs* $1/N_{DOF}$ (right)

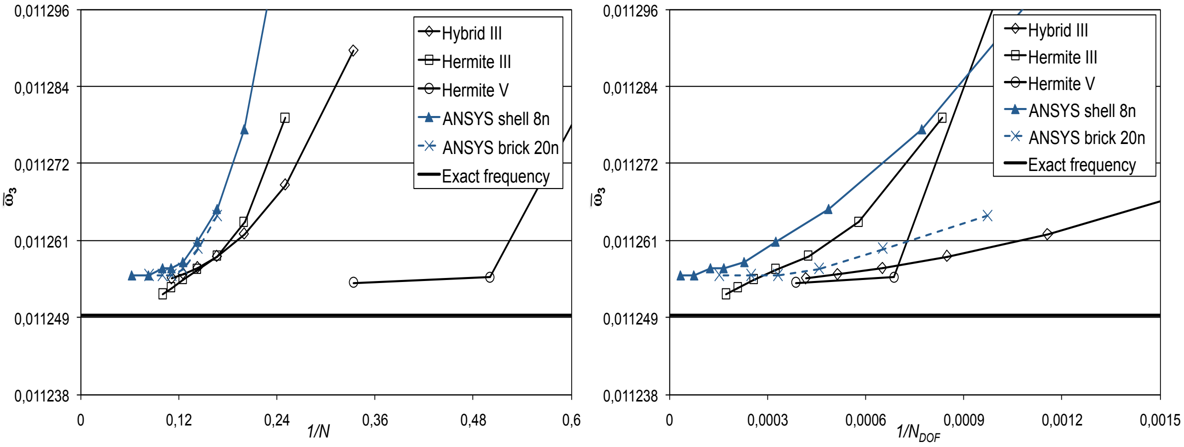

Figure 7.106: Free square plate: $\bar{\omega}_3$ *vs* $1/N$ (left) and *vs* $1/N_{DOF}$ (right)

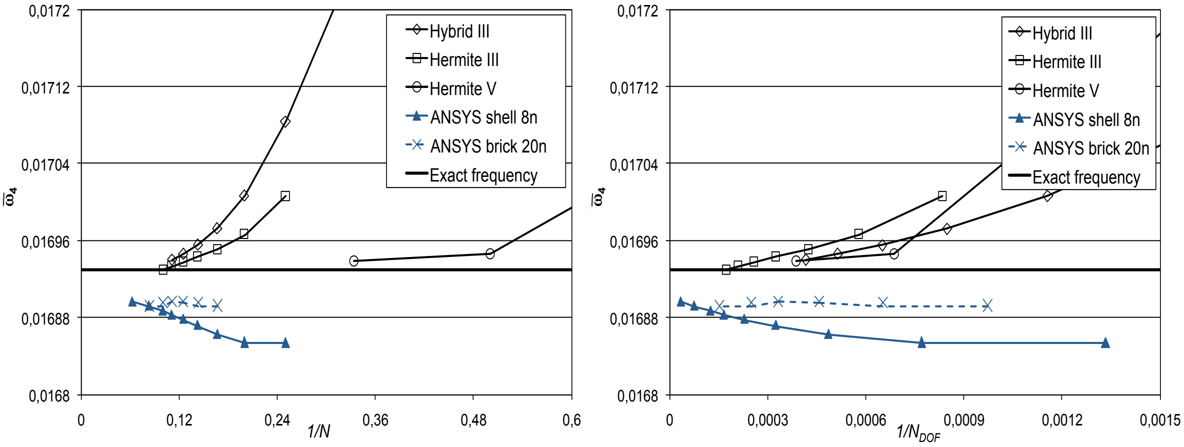

Figure 7.107: Free square plate: $\bar{\omega}_4$ *vs* $1/N$ (left) and *vs* $1/N_{DOF}$ (right)

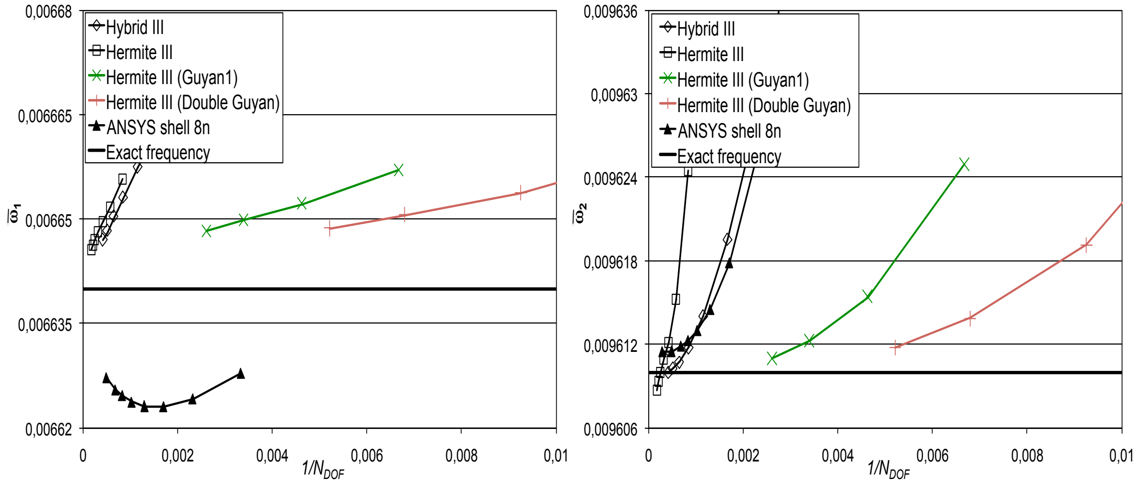

Figure 7.108: Free square plate: $\bar{\omega}_{1-2}$ vs $1/N_{DOF}$ with Guyan

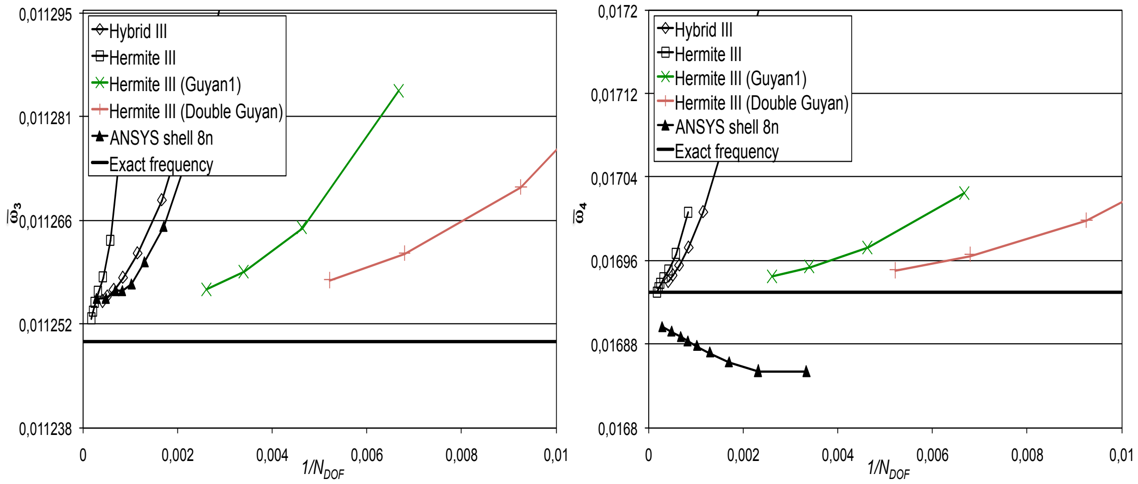

Figure 7.109: Free square plate: $\bar{\omega}_{3-4}$ vs $1/N_{DOF}$ with Guyan

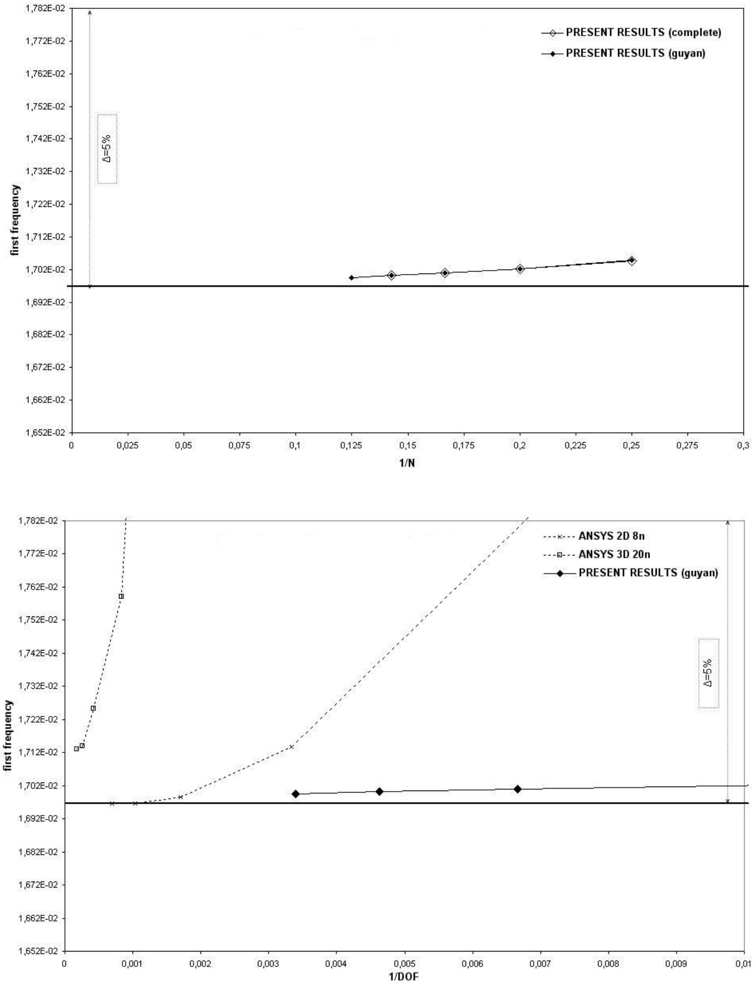

Figure 7.110: Clamped square plate: $\bar{\omega}_1$ *vs* $1/N$ (top) and *vs* $1/N_{DOF}$ (bottom) with Guyan

7.4.3 Hinged plates

Consider a rectangular plate, hinged at its boundaries, of edges $a = 1$, $b = 1.01$ and thickness $h = 0.01$. The natural frequencies are evaluated for different subdivisions of the geometry and are compared to those exact, relative to the bending modes of a hinged plate. In fact, in this case the modes are given by

$$\Phi_{mn}(x, y) = \sin \frac{m\pi x}{a} \ \sin \frac{n\pi y}{b}$$

whereas the natural frequencies are given by

$$\omega_{mn} = \sqrt{D/\rho}\left[\left(\frac{m\pi}{a}\right)^2 + \left(\frac{n\pi}{b}\right)^2\right]$$

where D denotes the bending stiffness of the plate. The exact eigenvalues are then given by $\mu_{mn} = \omega_{mn}^2$. For small thicknesses, these frequencies are much lower than those relative to in-plane motion and therefore are a good reference for the numerical results. Since the proposed methodology treats the geometry of each structure as a three–dimensional domain (indeed, only brick elements have been introduced), the eigenfunctions $\Phi_{mn} = \Phi_{mn}(x, y)$ have been used to obtain the three–dimensional functions $\hat{\Phi}_{mn} = \hat{\Phi}_{mn}(x, y, \pm h/2)$ (see Subsection 7.4.4 for details). Then, the numerical modes have been compared with the exact ones $\hat{\Phi}_{mn}$ using the definitions of ϵ_{mn}, e_{mn} and $e_{mn}\%$ given in Section 7.1 (Eqs. 7.5, 7.6 and 7.7 respectively). Note that, as for the results shown in Section 7.3, also in this context it is convenient to have a rectangular geometry so that to avoid, as much as possible, coupling between the modes related to close (numerically equal) eigenvalues.

Figures from 7.111 to 7.114 pertain the first seven eigenvalues (for which it results $n_w \leq 3$) as a function of the total unknowns N_{DOF}, obtained with and without reduction (the classical Guyan's technique has been applied). They are compared with those obtained using Ansys Solid-Shell element (that is a eight-noded, six-degrees-of-freedom per node element, specific for thin structures applications).

Next, Figs. from 7.115 to 7.128 regard relatively high frequencies, for both the modes and the eigenvalues, obtained with a complete formulation as well as with the application of a reduction algorithm. In particular, the reduced modes (*i.e.*, those obtained with a Guyan's reduction) have been compared with the exact ones, after having recovered the complete unknown vector from the master components through the transformation $\mathsf{z} = \mathsf{T}_G \mathsf{z}_m$ of Eq. E.6 (see Section E.1).

The considerations presented for the Laplacian expressed in Section 7.3, regarding the number of accurate frequencies, are extended for the structural results: in this case it appears that eigenvalues related to a number of waves $n_W \leq N - 1$ are acceptably captured (whereas modes related to a lower n_W show minimal errors). In addition, a key result concerns the application of the Guyan's reduction: in fact, in this case a negligible loss in accuracy is obtained for the whole set of eigenvalues captured with the complete formulation, despite having reduced by a factor 8 the total quantity of unknowns. Fig. 7.124 compares the Hermite 3rd order 8−node element with $N = 4$, in its complete and reduced formulation, with the Ansys Solid-Shell element with $N = 5$, specific for this structures analysis. According to the preceding discussion, the results are presented up to the $[3, 3]$ eigenvalue. Note that, the accuracy obtained is generally higher than that obtained with Ansys (even though a finer mesh is used). Note also that, in this figure the Ansys element has been used with 432 DOFs whereas the Hermite element reduced with the Guyan's technique has been used with 50 DOFs only.

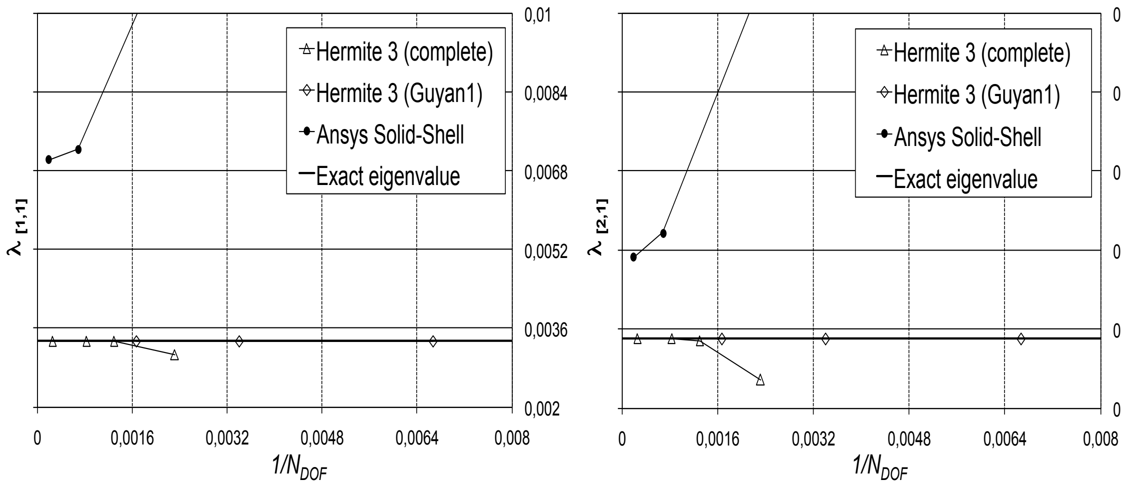

Figure 7.111: Hinged rectangular plate: $\lambda_{[1,1]}$ and $\lambda_{[2,1]}$ vs $1/N_{DOF}$

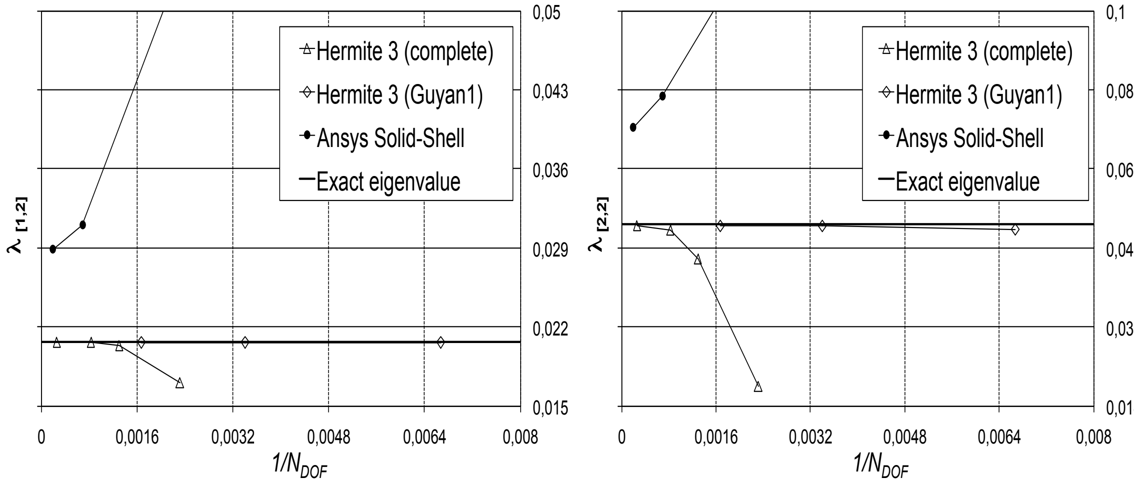

Figure 7.112: Hinged rectangular plate: $\lambda_{[1,2]}$ and $\lambda_{[2,2]}$ vs $1/N_{DOF}$

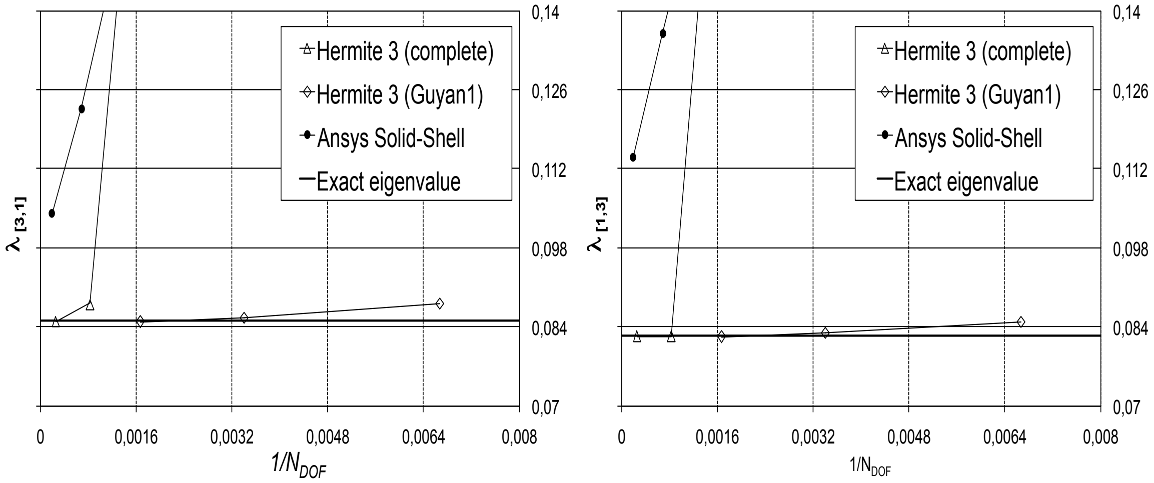

Figure 7.113: Hinged rectangular plate: $\lambda_{[3,1]}$ and $\lambda_{[1,3]}$ vs $1/N_{DOF}$

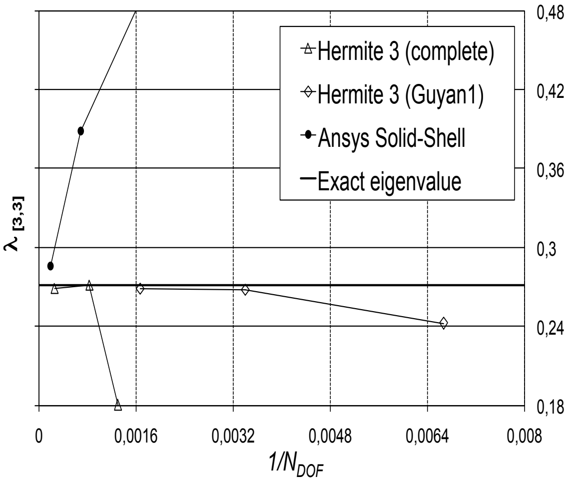

Figure 7.114: Hinged rectangular plate: $\lambda_{[3,3]}$ vs $1/N_{DOF}$

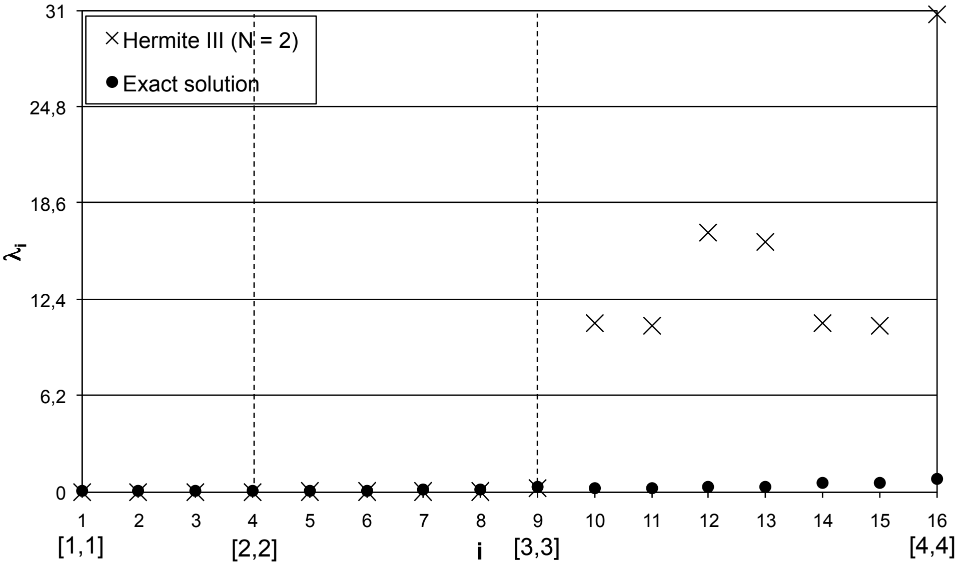

Figure 7.115: Hinged rectangular plate: modes with Hermite 3rd order (and with $N = 2$)

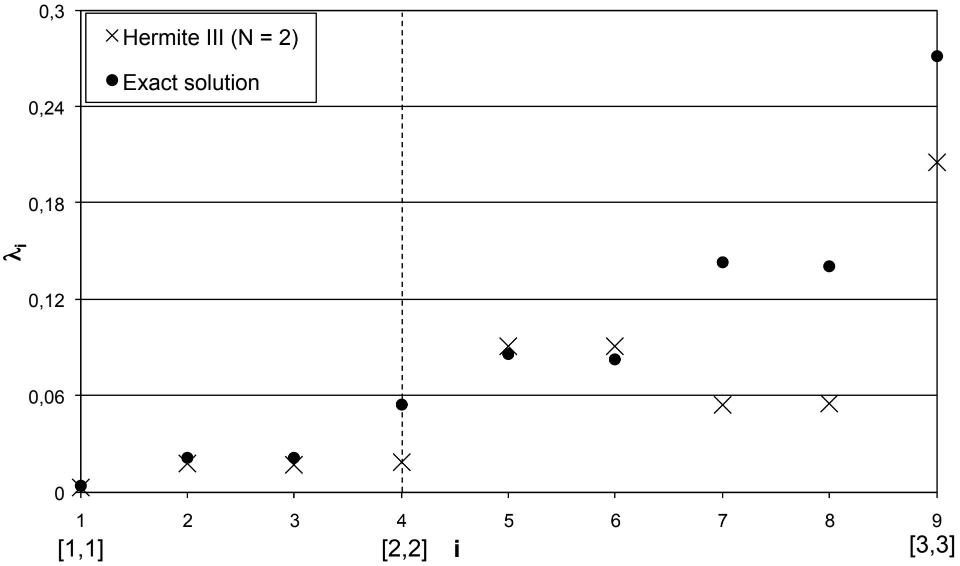

Figure 7.116: Zoom of Fig. 7.115

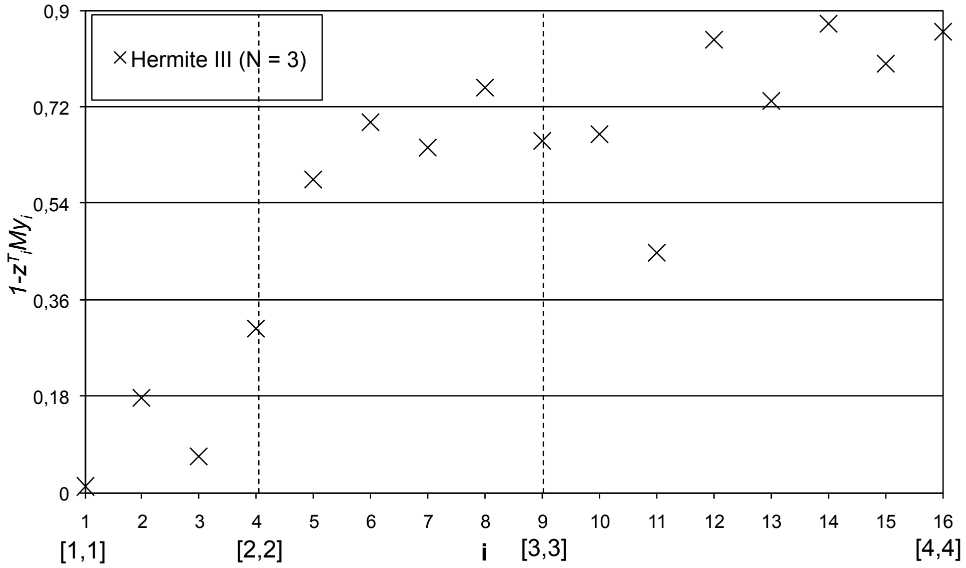

Figure 7.117: Hinged rectangular plate: modes with Hermite 3rd order (and with $N = 3$)

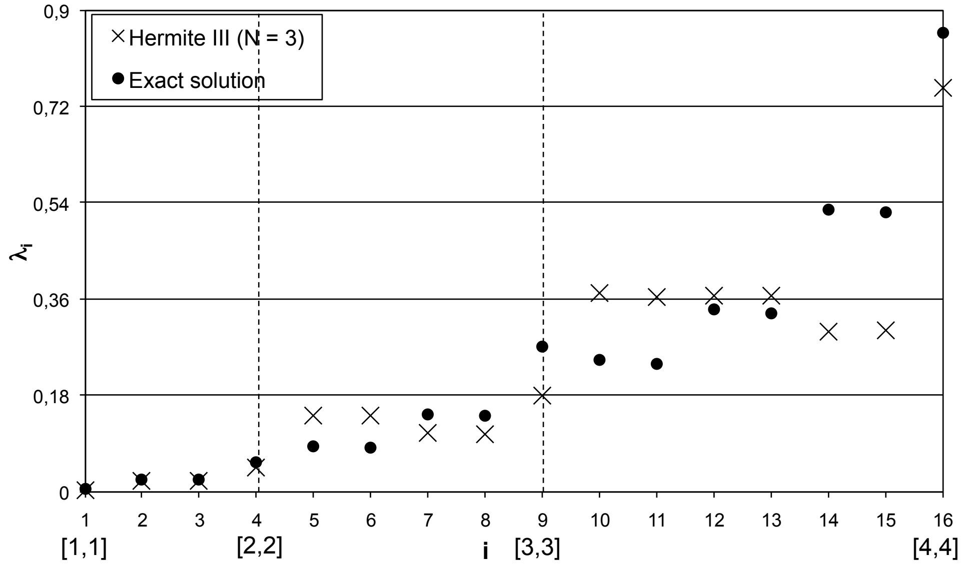

Figure 7.118: Hinged rectangular plate: eigenvalues with Hermite 3rd order (and with $N = 3$)

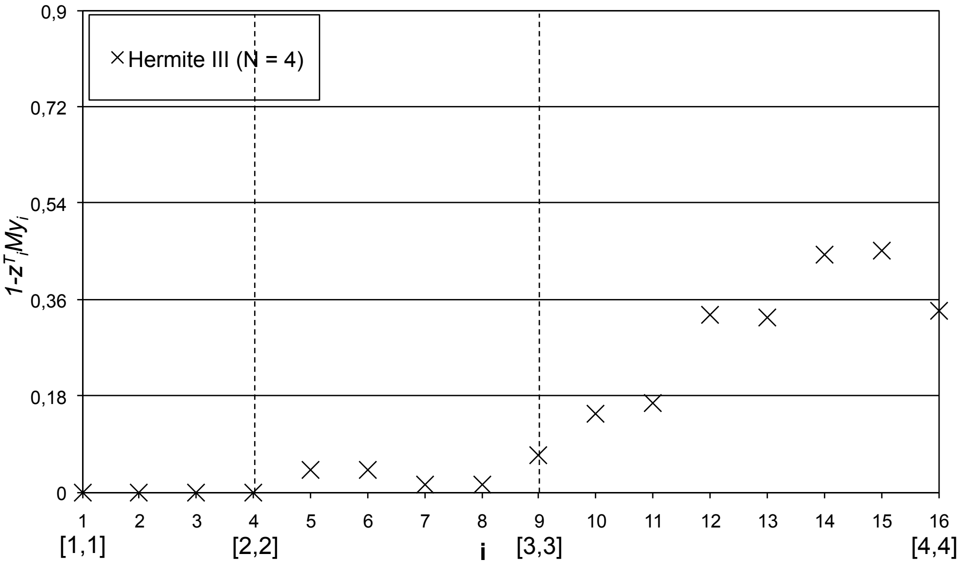

Figure 7.119: Hinged rectangular plate: modes with Hermite 3rd order (and with $N = 4$)

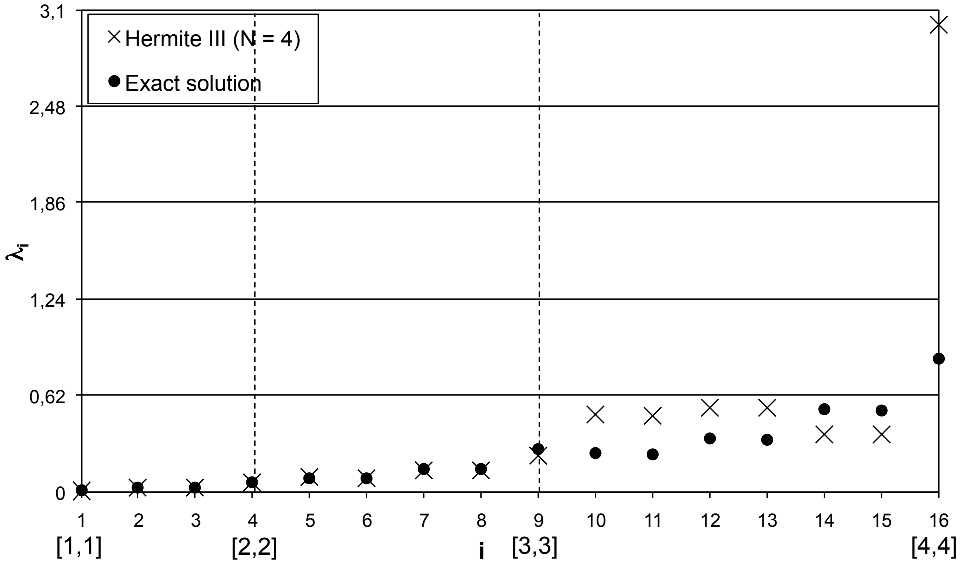

Figure 7.120: Hinged rectangular plate: eigenvalues with Hermite 3rd order (and with $N = 4$)

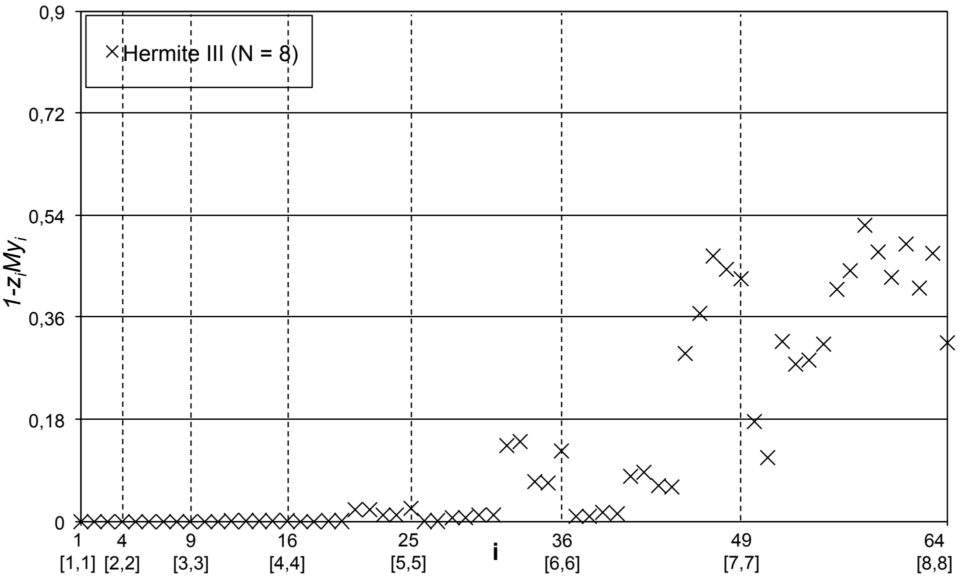

Figure 7.121: Hinged rectangular plate: modes with Hermite 3rd order (and with $N = 8$)

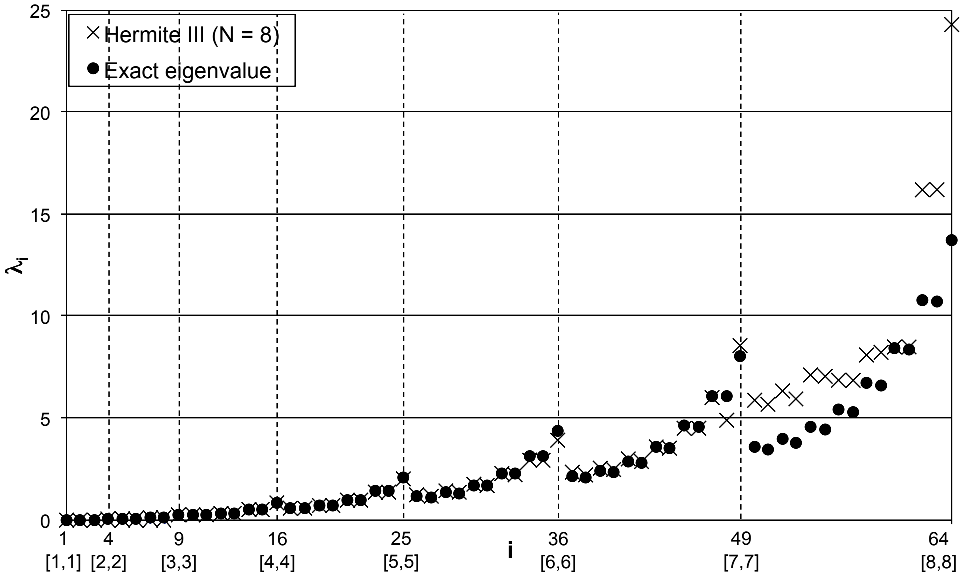

Figure 7.122: Hinged rectangular plate: eigenvalues with Hermite 3rd order (and with $N = 8$)

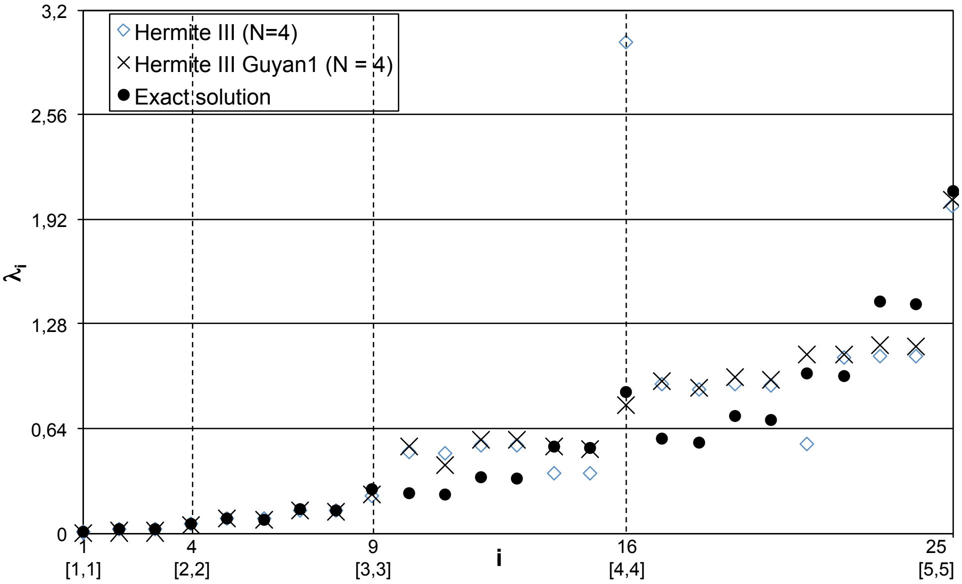

Figure 7.123: Hinged rectangular plate: eigenvalues with Hermite 3rd order and Guyan $(N = 4)$

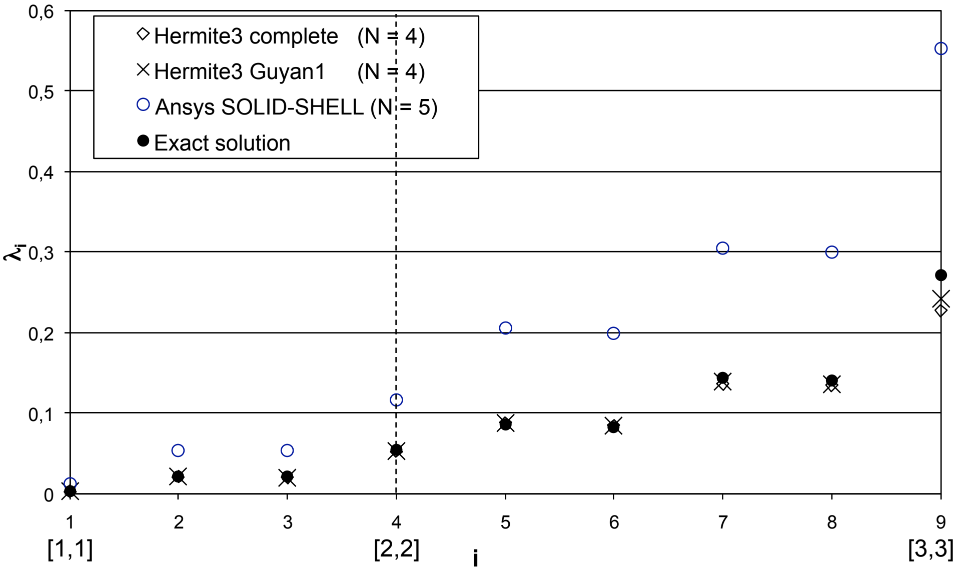

Figure 7.124: Hinged rectangular plate: eigenvalues with Hermite 3rd order and Guyan $(N = 4)$ *vs* Ansys Solid-Shell $(N = 5)$

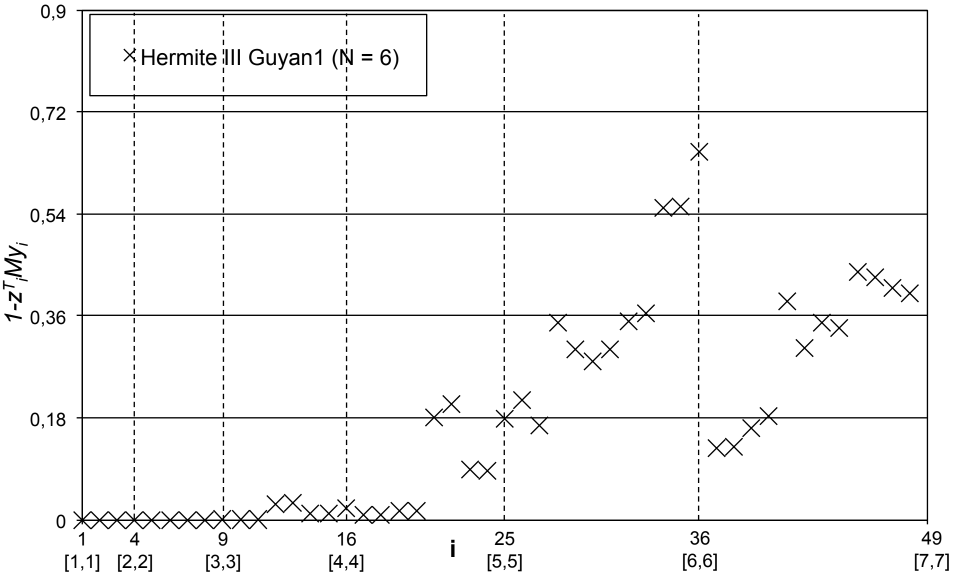

Figure 7.125: Hinged rectangular plate: modes with Hermite 3rd order and Guyan $(N = 6)$

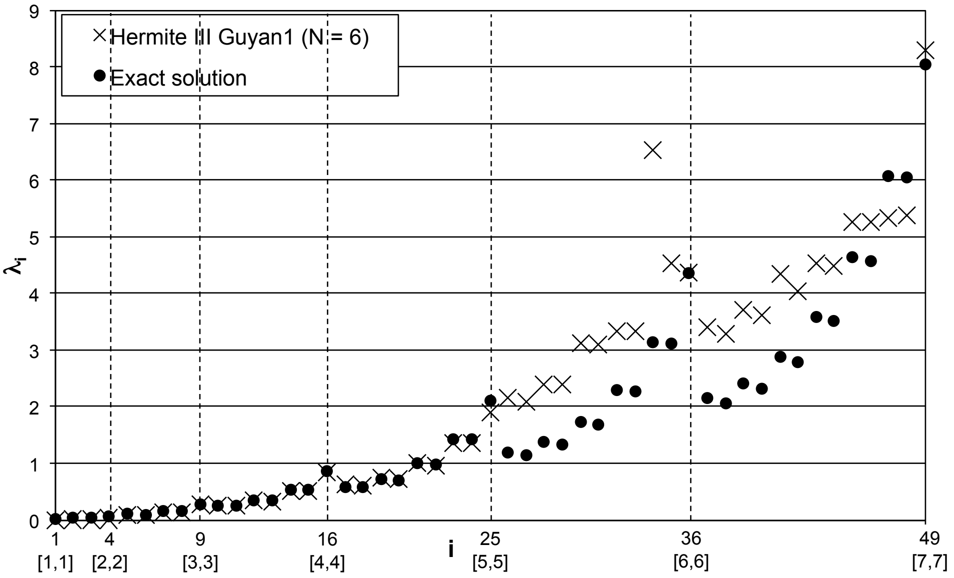

Figure 7.126: Hinged rectangular plate: eigenvalues with Hermite 3rd order with Guyan $(N = 6)$

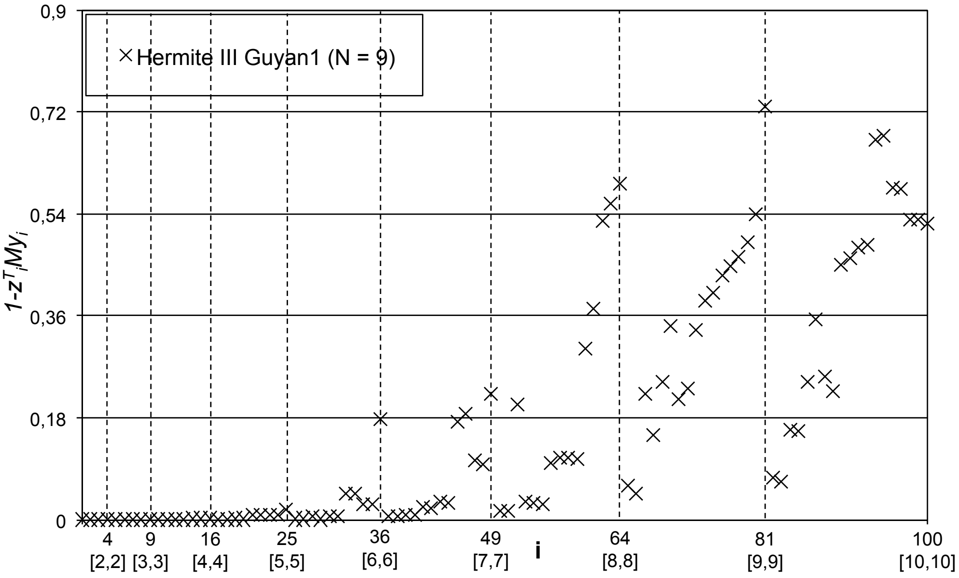

Figure 7.127: Hinged rectangular plate: modes with Hermite 3rd order and Guyan ($N = 9$)

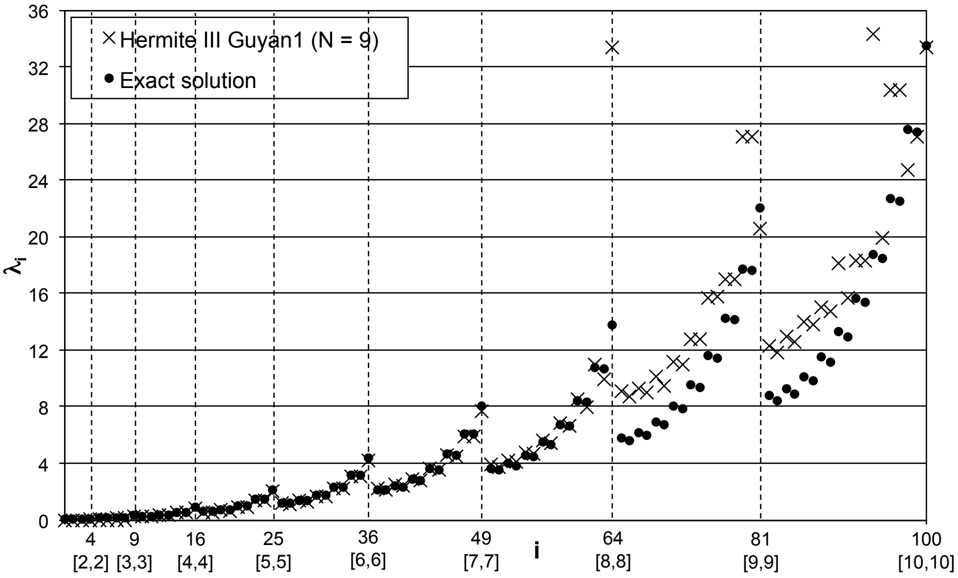

Figure 7.128: Hinged rectangular plate: eigenvalues with Hermite 3rd order with Guyan ($N = 9$)

7.4.4 From $2-$D plate theory to a $3-$D continuum

Consider a rectangular plate of sides a and b and thickness h, hinged at its edges. The modal shapes related to the $[m, n]$ eigenfunction for the related two–dimensional problem are given by, indicating with $\bar{u}$ the vertical displacement (of such a simplified model):

$$\bar{u} = \bar{u}(x, y) = \sin \frac{m\pi x}{a} \; \sin \frac{n\pi y}{b} \tag{7.11}$$

The objective of this subsection is to describe the procedure to transform the surface $\bar{u} = \bar{u}(x, y)$ in a three–dimensional vector function $\mathbf{u} = \mathbf{u}(x, y, z)$.

Note that, in this thesis no shell elements have been introduced and hence no two–dimensional formulations are required, since shell–like structures are treated as three–dimensional objects. For this reason, the three–dimensional form of Eq. 7.11 has been used to obtain a reference eigenfunction in evaluating the accuracy of the methodology in capturing structural modes (see results obtained in Subsection 7.4.3). In particularm, since a single element along the thickness h is used to model any thin structures, for a $8-$node formulation one has to determine the function $\mathbf{u} = \mathbf{u}(x, y, \pm\frac{h}{2})$.

Indicate with $\mathbf{x}_u$ and $\mathbf{x}_d$ the undeformed configuration and the modal shape (related to the mode $[m, n]$) and consider the following notations:

$$S_{mx} = \sin m\pi \; \frac{x+1}{2} \qquad \text{and} \qquad C_{mx} = \cos m\pi \; \frac{x+1}{2}$$
$$S_{ny} = \sin n\pi \; \frac{y+1}{2} \qquad \text{and} \qquad C_{ny} = \cos n\pi \; \frac{y+1}{2}$$

One has, using the local coordinates $\xi, \eta, \zeta \in [-1, 1]$:

$$\mathsf{x}_u = \mathsf{x}_u(\xi, \eta, \zeta) = \begin{pmatrix} a(\xi+1)/2 \\ b(\eta+1)/2 \\ 0 \end{pmatrix} + \zeta \begin{pmatrix} 0 \\ 0 \\ 1 \end{pmatrix} \tag{7.12}$$

$$\mathsf{x}_d = \mathsf{x}_d(\xi, \eta, \zeta) = \begin{pmatrix} a(\xi+1)/2 \\ b(\eta+1)/2 \\ S_{m\xi} S_{m\eta} \end{pmatrix} + \zeta \begin{pmatrix} n_\xi \\ n_\eta \\ n_\zeta \end{pmatrix} \tag{7.13}$$

Within the hypothesis of linear displacement, Eq. 7.13 can be rewritten as

$$\mathsf{x}_d = \mathsf{x}_d(\xi, \eta, \zeta) = \begin{pmatrix} a(\xi+1)/2 \\ b(\eta+1)/2 \\ S_{m\xi} S_{n\eta} \end{pmatrix} + \zeta \begin{pmatrix} n_\xi \\ n_\eta \\ 1 \end{pmatrix} \tag{7.14}$$

Then, denoting with $\mathbf{u}$ the (linearized) displacement vector such that $\mathbf{u} = \mathbf{x}_d - \mathbf{x}_u$, one obtains:

$$\mathsf{u} = \mathsf{u}(\xi, \eta, \zeta) = \begin{pmatrix} 0 \\ 0 \\ S_{m\xi} S_{n\eta} \end{pmatrix} + \zeta \begin{pmatrix} n_\xi \\ n_\eta \\ 0 \end{pmatrix} \tag{7.15}$$

In order to define the normal unit vector $\mathbf{n} = \mathbf{n}(\xi, \eta)$, we determine the two base vectors $\mathbf{a}_\xi = \mathbf{a}_\xi(\xi, \eta)$ and $\mathbf{a}_\eta = \mathbf{a}_\eta(\xi, \eta)$. It results:

$$\mathsf{a}_\xi = \mathsf{a}_\xi(\xi, \eta) = \partial \mathsf{x}_d / \partial \xi = \begin{pmatrix} a \\ 0 \\ S'_{m\xi} S_{n\eta} \end{pmatrix} \tag{7.16}$$

$$\mathsf{a}_\eta = \mathsf{a}_\eta(\xi, \eta) = \partial \mathsf{x}_d / \partial \eta = \begin{pmatrix} 0 \\ b \\ S_{m\xi} S'_{n\eta} \end{pmatrix} \tag{7.17}$$

$$\mathsf{n} = \frac{\mathsf{a}_\xi \times \mathsf{a}_\eta}{\|\mathsf{a}_\xi \times \mathsf{a}_\eta\|} = \begin{pmatrix} n_\xi \\ n_\eta \\ n_\zeta \end{pmatrix} = \frac{1}{\sqrt{A}} \begin{pmatrix} -bS'_{m\xi} S_{n\eta} \\ -aS_{m\xi} S'_{n\eta} \\ 1 \end{pmatrix} \tag{7.18}$$

where

$$A = b^2 S'^2_{m\xi} S^2_{n\eta} + a^2 S^2_{m\xi} S'^2_{n\eta} \tag{7.19}$$

and $\zeta = \pm h/2$. One obtains for the displacement:

$$\mathsf{u} = \begin{pmatrix} 0 \\ 0 \\ S_{m\xi} S_{n\eta} \end{pmatrix} + \zeta \begin{pmatrix} n_\xi \\ n_\eta \\ 0 \end{pmatrix} = \begin{pmatrix} 0 \\ 0 \\ S_{m\xi} S_{n\eta} \end{pmatrix} \pm \frac{h/2}{\sqrt{A}} \begin{pmatrix} -bS'_{m\xi} S_{n\eta} \\ -aS_{m\xi} S'_{n\eta} \\ 0 \end{pmatrix} \tag{7.20}$$

For example, in order to use the 3rd order 8−node Hybrid element, one needs to recast the corresponding set of parameters, that is the function and the three partial derivatives. Specifically, one has:

$$\begin{aligned} \frac{\partial u_\xi}{\partial \xi}(\xi, \eta) &= \pm \frac{h}{2}\ a^2 b m^2 n^2 \pi^4\ \frac{C^2_{n\eta} S_{m\xi} S_{n\eta}}{2A^{3/2}} \\ \frac{\partial u_\eta}{\partial \xi}(\xi, \eta) &= \mp \frac{h}{2}\ a b^2 m^3 n \pi^4\ \frac{S^2_{n\eta} C_{m\xi} C_{n\eta}}{2A^{3/2}} \\ \frac{\partial u_\zeta}{\partial \xi}(\xi, \eta) &= \quad S'_{m\xi} S_{n\eta} \end{aligned} \tag{7.21}$$

$$
\begin{aligned}
\frac{\partial u_\xi}{\partial \eta}(\xi,\eta) &= \mp\frac{h}{2}\ a^2 b m n^3 \pi^4\ \frac{S_{m\xi}^2 C_{m\xi} C_{n\eta}}{2A^{3/2}} \\
\frac{\partial u_\eta}{\partial \eta}(\xi,\eta) &= \pm\frac{h}{2}\ a b^2 m^2 n^2 \pi^4\ \frac{C_{m\xi}^2 S_{m\xi} S_{n\eta}}{2A^{3/2}} \\
\frac{\partial u_\zeta}{\partial \eta}(\xi,\eta) &= \quad S_{m\xi} S'_{n\eta}
\end{aligned}
\tag{7.22}
$$

If the Hermite 3rd order 8−node element is used, it is apparent that one needs also the second mixed derivatives and the third mixed derivative. For higher–order schemes, higher–order derivatives are required.

7.5 Block–boundary problem: Scheme C

In order to validate the *Scheme C* introduced in Section 2.4, a thin square plate, free at its boundaries, is initially considered. Here, the plate is artificially divided into two halves, and each of the two resulting plates is treated as a different block. Thus, for the same plate we can use three schemes: (a) Scheme A (*i.e.*, that used in the preceding section), (b) Scheme B (in which each element is considered as a separate block), and (c) Scheme C in which each of the two portion is treated as a separate block. As a preliminary result, the first twenty frequencies obtained using the three different schemes are presented in Fig. 7.129. In this figure, Kode 0−0 denotes *Scheme A* for all the plate (this is the same approach used in the preceding sections), whereas Kode 1 − 0 and Kode 1 − 1 denotes *Scheme C* and *Scheme B*, respectively.

Next, consider a rectangular plate, free at its boundaries, of edges $a = 1$, $b = 2$ and thickness $h = 0.01$. As a *Scheme A*, the structure is divided in $N \times 2N \times 1$ elements, so that to have square elements of size $h_N = 1/N$. Instead, as a *Scheme C*, the plate has been divided in two square halves of side 1, on their turn subdivided in $N \times N \times 1$ elements.

Figures from 7.130 to 7.134 depict the h–convergences for the first five eigenvalues in terms of the number of elements N (the images on the left) and of the total number of unknowns N_{DOF} (the image on the right), using both Schemes A and C and comparing the results with the new Ansys Solid-Shell element, specific for thin-wall structure analyses. It appears that the results obtained are still better than those obtained with Ansys.

In Figures from 7.135 to 7.137, *Scheme C* has been assessed for acoustics. Specifically, consider a parallelepiped cavity of sides $a = 2\pi$ and $b = c = \pi$. Similarly to the structural approach, for *Scheme A* a mesh of $2N \times N \times N$

elements has been generated, so that to obtain cubic elements of size $h_N = \pi/N$. On the other hand, for *Scheme C* the plate has been divided in two blocks, on their turn sub-divided in $N \times N \times N$ elements. Now a exact solution is available (indeed, one has $\mu_{mnp} = \omega^2_{mnp} = (m/2)^2 + n^2 + p^2$ if the speed of sound $c_s = 1$, see Section 7.3). Thus the error $e_{[m,n,p]}$ will be showed, since the analysis is now limited to eigenvalues. In particular, the first three eigenvalues (*i.e.*, those related to $[1,0,0]$, $[1,1,0]$ and $[1,1,1]$), evaluated using both *Scheme A* and *Scheme C*. Note that, in this case, the interface presents $(N+1)^2$ nodes (that are the nodes for which the *Scheme C* must be applied) whereas, for the preceding plate, Scheme C applies only to $2(N+1)$ nodes. Therefore, the penalization is expected to be higher for the 3–D acoustic domains than that obtained for thin structures domains.

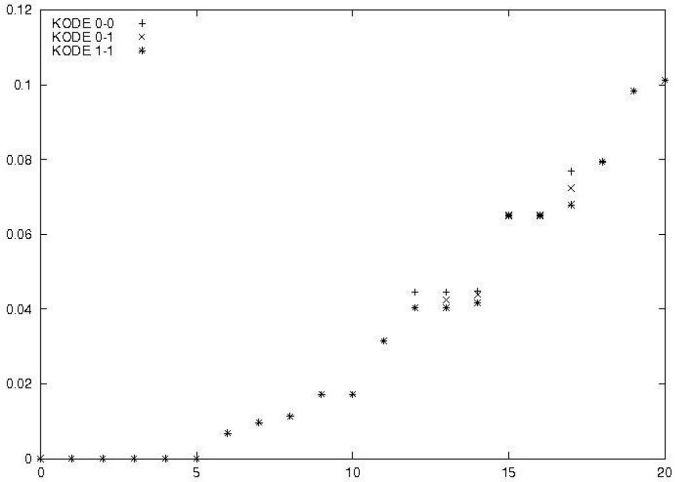

Figure 7.129: Free square plate: Schemes A, B and C

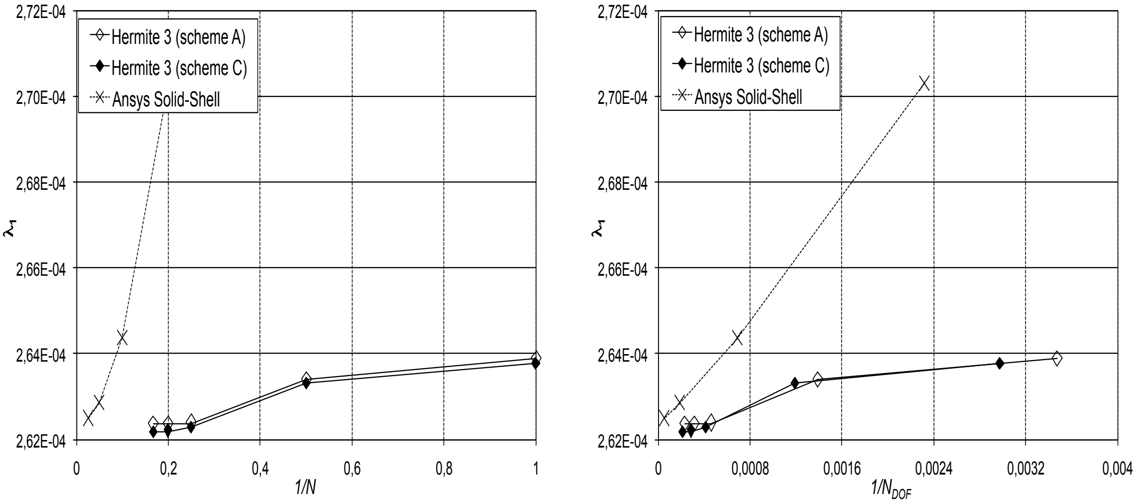

Figure 7.130: Free rectangular plate: λ_1 with Scheme C

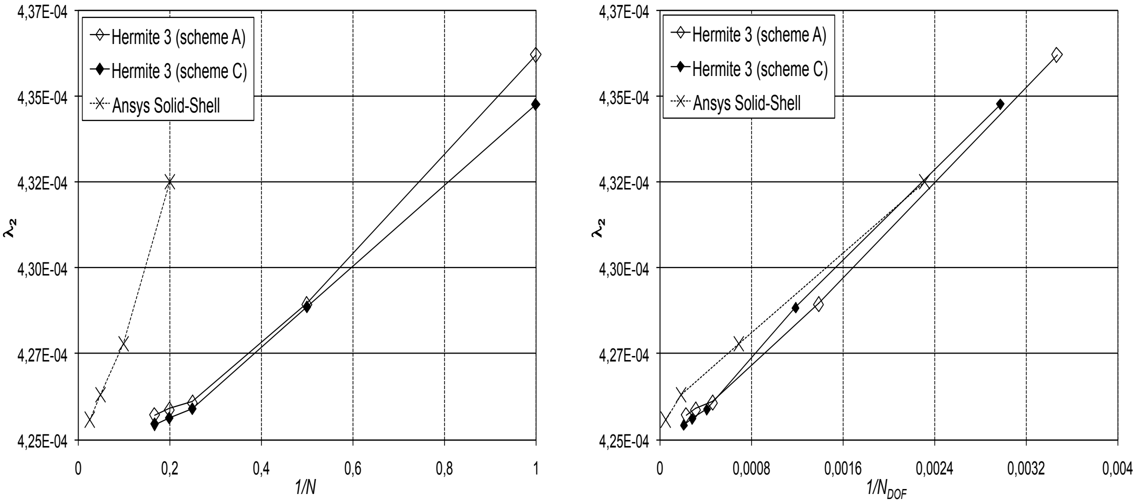

Figure 7.131: Free rectangular plate: λ_2 with Scheme C

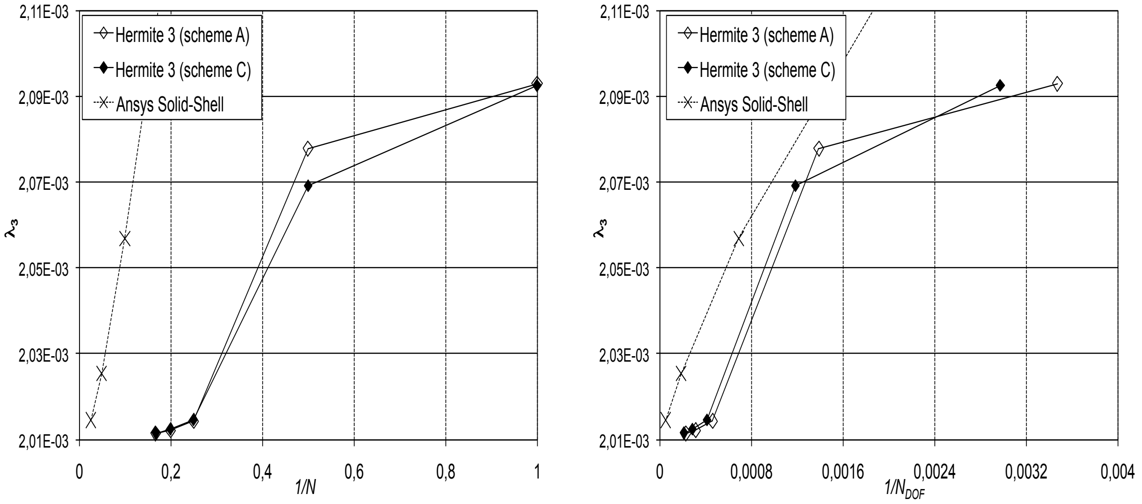

Figure 7.132: Free rectangular plate: λ_3 with Scheme C

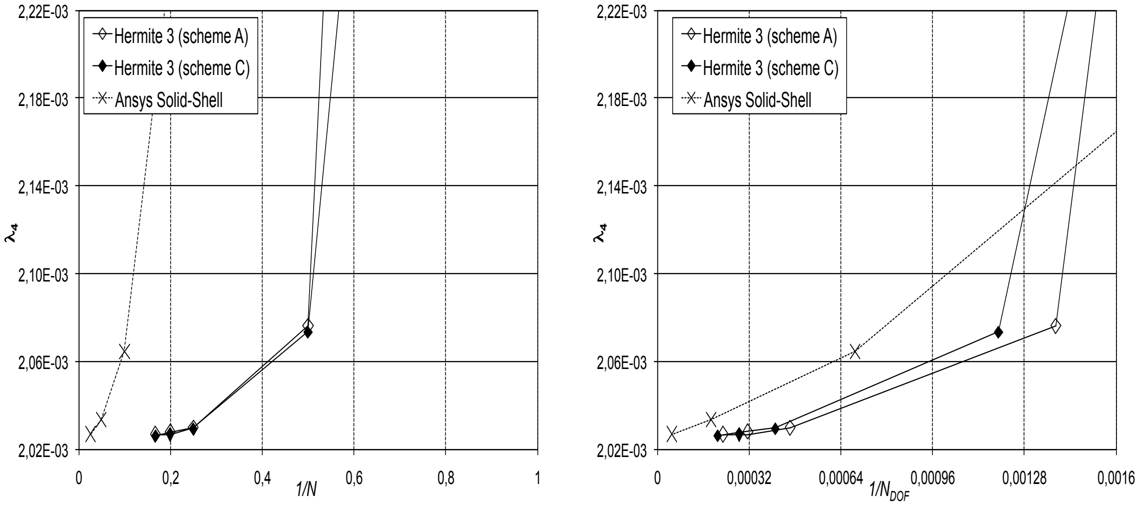

Figure 7.133: Free rectangular plate: λ_4 with Scheme C

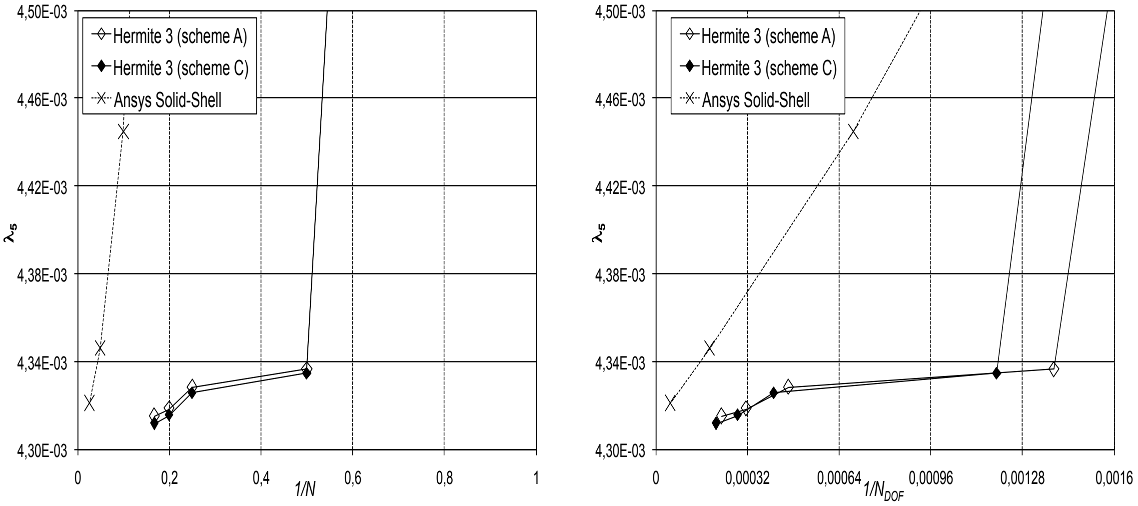

Figure 7.134: Free rectangular plate: λ_5 with Scheme C

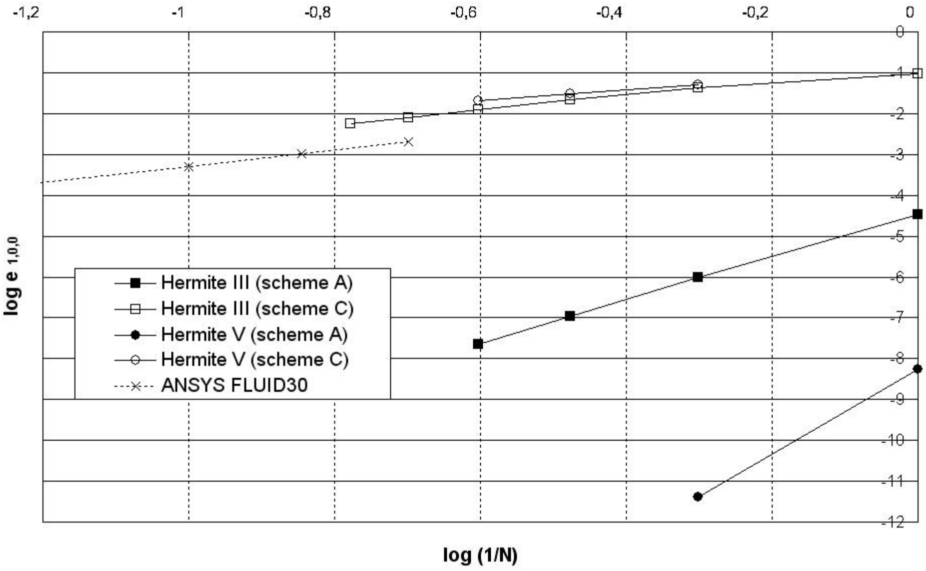

Figure 7.135: Rectangular cavity: $e_{[1,0,0]}$ with Scheme C

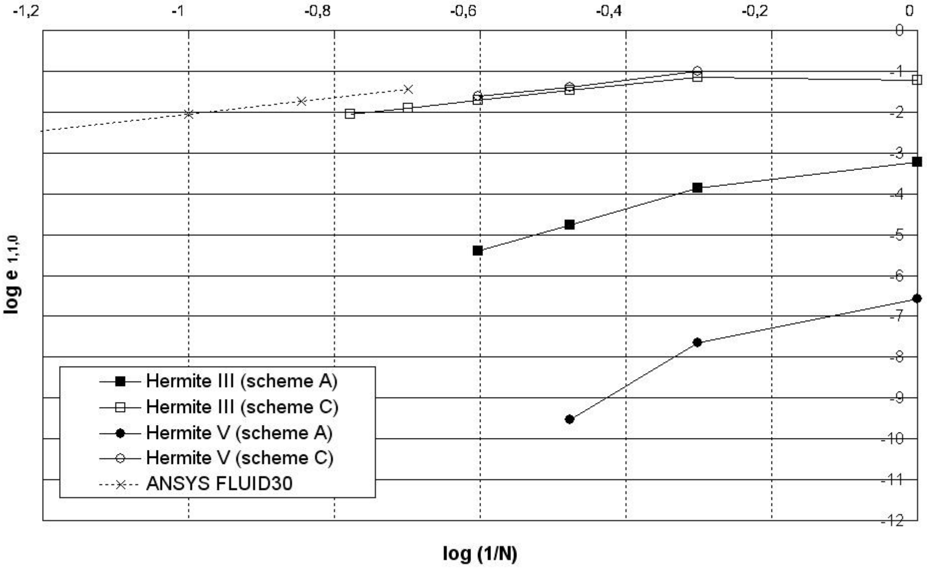

Figure 7.136: Rectangular cavity: $e_{[1,1,0]}$ with Scheme C

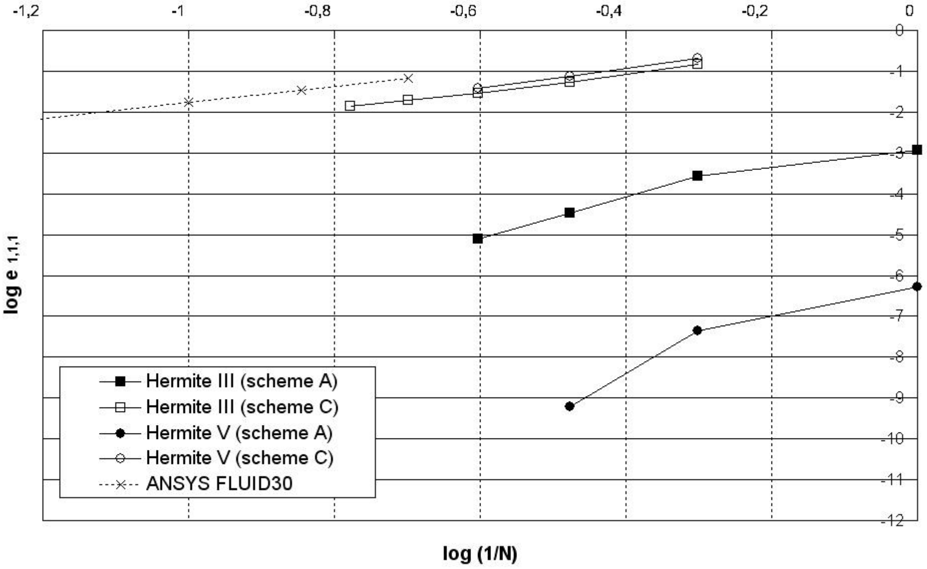

Figure 7.137: Rectangular cavity: $e_{[1,1,1]}$ with Scheme C

Chapter 8

Test cases

In this chapter applications of the proposed methodology to various problems are presented. Specifically, the chapter is structured in three sections.

First, Section 8.1 is dedicated to a comparison with the work presented in[1] by G. C. Provatidis. Specifically, in this section it is wanted to prove the effectiveness of the proposed Hybrid methodology and its advantages above the *Coons' Macroelements* introduced in.[1]

Section 8.2.1 regards curved domains in interior acoustics. Specifically, it concerns the problem of the air vibrating inside a cylindrical volume.

Section 8.3.1 pertains the modal analysis of a very simplified wing–box. The aim is to assess the performance of the proposed methodology for more complicated geometries. Preliminary results concerning this problem have just been presented in.[7]

8.1 Comparisons with the literature

In this section a rectangular acoustic cavity of dimensions $a = 2.5\ m$, $b = 1.1\ m$ and $c = 1\ m$ with a speed of sound $c_s = 1\ m/s$ is considered. The problem of the air vibrating inside this domain is the same that has been investigated by C. G. Provatidis in,[1] used to assess the validity of the so called *Coons' Macroelement*. Specifically, this is a brick element with nodes arranged only along the twelve edges and not throughout the volume (as the proposed Hermite or Hybrid bricks) or throughout the boundary (as the most conventional finite elements). In this element, the cubic B–Spline interpolation is used for the potential velocity.

The analysis proposed in[1] has been repeated here and the errors related to the eigenvalues with respect to the exact ones (that are given by Eq. 7.10 at the beginning of Section 7.3) has been compared with those presented by the author. The analysis regards only the 8 eigenvalues which results are available in the work of Provatidis. Specifically, the eigenvalues treated are those related to the $[0,0,0]$, $[1,0,0]$,$[0,1,0]$,$[0,0,1]$,$[1,1,0]$,$[1,0,1]$,$[2,0,0]$,$[3,0,0]$ modes. In figures, the Coons Macroelement will be referred to as the Provatidis Element.

Figure 8.1 shows the relative error (per cent) for each of the above mentioned eigenvalues, as evaluated in[1] as well as obtained using a Hybrid 3rd order formulation. The Coons Macroelement is chosen with a total number of nodes $n = 76$ whereas the Hybrid element has been used with $n = 27, 64$ (that correspond to $N = 2, 3$ elements in each direction respectively). According to the validation analysis presented in Subsection 7.3.6, the $[m, n, p]$ eigenvalue for the Hybrid 3rd order 8−node element is considered acceptably accurate only if $m, n, p \leq N$, where N is the number of subdivisions. Thus, the error for the last eigenvalue (*i.e.*, that related to the $[3, 0, 0]$ mode) is not considered for the Hybrid with $n = 27$ nodes (since it corresponds to a mesh of $N = 2$). For the set of results showed, it appears that, even though the Hybrid has been applied with less nodes, the relative errors are generally much lower. Table 8.1 contains the numerical results depicted in the preceding figure.

The Coons Macroelement uses a cubic B–Spline interpolation and needs the potential velocity as nodal unknown whereas the Hybrid uses the three–dimensional extension of the Coons Patch of Section 4.4 and uses 4 nodal unknowns. Since the amount of nodal unknowns is different in these two elements, the results should be showed also as a function of $1/N_{DOF}$. This is shown in Figs. 8.2 and 8.3 that depict the relative error (per cent) as a function of the degrees of freedom, for the eigenvalues related to the two sets $J1 = \{[1, 0, 0]; [0, 1, 0]; [0, 0, 1]\}$ and $J2 = \{[1, 1, 0]; [1, 0, 1]\}$. In particular, they show the superiority of the Hybrid over the Coons Macroelement also using less unknowns and hence, a minor computational effort.

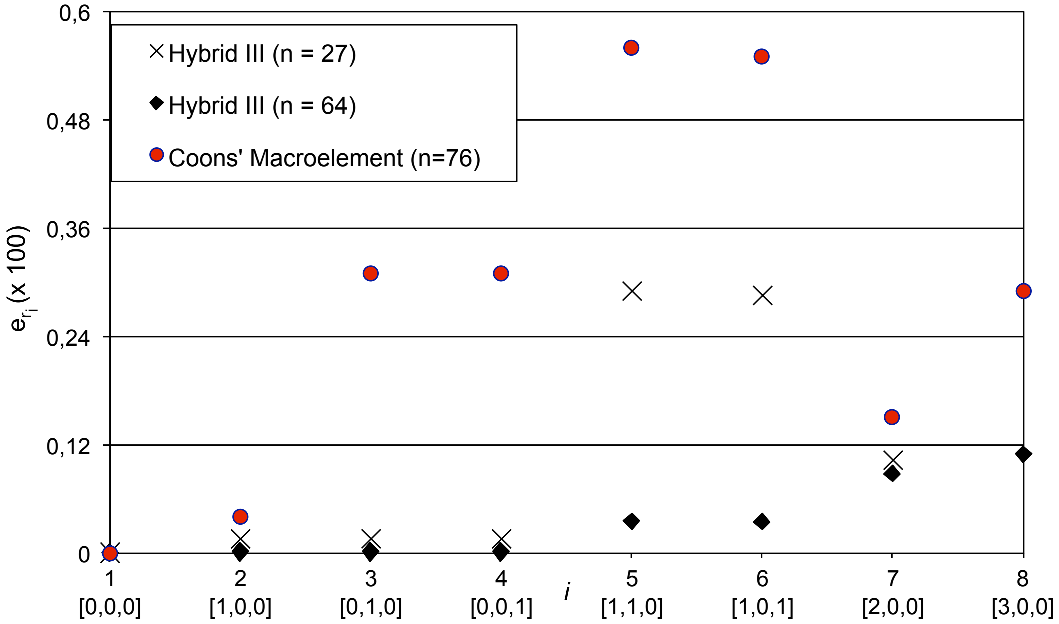

Figure 8.1: The Hybrid 3rd order 8−node *vs* the Provatidis Element

$[m,n,p]$	$\mu_{[m,n,p]}$	$e_{r_{[m,n,p]}}$ $(\times 100)$		
		Macroelement $(n=76)$	Hybrid III $(n=27)$	Hybrid III $(n=64)$
$[0,0,0]$	0	0	0.00	0.00
$[1,0,0]$	1.579	0.04	0.01	0.00
$[0,1,0]$	8.157	0.31	0.01	0.00
$[0,0,1]$	9.870	0.31	0.01	0.00
$[1,1,0]$	9.736	0.56	0.29	0.03
$[1,0,1]$	11.449	0.55	0.29	0.03
$[2,0,0]$	6.317	0.15	0.10	0.09
$[3,0,0]$	14.212	0.29	–	0.11

Table 8.1: Relative errors (per cent) of Fig. 8.1

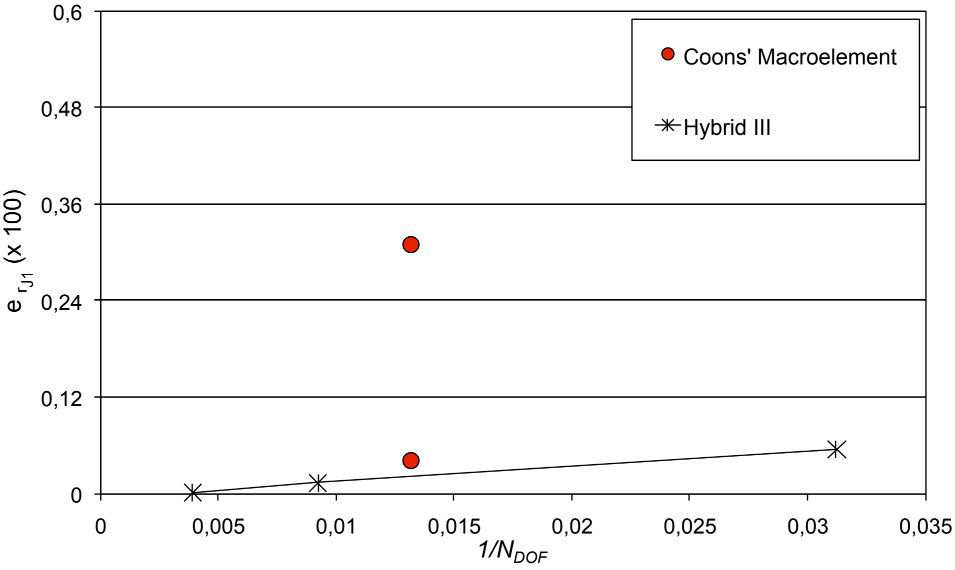

Figure 8.2: The Hybrid 3rd order $8-$node and the Provatidis Element vs $1/N_{DOF}$ (eigenvalues $[1,0,0];[0,1,0];[0,0,1]$)

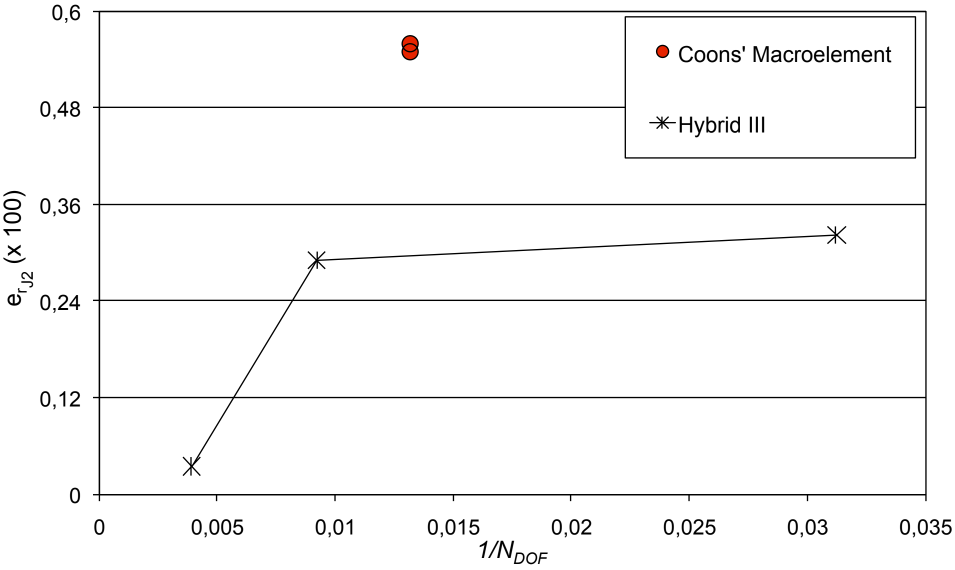

Figure 8.3: The Hybrid 3rd order $8-$node and the Provatidis Element vs $1/N_{DOF}$ (eigenvalues $[1,1,0];[1,0,1]$)

8.2 Acoustics

8.2.1 Cylindrical cavity

The proposed methodology has been applied to interior acoustics of curved volumes, such as cylindrical geometries. Specifically, the cylindrical cavity chosen has inner radius $R_i = 1$ and outer radius $R_o = 32$, with a length $\ell = 4$ (along the z–axis) and an angle of π. For simplicity, a speed of sound $c_s = 1m/s$ has been considered. The geometry has been meshed with an equal number of elements N along each direction (that now are r, θ and z of a cylindrical frame of reference). Since the geometry has been generated through the use of a single block, no block–boundary problem has to be managed. The Hermite 3rd order 8 node brick element has been used for the modal analysis.

The h–convergences for the first six eigenvalues are presented in Figs. from 8.4 to 8.9. In these images, those on the left represent the evaluated eigenvalues as a function of the number of elements N whereas those on the right depict the evaluated eigenvalues as a function of the total degrees of freedom N_{DOF}. The results obtained are compared with those related to the Ansys Fluid 30 element, specific for acoustic applications.

Results include the application of a reduction technique. Specifically, according to the results of Subsection 7.3.9 for acoustics applications, the IRS extension of the classical Guyan's reduction is used here. The left–side images reveal that the accuracy obtained with the reduced formulation is comparable with that related to the complete scheme, for a given subdivision N, even though the unknowns are reduced here by a factor 8 (all the derivatives are in fact considered as slave variables). This advantage is clearly shown in the right–side images, which reveal the better accuracy of the reduced formulation with respect to the complete one, as a function of the quantity of unknowns (and hence, as a function of the computational effort).

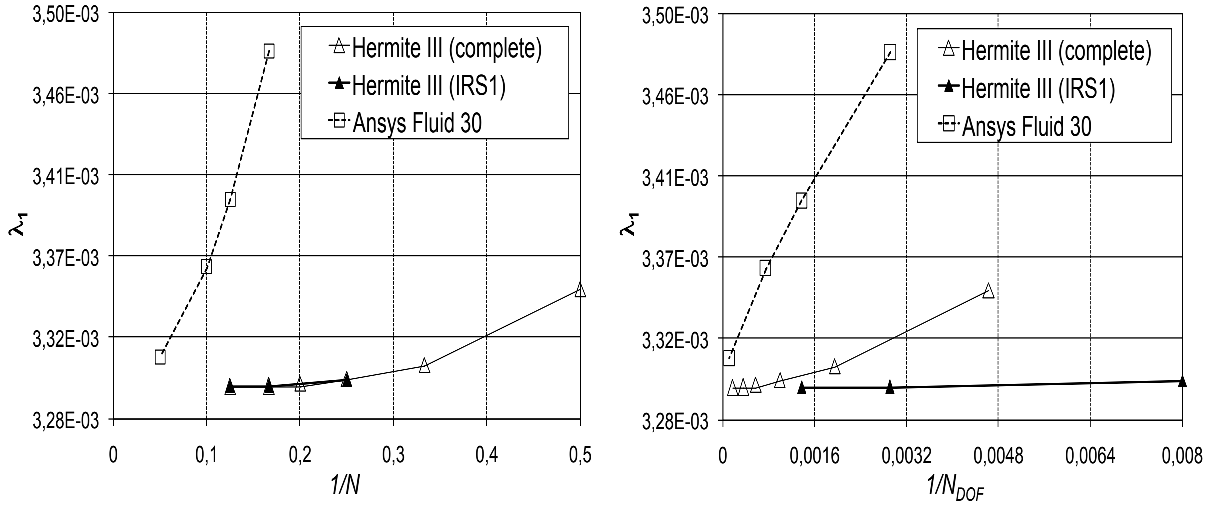

Figure 8.4: Cylindrical cavity: λ_1 vs $1/N$ and vs $1/N_{DOF}$

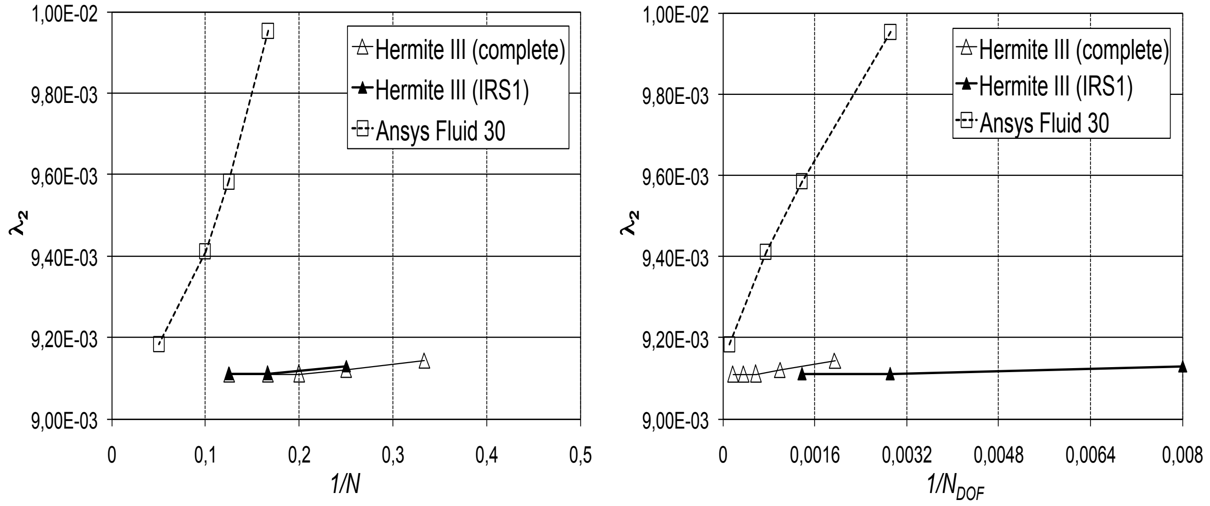

Figure 8.5: Cylindrical cavity: λ_2 vs $1/N$ and vs $1/N_{DOF}$

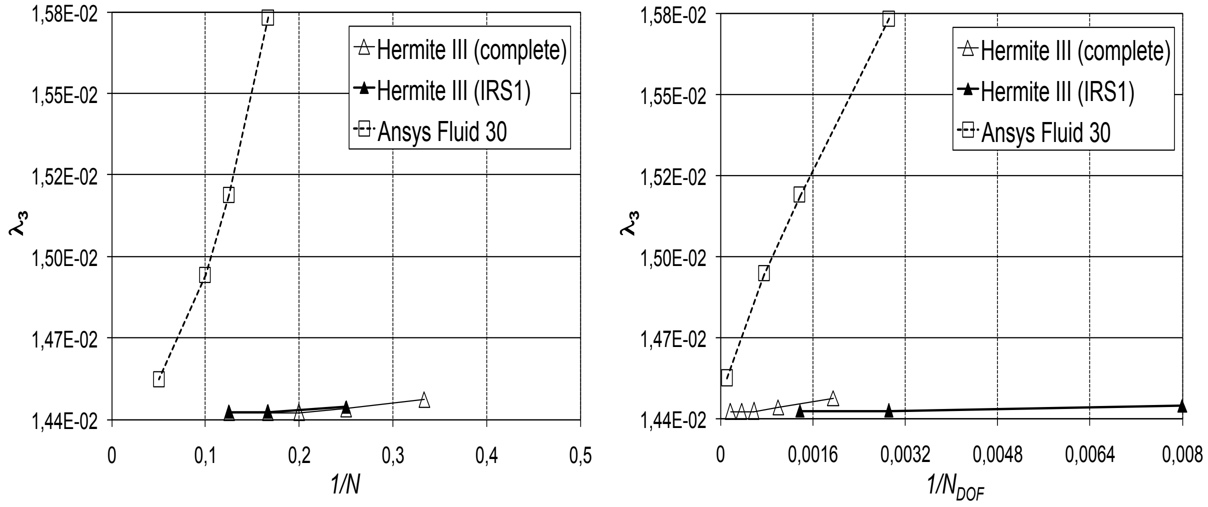

Figure 8.6: Cylindrical cavity: λ_3 *vs* $1/N$ and *vs* $1/N_{DOF}$

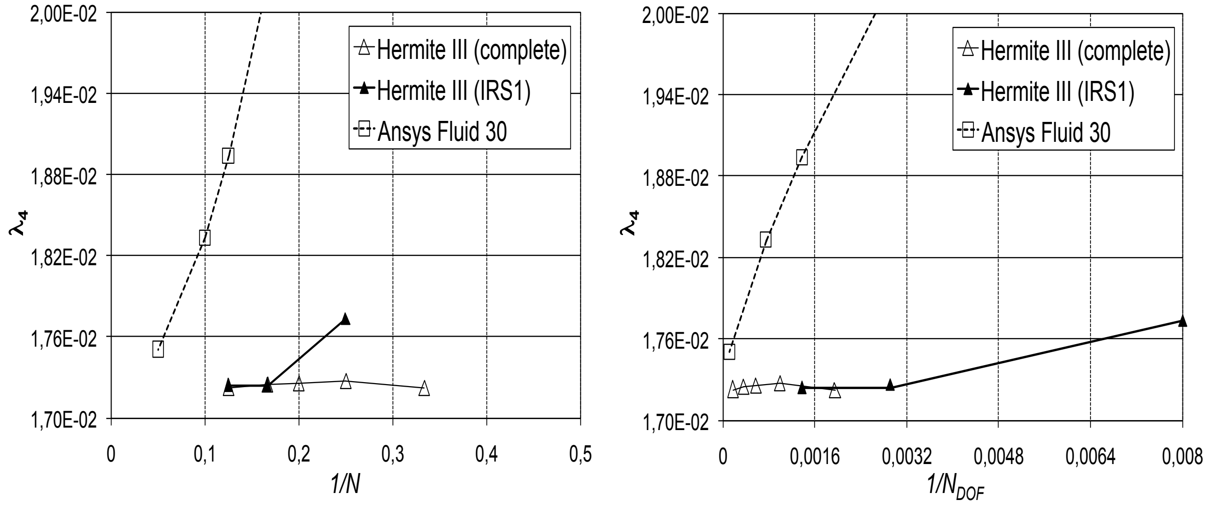

Figure 8.7: Cylindrical cavity: λ_4 *vs* $1/N$ and *vs* $1/N_{DOF}$

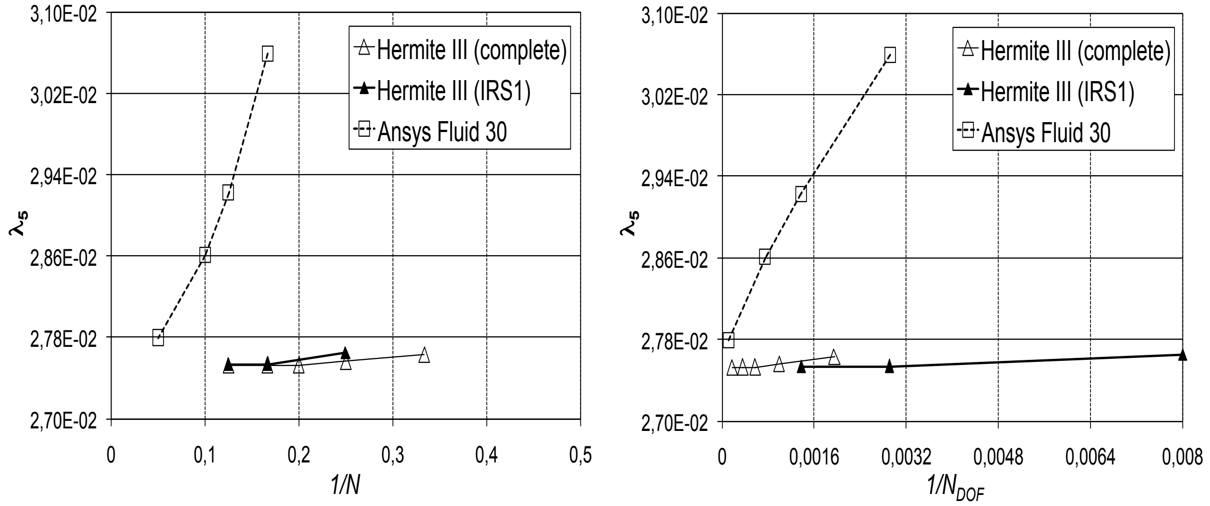

Figure 8.8: Cylindrical cavity: λ_5 vs $1/N$ and vs $1/N_{DOF}$

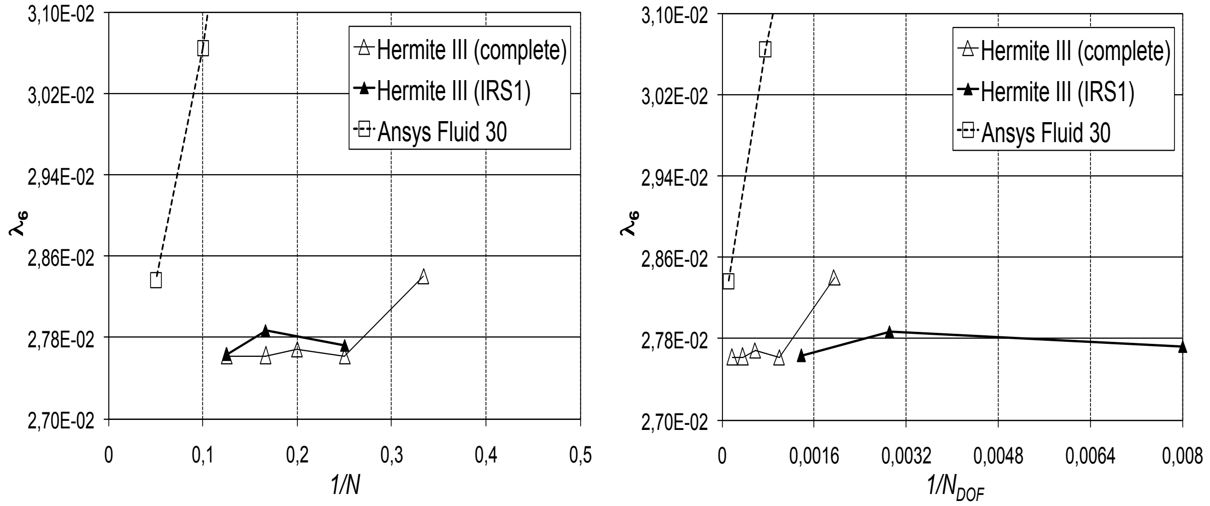

Figure 8.9: Cylindrical cavity: λ_6 vs $1/N$ and vs $1/N_{DOF}$

8.3 Structures

8.3.1 Simplified wing–box

Finally, in order to assess the method for relatively complex structures, consider the results for a simplified rectangular cross–section wing box model, that is, an aluminum ($E = 70GPa$, $\nu = .35$, $\rho = 2.7Kg/dm^3$) structure, with no ribs, no spars, no stringers, and with uniform thickness $\tau = .005m$. The structure has height $= 1.0m$, width $= 2.0m$, and length $= 5.0m$. This study has been preliminary addressed in the past and a first set of results is addressed in.[7]

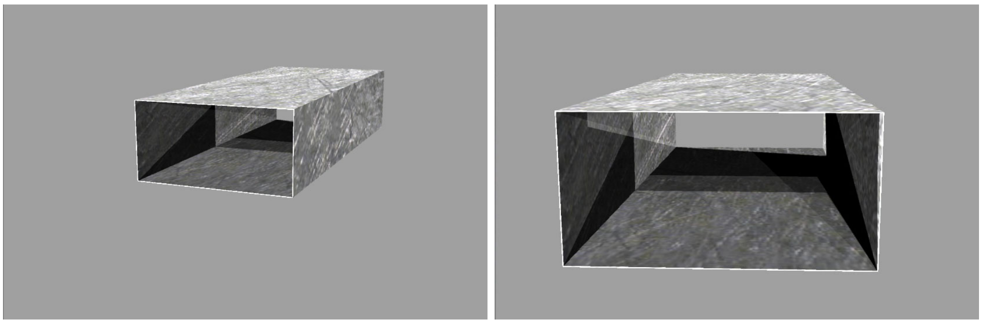

Figure 8.10: Simplified wing–box: lay–out

The structure is conceived as a combination of 8 blocks (*i.e.*, four blocks to describe the faces plus the four blocks to define the edges); hence, the block–boundary nodes problem of Section 2.3 may be considered. To avoid this issue a Hybrid third–order element is used along with its reduced formulation. Since the problem is purely structural, the reduction is accomplished using the standard Guyan's technique.

The results are presented in Figures from 8.11 to 8.15, which depict the five lowest bending frequencies ω_i expressed in Hertz. In the images on the left, the frequencies are presented as functions of $1/N$ whereas in those on the right they are depicted as functions of $1/N_{DOF}$. The left set of figures shows the negligibility of the loss in accuracy obtained applying the Guyan's reduction to all the nodal derivatives (the reduction factor here is hence of 1:4). The overall results indicate that the accuracy of the reduced Guyan element is comparable to that of the Hybrid third–order element in its complete formulation. The results are compared with those obtained using a Solid 186 element of Ansys, that is a 20 node brick with quadratic shape functions.

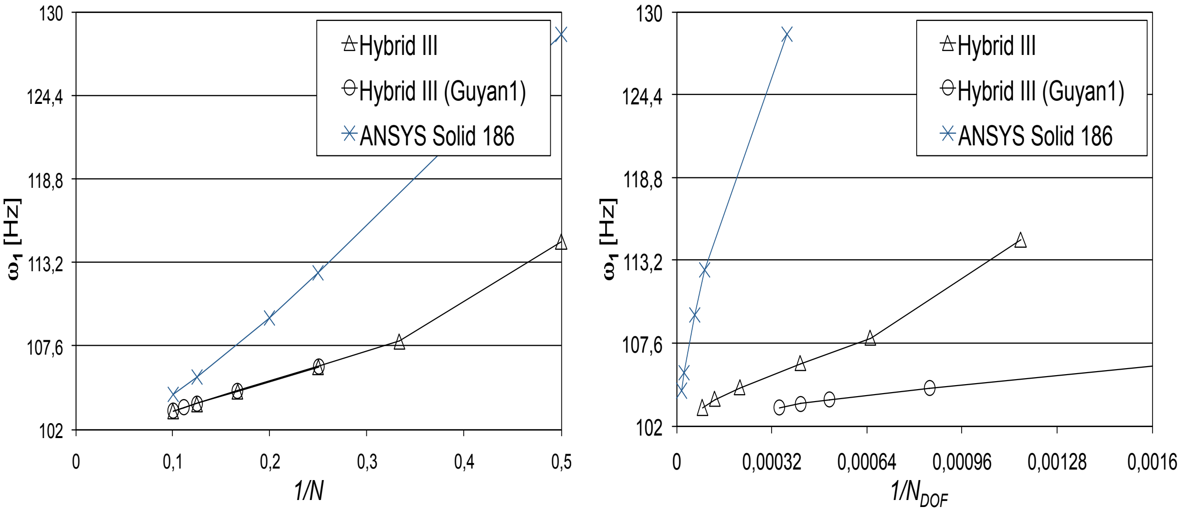

Figure 8.11: Simplified wing–box: ω_1 *vs* $1/N$ and *vs* $1/N_{DOF}$

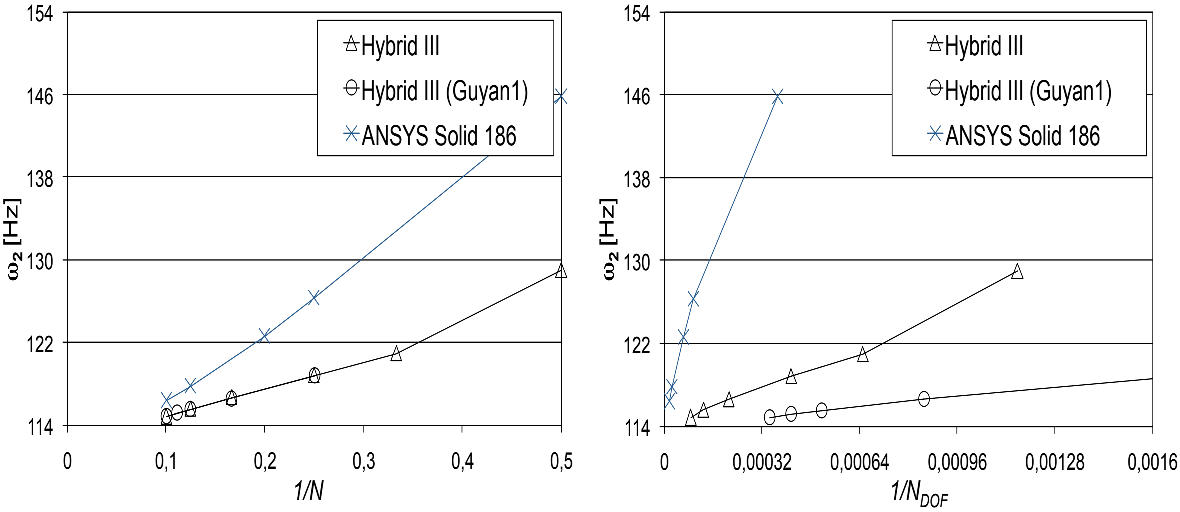

Figure 8.12: Simplified wing–box: ω_2 *vs* $1/N$ and *vs* $1/N_{DOF}$

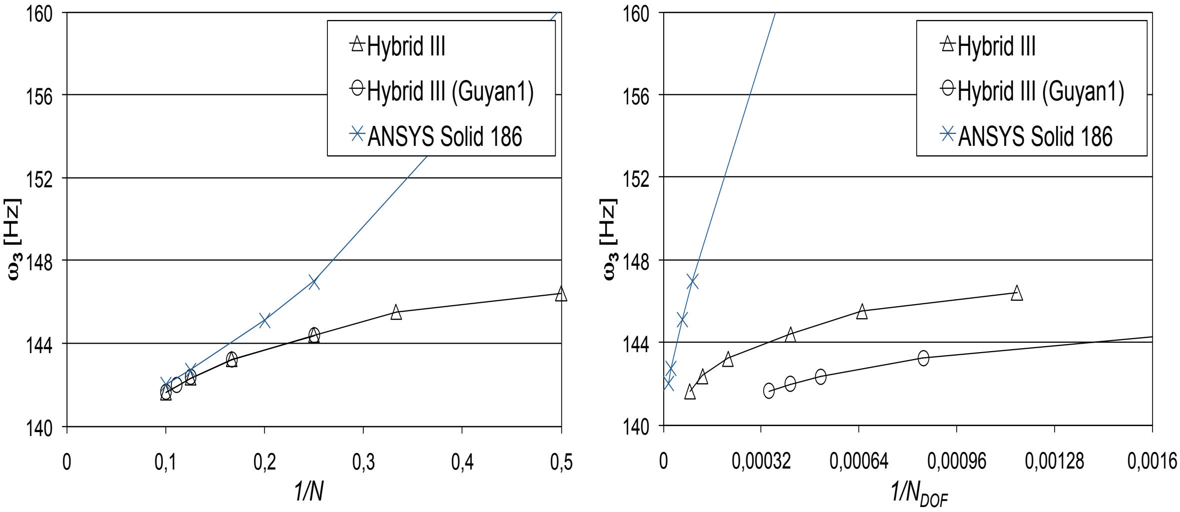

Figure 8.13: Simplified wing–box: ω_3 *vs* $1/N$ and *vs* $1/N_{DOF}$

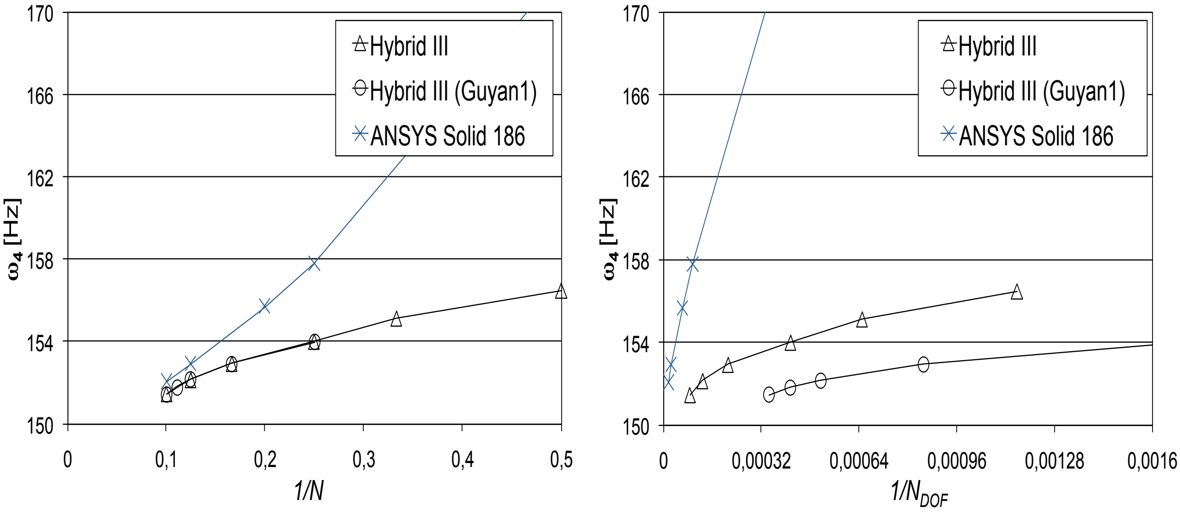

Figure 8.14: Simplified wing–box: ω_4 *vs* $1/N$ and *vs* $1/N_{DOF}$

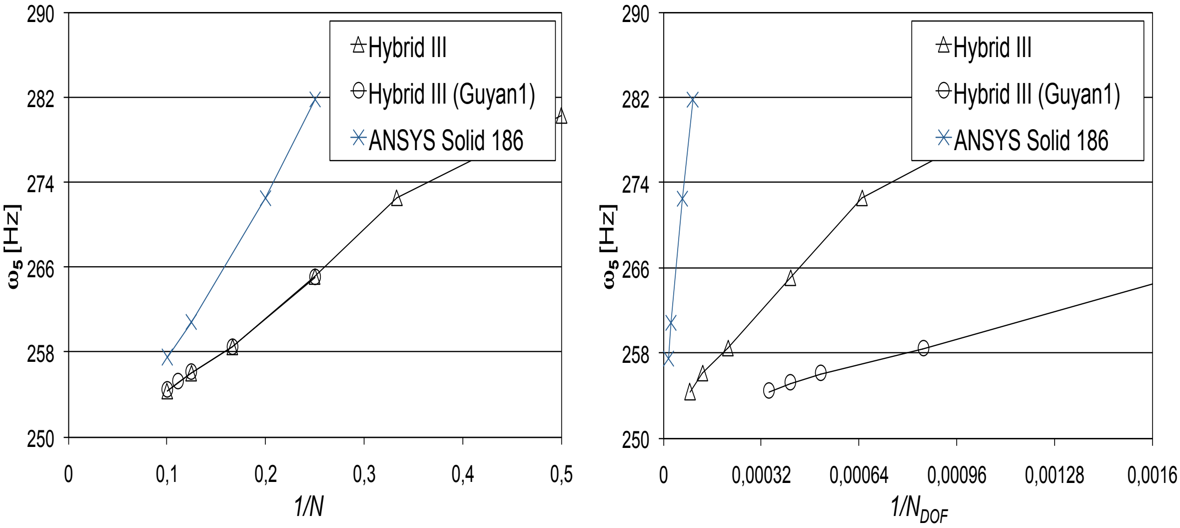

Figure 8.15: Simplified wing–box: ω_5 *vs* $1/N$ and *vs* $1/N_{DOF}$

Chapter 9

Concluding remarks

On the basis of the formulations proposed and considering the results presented, final considerations are in order.

To begin with, consider the 3rd order $8-$node Hybrid element. In such a formulation, all the monomials $\xi^p\eta^q\zeta^r$ with $p+q+r \leq 3$ are included in the shape functions. Hence, the scheme is of order three as it is for the Hermite scheme, even though half nodal unknowns are required. Same considerations hold for the Hybrid 7th order with respect to the Hermite 7th order (in this case one has a total of 256 unknowns for the Hybrid element *vs* 512 of the Hermite one). It means that, with a Hybrid formulation, one can reach the same (or a quite close) accuracy with half unknowns and hence, with a less computational effort. This is a first advantage of the Hybrid formulation (in both WIP and WEP configuration)

In addition, for the Hybrid 3rd order $8-$nodes and for the Hybrid 5th order $27-$nodes, only the nodal values of the function and of its three first–order partial derivatives are required to define the element geometry and the function (isoparametric formulation).

Thus, the key advantage of the WIP Hybrid elements is that they are exempt from the block–boundary problem, that affects the WEP schemes in case of discontinuous base vectors (see Section 2.3).

Hence, the goal of implementing an effective high–order elements based upon the Hermite interpolation is considered reached, at least in the sense of a first step toward the development of a FEM tool, to be efficiently used for acoustic design.

Of course, the WEP $p-$th order element provides an interpolation that is of class $\mathcal{C}^p$ (continuous with its derivatives up to the order p), whereas the

WIP element of same order, which is of class $\mathcal{C}^p$ within the element, is only of class $\mathcal{C}^1$ at the boundary between elements (however, this implies minimal penalization). Furthermore, a large percentage of the nodal unknowns in a WEP formulation are related to the derivatives. To be specific, for a WEP Hermite scheme of order p one has $(p+1)^3/8$ nodal unknowns, one of which is related to the function and the other $1-8/(p+1)^3$ related to the derivatives. Similarly, for a WEP Hybrid scheme, one has $(p+1)^3/16$ nodal unknowns (a half of the WEP Hermite), of which $1-(p+1)^3/16$ are derivatives. Instead, for a WIP Hybrid formulation only half unknowns are related to the (first) derivatives. This implies that the reduction of order, when applicable, is more effective when used on a WEP Hermite scheme.

The choice between the Hybrid schemes and the Hermite schemes depends upon both the complexity of the domain and the accuracy needed. A WIP Hybrid scheme leads to a very effective element in terms of user–friendliness. On the contrary, the WEP formulation, even though highly–accurate (class $\mathcal{C}^p$ at the interfaces) is quite more cumbersome to implement and, above all, affected by the block–boundary problem when the geometry presents discontinuous base vectors.

A final consideration about the future work required. As a first step, applications to various realistic coupled (fluid–structure) problems should be performed (also evaluating the possibility of parallel calculus). In particular, the noise generated by the turbolent boundary layer and the interior acoustic comfort may be studied. Also, the extension to dynamic problems may be analyzed. Also, it should be necessary to extend the possibility of analysis. In particular, it may be included in the code the possibility of having a certain acoustic impedance as well as different material models for the structural modeling. Then, dynamic analysis as well as harmonic response analysis of coupled systems may be performed.

Part III

Appendix

Appendix A

Interior acoustics – structural dynamics coupling

In this section the interaction between the dynamic of the air vibrating inside a cavity and the dynamics of the elastic structure that surrounds it is formulated and used in very simple test cases. Specifically, in Subsection A.1 the problem is formulated in terms of the displacement and the pressure whereas in Subsection A.2 an approach in terms of the displacement and the potential velocity is given.

A.1 Pressure–displacement formulation

The interaction between the dynamic of the fluid inside a cavity and that of the structure that surround it, can be formulated in terms of the displacement field $\mathbf{u}$ and of the pressure p. Consider an acoustic domain D_{A} surrounded by a structural domain D_{S}, such that Ω is the interface surface between the two adjacent domains ($i.e.$, $\Omega = \partial D_{\mathsf{A}} = \partial D_{\mathsf{S}}$). In this case, one has the governing equations given by:

$$\begin{aligned} &\rho_{\mathsf{S}}\ddot{\mathbf{u}}\left(\mathbf{x}_{\mathsf{S}},t\right) + L_{\mathsf{S}}\mathbf{u}\left(\mathbf{x}_{\mathsf{S}},t\right) = \mathbf{f}\left(\mathbf{x}_{\mathsf{S}},t\right) \qquad \mathbf{x} \in D_{\mathsf{S}} \\ &\frac{1}{c_s^2}\ddot{p}\left(\mathbf{x}_{\mathsf{A}},t\right) - \nabla^2 p\left(\mathbf{x}_{\mathsf{A}},t\right) = 0 \qquad \mathbf{x} \in D_{\mathsf{A}} \end{aligned} \tag{A.1}$$

where ρ_{S} is the density of the elastic structure (assumed to be homogeneous in D_{S}) and $\mathbf{u} = \mathbf{u}\left(\mathbf{x}_{\mathsf{S}},t\right)$ is the 3–D displacement function whereas $p = p\left(\mathbf{x}_{\mathsf{A}},t\right)$ is the pressure field. Boundary conditions have to be imposed. For the force $\mathbf{f} = \mathbf{f}\left(\mathbf{x}_{\mathsf{S}},t\right)$ assume that,

$$\mathbf{f} = p\,\mathbf{n} \tag{A.2}$$

where $\mathbf{n} = \mathbf{n}\left(\mathbf{x}_\mathsf{S}, t\right)$ is the normal unit vector at the interface fluid–structure. Considering Eqs. 2.4 and 2.5 and indicating with $\boldsymbol{\Psi}_n = \boldsymbol{\Psi}_n(\xi^\alpha)$ and $\chi_n = \chi_n(\xi^\alpha)$ the shape functions used to interpolate the displacement and the pressure respectively, one has:

$$\mathbf{u} = \sum_n u_n \boldsymbol{\Psi}_n \qquad \text{and} \qquad p = \sum_n p_n \chi_n \tag{A.3}$$

Using Eq. A.3 in a Galerkin approximation of Eqs. A.1, the first equation of Eqs. A.1, expressed in frequency, becomes

$$-\,\omega^2 \mathsf{M}_\mathsf{S} \mathsf{u} + \mathsf{K}_\mathsf{S} \mathsf{u} = \mathsf{R}\mathsf{p} \tag{A.4}$$

where M_S and K_S are the structural mass and stiffness matrices introduced in Section 6.2 whereas $\mathsf{R} = [r_{mn}]$ is given by

$$r_{mn} = \int_\Omega \boldsymbol{\Psi}_m(\xi^\alpha) \cdot \mathbf{n}\; \chi_n(\xi^\alpha)\; \mathrm{d}\Omega. \tag{A.5}$$

having indicated with Ω the fluid–structure interface (that is a surface for three–dimensional domains).

Next, in view of the use of the second equation of Eqs. A.1, consider the acoustic boundary condition of impermeable wall[1]

$$\frac{\partial p}{\partial n} = \rho_\mathsf{A} \ddot{\mathbf{u}} \cdot \mathbf{n} \qquad \mathbf{x} \in \Omega \tag{A.6}$$

Introduce a function $\delta = \delta(\mathbf{x}_\mathsf{A})$ such that:

$$\delta(\mathbf{x}_\mathsf{A}) = 0 \qquad \mathbf{x}_\mathsf{A} \in D_\mathsf{A} \qquad \text{and} \qquad \lim_{\mathbf{x}_\mathsf{A} \to\, \Omega} \delta(\mathbf{x}_\mathsf{A}) = 1 \tag{A.7}$$

The second equation of Eqs. A.1 can be rewritten, taking into the domain D_A the condition at the boundary Ω of Eq. A.6 through the function $\delta = \delta(\mathbf{x}_\mathsf{A})$ of Eq. A.7, as:

$$\frac{1}{c_s^2} \ddot{p}\left(\mathbf{x}_\mathsf{A}, t\right) - \nabla^2 p\left(\mathbf{x}_\mathsf{A}, t\right) = \rho_\mathsf{A} \ddot{\mathbf{u}} \cdot \mathbf{n}\; \delta \qquad \mathbf{x} \in D_\mathsf{A} \tag{A.8}$$

Similarly to the discretization approach used for the first equation of Eqs. A.1, one has:

$$-\,\omega^2 \mathsf{M}_\mathsf{A} \mathsf{p} + \mathsf{K}_\mathsf{A} \mathsf{p} = -\omega^2 \mathsf{R}^T \mathsf{u} \tag{A.9}$$

---

[1] Equation A.6 can be explained considering that $p = \dot{\varphi}$ and $\nabla\varphi = \dot{\mathbf{u}}$. In fact, $\frac{\partial p}{\partial n} = \frac{\partial}{\partial n}(\rho_\mathsf{A} \dot{\varphi}) = \rho_\mathsf{A} \frac{\partial \dot{\varphi}}{\partial n} = \rho_\mathsf{A} \frac{\partial}{\partial t} \frac{\partial \varphi}{\partial n} = \rho_\mathsf{A} \frac{\partial}{\partial t} \nabla\varphi \cdot \mathbf{n} = \rho_\mathsf{A} \ddot{\mathbf{u}} \cdot \mathbf{n}$.

In summary, one has for the discretization of the problem given by Eqs. A.1 the following coupled system

$$\begin{cases} -\omega^2 \mathsf{M}_\mathsf{S} \mathsf{u} + \mathsf{K}_\mathsf{S} \mathsf{u} = \mathsf{R}\mathsf{p} \\ \\ -\omega^2 \mathsf{M}_\mathsf{A} \mathsf{p} + \mathsf{K}_\mathsf{A} \mathsf{p} = -\omega^2 \mathsf{R}^T \mathsf{u} \end{cases} \tag{A.10}$$

that can be rewritten as

$$-\omega^2 \mathsf{M}\mathsf{z} + \mathsf{K}\mathsf{z} = 0 \tag{A.11}$$

with

$$m_{mn} = \begin{bmatrix} \mathsf{M}_S & 0 \\ -\mathsf{R}^T & \mathsf{M}_A \end{bmatrix} \qquad \text{and} \qquad k_{mn} = \begin{bmatrix} \mathsf{K}_S & \mathsf{R} \\ 0 & \mathsf{K}_A \end{bmatrix} \tag{A.12}$$

where now $\mathsf{z}^\mathsf{T} = [\mathsf{z}^\mathsf{T}_{S_n}, \mathsf{z}^\mathsf{T}_{A_n}]$ is the vector of the unknown nodal values referred to the coupled system (structure and air). The meaning of the matrix R in equation A.12 is that of a structure/air coupling.

A.2 Potential velocity–displacement formulation

The interaction between the dynamic of the fluid inside a cavity and that of the structure that surround it, can be also formulated in terms of the potential velocity φ.

The formulation in terms of the velocity potential φ is immediately given from Subsection A.1, once considered that $p = \dot{\varphi}$ and $\nabla\varphi = \dot{\mathbf{u}}$. In particular, one obtains:

$$-\omega^2 \mathsf{M}\mathsf{z} + i\omega \mathsf{G}\mathsf{z} + \mathsf{K}\mathsf{z} = 0 \tag{A.13}$$

where again $\mathsf{z}^\mathsf{T} = [\mathsf{z}^\mathsf{T}_{S_n}, \mathsf{z}^\mathsf{T}_{A_n}]$ is the vector of the unknown nodal values referred to the coupled system (structure and air), whereas the mass and stiffness matrices are respectively given by $\mathsf{M} = [m_{mn}]$ and $\mathsf{K} = [k_{mn}]$, with

$$\mathsf{M} = \begin{bmatrix} \mathsf{M}_\mathsf{S} & \mathsf{O} \\ \mathsf{O} & \mathsf{M}_\mathsf{A} \end{bmatrix} \qquad \mathsf{K} = \begin{bmatrix} \mathsf{K}_\mathsf{S} & \mathsf{O} \\ \mathsf{O} & \mathsf{K}_\mathsf{A} \end{bmatrix} \tag{A.14}$$

In addition, it may be shown that the coupling is expressed through an antisymmetric matrix G and hence it is of gyroscopic nature. Specifically, we have $\mathsf{G} = [g_{mn}]$ with:

$$\mathsf{G} = \begin{bmatrix} \mathsf{O} & \mathsf{R} \\ -\mathsf{R}^T & \mathsf{O} \end{bmatrix} \tag{A.15}$$

$\mathsf{R} = [r_{mn}]$ is the gyroscopic coupling matrix, that has been introduced in Eq. A.5 of the preceding subsection.

In order to solve the linear system of Eq. A.13, consider the transformation

$$i\omega \mathsf{z} = \mathsf{x} \tag{A.16}$$

Eq. A.13 may be rearranged in a first–order system as:

$$\left\{ \begin{bmatrix} \mathsf{O} & -\mathsf{I} \\ \mathsf{K} & \mathsf{G} \end{bmatrix} + i\omega \begin{bmatrix} \mathsf{I} & \mathsf{O} \\ \mathsf{O} & \mathsf{M} \end{bmatrix} \right\} \begin{bmatrix} \mathsf{z} \\ \mathsf{x} \end{bmatrix} = \begin{bmatrix} \mathsf{O} \\ \mathsf{O} \end{bmatrix} \tag{A.17}$$

Then, left–multiplying the first set of equations by $i\mathsf{K}$, one obtains:

$$\left\{ \begin{bmatrix} \mathsf{O} & -i\mathsf{K} \\ i\mathsf{K} & i\mathsf{G} \end{bmatrix} - \omega \begin{bmatrix} \mathsf{K} & \mathsf{O} \\ \mathsf{O} & \mathsf{M} \end{bmatrix} \right\} \begin{bmatrix} \mathsf{z} \\ \mathsf{x} \end{bmatrix} = \begin{bmatrix} \mathsf{O} \\ \mathsf{O} \end{bmatrix} \tag{A.18}$$

Let

$$\mathsf{A} = \begin{bmatrix} \mathsf{O} & -i\mathsf{K} \\ i\mathsf{K} & i\mathsf{G} \end{bmatrix} \quad ; \quad \mathsf{B} = \begin{bmatrix} \mathsf{K} & \mathsf{O} \\ \mathsf{O} & \mathsf{M} \end{bmatrix} \quad \text{and} \quad \mathsf{y} = \begin{bmatrix} \mathsf{z} \\ \mathsf{x} \end{bmatrix} \tag{A.19}$$

so as Eq. A.18 can be written as $(\mathsf{A} - \omega\mathsf{B})\mathsf{y} = 0$. Note that A is Hermitian, since G is antisymmetric (and clearly, K is symmetric)[2] whereas B is a real symmetric, positive definite matrix; hence the eigenvalues are expected to be real.

---

[2] In fact, since $\mathsf{G}^T = -\mathsf{G}$ and $\mathsf{K}^T = \mathsf{K}$, one has

$$\mathsf{A}^T = \begin{bmatrix} \mathsf{O} & i\mathsf{K}^T \\ -i\mathsf{K}^T & i\mathsf{G}^T \end{bmatrix} = \begin{bmatrix} \mathsf{O} & i\mathsf{K} \\ -i\mathsf{K} & -i\mathsf{G} \end{bmatrix} = \mathsf{A}^*$$

being A^* the complex conjugate of A.

Appendix B

An algorithm for geometry generation

Here, a user–friendly algorithm that allows one to generate a block, starting from the description of the twelve edges is presented. Indeed, the geometry preprocessor may be conceived as a collection of blocks as it is simpler and clearer to talk about the 'edge of the block', rather than the 'values of the unknown function along the edge of the brick'. These blocks would then constitute the building blocks of a geometry processor for complicated surface geometries. The starting point is the generation of the six surfaces. For this, an extension of the Coons patch[9] has been used (see also the work of Paoluzzi[18]). The extension is motivated by the desire to have, at the boundaries, a continuous normal, at least for those patch surfaces that constitute the boundary of the overall geometry.

The objective is obtained in two steps. In the first one, the basic surface (*i.e.*, the surface that goes through the edges, without imposing the condition on the normal at the boundary), which consists of a Coons patch, has been defined. This is presented in Section B.1, which is basically a review the Coons patch formulation. In order to avoid slope discontinuities between adjacent patches, we impose an additional condition on the normal at the patch boundary. The resulting surface is referred to as the "continuous–normal surface", the continuity of the normal being understood at the patch boundary (Section B.2). Finally, one can use the three–dimensional extension of the Coons patch (see Section 4.3) to build a block, starting from the six boundary surfaces thereby obtained.

B.1 The basic surface: a Coons patch

Consider the Coons patch defined in Section 4.2. We assume the functions $\mathbf{x}_1(\eta)$, $\mathbf{x}_2(\xi)$, $\mathbf{x}_3(\eta)$, $\mathbf{x}_4(\xi)$ to be prescribed and we want to obtain a surface having these lines as edges. The function $\mathbf{x}_0(\xi,\eta)$, which describes the basic surface, is a Coons patch, therefore

$$\begin{aligned}&\mathbf{x}_0(\xi,\eta)\\&=\frac{1+\xi}{2}\mathbf{x}_1(\eta)+\frac{1+\eta}{2}\mathbf{x}_2(\xi)+\frac{1-\xi}{2}\mathbf{x}_3(\eta)+\frac{1-\eta}{2}\mathbf{x}_4(\xi)\\&-\frac{1+\xi}{2}\frac{1+\eta}{2}\mathbf{x}_{++}-\frac{1+\xi}{2}\frac{1-\eta}{2}\mathbf{x}_{+-}-\frac{1-\xi}{2}\frac{1+\eta}{2}\mathbf{x}_{-+}-\frac{1-\xi}{2}\frac{1-\eta}{2}\mathbf{x}_{--}\end{aligned} \tag{B.1}$$

For future reference we introduce the base vectors of the patch

$$\mathbf{a}_{0_1}(\xi,\eta):=\frac{\partial\mathbf{x}_0}{\partial\xi}\quad\text{and}\quad\mathbf{a}_{0_2}(\xi,\eta):=\frac{\partial\mathbf{x}_0}{\partial\eta}, \tag{B.2}$$

and its normal

$$\mathbf{n}_0(\xi,\eta)=\frac{\mathbf{a}_{0_1}\times\mathbf{a}_{0_2}}{\|\mathbf{a}_{0_1}\times\mathbf{a}_{0_2}\|}. \tag{B.3}$$

To be specific, we have

$$\begin{aligned}&\mathbf{a}_{0_1}(\xi,\eta)\\&=\frac{1}{2}\mathbf{x}_1(\eta)+\frac{1+\eta}{2}\,\mathbf{x}_2'(\xi)-\frac{1}{2}\mathbf{x}_3(\eta)+\frac{1-\eta}{2}\,\mathbf{x}_4'(\xi)\\&-\frac{1+\eta}{2}\,\frac{\mathbf{x}_{++}-\mathbf{x}_{-+}}{2}-\frac{1-\eta}{2}\,\frac{\mathbf{x}_{+-}-\mathbf{x}_{--}}{2}\\&\mathbf{a}_{0_2}(\xi,\eta)\\&=\frac{1+\xi}{2}\,\mathbf{x}_1'(\eta)+\frac{1}{2}\mathbf{x}_2(\xi)+\frac{1-\xi}{2}\,\mathbf{x}_3'(\eta)-\frac{1}{2}\mathbf{x}_4(\xi)\\&-\frac{1+\xi}{2}\,\frac{\mathbf{x}_{++}-\mathbf{x}_{+-}}{2}-\frac{1-\xi}{2}\,\frac{\mathbf{x}_{-+}-\mathbf{x}_{--}}{2}\end{aligned}$$

which may be used to evaluate $\mathbf{n}_0(\xi,\eta)$ according to Eq. B.3.

B.2 The continuous–normal surface

Next, as mentioned above, we impose normal continuity between adjacent patches (using the procedure illustrated below). The resulting surface is denoted as the "continuous–normal surface". We seek for a surface described in the form

$$\mathbf{x}(\xi,\eta)=\mathbf{x}_0(\xi,\eta)+\zeta(\xi,\eta)\mathbf{n}_0(\xi,\eta) \tag{B.4}$$

where the function $\zeta(\xi,\eta)$ is to be determined. To begin with, $\zeta(\xi,\eta)=0$ must be imposed at the patch boundary, so as not to alter the boundary itself.

Next, we want to impose that the surface $\mathbf{x} = \mathbf{x}(\xi, \eta)$ assumes a prescribed normal $\mathbf{n}$ at the boundary. Hence, $\mathbf{n}(\pm 1, \eta)$ and $\mathbf{n}(\xi, \pm 1)$ are assumed to be known. In order to do this, note that the base vectors of the continuous–normal surface are given by

$$\begin{aligned} \mathbf{a}_1(\xi, \eta) &:= \frac{\partial \mathbf{x}(\xi, \eta)}{\partial \xi} = \mathbf{a}_{0_1} + \frac{\partial \zeta}{\partial \xi}\mathbf{n}_0 + \zeta \frac{\partial \mathbf{n}_0}{\partial \xi} \\ \mathbf{a}_2(\xi, \eta) &:= \frac{\partial \mathbf{x}(\xi, \eta)}{\partial \eta} = \mathbf{a}_{0_2} + \frac{\partial \zeta}{\partial \eta}\mathbf{n}_0 + \zeta \frac{\partial \mathbf{n}_0}{\partial \eta}. \end{aligned} \tag{B.5}$$

In order for the surface to assume the prescribed normal $\mathbf{n}$ at the edges 1 or 3 (*i.e.*, for $\xi = \pm 1$), it is sufficient to impose that

$$\mathbf{a}_1 \cdot \mathbf{n} = 0 \qquad (\xi = \pm 1). \tag{B.6}$$

This yields, recalling that $\zeta = 0$ along the boundary and using Eq. B.5,

$$\mathbf{a}_{0_1} \cdot \mathbf{n} + \frac{\partial \zeta}{\partial \xi}\mathbf{n}_0 \cdot \mathbf{n} = 0 \qquad (\xi = \pm 1) \tag{B.7}$$

Similarly, for the boundaries 2 and 4,

$$\mathbf{a}_{0_2} \cdot \mathbf{n} + \frac{\partial \zeta}{\partial \eta}\mathbf{n}_0 \cdot \mathbf{n} = 0 \qquad (\eta = \pm 1) \tag{B.8}$$

Hence, we have

$$\left.\frac{\partial \zeta}{\partial \xi}\right|_{\xi = \pm 1} = -\left.\frac{\mathbf{a}_{0_1} \cdot \mathbf{n}}{\mathbf{n}_0 \cdot \mathbf{n}}\right|_{\xi = \pm 1} =: F_\pm(\eta) \tag{B.9}$$

$$\left.\frac{\partial \zeta}{\partial \eta}\right|_{\eta = \pm 1} = -\left.\frac{\mathbf{a}_{0_2} \cdot \mathbf{n}}{\mathbf{n}_0 \cdot \mathbf{n}}\right|_{\eta = \pm 1} =: G_\pm(\xi) \tag{B.10}$$

where $F_\pm(\eta)$ and $G_\pm(\xi)$ are known functions.

Recall that $N_\pm(\alpha)$ (for $\alpha \in [-1, 1]$) denotes the Hermite interpolation polynomials connected to the derivatives (see Eq. 2.2 of Section 2.1), which are such that $N_+(\pm 1) = 0$, $N'_+(1) = 1$, $N'_+(-1) = 0$ and $N_-(\pm 1) = 0$, $N'_-(1) = 0$, $N'_-(-1) = 1$. We seek for a distribution $\zeta(\xi, \eta)$ of the type

$$\zeta(\xi, \eta) = f_+(\eta)N_+(\xi) + f_-(\eta)N_-(\xi) + g_+(\xi)N_+(\eta) + g_-(\xi)N_-(\eta) \tag{B.11}$$

which automatically satisfies the condition $\zeta = 0$ at the boundary. Imposing the conditions given in Eqs. B.9 and B.10, we have

$$\begin{aligned} \left.\frac{\partial \zeta}{\partial \xi}\right|_{\xi = \pm 1} &= f_\pm(\eta) + g'_+(\pm 1)N_+(\eta) + g'_-(\pm 1)N_-(\eta) = F_\pm(\eta) \\ \left.\frac{\partial \zeta}{\partial \eta}\right|_{\eta = \pm 1} &= g_\pm(\xi) + f'_+(\pm 1)N_+(\xi) + f'_-(\pm 1)N_-(\xi) = G_\pm(\xi) \end{aligned} \tag{B.12}$$

Next, note that the corner values of $F'_\pm(\eta)$ and $G'_\pm(\xi)$ are not independent. Indeed, using Eqs. B.9 and B.10, we have:

$$\begin{aligned}
\left.\frac{\partial^2\zeta}{\partial\xi\partial\eta}\right|_{\xi=+1,\eta=+1} &= F'_+(+1) = G'_+(+1)\\
\left.\frac{\partial^2\zeta}{\partial\xi\partial\eta}\right|_{\xi=+1,\eta=-1} &= F'_+(-1) = G'_-(+1)\\
\left.\frac{\partial^2\zeta}{\partial\xi\partial\eta}\right|_{\xi=-1,\eta=+1} &= F'_-(+1) = G'_+(-1)\\
\left.\frac{\partial^2\zeta}{\partial\xi\partial\eta}\right|_{\xi=-1,\eta=-1} &= F'_-(-1) = G'_-(-1)
\end{aligned}$$

On the other hand, Eq. B.12 implies

$$\begin{aligned}
\left.\frac{\partial^2\zeta}{\partial\xi\partial\eta}\right|_{\xi=+1,\eta=+1} &= f'_+(+1) + g'_+(+1)\\
\left.\frac{\partial^2\zeta}{\partial\xi\partial\eta}\right|_{\xi=+1,\eta=-1} &= f'_+(-1) + g'_-(+1)\\
\left.\frac{\partial^2\zeta}{\partial\xi\partial\eta}\right|_{\xi=-1,\eta=+1} &= f'_-(+1) + g'_+(-1)\\
\left.\frac{\partial^2\zeta}{\partial\xi\partial\eta}\right|_{\xi=-1,\eta=-1} &= f'_-(-1) + g'_-(-1)
\end{aligned}$$

Thus, we have, for instance

$$\begin{aligned}
g'_+(1) &= F'_+(+1) - f'_+(+1)\\
g'_-(1) &= F'_+(-1) - f'_+(-1)
\end{aligned}$$

and the first of Eqs. B.12 becomes

$$\begin{aligned}
&F'_+(\eta)\\
&= f'_+(\eta) + (F'_+(1) - f'_+(1))N_+(\eta) + (F'_+(-1) - f'_+(-1))N_-(\eta)
\end{aligned}$$

or

$$F'_+(\eta) - F'_+(1)N_+(\eta) - F'_+(-1)N_-(\eta) = f'_+(\eta) - f'_+(1)N_+(\eta) - f'_+(-1)N_-(\eta)$$

which is satisfied by $F_+(\eta) = f_+(\eta)$. Similar results are obtained from the other equations. Thus, we have, finally (combining with Eq. B.11):

$$\zeta(\xi,\eta) = F_+(\eta)N_+(\xi) + F_-(\eta)N_-(\xi) + G_+(\xi)N_+(\eta) + G_-(\xi)N_-(\eta) \quad \text{(B.13)}$$

with $F_\pm(\eta)$ and $G_\pm(\xi)$ defined in Eqs. B.9 and B.10. Once determined $\zeta = \zeta(\xi, \eta)$, combining with Eq. B.4 one obtains $\mathbf{x}(\xi, \eta)$, along with $\mathbf{a}_1$ and $\mathbf{a}_2$ from Eqs. B.5 as well as $\mathbf{n}(\xi, \eta)$ from $\mathbf{n}(\xi, \eta) = \mathbf{a}_1 \times \mathbf{a}_2 / \|\mathbf{a}_1 \times \mathbf{a}_2\|$.

Next, recall that $\mathbf{a}_\alpha$ are given by Eqs. B.5. In order to make use of these expressions, we need $\partial\zeta/\partial\xi$ and $\partial\zeta/\partial\eta$ as well as $\partial\mathbf{n}_0/\partial\xi$ and $\partial\mathbf{n}_0/\partial\eta$. The first two are obtained from Eq. B.5 which yelds

$$\frac{\partial\zeta}{\partial\xi} = F_+(\eta)N'_+(\xi) + F_-(\eta)N'_-(\xi) + G'_+(\xi)N_+(\eta) + G'_-(\xi)N_-(\eta) \tag{B.14}$$

$$\frac{\partial\zeta}{\partial\eta} = F'_+(\eta)N_+(\xi) + F'_-(\eta)N_-(\xi) + G_+(\xi)N'_+(\eta) + G_-(\xi)N'_-(\eta) \tag{B.15}$$

Therefore, we need $F'_\pm(\eta)$ and $G'_\pm(\xi)$ which, according to Eqs. B.9 and B.10 are given by

$$\begin{aligned} F'_\pm(\eta) &= -\frac{\partial}{\partial\eta}\left(\frac{\mathbf{a}_{01}\cdot\mathbf{n}}{\mathbf{n}_0\cdot\mathbf{n}}\right)\Bigg|_{\xi=\pm1} \\ &= -\frac{(\mathbf{a}_{01}\cdot\mathbf{n})_{/\eta}(\mathbf{n}_0\cdot\mathbf{n}) - (\mathbf{a}_{01}\cdot\mathbf{n})(\mathbf{n}_0\cdot\mathbf{n})_{/\eta}}{(\mathbf{n}_0\cdot\mathbf{n})^2}\Bigg|_{\xi=\pm1} \\ G'_\pm(\xi) &= -\frac{\partial}{\partial\xi}\left(\frac{\mathbf{a}_{02}\cdot\mathbf{n}}{\mathbf{n}_0\cdot\mathbf{n}}\right)\Bigg|_{\eta=\pm1} \\ &= -\frac{(\mathbf{a}_{02}\cdot\mathbf{n})_{/\xi}(\mathbf{n}_0\cdot\mathbf{n}) - (\mathbf{a}_{02}\cdot\mathbf{n})(\mathbf{n}_0\cdot\mathbf{n})_{/\xi}}{(\mathbf{n}_0\cdot\mathbf{n})^2}\Bigg|_{\eta=\pm1} \end{aligned} \tag{B.16}$$

where

$$\begin{aligned} (\mathbf{a}_{0_1}\cdot\mathbf{n})_{/\eta} &= \frac{\partial\mathbf{a}_{0_1}}{\partial\eta}\cdot\mathbf{n} + \mathbf{a}_{0_1}\cdot\frac{\partial\mathbf{n}}{\partial\eta} \\ (\mathbf{n}_0\cdot\mathbf{n})_{/\eta} &= \frac{\partial\mathbf{n}_0}{\partial\eta}\cdot\mathbf{n} + \mathbf{n}_0\cdot\frac{\partial\mathbf{n}}{\partial\eta} \end{aligned} \tag{B.17}$$

and

$$\begin{aligned} (\mathbf{a}_{0_2}\cdot\mathbf{n})_{/\xi} &= \frac{\partial\mathbf{a}_{0_2}}{\partial\xi}\cdot\mathbf{n} + \mathbf{a}_{0_2}\cdot\frac{\partial\mathbf{n}}{\partial\xi} \\ (\mathbf{n}_0\cdot\mathbf{n})_{/\xi} &= \frac{\partial\mathbf{n}_0}{\partial\xi}\cdot\mathbf{n} + \mathbf{n}_0\cdot\frac{\partial\mathbf{n}}{\partial\xi} \end{aligned} \tag{B.18}$$

Note that $\mathbf{n}$ along the four edges is assumed to be prescribed. Hence, its derivatives along the edges are prescribed as well. The only quantities that are still missing are thereby $\partial\mathbf{n}_0/\partial\xi$ and $\partial\mathbf{n}_0/\partial\eta$ which are needed in Eqs. B.17 and B.18 (as well as in Eqs. B.5, as mentioned above). We can obtain the $\partial \mathbf{n}_0/\partial\xi$ and $\partial \mathbf{n}_0/\partial\eta$ components from the fact that $\mathbf{n}_0 \cdot \mathbf{n}_0 = 1$ and $\mathbf{n}_0 \cdot \mathbf{a}_{0_\alpha} = 0$.[1] In particular, the former yields

$$\frac{\partial \mathbf{n}_0}{\partial \xi} \cdot \mathbf{n}_0 = 0 \qquad \frac{\partial \mathbf{n}_0}{\partial \eta} \cdot \mathbf{n}_0 = 0 \tag{B.19}$$

whereas the latter yields

$$\begin{aligned}
\frac{\partial \mathbf{n}_0}{\partial \xi} \cdot \mathbf{a}_{0_1} &= -\mathbf{n}_0 \cdot \frac{\partial \mathbf{a}_{0_1}}{\partial \xi} = -\mathbf{n}_0 \cdot \frac{\partial^2 \mathbf{x}_0}{\partial \xi^2} \\
\frac{\partial \mathbf{n}_0}{\partial \xi} \cdot \mathbf{a}_{0_2} &= -\mathbf{n}_0 \cdot \frac{\partial \mathbf{a}_{0_2}}{\partial \xi} = -\mathbf{n}_0 \cdot \frac{\partial^2 \mathbf{x}_0}{\partial \xi \partial \eta} \\
\frac{\partial \mathbf{n}_0}{\partial \eta} \cdot \mathbf{a}_{0_1} &= -\mathbf{n}_0 \cdot \frac{\partial \mathbf{a}_{0_1}}{\partial \eta} = -\mathbf{n}_0 \cdot \frac{\partial^2 \mathbf{x}_0}{\partial \xi \partial \eta} \\
\frac{\partial \mathbf{n}_0}{\partial \eta} \cdot \mathbf{a}_{0_2} &= -\mathbf{n}_0 \cdot \frac{\partial \mathbf{a}_{0_2}}{\partial \eta} = -\mathbf{n}_0 \cdot \frac{\partial^2 \mathbf{x}_0}{\partial \eta^2}
\end{aligned} \tag{B.20}$$

Finally, the expressions for $\partial^2\mathbf{x}_0/\partial\xi^2$, $\partial^2\mathbf{x}_0/\partial\xi\partial\eta$ and $\partial^2\mathbf{x}_0/\partial\eta^2$ are easily obtained from Eq. B.1 (or more directly from Eq. B.4) as

$$\begin{aligned}
&\frac{\partial^2 \mathbf{x}_0}{\partial \xi^2} = \frac{1+\eta}{2}\mathbf{x}_2''(\xi) + \frac{1-\eta}{2}\mathbf{x}_4''(\xi) \\
&\frac{\partial^2 \mathbf{x}_0}{\partial \xi \partial \eta} \\
&= \frac{\mathbf{x}_1'(\eta) - \mathbf{x}_3'(\eta)}{2} + \frac{\mathbf{x}_2'(\xi) - \mathbf{x}_4'(\xi)}{2} - \frac{1}{4}(\mathbf{x}_{++} - \mathbf{x}_{+-} - \mathbf{x}_{-+} + \mathbf{x}_{--}) \\
&\frac{\partial^2 \mathbf{x}_0}{\partial \eta^2} = \frac{1+\xi}{2}\mathbf{x}_1''(\eta) + \frac{1-\xi}{2}\mathbf{x}_3''(\eta)
\end{aligned} \tag{B.21}$$

Note again that $\mathbf{x}_1(\eta), \mathbf{x}_2(\xi), \mathbf{x}_3(\eta), \mathbf{x}_4(\xi)$ are assumed to be prescribed along the respective edge and hence their first and second derivatives are assumed to be prescribed as well.

B.3 From surfaces to blocks

Finally, akin to Section 4.3, the function $\mathbf{x}(\xi, \eta, \zeta)$, which describes the block is obtained as the sum of three linear interpolations between opposite boundary patches, minus the sum of three bilinear interpolations through parallel edges, plus a trilinear interpolation through the eight vertices.

---

[1] This may be obtained from the fact that, for a generic vector $\mathbf{v}$, we have $\mathbf{v} = v_1\mathbf{a}^1 + v_2\mathbf{a}^2 + v_3\mathbf{n}$ where $\mathbf{a}^1$ and $\mathbf{a}^2$ are the so–called contravariant base vectors

$$\mathbf{a}^1 = \frac{\mathbf{a}_2 \times \mathbf{n}}{\|\mathbf{a}_1 \times \mathbf{a}_2\|} \quad \text{and} \quad \mathbf{a}^2 = \frac{\mathbf{a}_1 \times \mathbf{n}}{\|\mathbf{a}_1 \times \mathbf{a}_2\|}$$

whereas $v_\alpha = \mathbf{v} \cdot \mathbf{a}_\alpha$ $(\alpha = 1, 2)$ and $v_3 = \mathbf{v} \cdot \mathbf{n}$.

Appendix C

Differential Geometry

In this Appendix, the problem of a layer that surrounds a surface has been addressed. Of course, the general differential–geometry results obtained thus far apply to this case as well. However, it is convenient to express them explicitly for the case under consideration. Before considering the geometry of a layer around a surface it is convenient to address the geometry of the surface itself. This is done in Subsection C.1. Then, in Subsection C.2 we address the differential geometry of a layer.

C.1 Differential geometry of a surface

Consider $\mathbf{x} = \mathbf{x}(\xi^\sigma)$. If we assume ξ^3 to be constant, say $\xi^3 = \xi^3_*$, this mapping defines a surface – the coordinate surface $\xi^3 = \xi^1_*$. Specifically, setting $\mathbf{x}(\xi^1, \xi^2, \xi^3_*) = \mathbf{p}(\xi^1, \xi^2)$, we have that

$$\mathbf{x} = \mathbf{p}(\xi^1, \xi^2) \tag{C.1}$$

defines a surface $\mathcal{S}$.

In the following, we obtain some results, utilizing exclusively Eq. C.1.

We begin with the following

Definition C.1 (Covariant base vectors for a surface) The *covariant base vectors for the surface $\mathcal{S}$* defined by Eq. C.1 are given by[1]

$$\mathbf{a}_\sigma = \frac{\partial \mathbf{x}}{\partial \xi^\sigma} \qquad (\sigma = 1, 2) \tag{C.2}$$

---

[1] An important **notice on notations**: in this section, the Greek subscripts σ, τ, and ρ range from 1 to 2 (even when not explicitly stated), the others from 1 to 3.

Note that $\mathbf{a}_\sigma$ lie in the tangent plane to $\mathcal{S}$ at (ξ^1, ξ^2).[2]

The vector $\mathbf{a}_1 \times \mathbf{a}_2$ is clearly normal to $\mathbf{a}_1$ and $\mathbf{a}_2$, and hence normal the surface. Thus, the unit normal to the surface is given by

$$\mathbf{n} = \frac{\mathbf{a}_1 \times \mathbf{a}_2}{\|\mathbf{a}_1 \times \mathbf{a}_2\|} \tag{C.3}$$

Next, we introduce the covariant components of the surface metric tensor (also referred to as the *first fundamental quadratic form of the surface*)

$$a_{\sigma\tau} = \mathbf{a}_\sigma \cdot \mathbf{a}_\tau \qquad (\sigma, \tau = 1, 2) \tag{C.4}$$

In addition, we may introduce the contravariant components of the metric tensor, so that

$$a^{\sigma\rho}\, a_{\rho\tau} = \delta_\sigma^\tau \qquad (\sigma, \tau = 1, 2) \tag{C.5}$$

which implies $a^{11} = a_{22}/a$, $a^{22} = a_{11}/a$, and $a^{12} = a^{21} = -a_{12}/a$, where

$$a = \left| a_{\sigma\tau} \right| = a_{11} a_{22} - a_{12}^2. \tag{C.6}$$

The contravariant base vectors are defined by

$$\mathbf{a}^\sigma = a^{\sigma\tau}\, \mathbf{a}_\tau \tag{C.7}$$

Note that $\mathbf{a}^\sigma$ also lie in the tangent plane to $\mathcal{S}$ at (ξ^1, ξ^2). Note also that

$$\mathbf{a}_\sigma \cdot \mathbf{a}^\tau = \delta_\sigma^\tau \qquad (\sigma, \tau = 1, 2) \tag{C.8}$$

as you may easily verify, by using Eqs. C.7 and C.5. Therefore, we have

$$\mathbf{a}^1 = \frac{\mathbf{a}_2 \times \mathbf{n}}{\|\mathbf{a}_1 \times \mathbf{a}_2\|} \qquad \mathbf{a}^2 = \frac{\mathbf{n} \times \mathbf{a}_1}{\|\mathbf{a}_1 \times \mathbf{a}_2\|} \tag{C.9}$$

as you may easily verify from Eq. C.8, and using $\mathbf{a}_1 \times \mathbf{a}_2 \cdot \mathbf{n} = \|\mathbf{a}_1 \times \mathbf{a}_2\|$ (from Eq. C.3).

In addition, we have

$$\mathbf{a}_\sigma \cdot \mathbf{n} = \mathbf{a}^\sigma \cdot \mathbf{n} = 0 \qquad (\sigma, \tau = 1, 2) \tag{C.10}$$

Thus, for any vector, $\mathbf{v}$, we can write

$$\mathbf{v} = v^\sigma\, \mathbf{a}_\sigma + v_n\, \mathbf{n} = v_\tau\, \mathbf{a}^\tau + v_n\, \mathbf{n} \tag{C.11}$$

---

[2] Note also the analogy with the base vectors $\mathbf{g}_\sigma = \partial \mathbf{x} / \partial \xi^\sigma$. Indeed, we have $\mathbf{a}_\sigma = \mathbf{g}_\sigma \big|_{\xi^3 = \xi^3_*}$. A deeper analysis of this and similar issues is presented in the next subsection.

where, using Eqs. C.8 and C.10 as well as Eq. C.4 and $\|\mathbf{n}\| = 1$, we have

$$v_\sigma = \mathbf{v}\cdot\mathbf{a}_\sigma = a_{\sigma\tau}v^\tau \qquad v^\tau = \mathbf{v}\cdot\mathbf{a}^\tau = a^{\tau\sigma}v_\sigma \qquad v_n = \mathbf{v}\cdot\mathbf{n} \tag{C.12}$$

Next, consider the surface element, which is given by $\mathrm{d}\mathcal{S} = \big\|\mathbf{a}_1\,\mathrm{d}\xi^1 \times \mathbf{a}_2\,\mathrm{d}\xi^2\big\|$. Note that, we have

$$\|\mathbf{a}_1\times\mathbf{a}_2\|^2 = \mathbf{a}_1\cdot\mathbf{a}_1\;\mathbf{a}_2\cdot\mathbf{a}_2 - \big(\mathbf{a}_1\cdot\mathbf{a}_2\big)^2 = a_{11}a_{22} - a_{12}^2 = a, \tag{C.13}$$

Hence,

$$\mathrm{d}\mathcal{S} = \|\mathbf{a}_1\times\mathbf{a}_2\|\,\mathrm{d}\xi^1\,\mathrm{d}\xi^2 = \sqrt{a}\,\mathrm{d}\xi^1\,\mathrm{d}\xi^2 \tag{C.14}$$

Also, consider the arclength of an element of a curve, which is defined over the surface by $\mathbf{x} = \mathbf{x}\big(\xi^1(t), \xi^2(t)\big)$. We have

$$\mathrm{d}s = \left\|\frac{\mathrm{d}\mathbf{x}}{\mathrm{d}t}\right\|\mathrm{d}t = \sqrt{a_{\sigma\tau}\,\dot{\xi}^\sigma\,\dot{\xi}^\tau}\,\mathrm{d}t \tag{C.15}$$

where $\dot{\xi}^\sigma = \mathrm{d}\xi^\sigma/\mathrm{d}t$.

Finally, consider the quantities

$$b_{\sigma\tau} := \frac{\partial\mathbf{a}_\sigma}{\partial\xi^\beta}\cdot\mathbf{n} = \frac{\partial^2\mathbf{x}}{\partial\xi^\sigma\partial\xi^\beta}\cdot\mathbf{n} \tag{C.16}$$

Note that $\mathbf{a}_\sigma\cdot\mathbf{n} = 0$. Hence, $\partial\mathbf{a}_\sigma/\partial\xi^\beta\cdot\mathbf{n} + \mathbf{a}_\sigma\cdot\partial\mathbf{n}/\partial\xi^\beta = 0$. Therefore, we have also

$$b_{\sigma\tau} = -\mathbf{a}_\sigma\cdot\frac{\partial\mathbf{n}}{\partial\xi^\beta} \tag{C.17}$$

It is apparent that the quantities $b_{\sigma\tau}$ are related to the curvature of the surface. Thus, the tensor

$$\mathbf{B} = b_{\sigma\tau}\,\mathbf{a}^\sigma\otimes\mathbf{a}^\tau = b_\sigma^{\ \tau}\,\mathbf{a}^\sigma\otimes\mathbf{a}_\tau = b^{\sigma\tau}\,\mathbf{a}_\sigma\otimes\mathbf{a}_\tau \tag{C.18}$$

(where $b_\sigma^{\ \tau} = b_{\sigma\rho}\,a^{\rho\tau}$ and $b^{\sigma\tau} = a^{\sigma\rho}\,b_\rho^{\ \tau}$) is called the *curvature tensor*.

C.2 Differential geometry for a layer

In this section, we study the differential geometry of a thin layer surrounding a given surface, and described by

$$\mathbf{x}(\xi^1,\xi^2,\eta) = \mathbf{p}(\xi^1,\xi^2) + \eta\,\mathbf{n}(\xi^1,\xi^2) \qquad \big(\eta\in[-\delta/2,\delta/2]\big) \tag{C.19}$$

where δ is the layer thickness, which is assumed to be sufficiently small so as to avoid singularities (such as the crossing of η–lines).

Of course, we are now back to a three–dimensional continuum, as you may easily convince yourself by setting $\eta = \xi^3$. In particular, we have

$$\mathbf{g}_3 = \frac{\partial \mathbf{x}}{\partial \eta} = \mathbf{n} \tag{C.20}$$

It is convenient to examine what happens in this case, because now the vector $\mathbf{g}_3$ is orthogonal to $\mathbf{g}_1$ and $\mathbf{g}_2$.

In order to show this, we want to obtain the expression for the covariant base vectors $\mathbf{g}_\sigma$. With this aim, we first derive the expression for $\partial \mathbf{n}/\partial \xi^\sigma$. Note that $\mathbf{n} \cdot \mathbf{n} = 1$, and hence $\partial(\mathbf{n} \cdot \mathbf{n})/\partial \xi^\sigma = 2\mathbf{n} \cdot \partial \mathbf{n}/\partial \xi^\sigma = 0$. Therefore, $\partial \mathbf{n}/\partial \xi^\sigma$ has zero component in the direction $\mathbf{n}$. Thus, recalling Eq. C.17, Eqs. C.11 and C.12 yield

$$\frac{\partial \mathbf{n}}{\partial \xi^\sigma} = -b_{\sigma\tau}\, \mathbf{a}^\tau = -b_\sigma^{\ \tau}\, \mathbf{a}_\tau \tag{C.21}$$

with $b_\sigma^{\ \tau} = b_{\sigma\rho}\, a^{\rho\tau}$. We are now in a position to evaluate $\mathbf{g}_\sigma$. From Eqs. C.19 and C.21, we have

$$\mathbf{g}_\sigma = \frac{\partial \mathbf{x}}{\partial \xi^\sigma} = \frac{\partial \mathbf{p}}{\partial \xi^\sigma} + \eta\, \frac{\partial \mathbf{n}}{\partial \xi^\sigma} = \mathbf{a}_\sigma - \eta\, b_\sigma^{\ \tau}\, \mathbf{a}_\tau \tag{C.22}$$

or

$$\mathbf{g}_\sigma = \left(\delta_\sigma^\tau - \eta\, b_\sigma^{\ \tau}\right) \mathbf{a}_\tau \tag{C.23}$$

Note that $\mathbf{g}_\sigma\big|_{\eta=0} = \mathbf{a}_\sigma$.

Note also that $\mathbf{g}_\sigma \cdot \mathbf{n} = 0$. Hence,

$$\left[g_{\alpha\beta}\right] = \begin{bmatrix} g_{11} & g_{12} & 0 \\ g_{12} & g_{22} & 0 \\ 0 & 0 & 1 \end{bmatrix} = \left[g_{\beta\alpha}\right] \tag{C.24}$$

Note that

$$\left[g_{\alpha\beta}\right]_{\eta=0} = \begin{bmatrix} a_{11} & a_{12} & 0 \\ a_{12} & a_{22} & 0 \\ 0 & 0 & 1 \end{bmatrix} \tag{C.25}$$

Moreover we have, using Eq. C.22,

$$\begin{aligned} \sqrt{g} = J = \mathbf{g}_1 \times \mathbf{g}_2 \cdot \mathbf{n} &= \left(\mathbf{a}_1 - \eta\, b_1^\sigma\, \mathbf{a}_\sigma\right) \times \left(\mathbf{a}_2 - \eta\, b_2^\tau\, \mathbf{a}_\tau\right) \cdot \mathbf{n} \\ &= \Big[1 - \left(b_1^1 + b_2^2\right)\eta + \left(b_1^1\, b_2^2 - b_1^2\, b_2^1\right)\eta^2\Big]\sqrt{a} \end{aligned} \tag{C.26}$$

Similar results are obtained for the contravariant base vectors, $\mathbf{g}^\alpha$, and the contravariant components of the metric tensor, $g^{\alpha\beta}$. In particular we have

$$\mathbf{g}^3 = \mathbf{n}. \tag{C.27}$$

In addition, in analogy with Eq. C.9, we have

$$\mathbf{g}^1 = \frac{1}{\sqrt{g}}\,\mathbf{a}_2 \times \mathbf{n} \qquad\qquad \mathbf{g}^2 = \frac{1}{\sqrt{g}}\,\mathbf{n} \times \mathbf{a}_1 \tag{C.28}$$

Note that the base vectors $\mathbf{g}_\sigma$ and $\mathbf{g}^\sigma$ are all perpendicular to the normal $\mathbf{n}$. Therefore, for any vector, $\mathbf{v}$ defined on the layer, we can write

$$\mathbf{v} = v^\sigma\,\mathbf{g}_\sigma + v_n\,\mathbf{n} = v_\tau\,\mathbf{g}^\tau + v_n\,\mathbf{n}. \tag{C.29}$$

Appendix D

Moving the hinge of a hinged plate

A final consideration concern a strange phenomenon, totally unexpected, that has been uncovered by examining the mode shapes of a square plate hinged at its edges. Specifically, contrary to the expectations, the way in which the boundary condition is implemented makes a big difference in the results for the mode shape.

Consider the hinged square plate introduced in Section 7.4.3 (*i.e.*, with $\ell = 1$, $h = 0.01$, $E = \rho = 1$, and $\nu = .225$).

For the sake of clarity, one may introduce a distinction between a simply–supported plate and a hinged plate. In the first case, we naturally think of the boundary condition, $\mathsf{u} = \mathsf{0}$, as being imposed at the edge of the lower surface of the plate, whereas in the hinged–plate boundary condition, the hinge may be located anywhere between the upper and the lower surface.

If the hinge is located along the mid–surface, one obtains the expected results, here proposed for the first mode, in FIg. D.1 (thus, this solution for the constraints application has been considered throughout Section 7.4.3).

On the contrary, if a simply–supported boundary condition is imposed, one obtains the results presented in Fig. D.2, which depicts the first mode, for $h/\ell = .01$, and $N = 8, 12, 14$. It is apparent that the issue is not attributable to lack of convergence.

What is even more startling is the fact that the results are independent of the ratio h/ℓ, as apparent from in Figure D.3, which depicts the first mode, for $h/\ell = .001, .01, .05$, with $N = 14$.

Finally, Figs. from D.4 to D.6 depict higher modes (the second, the third and the fourth) as obtained using a simply–supported boundary condition with a subdivision of $N = 6$ for a Hermite 3–rd order 8 nodes.

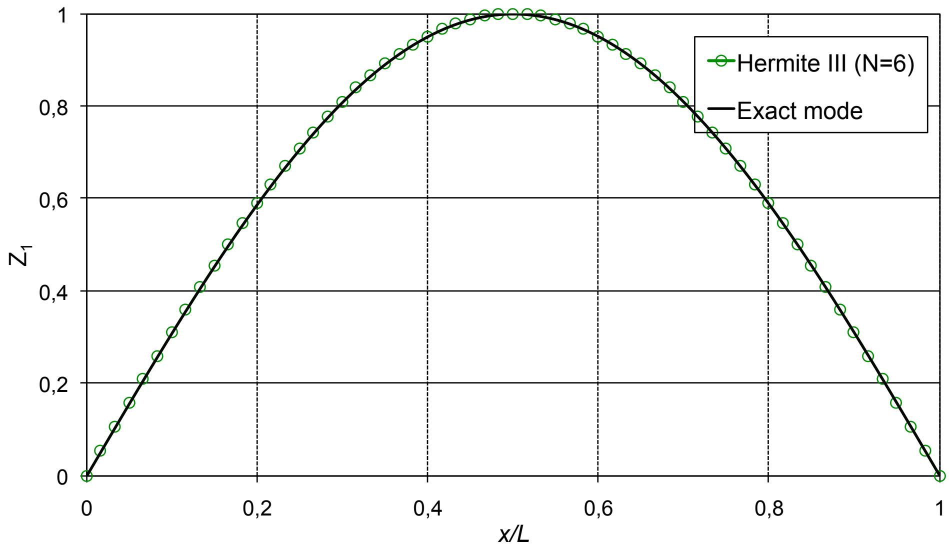

Figure D.1: Hinged plate: 1st mode $(N = 6;\ h = .01)$

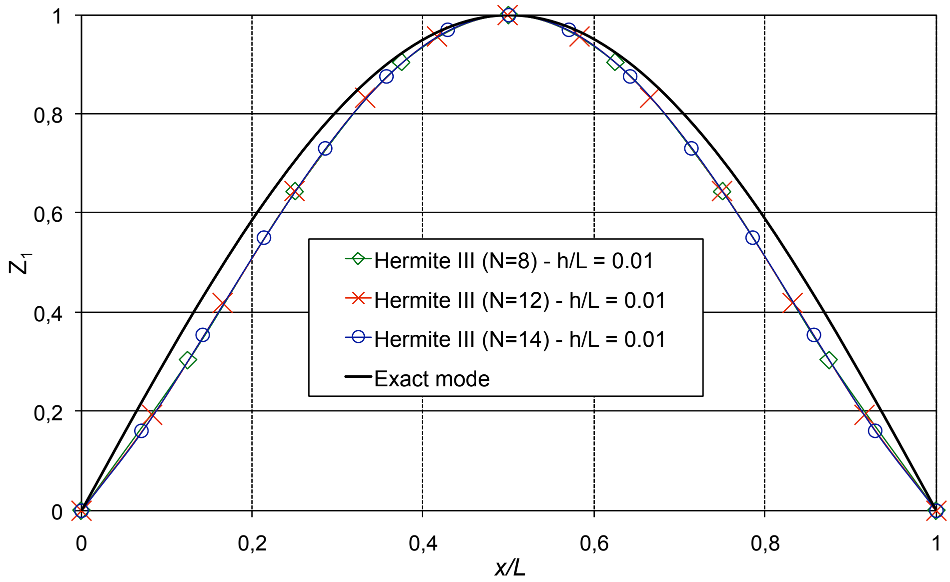

Figure D.2: Simply–supported plate: 1st mode $(N = 8, 12, 14;\ h = .01)$

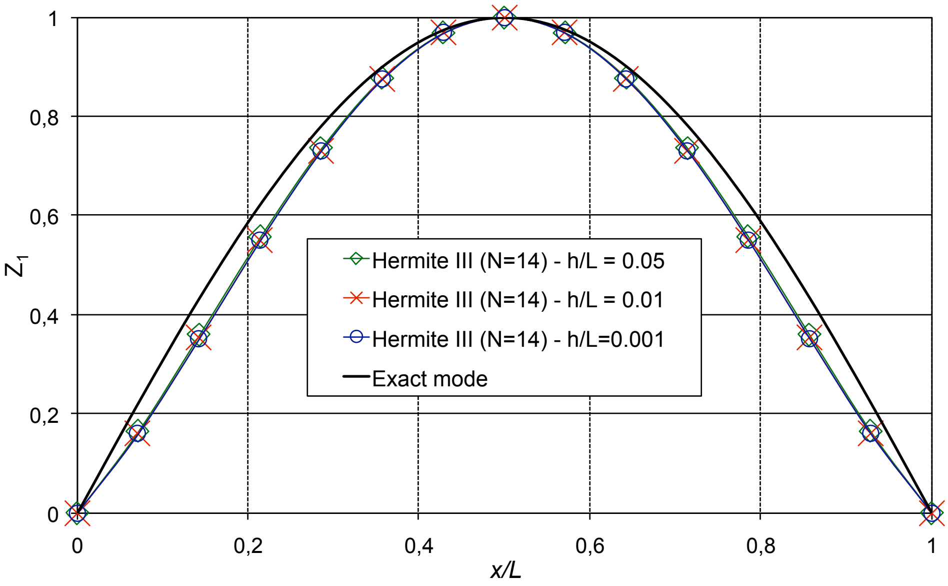

Figure D.3: Simply–supported plate: 1st mode ($N = 14$; $h = .001, .01, .05$)

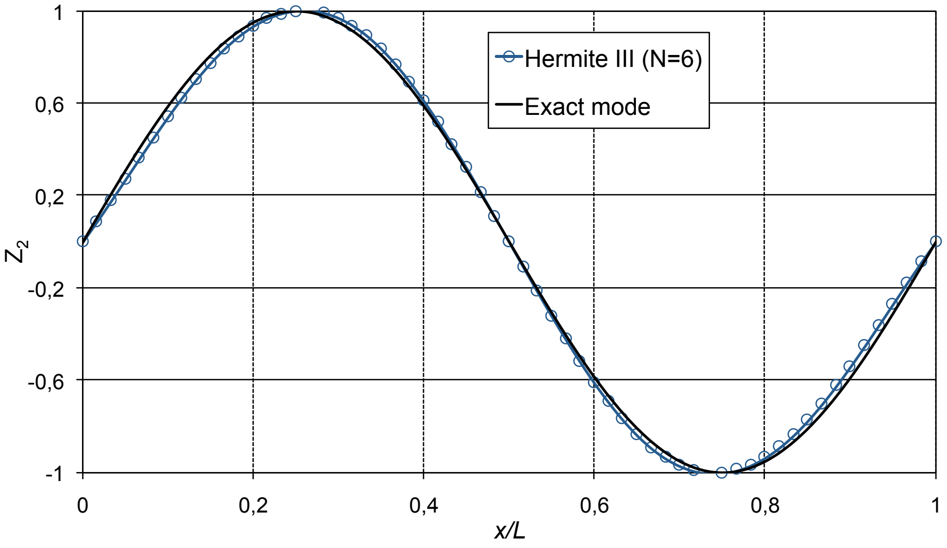

Figure D.4: Simply–supported plate: 2nd mode ($N = 6$; $h = .01$)

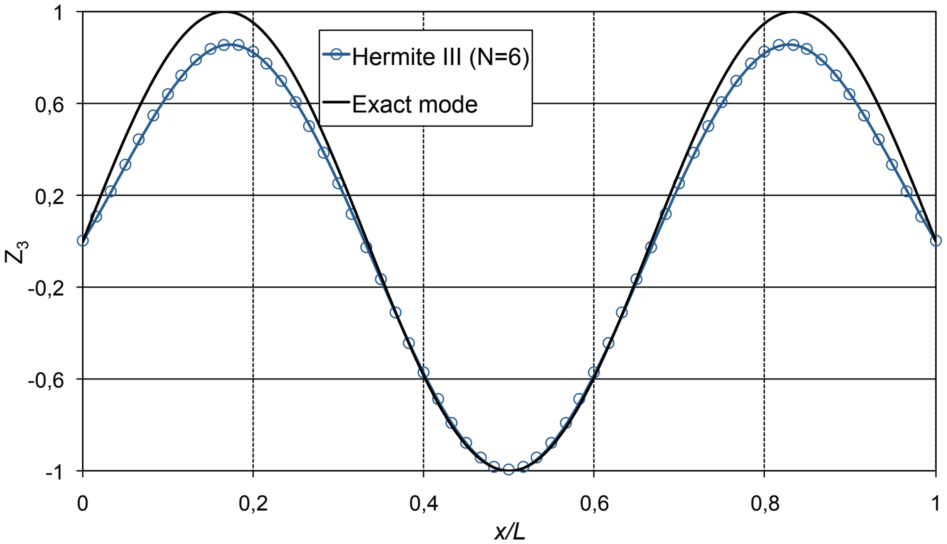

Figure D.5: Simply–supported plate: 3rd mode $(N = 6;\ h = .01)$

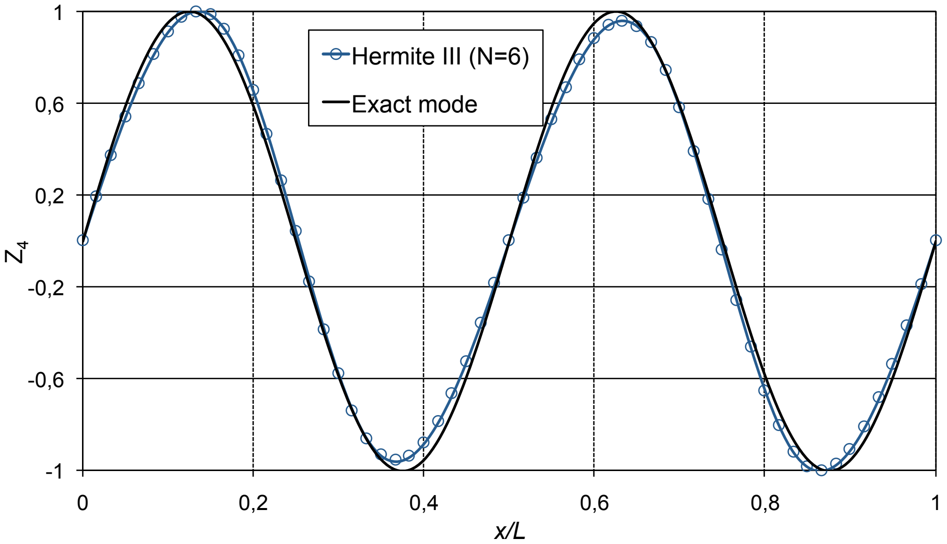

Figure D.6: Simply–supported plate: 4th mode $(N = 6;\ h = .01)$

Appendix E

Reduced Order Model

A Finite Element reduction is a technique which is used in the dynamic solution of very large problems (that is, with a large number of DOFS) to reduce the computational efforts or when only a small percentage of the frequency and mode shapes are desired. In particular, referring to the first intent, because of the cost of generating computer solutions for a dynamic analysis, it is often desirable to reduce the size of the problem by performing a reduction on the mass and stiffness matrices of the governing set of equations of motion. The well-known reduction proposed by Guyan[19] is the technique used by most of the large structural codes.

Next sections have the aim to give the mathematical background of the Guyan reduction technique,[19] as well as its basic extension proposed by O'Callahan,[20] with reference to the pros and cons in relation to the present work.

E.1 Guyan's quasi–static reduction

Guyan reduction is essentially a substructuring method which reduces the problem to a smaller one by relating certain degrees of freedom to certain others by means of constraint equations, thereby reducing the size of the problem. The first step in the method consists in the subdivision of the degrees of freedom between those to be retained and those to be eliminated. The degrees of freedom that are retained in the final solution are called *masters* whereas those that are eliminated are named *slaves* and are associated with large amounts of mass and inertia concentrations. Accuracy of the dynamic solution (natural frequencies and mode shapes) is largely dependent on the selection of the master degrees of freedom both in terms of number and direction.

If no force is applied and the damping is negligible, the governing equation of motion in frequency for the structure becomes

$$\omega^2 \mathsf{M}\mathsf{x} + \mathsf{K}\mathsf{x} = 0 \tag{E.1}$$

Pre–multiplying by x one obtains

$$\omega^2 \mathsf{x}^T \mathsf{M}\mathsf{x} + \mathsf{x}^T \mathsf{K}\mathsf{x} = 0 \tag{E.2}$$

According to the Guyan's procedure, the unknowns in Equation E.2 can be subdivided in the two sets: x_1, that holds to the master degrees of freedom and x_2, that regards the slave degrees of freedom. Hence, one has the following equation:

$$\omega^2 \begin{pmatrix} \mathsf{x}_1^T & \mathsf{x}_2^T \end{pmatrix} \begin{pmatrix} \mathsf{M}_{11} & \mathsf{M}_{12} \\ \mathsf{M}_{21} & \mathsf{M}_{22} \end{pmatrix} \begin{pmatrix} \mathsf{x}_1 \\ \mathsf{x}_2 \end{pmatrix} + \begin{pmatrix} \mathsf{x}_1^T & \mathsf{x}_2^T \end{pmatrix} \begin{pmatrix} \mathsf{K}_{11} & \mathsf{K}_{12} \\ \mathsf{K}_{21} & \mathsf{K}_{22} \end{pmatrix} \begin{pmatrix} \mathsf{x}_1 \\ \mathsf{x}_2 \end{pmatrix} = 0$$

that is equivalent to the following two sets of equations:

$$\begin{aligned} \omega^2(\mathsf{x}_1^T \mathsf{M}_{11}\mathsf{x}_1 + \mathsf{x}_1^T \mathsf{M}_{12}\mathsf{x}_2) + (\mathsf{x}_1^T \mathsf{K}_{11}\mathsf{x}_1 + \mathsf{x}_1^T \mathsf{K}_{12}\mathsf{x}_2) &= 0 \\ \omega^2(\mathsf{x}_2^T \mathsf{M}_{21}\mathsf{x}_1 + \mathsf{x}_2^T \mathsf{M}_{22}\mathsf{x}_2) + (\mathsf{x}_2^T \mathsf{K}_{21}\mathsf{x}_1 + \mathsf{x}_2^T \mathsf{K}_{22}\mathsf{x}_2) &= 0 \end{aligned} \tag{E.3}$$

Neglecting the inertia terms in the second set of Eqs. E.3, one has

$$\mathsf{x}_2^T(\mathsf{K}_{21}\mathsf{x}_1 + \mathsf{K}_{22}\mathsf{x}_2) = 0$$

that gives

$$\mathsf{x}_2 = -\mathsf{K}_{22}^{-1}\mathsf{K}_{21}\mathsf{x}_1 = \mathsf{T}\mathsf{x}_1 \tag{E.4}$$

Eq. E.4 relates, through the matrix $\mathsf{T} = -\mathsf{K}_{22}^{-1}\mathsf{K}_{21}$, the slave state variables to the master ones. Hence, the complete vector of state variables can be rewritten as:

$$\mathsf{x} = \begin{pmatrix} \mathsf{x}_1 \\ \mathsf{x}_2 \end{pmatrix} = \begin{pmatrix} \mathsf{I} \\ \mathsf{T} \end{pmatrix} \mathsf{x}_1 = \mathsf{T}_G \mathsf{x}_1 \tag{E.5}$$

where

$$\mathsf{T}_G = \begin{pmatrix} \mathsf{I} \\ \mathsf{T} \end{pmatrix} \tag{E.6}$$

The transformation matrix T_G is used to rearrange the complete vector of the state variables from the master sub–set (that is the only retained in the reduced formulation). The reduced mass and stiffness matrices are then given by

$$\mathsf{M}_R = \mathsf{T}_G^T \mathsf{M} \mathsf{T}_G \quad \text{and} \quad \mathsf{K}_R = \mathsf{T}_G^T \mathsf{K} \mathsf{T}_G \tag{E.7}$$

From a computational point of view, it is better to obtain the reduced matrices explicitly, by using the partitions of them (defined preliminarly at the beginning of the procedure and therefore available), in terms of masters and slaves components. Considering that

$$\mathsf{M}_R = \mathsf{T}_G^T \begin{pmatrix} \mathsf{M}_{11} & \mathsf{M}_{12} \\ \mathsf{M}_{21} & \mathsf{M}_{22} \end{pmatrix} \mathsf{T}_G \quad \text{and} \quad \mathsf{K}_R = \mathsf{T}_G^T \begin{pmatrix} \mathsf{K}_{11} & \mathsf{K}_{12} \\ \mathsf{K}_{21} & \mathsf{K}_{22} \end{pmatrix} \mathsf{T}_G \tag{E.8}$$

one has:

$$\begin{aligned} \mathsf{M}_R &= \mathsf{M}_{11} + \mathsf{M}_{12}\mathsf{T} + \mathsf{T}^T\mathsf{M}_{21} + \mathsf{T}^T\mathsf{M}_{22}\mathsf{T} \\ \mathsf{K}_R &= \mathsf{K}_{11} + \mathsf{K}_{12}\mathsf{T} + \mathsf{T}^T\mathsf{K}_{21} + \mathsf{T}^T\mathsf{K}_{22}\mathsf{T} \end{aligned} \tag{E.9}$$

Note that the symmetry of the reduced matrices M_R and K_R is ensured by the symmetry of the complete matrices M and K. In fact, the terms M_{11}, K_{11} and M_{22}, K_{22} are symmetric. The terms $\mathsf{M}_{12}\mathsf{T} + \mathsf{T}^T\mathsf{M}_{21}$ and $\mathsf{K}_{12}\mathsf{T} + \mathsf{T}^T\mathsf{K}_{21}$ are also symmetric because $\mathsf{M}_{21} = \mathsf{M}_{12}^T$ and $\mathsf{K}_{21} = \mathsf{K}_{12}^T$.

Also, note that this technique has an error of order ω^4. In fact one has, from the second set of Eqs. E.3

$$\mathsf{x}_2 = -\mathsf{K}_{22}^{-1} \left[\omega^2 \mathsf{M}_{21}\mathsf{x}_1 + \omega^2 \mathsf{M}_{22}\mathsf{x}_2 + \mathsf{K}_{21}\mathsf{x}_1\right] \tag{E.10}$$

Substituting Eq. E.10 in the first set of Eqs. E.3 that is hereafter rewritten

$$\omega^2(\mathsf{x}_1^T\mathsf{M}_{11}\mathsf{x}_1 + \mathsf{x}_1^T\mathsf{M}_{12}\mathsf{x}_2) + (\mathsf{x}_1^T\mathsf{K}_{11}\mathsf{x}_1 + \mathsf{x}_1^T\mathsf{K}_{12}\mathsf{x}_2) = 0$$

one obtains

$$\begin{gathered} \omega^2(\mathsf{x}_1^T\mathsf{M}_{11}\mathsf{x}_1 + \mathsf{x}_1^T\mathsf{M}_{12}\left[-\mathsf{K}_{22}^{-1}\left[\omega^2\mathsf{M}_{21}\mathsf{x}_1 + \omega^2\mathsf{M}_{22}\mathsf{x}_2 + \mathsf{K}_{21}\mathsf{x}_1\right]\right]) + \\ \mathsf{x}_1^T\mathsf{K}_{11}\mathsf{x}_1 + \mathsf{x}_1^T\mathsf{K}_{12}\left[-\mathsf{K}_{22}^{-1}\left[\omega^2\mathsf{M}_{21}\mathsf{x}_1 + \omega^2\mathsf{M}_{22}\mathsf{x}_2 + \mathsf{K}_{21}\mathsf{x}_1\right]\right] = 0 \end{gathered}$$

Substituting Eq. E.10 once again and neglecting those terms that are multiplied by ω^4 one obtains $\omega^2\mathsf{x}_1^T\mathsf{M}_R x_1 + \mathsf{x}_1^T\mathsf{K}_R x_1 = 0$.

The Guyan's method for matrix reduction is often called *static* since the reduction equations are developed using only the stiffness matrix. Therefore, the Guyan technique produces an exact reduction of the stiffness matrix but only an approximate reduction of the mass matrix if any DOF with mass are omitted. The loss of mass accuracy that is introduced using the Guyan reduction technique can sometimes be unacceptably large and improved techniques are required. The solution to this issue has been deeply analyzed and extensions of the Guyan's technique have been developed (see, for instance, Refs. [21] and [22]). One of the simplest modified version of the Guyan's technique is described in the following section.

E.2 O'Callaghan's IRS technique

Any frequency response functions generated by the Guyan's reduced matrices of Eq. E.7 are exact only at zero frequency. As the excitation frequency increases the inertia terms neglected in Eq. E.3 become more significant. O'Callaghan[20] improved the static reduction method by introducing a technique known as the Improved Reduced System (IRS) method. The method perturbs the transformation from the static case by including the inertia terms as pseudo–static forces. Obviously it is impossible to emulate the behaviour of a full system with a reduced model and every reduction transformation sacrifices accuracy for speed in some way. O'Callaghan's technique results in a reduced system which matches the low frequency resonances of the full system better than static reduction.

This section shows the fundamental mathematics of the IRS technique. Use the Guyan' subdivision in master and slave state variables itself. From the second set of Eqs. E.3 one obtains

$$\left(K_{22} + \omega^2 M_{22}\right) x_2 = -\left(K_{21} + \omega^2 M_{21}\right) x_1$$

and

$$x_2 = -\left(K_{22} + \omega^2 M_{22}\right)^{-1} \left(K_{21} + \omega^2 M_{21}\right) x_1 \tag{E.11}$$

Rearranging Eq. E.11 and using the Binomial Theorem gives:[1]

$$\begin{aligned} x_2 &= -K_{22}^{-1}\left(I + \omega^2 M_{22} K_{22}^{-1}\right)^{-1}\left(K_{21} + \omega^2 M_{21}\right) x_1 \\ &= -K_{22}^{-1}\left(I - \omega^2 M_{22} K_{22}^{-1} + o(\omega^4)\right)\left(K_{21} + \omega^2 M_{21}\right) x_1 \\ &= -K_{22}^{-1}\left(K_{21} + \omega^2 M_{21} - \omega^2 M_{22} K_{22}^{-1} K_{21} + o(\omega^4)\right) x_1 \\ &= \left[-K_{22}^{-1} K_{21} - K_{22}^{-1}\omega^2\left(M_{21} - M_{22} K_{22}^{-1} K_{21}\right)\right] x_1 \end{aligned}$$

Recalling that $T = -K_{22}^{-1} K_{21}$, one has:

$$x_2 = \left[T - K_{22}^{-1}\omega^2\left(M_{21} + M_{22} T\right)\right] x_1 \tag{E.12}$$

---

[1] Recall that the Binomial Theorem can be used to manipulate the inverse of the sum of two matrices A and B. It gives: $(A + B)^{-1} = A^{-1} - A^{-1}B(B + BA^{-1}B)^{-1}BA^{-1}$. Thus, $\left(I + \omega^2 B\right)^{-1} = I - \omega^2 B + o(\omega^4)$.

The first set of Eqs. E.3 can then be used to have:

$$\omega^2 \mathsf{x}_1 = -\mathsf{M}_{11}^{-1}\mathsf{K}_{11}\mathsf{x}_1 \tag{E.13}$$

Substituting Eq. E.13 in Eq. E.12 one obtains:

$$\mathsf{x}_2 = \left[\mathsf{T} + \mathsf{K}_{22}^{-1}\left(\mathsf{M}_{21} + \mathsf{M}_{22}\mathsf{T}\right)\mathsf{M}_{11}^{-1}\mathsf{K}_{11}\right]\mathsf{x}_1 = \mathsf{S}\mathsf{x}_1 \tag{E.14}$$

Eq. E.14 relates, through the matrix S, the slave state variables to the master ones. Hence, the complete vector of state variables can be rewritten as:

$$\mathsf{x} = \begin{pmatrix} \mathsf{x}_1 \\ \mathsf{x}_2 \end{pmatrix} = \begin{pmatrix} \mathsf{I} \\ \mathsf{S} \end{pmatrix}\mathsf{x}_1 = \mathsf{T}_{IRS}\mathsf{x}_1 \tag{E.15}$$

where

$$\mathsf{T}_{IRS} = \begin{pmatrix} \mathsf{I} \\ \mathsf{S} \end{pmatrix} \tag{E.16}$$

The transformation matrix T_{IRS} now obtained, can used to rearrange the complete vector of the state variables from the master sub–set (that, also here, is the only retained in the reduced formulation). The reduced mass and stiffness matrices are then given by

$$\mathsf{M}_R = \mathsf{T}_{IRS}^T\mathsf{M}\mathsf{T}_{IRS} \quad \text{and} \quad \mathsf{K}_R = \mathsf{T}_{IRS}^T\mathsf{K}\mathsf{T}_{IRS} \tag{E.17}$$

It is apparent that the Guyan's procedure and the IRS one are implemented in the same way and that it is possible to shift from a technique to each other just changing the transformation matrix to be used (i.e. T_G that is the Guyan's one, defined in section E.1 and T_{IRS}).

The method is also computationally effective, since it is generally more accurate than Guyan. Nevertheless, some weaknesses have been proved (Gordis, 1992) like inaccuracy in case of a poor choice of the master unknowns. Also, it has been proved (see the works of Gordis[23] and Friswell[21]) that the IRS reduced stiffness matrix will be stiffer than the Guyan reduced matrix and the reduced mass matrix is less suitable for othogonality checks than the reduced mass matrix from Guyan reduction.

Finally, the combination of these two procedures has been revealed enough accurate limiting to the scope of this work.

Bibliography

[1] Provatidis, G. C., "Three–Dimensional Coons Macroelements in Laplace and Acoustics Problems," *Computers & Structures*, Vol. 83, 2005, pp. 1572–1583.

[2] Chen, G. and Zhou, J., *Boundary Element Methods*, Academic Press, 1992.

[3] Morino, L., Bernardini, G., Cerulli, C., and Cetta, F., "A Hermite High–Order Finite Element for Structural Optimal Design," *ICCES'04 Conference*, Madeira, Portugal, July 16–19 2004.

[4] Morino, L., Mastroddi, F., Bernardini, G., and Piccirilli, M., "A Hermite–Interpolation Finite Element for Structural Dynamics," *XVI Congresso Nazionale AIDAA*, Palermo, Italy, September 24–28 2001.

[5] Gennaretti, M., Calcagno, G., Zamboni, A., and Morino, L., "A High Order Boundary Element Formulation for Potential Incompressible Aerodynamics," *The Aeronautical Journal*, Vol. 102, No. 1014, 1998, pp. 211–219.

[6] Macneal, R. H., *Finite Elements: Their Design and Performance*, Marcel Dekker, Inc., 1994.

[7] Morino, L. and Cetta, F., "Coons Patch, Hermite Interpolation, and High–Order Finite Elements in Structural Dynamics," *47th AIAA/ASME/ASCE/AHS/ASC Structures, Structural Dynamics and Materials Conference*, Vol. AIAA-2006-1749, Newport, USA-RI, May 1–4 2006.

[8] Coons, S. A., *Surfaces for Computer Aided Design of Space Forms*, Massachusetts Institute of Technology, 1967.

[9] Coons, S. A., *Surface Patches and B-Spline Curves*, Eds. R.E. Barnhill and R.F. Riesenfeld, Academic Press, 1974.

[10] Coons, S. A., "Constrained Least Squares," *Computers & Graphics*, Vol. 3, 1978.

[11] Brenner, S. C. and Scott, L. R., *The Mathematical Theory of Finite Element Methods*, Springer–Verlag, 1996.

[12] Braess, D., *Finite Elements: Theory, Fast Solvers, and Applications in Solid Mechanics*, Cambridge University Press, 1997.

[13] Quarteroni, A. and Saleri, F., *Calcolo Scientifico*, Springer–Verlag, 2008.

[14] Anonimous, *Introduction to ANSYS*, ANSYS, Release 5.5, ANSYS Inc., 1998.

[15] Morino, L. and Cetta, F., "Hermite High–Order Finite Elements for Aeroacoustic Analysis," *12th AIAA/CEAS Aeroacoustics Conference*, Vol. AIAA-2006-2492, Cambridge, USA-MA, May 8–10 2006.

[16] Morino, L. and Cetta, F., "High–Order Finite Elements for Interior Acoustics," *13th AIAA/CEAS Aeroacoustics Conference*, Vol. AIAA-2007-3574, Rome, Italy, May 21–23 2007.

[17] Morino, L., Iemma, U., and Cetta, F., "Hermite, Coons and Guyan: a Highly Efficient High–Frequency Finite Element," *15th AIAA/CEAS Aeroacoustics Conference*, Vol. AIAA-2009-3391, Miami, FL-USA, May 11–13 2009.

[18] Paoluzzi, A., *Geometric Programming for Computer Aided Design*, Wiley, New York, 2003.

[19] Guyan, "Reduction of Stiffness and Mass Matrices," *AIAA Journal*, Vol. 3, No. 2, 1965.

[20] O'Callahan, J., "A Procedure for an Improved Reduced System (IRS) Model," *7th IMAC Conference*, Las Vegas, NV-USA, May 21–23 1989, pp. 17–21.

[21] Friswell, M. I., Garvey, S. D., and Penny, J. E. T., "Model Reduction Using Dynamic and Iterated IRS Techniques," *Journal of Sound and Vibration*, Vol. 186, No. 2, 1995, pp. 311–323.

[22] Flanigan, C. C., “Implementation of the IRS Dynamic Reduction Method in MSC/NASTRAN,” *MSC/NASTRAN World Users Conference*, Los Angeles, USA-CA, 1990.

[23] Gordis, J. H., “An Analysis of the Improved Reduced System (IRS) Model Reduction Procedure,” *10th International Modal Analysis Conference*, Vol. 1 (A94-12476 02-39), San Diego, CA-USA, February 3–7 1992, pp. 471–479.

[24] Morino, L. and Cetta, F., “A Hermite High–Order Finite Element for Aeroacoustic Analysis,” *11th AIAA/CEAS Aeroacoustics Conference*, Vol. AIAA-2005-3081, Monterey, USA-CA, May 23–25 2005.

[25] Morino, L. and Cetta, F., “A Hermite High–Order Finite Element in Structural Dynamics,” *XVIII Congresso Nazionale AIDAA*, Volterra, Italy, September 19–22 2005.

[26] Garvey, S. D., Penny, J. E. T., and Friswell, M. I., “Quantifying the Correlation Between Measured and Computed Mode Shapes,” *Journal of Vibration and Control*, Vol. 2, No. 2, 1996, pp. 123–144.

[27] Haac, T. R., Corcoran, J. M., Remillieux, M. C., Reichard, G., and Burdisso, R. A., “Experimental Characterization of the Vibro–Acoustic Response of a Simple Residential Structure to a Simulated Sonic Boom,” *15th AIAA/CEAS Aeroacoustics Conference*, Vol. AIAA-2009-3386, Miami, FL–USA, May 11–13 2009.

[28] Saeed, M., *Finite Element Analysis - Theory and Application with ANSYS*, Prentice–Hall, New Jersey, 1999.

[29] Abramowitz, M. and Stegun, I. A., *Handbook of Mathematical Functions with Formulas, Graphs, and Mathematical Tables*, Dover, New York, 9th dover printing, 10th gpo printing ed., 1964.

[30] Press, W. H., Teukolsky, S. A., Vetterling, W. T., and Flannery, B. P., *Numerical Recipes in FORTRAN 77 : the Art of Scientific Computing*, Cambridge University Press, New York, 2nd ed., 1992.

[31] Bernardini, G., Frediani, A., and Morino, L., “MDO of an Innovative Configuration - Aerodynamic Issues,” *1999 CEAS/AIAA/ICASE/NASA Langley Research Center International Forum on Aeroelasticity and Structural Dynamics*, Vol. NASA/CP-1999-209136/PT2, Williamsburg, Virginia-USA, June 22–25 1999, pp. 43–52.

[32] Brebbia, C. A. and Connor, J. J., *Fondamenti del Metodo agli Elementi Finiti*, Città Studi, 1997.

[33] Gambolati, G., *Elementi di Calcolo Numerico*, Edizioni Libreria Cortina, Padova, Italy, 1997.

[34] Timoshenko, S. and Woinowsky-Krieger, S., *Theory of Plates and Shells*, McGraw–Hill, International Book Company, Inc., 2nd ed., 1970.

[35] Timoshenko, S. and Young, D. H., *Vibration Problems in Engineering*, D. Van Nostrand Company, Inc., 3rd ed., 1955.

[36] Reddy, J. N., *Theory and Analysis of Elastic Plates*, Taylor & Francis, 1999.

[37] Weawer, W. J. and Jhonston, P. R., *Finite Elements for Structural Analysis*, Prentice–Hall, Inc., 1984.

[38] Zienkiewicz, O. C., *The Finite Element Method*, McGraw–Hill Book Company, UK, 3rd ed., 1977.

[39] Zienkiewicz, O. C. and Taylor, R. L., *The Finite Element Method*, Butterworth–Heinemann, 5th ed., 2000.

[40] Iemma, U., Trainelli, L., and Morino, L., "A Finite State Beam Method for Acustoaeroelasticity of Shell," *Second AIAA/CEAS Aeroacoustics Conference*, State College, PA, USA, May 1996.

[41] Morino, L., Iemma, U., and Trainelli, L., "Finite–State Acustoaeroelasticity," *IABEM Conference*, Mauna Lani, Hawaii, USA, 1995.

[42] Iemma, U., Morino, L., and Trainelli, L., "Internal Noise Generated by Sources External to an Elastic Shell," *First joint AIAA/CEAS Aeroacoustics Conference (*16*th AIAA Aeroacoustics Conference*, Munich, Germany, June 1995.

[43] Cetta, F., *Elementi Finiti alla Hermite per l'Analisi della Risposta Dinamica Strutturale in Campo Elasto-Plastico*, Master's thesis, Università degli Studi di Roma, Roma Tre, Dipartimento di Ingegneria Meccanica, 2003.

List of Figures

2.1 Hermite polynomials: M_- (dashed line) and M_+ (continuous line) 12

2.2 Hermite polynomials: N_- (dashed line) and N_+ (continuous line) 12

3.1 5th order Hermite polynomials: M_{0_-} (dashed line) and M_{0_+} (continuous line) 25

3.2 5th order Hermite polynomials: M_{1_-} (dashed line) and M_{1_+} (continuous line) 25

3.3 5th order Hermite polynomials: M_{2_-} (dashed line) and M_{2_+} (continuous line) 26

3.4 7th order Hermite polynomials: M_{0_-} (dashed line) and M_{0_+} (continuous line) 28

3.5 7th order Hermite polynomials: M_{1_-} (dashed line) and M_{1_+} (continuous line) 28

3.6 7th order Hermite polynomials: M_{2_-} (dashed line) and M_{2_+} (continuous line) 29

3.7 7th order Hermite polynomials: M_{3_-} (dashed line) and M_{3_+} (continuous line) 29

5.1 5th order WIP polynomials: M_- (dashed line), M_+ (continuous line) and M_0 (points) 52

5.2 5th order WIP polynomials: N_- (dashed line), N_+ (continuous line) and N_0 (points) 52

7.1 Closed–end pipe: 1st mode (left) and eigenvalue (right); expected trend (top) and obtained trend (bottom) 67

7.2 Closed–end pipe: 2nd mode (left) and eigenvalue (right); expected trend (top) and obtained trend (bottom) 68
7.3 Closed–end pipe: 3rd mode (left) and eigenvalue (right); expected trend (top) and obtained trend (bottom) 69
7.4 Closed–end pipe: 4th mode (left) and eigenvalue (right); expected trend (top) and obtained trend (bottom) 70
7.5 Closed–end pipe: 5th mode (left) and eigenvalue (right); expected trend (top) and obtained trend (bottom) 71
7.6 Closed–end pipe: 6th mode (left) and eigenvalue (right); expected trend (top) and obtained trend (bottom) 72
7.7 Closed–end pipe: 7th mode (left) and eigenvalue (right); expected trend (top) and obtained trend (bottom) 73
7.8 Closed–end pipe: 8th mode (left) and eigenvalue (right); expected trend (top) and obtained trend (bottom) 74
7.9 Closed–end pipe: 9th mode (left) and eigenvalue (right); expected trend (top) and obtained trend (bottom) 75
7.10 Closed–end pipe: 10th mode (left) and eigenvalue (right); expected trend (top) and obtained trend (bottom) 76
7.11 Closed end pipe: equidistant (left) and Gauss–Chebishev–Lobatto (right) nodes distribution for WIP schemes 77
7.12 Closed end pipe: WIP $p-$convergence for eigenvalues $1-5$. 78
7.13 Closed end pipe: Hermite h–convergence for eigenvalues ($N = 1, 2, 3, 4, 5$) 80
7.14 Closed end pipe: Hermite h–convergence for eigenfunctions ($N = 1, 2, 3, 4, 5$) 81
7.15 Closed end pipe: Hermite h–convergence for eigenvalues ($N = 1, 2, 4, 8, 16$) 81
7.16 Closed end pipe: Hermite h–convergence for eigenfunctions ($N = 1, 2, 4, 8, 16$) 82
7.17 Closed end pipe: WIP p–convergence for eigenvalues ($N = 1$) 82
7.18 Closed end pipe: WIP p–convergence for eigenfunctions ($N = 1$) 83
7.19 Closed end pipe: WIP p–convergence for eigenvalues ($N = 2$) 83
7.20 Closed end pipe: WIP p–convergence for eigenfunctions ($N = 2$) 84
7.21 Closed end pipe: WEP p–convergence for eigenvalues 84
7.22 Closed end pipe: WEP p–convergence for eigenfunctions . . . 85
7.23 Closed end pipe: 3rd *vs* 5th order WEP schemes 86
7.24 Zoom of Fig. 7.23 86
7.25 Closed end pipe: 3rd *vs* 5th *vs* 7th order WEP schemes . . . 87
7.26 Zoom of Fig. 7.25 87

7.27 Closed end pipe: 3rd *vs* 5th *vs* 7th *vs* 9th *vs* 11th order WIP schemes 88
7.28 Zoom of Fig. 7.27 88
7.29 Logarithmic errors representation of Fig. 7.27 89
7.30 Zoom Fig. 7.29 89
7.31 Closed end pipe: 5th order WEP *vs* WIP scheme (λ_i *vs* i) . . 90
7.32 Zoom of Fig. 7.31 90
7.33 Closed end pipe: 7th order WEP *vs* WIP scheme (λ_i *vs* i) . . 91
7.34 Zoom of Fig. 7.33 91
7.35 Closed end pipe: 5th order WEP *vs* WIP scheme ($\log e_i$ *vs* i) 92
7.36 Closed end pipe: 7th order WEP *vs* WIP scheme ($\log e_i$ *vs* i) 92
7.37 Cubic cavity: h–convergence for $\lambda_{[1,1,1]}$ 95
7.38 Convergence rates of Fig. 7.37 95
7.39 Cubic cavity: h–convergence for $\lambda_{[2,2,2]}$ 96
7.40 Convergence rates of Fig. 7.39 96
7.41 Cubic cavity: h–convergence for $\lambda_{[3,3,3]}$ 97
7.42 Convergence rates of Fig. 7.41 97
7.43 Cubic cavity: $\lambda_{[1,1,1]}$ *vs* $1/N_{DOF}$ 98
7.44 Cubic cavity: $\lambda_{[2,2,2]}$ *vs* $1/N_{DOF}$ 98
7.45 Cubic cavity: $\lambda_{[3,3,3]}$ *vs* $1/N_{DOF}$ 98
7.46 Cubic cavity: coupled modes with Hybrid 3rd order ($N = 1$) 100
7.47 Cubic cavity: coupled modes with Hybrid 3rd order ($N = 2$) and Hybrid 5th order ($N = 1$) 100
7.48 Rectangular cavity: eigenfunctions with the Hermite 3rd order $8-$node ($N = 1$) 102
7.49 Rectangular cavity: eigenvalues with the Hermite 3rd order $8-$node ($N = 1$) 102
7.50 Rectangular cavity: eigenfunctions with the Hermite 3rd order $8-$node ($N = 2$) 103
7.51 Rectangular cavity: eigenvalues with the Hermite 3rd order $8-$node ($N = 2$) 103
7.52 Rectangular cavity: eigenfunctions with the Hermite 3rd order $8-$node ($N = 3$) 104
7.53 Rectangular cavity: eigenvalues with the Hermite 3rd order $8-$node ($N = 3$) 104
7.54 Rectangular cavity: eigenfunctions with the Hermite 5th order $8-$node ($N = 1$) 107
7.55 Rectangular cavity: eigenvalues with the Hermite 5th order ($N = 1$) and the Hermite 3rd order ($N = 2$) 107
7.56 Zoom of Fig. 7.55 108

7.57 Rectangular cavity: Hermite 5th order ($N = 1, 3$) *vs* Hermite 3rd order ($N = 2, 5$) 108
7.58 Rectangular cavity: modes $[1, 1, 1]$ and $[2, 2, 2]$ with Hermite 5th order ($N = 3$) and Hermite 3rd order ($N = 5$) 109
7.59 Rectangular cavity: modes $[3, 3, 3]$ and $[4, 4, 4]$ with Hermite 5th order ($N = 3$) and Hermite 3rd order ($N = 5$) 109
7.60 Rectangular cavity: modes $[5, 5, 5]$ and $[6, 6, 6]$ with Hermite 5th order ($N = 3$) and Hermite 3rd order ($N = 5$) 109
7.61 Rectangular cavity: modes $[10, 10, 10]$ and $[11, 11, 11]$ with Hermite 5th order ($N = 3$) and Hermite 3rd order ($N = 5$) . 110
7.62 Cubic cavity: 5th and 3rd order Hermite elements *vs* Ansys . 110
7.63 Rectangular cavity: eigenfunctions with the Hermite 7th order ($N = 1$) 113
7.64 Rectangular cavity: eigenvalues with the Hermite 7th order ($N = 1$) and Hermite 3rd order ($N = 3$) 113
7.65 Cubic cavity: Hermite elements of orders 3, 5 and 7 114
7.66 Cubic cavity: 7th and 3rd order Hermite elements *vs* Ansys . 114
7.67 Rectangular cavity: eigenfunctions with the Hybrid 3rd order 8−node element ($N = 1$) 116
7.68 Rectangular cavity: eigenvalues with the Hybrid 3rd order 8−node element ($N = 1$) 116
7.69 Rectangular cavity: eigenfunctions with the Hybrid 3rd order 8−node element ($N = 2$) 117
7.70 Rectangular cavity: eigenvalues with the Hybrid 3rd order 8−node element ($N = 2$) 117
7.71 Rectangular cavity: eigenfunctions with the Hybrid 3rd order 8−node element ($N = 3$) 118
7.72 Rectangular cavity: eigenvalues with the Hybrid 3rd order 8−node element ($N = 3$) 118
7.73 Rectangular cavity: eigenfunctions with the Hybrid 7th order 8−node ($N = 1$) 120
7.74 Rectangular cavity: eigenvalues with the Hybrid 7th order 8−node ($N = 1$) 121
7.75 Zoom of Fig. 7.74 121
7.76 Cubic cavity: Hybrid 7th order ($N = 1$) *vs* Hybrid 3rd order ($N = 3$) 122
7.77 Cubic cavity: Hybrid 7th order ($N = 2$) *vs* Hybrid 3rd order ($N = 5$) 122
7.78 Rectangular cavity: eigenfunctions with the Hybrid 5th order 27−node ($N = 1$) 124

7.79 Rectangular cavity: eigenvalues with the Hybrid 5th order 27−node ($N = 1$) and Hybrid 3rd order 8−node ($N = 2$) . . 124
7.80 Zoom of Fig. 7.79 125
7.81 Rectangular cavity: eigenfunctions with the Hybrid 5th order 27−node ($N = 2$) 126
7.82 Rectangular cavity: eigenvalues with the Hybrid 5th order 27−node ($N = 2$) 126
7.83 Cubic cavity: Hermite 3rd order with Guyan 128
7.84 Cubic cavity: Hermite 5th order with Guyan 129
7.85 Cubic cavity: eigenvalue $[1, 0, 0]$ with Guyan and IRS 129
7.86 Cubic cavity: eigenvalue $[1, 1, 0]$ with Guyan and IRS 130
7.87 Cubic cavity: eigenvalue $[1, 1, 1]$ with Guyan and IRS 130
7.88 Cubic cavity: eigenvalues $1 - 8$ with $N = 2$ (Guyan and IRS) 131
7.89 Cubic cavity: eigenvalues $1 - 27$ with $N = 3$ (Guyan and IRS) 131
7.90 Free rectangular cross–section beam: λ_1 with Guyan 133
7.91 Free rectangular cross–section beam: λ_2 with Guyan 134
7.92 Free rectangular cross–section beam: λ_3 with Guyan 134
7.93 Free rectangular cross–section beam: λ_4 with Guyan 135
7.94 Free rectangular cross–section beam: λ_5 with Guyan 135
7.95 Free rectangular cross–section beam: λ_6 with Guyan 136
7.96 Free rectangular cross–section beam: λ_7 with Guyan 136
7.97 Free rectangular cross–section beam: λ_8 with Guyan 137
7.98 Free rectangular cross–section beam: λ_9 with Guyan 137
7.99 Free rectangular cross–section beam: λ_{10} with Guyan 138
7.100 Free square plate: Hybrid and Hermite 3rd order ($\bar{\omega}_i$ *vs* i) . . 140
7.101 Zoom of Fig. 7.100 141
7.102 Free square plate: Hermite 3rd order and 5th order ($\bar{\omega}_i$ *vs* i) . 141
7.103 Zoom of Fig. 7.102 142
7.104 Free square plate: $\bar{\omega}_1$ *vs* $1/N$ (left) and *vs* $1/N_{DOF}$ (right) . . 142
7.105 Free square plate: $\bar{\omega}_2$ *vs* $1/N$ (left) and *vs* $1/N_{DOF}$ (right) . . 143
7.106 Free square plate: $\bar{\omega}_3$ *vs* $1/N$ (left) and *vs* $1/N_{DOF}$ (right) . . 143
7.107 Free square plate: $\bar{\omega}_4$ *vs* $1/N$ (left) and *vs* $1/N_{DOF}$ (right) . . 143
7.108 Free square plate: $\bar{\omega}_{1-2}$ *vs* $1/N_{DOF}$ with Guyan 144
7.109 Free square plate: $\bar{\omega}_{3-4}$ *vs* $1/N_{DOF}$ with Guyan 144
7.110 Clamped square plate: $\bar{\omega}_1$ *vs* $1/N$ (top) and *vs* $1/N_{DOF}$ (bottom) with Guyan 145
7.111 Hinged rectangular plate: $\lambda_{[1,1]}$ and $\lambda_{[2,1]}$ *vs* $1/N_{DOF}$ 147
7.112 Hinged rectangular plate: $\lambda_{[1,2]}$ and $\lambda_{[2,2]}$ *vs* $1/N_{DOF}$ 147
7.113 Hinged rectangular plate: $\lambda_{[3,1]}$ and $\lambda_{[1,3]}$ *vs* $1/N_{DOF}$ 148
7.114 Hinged rectangular plate: $\lambda_{[3,3]}$ *vs* $1/N_{DOF}$ 148

7.115 Hinged rectangular plate: modes with Hermite 3rd order (and with $N = 2$) . . . 149
7.116 Zoom of Fig. 7.115 . . . 149
7.117 Hinged rectangular plate: modes with Hermite 3rd order (and with $N = 3$) . . . 150
7.118 Hinged rectangular plate: eigenvalues with Hermite 3rd order (and with $N = 3$) . . . 150
7.119 Hinged rectangular plate: modes with Hermite 3rd order (and with $N = 4$) . . . 151
7.120 Hinged rectangular plate: eigenvalues with Hermite 3rd order (and with $N = 4$) . . . 151
7.121 Hinged rectangular plate: modes with Hermite 3rd order (and with $N = 8$) . . . 152
7.122 Hinged rectangular plate: eigenvalues with Hermite 3rd order (and with $N = 8$) . . . 152
7.123 Hinged rectangular plate: eigenvalues with Hermite 3rd order and Guyan ($N = 4$) . . . 153
7.124 Hinged rectangular plate: eigenvalues with Hermite 3rd order and Guyan ($N = 4$) *vs* Ansys Solid-Shell ($N = 5$) . . . 153
7.125 Hinged rectangular plate: modes with Hermite 3rd order and Guyan ($N = 6$) . . . 154
7.126 Hinged rectangular plate: eigenvalues with Hermite 3rd order with Guyan ($N = 6$) . . . 154
7.127 Hinged rectangular plate: modes with Hermite 3rd order and Guyan ($N = 9$) . . . 155
7.128 Hinged rectangular plate: eigenvalues with Hermite 3rd order with Guyan ($N = 9$) . . . 155
7.129 Free square plate: Schemes A, B and C . . . 159
7.130 Free rectangular plate: λ_1 with Scheme C . . . 160
7.131 Free rectangular plate: λ_2 with Scheme C . . . 160
7.132 Free rectangular plate: λ_3 with Scheme C . . . 161
7.133 Free rectangular plate: λ_4 with Scheme C . . . 161
7.134 Free rectangular plate: λ_5 with Scheme C . . . 162
7.135 Rectangular cavity: $e_{[1,0,0]}$ with Scheme C . . . 162
7.136 Rectangular cavity: $e_{[1,1,0]}$ with Scheme C . . . 163
7.137 Rectangular cavity: $e_{[1,1,1]}$ with Scheme C . . . 163

8.1 The Hybrid 3rd order 8−node *vs* the Provatidis Element . . . 167
8.2 The Hybrid 3rd order 8−node and the Provatidis Element *vs* $1/N_{DOF}$ (eigenvalues $[1,0,0]; [0,1,0]; [0,0,1]$) . . . 168

8.3 The Hybrid 3rd order 8−node and the Provatidis Element *vs* $1/N_{DOF}$ (eigenvalues $[1,1,0];[1,0,1]$) 168
8.4 Cylindrical cavity: λ_1 *vs* $1/N$ and *vs* $1/N_{DOF}$ 170
8.5 Cylindrical cavity: λ_2 *vs* $1/N$ and *vs* $1/N_{DOF}$ 170
8.6 Cylindrical cavity: λ_3 *vs* $1/N$ and *vs* $1/N_{DOF}$ 171
8.7 Cylindrical cavity: λ_4 *vs* $1/N$ and *vs* $1/N_{DOF}$ 171
8.8 Cylindrical cavity: λ_5 *vs* $1/N$ and *vs* $1/N_{DOF}$ 172
8.9 Cylindrical cavity: λ_6 *vs* $1/N$ and *vs* $1/N_{DOF}$ 172
8.10 Simplified wing–box: lay–out 173
8.11 Simplified wing–box: ω_1 *vs* $1/N$ and *vs* $1/N_{DOF}$ 174
8.12 Simplified wing–box: ω_2 *vs* $1/N$ and *vs* $1/N_{DOF}$ 175
8.13 Simplified wing–box: ω_3 *vs* $1/N$ and *vs* $1/N_{DOF}$ 175
8.14 Simplified wing–box: ω_4 *vs* $1/N$ and *vs* $1/N_{DOF}$ 176
8.15 Simplified wing–box: ω_5 *vs* $1/N$ and *vs* $1/N_{DOF}$ 176

D.1 Hinged plate: 1st mode ($N = 6$; $h = .01$) 198
D.2 Simply–supported plate: 1st mode ($N = 8, 12, 14$; $h = .01$) . . 198
D.3 Simply–supported plate: 1st mode ($N = 14$; $h = .001, .01, .05$) 199
D.4 Simply–supported plate: 2nd mode ($N = 6$; $h = .01$) 199
D.5 Simply–supported plate: 3rd mode ($N = 6$; $h = .01$) 200
D.6 Simply–supported plate: 4th mode ($N = 6$; $h = .01$) 200

List of Tables

3.1 3rd order Hermite polynomials' coefficients 22
3.2 5th order Hermite polynomials' coefficients 22
3.3 7th order Hermite polynomials' coefficients 23

7.1 Closed–end pipe: convergence rates for eigenvalues 66
7.2 Closed–end pipe: convergence rates for eigenfunctions 66
7.3 Cubic cavity: convergence rates for eigenvalues 94

8.1 Relative errors (per cent) of Fig. 8.1 167

List of Acronyms

CAD *Computer Aided Design*

DOF *Degree of Freedom*

IRS *Improved Reduced System*

MDO *Multidisciplinary Design and Optimization*

WEP *With End Points*

WIP *With Intermediate Points*